DEVELOPMENT OF A NANOCOMPOSITE MICRONEEDLE BIOSENSOR FOR RAPID INTRADERMAL BIOANALYSIS

ELDHOSE SKARIA

PhD 2018

ABSTRACT

Intradermal bioanalysis via microneedle array (MNA) based electrodes are attracting significant research interests because their active components can be modified to selectively detect and monitor analytes of clinical interest in real-time; ranging from biofluids to solid tissues in a minimally invasive manner. The electrochemical detection strategies employed by these sensors are distinctly advantageous as they are generally low-cost, non-complex and can be effectively utilised by a minimally trained individual. However, clinical acceptability of MNA-based electrochemical sensors is dependent on developing highly selective and sensitive electrodes through a scalable fabrication strategy. The aim of this research was to therefore evaluate the potential of using carbon nanotubes (CNT's) based polymeric nanocomposites to develop electrochemical MNA-based electrodes.

A simple fabrication strategy of dispersing CNT's into epoxy resin via add/solution mixing and casting as MNA's was initially investigated. However, a poor interfacial interaction between the epoxy-resin and CNT's was found. Thus, a biodegradable polymer (poly (lactic) acid – PLA) was chosen as an alternative for the production of nanocomposites. A combinatorial approach involving carboxyl-functionalised MWCNT's and sonication produced nanocomposites with excellent interfacial interaction and minimal aggregation. Using this approach, nanocomposite MNA's were fabricated effectively at a maximum CNT loading of 6 wt%, at which the MNA's displayed improved mechanical strength and the optimal electrochemical properties. The nanocomposite MNA's were able to detect varying concentrations of ascorbic acid (AA), and demonstrated a linear oxidative response with a limit of detection (LOD) at 164.38μM and 16.79μM using differential pulse voltammetric (DPV) and amperometric, respectively. *In situ* electrochemical performance was further assessed in porcine skin. MNA's could detect active changes in the skin, characterised by the appearance of two oxidative peaks. Upon inducing an artificial burn wound, the oxidative response was significantly attenuated, and importantly the impact of the burn could be measured at progressive distances from the burn site.

Further optimisation was however required to reduce the MNA's resistive behaviour. Firstly, the method of sonication was investigated. Replacing the bath sonicator with a probe-type sonicator improved dispersions. The resultant 6 wt% CNT-loaded MNA's had a better LOD of 0.51μM for AA, when measured amperometrically. Secondly, the influence of different dimensionalities (i.e. shorter lengths and smaller diameters) and functional groups (-NH_2, -N_2 and -COOH) were evaluated. Results highlighted the need to lower the concentration at which the CNT's (particularly -NH_2 and -N_2 functionalised MWCNT's) were dispersed. The maximum loading that could be incorporated for the shorter MWCNT's with various functional groups was found to be 1 wt%. At this low CNT loading, the performance of -N_2 functionalised MWCNT-based MNA's was comparable to the sonication-optimised MNA's.

The biocompatibility of -N_2 and -COOH MNA's was then assessed *in vitro*. Exposure to MNA device-based extracts on the human keratinocyte cell line (HaCaT) and human malignant melanoma cell line (A375) produced contradictory results, possibly due the influence of released nanoparticulates from the MNA's. Toxicity was however only evident after a prolonged exposure to the extracts (i.e. ≥24 hrs). Further assessment using DPV and amperometric simulations showed no evidence of voltage-mediated cell toxicity.

In conclusion, this research highlights the potential of using CNT's based nanocomposites to produce electroactive MNA's, with limited toxicity, for bioanalytical studies. The fabrication steps are simple and easy to scale-up, and result in the development of MNA based electrodes in a single step.

CONTENTS

LIST OF TABLES

LIST OF FIGURES

ABBREVIATIONS

AA	Ascorbic acid
ACT	Acetaminophen
AE	Auxiliary Pt electrode
AFS	Axial fracture strength
ANOVA	Analysis of variance
BFC	Biofuel-cell
BSA	Bovine serum albumin
CCVD	Catalytic chemical vapour deposition
CE	Counter electrode
CGM	Continuous glucose monitoring
CMC	Critical micelle concentration
CNT's	Carbon nanotubes
CP	Conductive polymers
CPE	Carbon plate electrode
CPyCl	Cetylpyridinium chloride
CTAB	Cetyltrimethyl ammonium bromide
CTAC	Cetyltrimethyl ammonium chloride
CV	Cyclic voltammetric
CY	Cysteine
DA	Dopamine
DAB	Droplet-borne air blowing
DCM	Dichloromethane
DGEBA	Diglycidyl ether of bisphenol A
DLS	Dynamic light scattering
DMEM	Dubelcco's Modified Eagle Medium
DMSO	Dimethyl sulphoxide
DPV	Differential pulse voltammetry
DRIE	Deep reactive ion etching
EDC	1-Ethyl-3-(3-dimethylaminoproprly) carbodiimide
EDM	Electrical discharge machining
ELISA	Enzyme-linked immunosorbent assay
EMI	Electromagnetic interference
FBS	Foetal bovine serum
FDA	Food and drug administration
f-MWCNT	Carboxyl-functionalised multiwalled carbon nanotubes
GCE's	Glassy carbon electrodes
GOx	Glucose oxidase
HIPCO	High pressure carbon monoxide
ISE	Ion-selective-electrode
ISF	Interstitial fluid
ISO	International organisation of standardisation
IV	Intravenous

LCP	Liquid crystal polymer
LDH	Lactate dehydrogenase
LOD	Limit of detection
LSV	Linear sweep voltammetry
MEMS	Microelectromechanical systems
MNA	Microneedle arrays
MPA	3-Mercaptopropionic acid
MPOx	Methyl paraoxon
MTT	3-(4,5-Dimethylthiazol-2-yl)-2,5-diphenyl-2H-tetrazolium bromide
MWCNT	Multiwalled carbon nanotubes
NADH	Nicotinamide adenine dinucleotide
NHS	N-hydroxyscucciniminde
N-IUCD	Nitrogen incorporated ultrananocrystalline diamond
NO	Nitric oxide
OCT	Optical coherence tomography
OD	Optical density
OPH	Organophosphorus hydrolase
PAA	Polyamic acid
PB	Prussian blue
PBS	Phosphate buffered saline
PC	Pyrolysed carbon
PC	Polycarbonate
PCL	Polycaprolactone
Pd	Palladium
PD	polydopamine
PDMS	Polydimethylsiloxane
PEDOT	Poly(3,4-ethylenedioxythiophene)
PEI	Polyethyleneimine
PG	Porous graphene
PGA	Polyglycolic acid
PI	Polyimide
PLA	Poly(lactic acid)
PLGA	Poly(lactic-co-glycolic acid)
PMMA	Poly(methyl methacrylate)
POC	Point-of-care
PPD	Poly(o-phenylenediamine)
PS	Polystyrene
Pt	Platinum
PU	Polyurethane
RE	Reference electrode
RSD	Relative standard deviation
RT	Room temperature
SAM	Self-assembled monolayer

SDBS	Sodium dodecyl benzene sulfonate
SFS	Shear fracture strength
SMA	Shape memory actuator
SSMA	Straight silicon microneedle array
SWCNT	Single walled carbon nanotubes
SWV	Square wave voltammetry
T1D	Type 1 diabetes
TA	Texture analyser
TS	Tensile strength
TSMA	Tapered silicon microneedle array
TTF	Tetrathiafulvalene
UA	Uric acid
UHA	Ultrahigh aspect ratio
VAS	Visual Analogue Scale
WE	Working electrode
YM	Young's modulus

ACKNOWLEDGMENTS

I, first and foremost, wish to sincerely thank my supervisors Dr. Keng Wooi Ng, Dr. Melanie S. Flint and Dr. Bhavik A Patel Meikle for their continued guidance and support throughout the course of my PhD. They have been great mentors and a source of inspiration. I am particularly grateful to them for entrusting me with the confidence to independently develop my owns research ideas and pursue them deeply. I would also like to formally acknowledge the School of Pharmacy and Biomolecular Sciences for not only awarding this PhD studentship, but also for their continued investment in supporting national and international conferences.

I wish to extend my gratitude to colleagues of past and present who have helped me with various aspects along the course of this PhD. In particular, Dr. Andrew Flint for help with SEM; Mr Chris Morris and Mr Maurizio Valeri for help and support with tissue culture, Dr. Diapak Sarker for help with contact angle measurements and surfactant work and Dr. Santanu Ray for XPS-based analysis and experimentation. I also wish to thank the technical support team, especially Mrs Christine Smith. Lastly, I am thankful to Dr. Ryan Waters (Pirbright Institute, Pirbright, UK) for donating the porcine ears used in this research.

I am extremely grateful for the encouragement, care and support that I have received through the many friendships created. They have had a huge role in every step of this journey and helped create many and unforgettable joyous memories. In particular, I wish to thank Megi Kamenica, who has gone above and beyond to help me at challenging times. My lab partners Ella Sirjani, Gennaro, Blaise Geohegan who were at hand to help when needed and were a continued source of entertainment. Special mentions to Renee Flaherty, Haya Intabli, Myrthe Mampay and Marta Falcinell.

Above all, I wish to thank my parents, Mr. Skaria V Joseph and Mrs. Reeni Skaria; who have dedicated their life towards giving me the best opportunities in life. Without their support, love and innumerous packed meals none of this would have been possible. I want to thank my brother, Edin, who has been keeping my parents entertained for the long years I have been away. Last and but not least, to my dearest girlfriend, Rahaf Issa, you have been amazing. If I were to write to what I was thankful for, the list would be longer than my abbreviations list. You have helped in more ways than I could imagine, and I will never forget any of it; from the very first coffee together to the countless meals and discussions we have enjoyed, and more recently our fur-child, Frank. I look up to you professionally and personally. Needless to say, I yearn towards making a great team with you one day.

Finally, thank you to the prayers and blessing of my grandparents and loved ones.

AUTHOR'S DECLARATION

I declare that the research contained in this thesis, unless otherwise formally indicated within the text, is the original work of the author. The thesis has not been previously submitted to this or any other university for a degree, and does not incorporate any material already submitted for a degree.

Signed 

Dated 06-Aug-2018

Chapter 1. Introduction and literature review

1.1 Introduction

Microneedle arrays (MNA's) are medical devices consisting of several miniaturised replica of hypodermic needles that are designed to penetrate and target specific regions of biological membranes in a minimally invasive manner. By design, there are various classes of MNA's i.e. solid, coated, hollow, dissolving and hydrogel forming; that are produced from a wide variety of materials, in different sizes and shapes. Typically, individual microneedles feature lengths of up to 1mm and are hundreds of micrometres wide. These devices have been designed as microarray patches to perforate the skin, but their use on other organs has been explored, including the eye[1] and colon[2].

The concept of using skin-perforating needles, 'preferably 1-2mm in length' was first recorded in 1948 for drug delivery applications[3]. Descriptions of such devices for similar applications did not appear until a decade later[4] and the first patent, submitted by Gerstel and Place, was approved in 1976 for applications in drug delivery, based on a device consisting of a plurality of micron-sized projections extending from a drug reservoir[5]. However, microneedle research only intensified in the mid 1990's, as the microelectronics industry revolutionised manufacturing tools that facilitated precise and scalable fabrication of microneedles[6]. Research group led by Prausnitz then coined the term 'microneedle' and published a novel study on micro-fabricated needles to enhance transdermal drug delivery[7]. This earmarked the beginning of a plethora of researches over the next decade, describing novel applications in dermal immunisation[8], delivery of macromolecules and nanoparticles[9], bioanalytical sensors based on both dermal interstitial fluid (ISF) extraction and analysis[10] or *in* situ monitoring[11,12] and finally, point-of-care (POC) molecular diagnostic devices[13]. Intensified research efforts in these areas has now helped establish MNA's as an enabling medical device technology, supported by the public and clinicians for their use in clinical practice.

Transdermal delivery of drugs and vaccines represents the most studied applications in microneedle research to date. The transdermal route offers distinct advantageous over conventional means such as oral administration and injections. These include: (1) avoidance of degradation in the gastro-intestinal tract and bypassing the hepatic first-pass effect of the liver; (2) maintenance of a relatively constant plasma concentrations; thereby avoiding

toxicity and inefficiency associated with fluctuations; (3) potential for targeted delivery, especially of vaccines to antigen-presenting cells in the skin, and finally, (4) those associated with microneedles themselves i.e. elimination of pain, discomfort and needle phobia resulting in improved patient compliance, reduced risk of infection and potential for self-administration by the patients themselves[6,14–16].

The aim of this review is to highlight recent findings on MNA based diagnostic and bioanalytical sensors with particular emphasis given towards their fabrication, architecture and method of analysis. Research concerning these applications is continually emerging and offering divergent applications aside of MNA based Continuous Glucose Monitoring (CGM) devices; which remains to the most active area of research in this field to date. The skin in replete with disease markers, small molecules, proteins and lipids that are either circulating or constitutively present. As such it offers a unique window to monitor the body's health[17]. However, skin chemistry is rarely used in routine clinical practice due to a lack of convenient and standardised method for routine collection of biomolecules from the skin. Histopathological analysis, though is the gold standard, is limited by its qualitative and variable nature[18,19]. Developing MNA based sensors is therefore most advantageous as it can be utilised to extract quantitative information in a fast, reliable and pain-free manner for frequent monitoring and diagnostic purposes. Moreover, transdermal biosensing via MNA based devices that are integrated with biochips, offers the potential to move laboratory scale instruments into miniaturised platforms that can be utilised by a minimally trained individuals[20]. Thus, it can radically transform clinical practice into a more efficient, economically viable and highly accessible format.

MNA based transdermal sensors can be broadly distinguished into two types i.e. one that can extract biofluid for analysis outside of the skin and the other capable of performing *in situ* bioanalysis. Initially research into CGM devices are discussed by differentiating various formats of such sensors. This is followed by an in-depth analysis of current literature on bioanalytical and diagnostics devices, again differentiated by their design. Finally, future directions are pointed out and discussed in line with the goal of this thesis.

1.2 Continuous glucose monitoring

The primary form of treatment for type 1 (where insulin is not produced) and some advanced type 2 diabetes (associated with the inability to use the insulin effectively) is insulin replacement[21,22]. This entails periodic monitoring of blood glucose levels and

intermittent insulin injections into the subcutaneous tissue to maintain normoglycemia. Subcutaneous injections using syringe needles causes pain and trauma, all of which negatively influence patient adherence to an optimal treatment regime[23,24]. Since insulin production is non-linear and injections cannot replicate optimum levels, this form of treatment is rather, "approximate" (Figure 1.1)[23,25]. Therefore, minimally invasive CGM devices combined with optimal drug delivery methods offers much effectiveness, improves compliance and are convenient for the patients. CGM devices were first approved by the Food and Drug Administration (FDA) for managing diabetes in 1999[24,26]. However, they were used mainly from a diagnostic viewpoint i.e. to identify episodes of hyperglycaemia (high blood glucose) and hypoglycaemia (low blood glucose), in order to adapt insulin therapy[24]. Commercially available continuous CGM devices are based on an electrochemical technique i.e. amperometry, utilising the enzyme glucose oxidase (GOx) to detect glucose in the ISF[10,27].

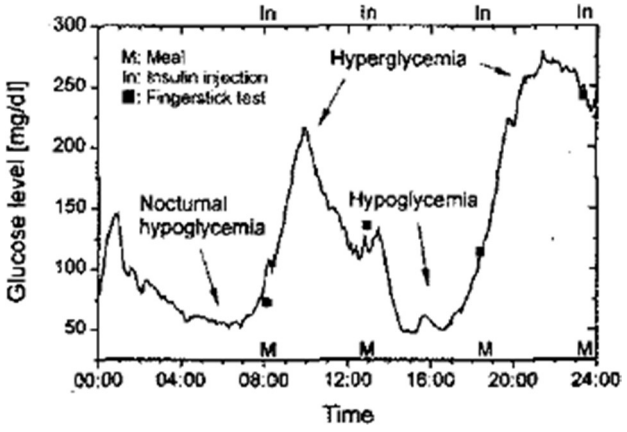

Figure 1.1. Continuous glucose monitoring from ISF using MiniMed CGMs™ compared with finger stick measurements. Data shown, is from a patient with type 1 diabetes. Glucose levels are seen to change rapidly (i.e. non-linear, 2.25 mg/dl/min); therefore, not all episodes of hypoglycaemia and hyperglycaemia (especially nocturnal hypoglycaemia) are detected by finger stick measurements. Treatment with insulin in therefore an approximate. Reprinted with permission[25]. Copyright © 2003, IEEE.

The most widely used CGM device in clinical practice today is based on a needle-type enzymatic electrochemical sensor that monitors glucose from ISF in the subcutaneous tissue. There is a high correlation between glucose levels in the ISF and the blood, but with an estimated lag time of 0 – 45 mins[28], with a mean of 6 – 7 mins[29]. This is because, the glucose concentration in the ISF is dependent on blood flow, metabolic rate and the rate of change of glucose concentration in the blood[24]. The lag means that, CGM devices require calibration against the blood, up to 4 times a day. Nevertheless, CGMs have been proven to be useful in detecting episodes of hyperglycaemia and hypoglycaemia; resulting in overall

better glycemia control. On quantification of the effectiveness of CGM devices on regular usage has shown that, for every 1-day increase in sensor usage per week, the levels of glycated haemoglobin (HbA1c) was reduced by 0.15%[30]. Despite these advantages, their major limitation is associated with invasiveness and discomfort, which reduces patient compliance over long-term usage[31]. Functionally, the sensor accuracy of CGM devices have been demonstrated to be reduced over the hypoglycaemic range, whilst surface deposition of proteins and cells, alongside tissue encapsulation results in signal drift, reduced accuracy and limited life span[31,32]. Microelectromechanical systems (MEMS) technologies are ideally positioned to address the limitations associated with the CGM devices, including MNA based devices[25].

MNA based CGM sensors are being developed with the aim of reducing invasiveness, whilst improving sensor accuracy and life span by its transdermal application; and have been predicted to be significantly better than current CGM devices. Research into MNA based CGM devices at the early stages were primarily concerned with the extraction of blood or ISF using microneedles for measurement of glucose via a standard off-line commercial method or by in-line microfluidic devices. However, recent research has now showcased various *in situ* devices capable of monitoring glucose content in the ISF continuously.

1.2.1 Microfluidic sensors

Biofluid extraction using microneedles have been typically carried out using hollow microneedles. In this approach, blood or ISF is draw up into cavities of the hollow microneedles via capillary action by combination of surface tension and adhesive forces. This fluid is then fed into an analytical chamber through a microfluidic system for analysis outside of the skin. The analytical chamber incorporates the enzyme GOx, which catalyses the oxidation of β-d-glucose to β-d-glucono-1,5-lactone (gluconic acid) and hydrogen peroxide (H_2O_2), using molecular oxygen as an electron acceptor. Quantification of glucose is then achieved by detecting the hydrogen peroxide generated or the oxygen consumed. There are three generations of GOx biosensors (Figure 1.2)[33]. In the first generation, as previously mentioned, oxygen is used an electron acceptor and H_2O_2 generated is measured. The second generation of sensors uses an artificial electron mediators or redox dyes to transport electrons from the enzyme active site to the electrode. The reduced electron acceptors are then monitored electrochemically or calorimetrically in order to quantify

glucose concentration. Artificial electron mediators used instead of oxygen, helps reduce interference from other redox species and can also account for errors due to variations in the concentration of oxygen in the blood. However, artificial electron mediators are toxic. Therefore, third generation sensors have been developed, which can facilitate direct electron transfer to the electrode. In terms of MNA's for glucose monitoring, majority of the research have focused on the development of 1st and 2nd generation type devices. The following subsections address the state-of-the-art of MNA based CGM's depending on their type.

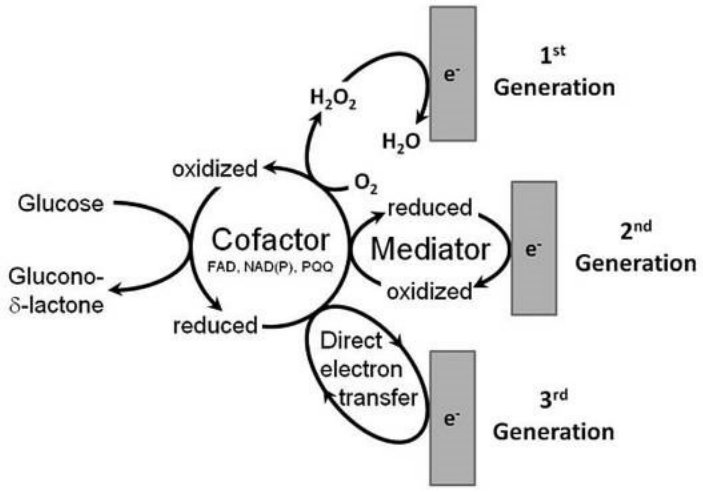

Figure 1.2. Schematic representation of the three generations of glucose sensors. Initially, electrons from the oxidation of glucose are taken up by the enzyme's cofactor. They are then transferred onto: molecular oxygen to form a 1st generation sensor; to a mediator to form a 2nd generation sensor and finally, onto the electrode surface directly to form 3rd generation sensors. Reprinted with permission[33]. Copyright © 2011, Diabetes Technology Society, SAGE.

1.2.1.1 Analysing Blood glucose

In the year 2000, Smart and Subramanian published the first study towards commercialisation of a glucose monitoring device fabricated by MEMS technology consisting of a 2 mm long hollow silicon microneedle, connected via a microfluidic channel to a silicon microcuvette incorporating assay reagents to convert glucose to gluconic acid, using the tetrazolium salt MTT [3-(4,5-Dimethylthiazol-2-yl)-2,5-diphenyl-2H-tetrazolium bromide] as an electron acceptor (i.e. glucose dehydrogenase-formazan dye chemistry)[34]. The reduced MTT, known as a formazan dye, absorbs in the visible region and its optical absorbance was measured at λ_{max} = 621 nm using an optoelectronic device. *In vitro* analysis showed the device to draw in whole blood efficiently by capillary action alone. The results obtained from the whole blood assay using the microneedle-based device was comparable to that of a commercial system (HemoCue β-Glucose analyser; employing the same assay

chemistry), with an average coefficient of variation at 5.12%. Clinical studies showed good mechanical robustness, and importantly, out of the 62 subjects tests, 73% percent said the pain to be barely/non-noticeable. Only 2% said the device was somewhat painful. Despite these results, a calibration for the glucose assay was not given and the silicon microchip used was for single usage. Significant challenges were also pointed out in terms of reagent formulation, sterilisation procedure, optimisation of shelf-life and finally, integration of an electrochemical sensor in their system.

Kobayashi *et al.* introduced the concept of "intelligent mosquito", a device comprising of a hollow 1 mm long platinum (Pt) microneedle integrated with a sampling mechanism that employed a volume phase-transition gel (poly(N-isopropylacrylamide)) (polyNIPAAm), together with a GOx enzymatic biosensor to measure glucose in the blood amperometrically by measuring H_2O_2[35]. The goal behind this approach was to develop a system that draws in the sample solution in response to the human body temperature. The microsystem (Figure 1.3) was obtained by bonding a silicon substrate containing the sampling mechanism and a microneedle, to a glass substrate that incorporated the biosensing chip. The phase-transition gel was formed inside a microcontainer that was etched onto the silicon substrate, and the biosensing components including the Ag|AgCl reference electrode (RE), the auxiliary Pt electrode (AE), and the Pt working electrode (WE) was patterned photolithographically onto the glass substrate. The GOx oxidase enzyme was immobilised on to the Pt WE and connected to the microcontainer through an inlet flow channel. The sampling mechanism (i.e. the extraction of biofluid) worked on the basis of changing temperature in pure water, which causes the gel to shrink and expand (Figure 1.3, C.1 – C.3). This resulted in a pressure change inside the flow channel, which consequently withdraws biofluid for analysis. The complete working device was able to produce a linear response for glucose concentration below 5mM. However, there were significant challenges to be resolved, such as the reduced sensitivity and longer response times, as compared to devices fabricated without the microneedles; found during independent evaluation of each component. Sampling temperature was outside the physiological range (the gel shrunk at 40°C and drew in the sample at 30°C) and the pumping mechanism was one directional, i.e. it did not allow the

glucose solution to be pumped outside of the microsystem. This is detrimental because even for a one-off measurement, a single pumping out mechanism is necessary.

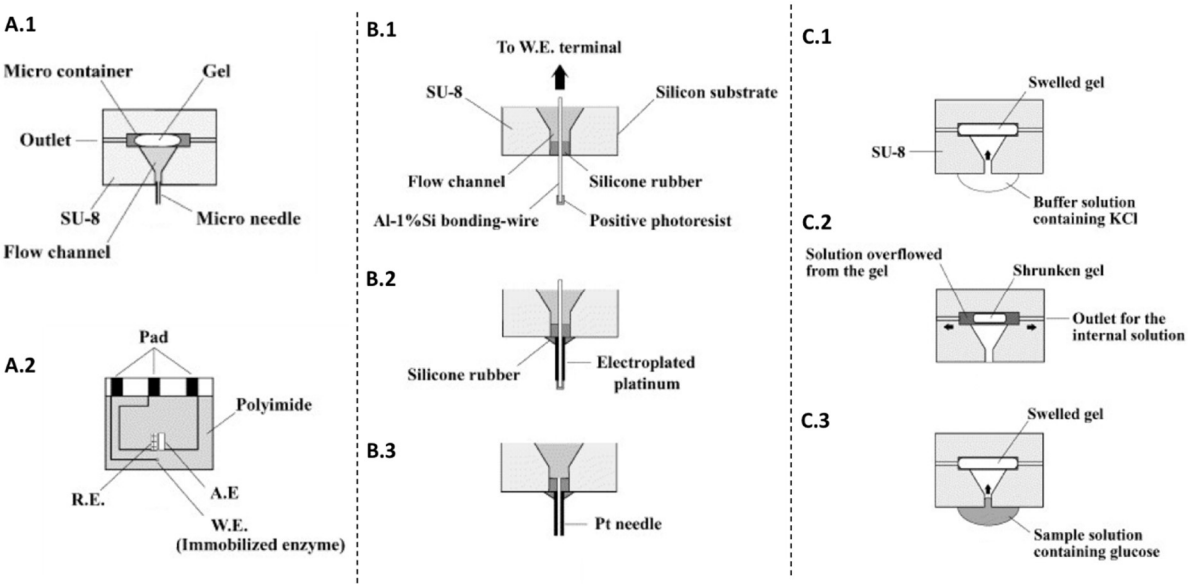

Figure 1.3. Fabrication and functioning of the intelligent mosquito. Construction of the microanalysis systems is shown in A.1 and A.2. The former shows a *silicon substrate* with a micro-container for incorporating the gel, a flow channel connecting the microneedle to the gel and outlets for the solution to flow out of the gel. The latter is a *glass substrate* with electrodes patterned by photolithography. The pad interfaced with a potentiostat. The *silicon* and the *glass* substrates were bonded together to form the complete system. B.1 – B.3, shows construction of the microneedle. The three consecutive steps involved were: (B.1) fixation of an Al-1% Si wire into the flow channel using a silicon rubber and ensuring that it is protruding from the micro-container in order to make an electrical contact, (B.2) electroplating platinum and finally, (B.3) removal of the positive photoresist and dissolving the Al-1% Si wire to form a microneedle with a bore diameter of 50 μm. C.1 – C3 illustrates functioning of the sampling mechanism. Initially, the flow channel is filled with a buffer solution (C.1). The gel then shrinks at 40°C, expelling the solution out through the outlets. (C.2) The gel then swells at 30°C, creating a pressure difference and pulling the sample solution inwards. Reproduced with permission[35]. Copyright © 2001, Elsevier.

A year later, the same group reported an improved device (based on the same principle as above), that addressed the chief issues associated with the operating temperature of the sampling mechanism and the unidirectional pumping mechanism[36]. In this improved device, a reversible sampling mechanism was introduced. As compared to the above device, two microcontainers was etched onto a silicon substrate, one that incorporated the gel and the other to store expelled water as the gel shrinks; serving as a reservoir. This meant that only the extracted volume is fed into the flow channels as opposed to their previous design above. The reversible sampling was achieved by using the elasticity of a silicon rubber layer formed underneath the gel in order to separate it from the flow channel. This functions by causing reversible movement in response to gel transitions i.e. at temperatures lower than

the gel transition temperature, water from the reservoir is absorbed by the gel, pushing the silicon rubber into the flow channel; whereas when the external solution is sucked in at higher transition temperature, the gel shrinks, and the silicon pushes inwards preventing the collection of expelled water along the with sample. The functioning of this device was successfully demonstrated *in vitro*, detecting glucose concentrations in the range of 0 – 12 mM glucose, up to 8 mM in the linear range (improved response as opposed to the previous device). The response time of the biosensor had also improved; from 1 – 4 mins in the previous device to 30 – 40 s in the device described here. However, the authors described continuous sampling to become more time consuming and laborious, because of the small inner diameter of the microneedle.

In the work that followed, a disposable continuous sampling and monitoring device was described as opposed to the single use devices above[37]. The same components were used, but adaptations were made to enable continuous sampling. GOx enzyme was immobilised on a Nafion layer to prevent interfering compounds, and enzyme layer was coated with a diffusion-limiting membrane of poly(2-hydroxyethylmethacrylate) (polyHEMA) to reduce the consumption of glucose. The microneedle was made of stainless steel, with 1 mm length and bore diameter of 50 μm. Continuous sampling needed a larger volume change and a low sampling rate, therefore polyNIPAAm was copolymerised with acrylic acid to introduce ionized moieties in the polymer backbone. In general, as the ionisation increases, the transition temperature and the volume change increases. However, this modification alone cannot induce sufficient volume change, hence three other functionally related factors were also investigated i.e. variation in temperature (20 to 37°C), temperature and pH (alkaline buffer in the gel and acidic buffer in the reservoir), and GOx enzyme loaded gel (5 mM KH_2PO_4–NaOH buffer solution at pH 7.0), where the gel shrunk, in response to pH change caused by the production of gluconic acid. It was found that, the sampling rate slowed down more effectively with the GOx enzyme loaded gel as compared to the other two where the sampling rate was 73 and 24 μl h^{-1}, respectively. The sampling rate for the enzyme loaded gel was 4 μl h^{-1} and it withdrew solutions continuously for 10 hrs. Hence, the GOx enzyme gel system was utilised in the microsystem and biosensor was evaluated with randomly changing glucose concentration over the range of 0 to 20 mM. The calibration curve obtained as a result showed a linear response from device. The authors described the major challenge that remained, is associated with the fabrication of

microneedles with sufficient mechanical strength and appropriate shape, so that it penetrates without breaking and remains in the skin.

Another microneedle-based blood sampling system for glucose monitoring was reported by Tsuchiya *et al.*[38]. This device consisted of a hollow 1 mm long titanium microneedle with a bore diameter of 25 μm; an indentation unit making use of shape memory actuator (SMA) for microneedle insertion into the skin; a bimorph piezoelectric actuator (i.e. micropumping system) to generate negative pressure for extracting blood and lastly, a biosensing component for detection and evaluation of glucose. *In vitro* characterisation was completed with another microneedle device however, made of stainless steel with a bore diameter of 100 μm, operating at a resonant frequency of 25 kHz (applied voltage of 20 V). The sampling rate of whole blood using this device was 2 μl min^{-1}, comparable to that of a female mosquito. Glucose detection was demonstrated by a single measurement at 0.5 mM, after an extraction time of 30 s. Therefore, no calibration was provided. On monitoring the output voltage of the biosensor, a voltage peak was identified at 30 s, which decreased until 120 sec, where a steady state was reached.

Due to challenges associated with miniaturisation, systems integrations, and complexity of the devices in achieving good reliability and reproducibility, progressive research on the devices above were not carried out and in fact the concept of blood sampling microneedle-based glucose monitoring system had been overlooked for several years. Li *et al*. recently proposed novel blood-extraction system consisting of; an ultrahigh aspect ratio (UHA) hollow nickel microneedle, a polydimethylsiloxane (PDMS) elastic self-recovery actuator (referred to as a PDMS switch)[39] and a PDMS chamber with an inlet and outlet valve to control the extraction and transport of blood for analysis. The working principles of the device is illustrated in Figure 1.4. Briefly, the system is activated by pressing the PDMS switch with a finger, when then drives the microneedle into the skin. This in turn activated pneumatic force inside the chamber leading to a sequence where the inlet valve is closed, and the outlet is open, driving air out of the chamber and when the finger compressive force is removed, the reserve occurs building up negative pressure and results in the biological sample being drawn into the microsystem. Once the chamber is filled, the microneedle retracts and the PDMS switch is pressed again, allowing transport of the blood through the open outlet valve for analysis. Utilising this mechanism, both *in vitro* and *in vivo* extraction was demonstrated, at a flow rate of 0.2 μL s^{-1} with a 60 μm bore microneedle. A glucose analysis system was not reported in this study. The study that followed later,

assessed the characteristics of the microneedles themselves i.e. inner diameter (bore), tip diameter and bevelled tip angles[40]. Nickel was the metal utilised. The optimum dimensions for a fixed length microneedle (i.e. 1,800 μm long with an outer dimeter of 120 μm) that is mechanically strong and can penetrate the skin effectively was required to have a bore diameter of 60 μm, and a bevelled tip angle of 15°C. The extraction rate for this device was 0.8 μL s^{-1}; demonstrated *in vivo*. An analysis system was not fabricated here either and moreover, haemolysis of blood following extraction and biocompatibility issues associated with nickel are issues that needs careful consideration before clinical translation. Importantly, the current format of the device is for single usage only.

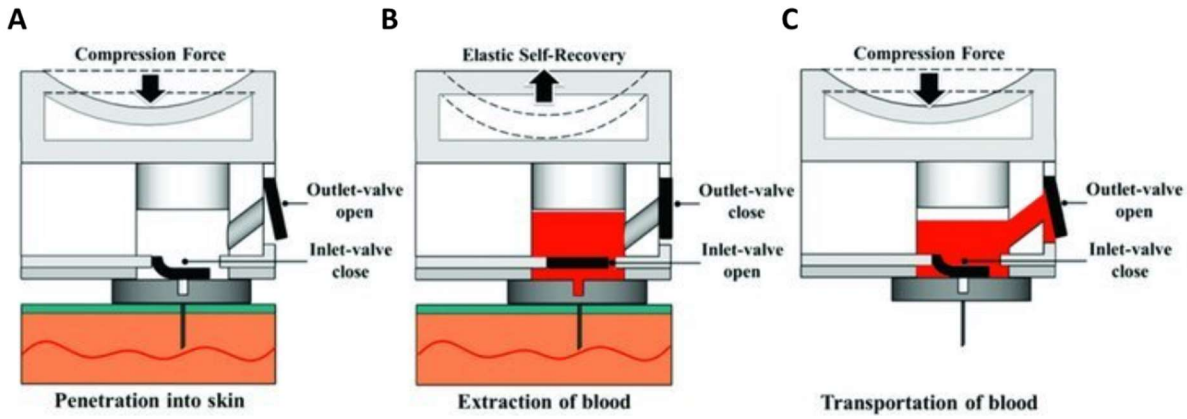

Figure 1.4. Functioning of the elastic self-recovery actuator integrated with a hollow nickel microneedle. A – C, shows the process of whole blood extraction and transportation with reference to activation by thumb pressure (i.e. compressive force). Reprinted with permission[39]. Copyright © 2012, John Wiley and Sons.

The first *in situ* blood glucose monitoring device was reported by Windmiller *et al*. in 2011[11]. Developed by standard UV rapid prototyping technique using E-Shell 200 (an acrylate-based polymer), the authors presented a novel bi-component design in which hollow pyramid-shaped microneedles with a triangular base (dimensions: 1174 ± 13 μm in length, 1366 ± 15 μm in height and 342 ± 5 μm bore diameter) housed solid conical shaped microneedles (dimensions: 390 ± 13 μm in dimeter and 818 ± 35 μm in height) (Figure 1.5). The two layers were affixed using non-conductive epoxy. To enable biosensing, the solid microneedles were coated with a layer of Pt (~12 nm) using pulse laser deposition. Poly(o-phenylenediamine) (PPD) film was then electropolymerized onto the solid microneedles for entrapment of GOx enzyme and to prevent interference from other electroactive compounds; whilst measuring the enzymatic biproduct H_2O_2. Chronoamperometric detection of glucose showed well defined responses that were linear at a range of concentrations (0 – 14 nm), with high sensitivity (0.353 μA mM^{-1}), low standard deviation

(SD) between devices (i.e. 6.44%) and a detection limit of 0.1 mM. This device also showed excellent selectivity, when the electrochemical measurements were carried out in the presents common interferants such as ascorbic acid (AA), uric acid (UA), cysteine (Cys) and acetaminophen (ACT) at physiological concentrations. SD for the response at 10 mM glucose concentration, was negligible, in the range of 0.88 – 2.21%. The biosensor also showed excellent stability over time, as 97% of the signal was retained over a period of 8 hrs for 10 mM glucose concentration.

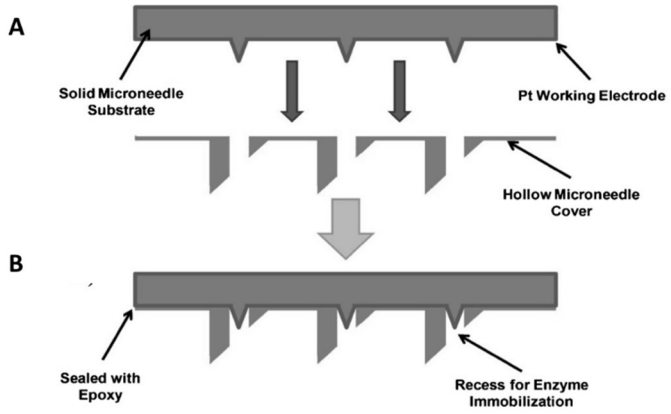

Figure 1.5. Bi-component design. (A) Solid and hollow microneedle components fabricated using E-Shell 200, with the former coated with platinum to form an electroactive surface. (B) components were assembled and sealed with non-conductive epoxy, and the enzyme was immobilised into the recess as shown. Reprinted with permission[11]. Copyright © 2011, John Wiley and Sons.

Utilising a similar approach as above, Innervale *et al*. electropolymerized a conducting polymer, poly(3,4-ethylenedioxythiophene) (PEDOT) to entrap GOx on the surface of stainless steel and Pt coated stainless-steel microneedle electrodes (Pt thickness 450 nm) and measured glucose concentrations (2 – 26 mM) chronoamperometrically[41]. PEDOT is advantageous, because it provides a low voltage signal transduction pathway and importantly, the swelling of the polymer is sufficient for glucose diffusion to the enzyme, while not large enough for the enzyme to escape. On evaluating the biosensor, Pt coated microneedles were found to be better, sensing glucose over the entire concentration range of 2 – 26 mM, whereas the stainless-steel microneedle detected glucose in the range of 4 – 12 mM and had a high signal to noise ratio of 33.8, as compared to 9.0 for the Pt coated microneedle. The effect of electrochemical interferents in blood were also analysed, and the signal from glucose biosensor was far higher than any of the interfering compounds. Regardless of the storage conditions i.e. wet or dry, the Pt coated biosensor maintained high linearity as opposed to the stainless-steel microneedle. However, the measurement range

was higher at ~22 mM when stored in PBS in comparison to dry storage conditions, where it was reduced to ~14 mM.

An integrated microneedle-based three-electrode enzyme free sensor and its characterisation *in vitro* was reported by Yoon *et al.*[42]. The enzyme free sensor is beneficial, as it avoids problems associated with stability and loss of activity from long-term storage. Importantly, the performance of GOx enzyme-based electrodes is limited by the fact the enzymes' active centre is covered by a protein shell, making electron transfer between the enzyme and the electrode a difficult process. This can be overcome by using nano-scale electrodes, which provides a greater electroactive surface area, resulting in enhanced electrocatalysis. Therefore, Yoon *et al.* fabricated silicon microneedles that were 380 μm in height and achieved a tip diameter smaller than 1 μm through an anisotropic dry etching process to form micropillars, followed by a wet etching process. A 500nm layer of silicon dioxide was then deposited onto silicon microneedles by plasma enhanced chemical vapour deposition. This was followed by iron catalyst deposition by electron beam evaporation in specified areas on the array (through a shadow mask) to create the WE and counter electrodes (CE). In order to increase the electroactive surface area on the microneedles, a vertically aligned forest of multiwalled carbon nanotubes (MWCNT's) were grown directly on iron-coated silicon microneedles and moreover, Pt nanoparticles was electrodeposited on the surface for enhancing non-enzymatic electrochemical reaction. An integrated RE was fabricated similarly, but after a selectively deposition a layer of titanium, followed by silver (Ag) deposition. The silver layer was then chlorinated with 1 M KCl/HCl buffer with applied current to form Ag/AgCl reference electrode. This three-electrode sensor was tested by chronoamperometry to measure different concentrations of glucose (i.e. 3 – 20 mM) *in vitro*. A linear response was seen, in response to additions of glucose at 3 mM concentration at regular intervals. The sensitivity of this microneedle-based sensor was 17.73 ± 3 μA mM^{-1}, which is on par with or higher than other non-enzymatic sensors reported in the literature. This is owed to the enhanced surface area provided by the MWCNT forest and the Pt nanoparticles.

1.2.1.2 ISF based glucose monitoring

1.2.1.2.1 Microfluidic devices

Over the period of 2003 to 2005, it was addressed whether microneedle technologies can be utilised to extract ISF rather than blood. Zimmerman *et al.* was the first to develop

an in-device self-calibrating enzymatic glucose sensor, monitoring ISF, in 2003[25]. Eight "volcano-like" hollow microneedles were made out of silicon by means of both anisotropic and isotropic etching steps, with a length of 200 μm and a bore dimeter of 40 μm. These effectively pierced the skin and sampled ISF from the epidermis by capillary forces. For in-line electrochemical detection, the ISF was then transported to a porous poly-silicon dialysis membrane, where the larger proteins are retained (in order to improve long-term sensor stability) and the remainder was mixed with a buffer solution and pumped past an integrated enzyme-based flow through sensor. H_2O_2 derived as by product of the catalysis was oxidised at the working electrode and the resultant current was measured. Preliminary calibration of the biosensor for glucose concentrations in the range of 0 – 600 mg dL^{-1} indicated a linear response between 0 – 160 mg dL^{-1}, at an optimum flow rate of 25 μL min^{-1}. When the measurements were made in the skin, a significant sensor response was seen, however it was found that there were large variations in the measured current; resultant of the fact that capillarity was insufficient to maintain a constant flow rate through the microneedle. As a result, a calibration of the whole microsystem was not provided.

In contrast, Mukerjee *et al.* demonstrated that ISF extraction is possible by capillary action alone[43]. The microsystem was made of a silicon/glass bilayer chip with a 20 x 20 array of hollow silicon microneedles that were integrated with fluidic channels for ISF extraction on the front side and a reservoir for storage of the extracted ISF via microchannels on the back side. The microneedles were fabricated by a combination of processes such as deep reactive ion etching (DRIE), diamond blade circular sawing and isotropic etching. An array consisted of 400 microneedles, that were 250 – 350 μm tall, with a base dimeter of 120 μm. ISF extraction by capillary action occurred through the microneedle bores with a diameter of 10 – 15 μm in approximately 10% of the 400 microneedles per chip (i.e. only those in centre were hollow, and the others were solid; which aided in skin penetration by stretching the skin and also ensured good anchorage). Although different designs were evaluated i.e. volcano-like, micro-hypodermic and snake-fang; only snake-fang shaped microneedles were used to demonstrate ISF extraction. In order to evaluate the performance of the microsystem, the microneedle was pressed against the authors earlobe and held in place for collection of ISF. It was found that, between 20 – 30 mins was initially required to fill the reservoir. In order to validate that the fluid filled was indeed ISF, a simple glucose detection assay was performed by placing a commercial calorimetric glucose strip inside the reservoir. The colour change from clear to deep blue indicated glucose concentration in

the range of 80 – 20 mg/dl and this correlated well with blood glucose measurements using the same type. Contrary to that of Zimmerman's device, an opening at the distal end of the reservoir allowed evaporation to take place and thus a pressure gradient was built up allowing for continuous draw of ISF from the skin. However, no calibration against glucose concentration was provided yet again.

Wang *et al*. applied negative pressure by vacuum to resolve the time lag using physiologically inert glass microneedles and demonstrated *in vivo* extraction followed by *in vitro* glucose detection[10]. A thermal puller was used to fabricate individual or an array of microneedle of conical shape with a tip radius of 15 – 40 μm, to penetrate 700 – 1500 μm deep into the skin. Although the microneedles had a hollow bore, the tips were sealed by melting glass to increase mechanical strength. Thereby, the function of the microneedle was only to pierce a hole in skin for ISF, as a form of bloodless lancet. The authors claimed that separate experiments were carried to determine whether ISF could be extracted through the bore of the microneedle, but it failed to do so. Hence in this study, ISF was extracted by applying a negative pressure of 200 – 500 mm Hg for either 2 – 10 mins in rat or 5 – 20 mins in humans. The ISF samples were immediately analysed using a glucose strip. In agreement with previous findings, Clark's Error Grid Analysis demonstrated excellent correlation on comparing blood glucose and ISF levels with 95% and 100% of measurements (in 15 rats and 6 human subjects respectively) falling in the clinically relevant A + B region. Finally, a kinetic study evaluated glucose levels in ISF and blood glucose levels at 20 min intervals before and after 1 U of intraperitoneal insulin injection. The measurements showed a rapid decrease in blood glucose levels following insulin injection in blood, followed closely by glucose levels in the ISF. Given the resolution of the device was 20 mins, there was no significant time lag between ISF and blood glucose levels.

More recently, Chua *et al*. reported the use of hollow silicon MNA for CGM[44]. The study investigated impact of microneedle shape in facilitating efficient uptake of ISF and measurement of glucose levels. By employing silicon micromachining, two different shapes of microneedles were produced; a straight silicon microneedle array (SSMA) and a tapered silicon microneedle array (TSMA) (Figure 1.6, A). Both devices contained a similar number of microneedles; were similar in height and had a bore diameter of 50 μm. A CGM system was assembled, by having an electrochemical biosensor (with screen printed Pt WE and Ag|AgCl RE and CE) and the MNA affixed on the opposite sides of a sensor chamber (Figure 1.6, B). After application of the MNA into the skin (application velocity ~10 ms^{-1}),

the sensing chamber was filled with phosphate buffered saline (PBS). This resulted in the diffusion of glucose from the ISF through the MNA lumens into the sensing chamber. The WE was functionalised with GOx chemistry, measuring (via amperometry) the reduction of H_2O_2; generated from the oxidation of glucose. *In vivo* experiments were carried using both types of MNA's on human subjects fasted for 2 hrs, followed by consumption of a meal to increase blood glucose levels. The total experiment lasted 6.5 hrs. It was found that, although both sensors were able to match the levels of glucose closely to the reference blood glucose values (90 – 220 mg dL^{-1}), the SSMA was found to produce lower sensor current (100 – 250 nA) as compared to the TSMA (200 – 400 nA). Examining the penetrations caused by the two MNA's, it was found that the SSMA lumens are prone to blockage caused by displacement of the skin, whereas the occurrence of such is unlikely to happen when using the TSMA's. Hence, the sensor current for the TSMA's were higher.

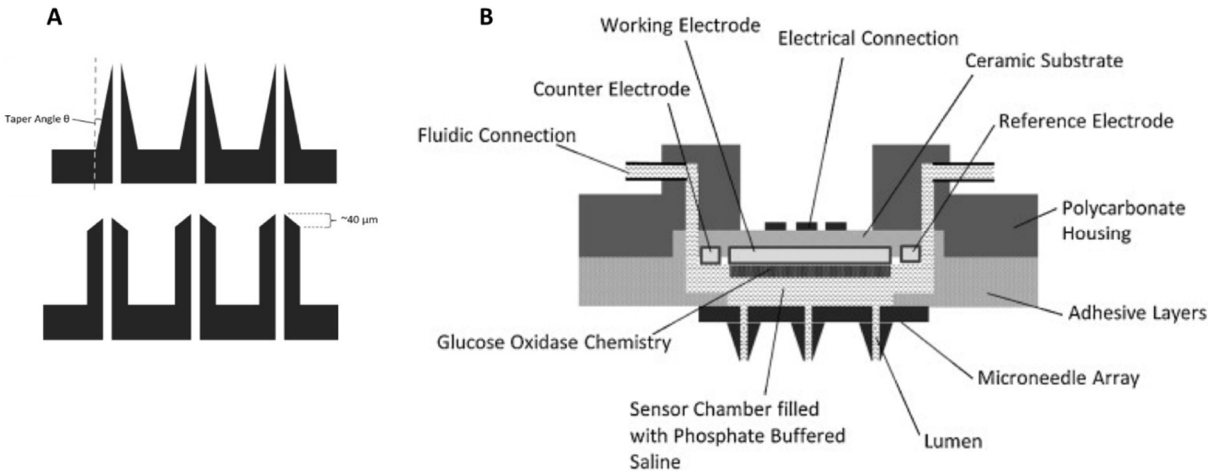

Figure 1.6. Microneedle architecture and complete device. (A) TSMA (top), SSMA (bottom). (B) MNA device prototype (cross sectional view) with all components illustrated. Reprinted with permission[44]. Copyright © 2013 Elsevier.

The TSMA device used in the previous study was carried forward to a clinical trial in diabetic patients by Jina *et al.*[45] Glucose concentrations was analysed in patients with insulin dependent diabetes (including those with type 1 (n = 7) and type 2 (n = 3) diabetes), in both hypo and hyperglycaemic ranges. Average age of the subjects were 61.1 years and average duration on insulin treatment was 16.1 years. Measurements were taken from 4 devices simultaneously and is the first study to monitor glucose changes up to 72 hrs using a MNA device. Citrate ions were incorporated into buffer solution inside the sensing chamber in order to slow down wound healing after the MNA insertions. Moreover, the devices were calibrated for an initial warm up period of 2 hrs against a reference blood glucose value

before application and further calibrated once daily with morning fingerstick blood glucose values. In agreement with previous literature, a lag time of 17 minutes was found between fingerstick and ISF glucose value in healthy volunteers and this was later applied to the clinical data. The results from the clinical study showed good agreement between the CGM system and finger stick measurements (Figure 1.7), with Clark's Error Grid for the entire data set showing 74.6% paired point in the A-region and 98.4% in the A + B region (total paired points – 1396, from 37 devices). Between the finger stick and CGM devices, the mean absolute relative difference (MARD) was found to be 15%, indicating both low system (bias) and random (scatter) error. In terms of precision between the device, the MARD was 10.4%, with a mean percentage coefficient variation of 7.3%. Overall, these results indicated good reliability and accuracy for the CGM systems, however, further improvements need to be made in integration, sensor auto-calibration and miniaturisation of the electronics.

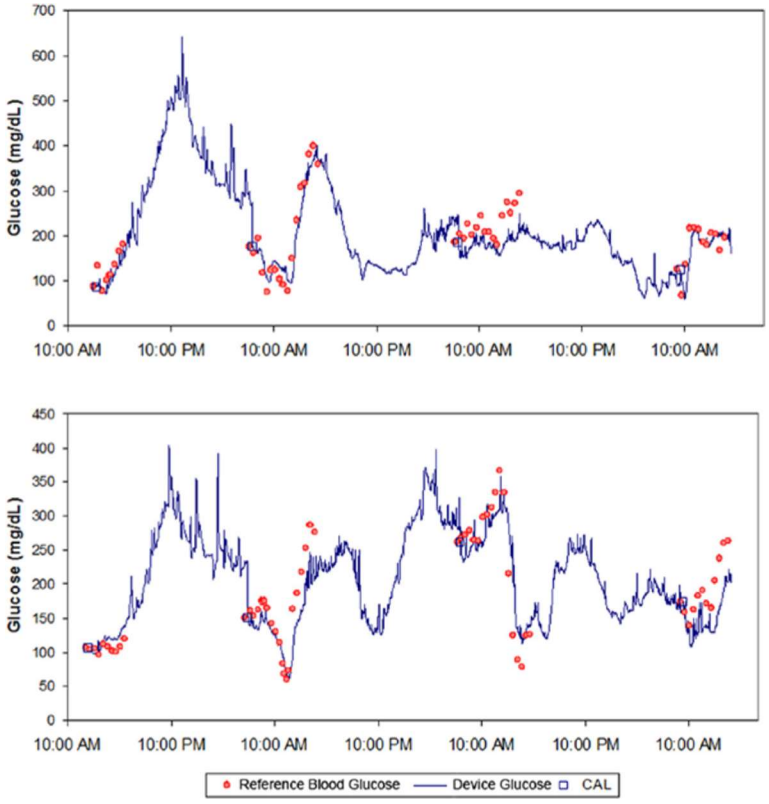

Figure 1.7. Two independent MNA device performance over 72 hours. A good correlation is seen with finger stick measurements (red dots). Calibration points used are shown as squares. Reprinted with permission[45]. Copyright © 2014, Diabetes Technology Society, SAGE.

Continuing along the theme of self-powered (i.e. pump free) ISF CGM, Strambini *et al.*[46] demonstrated how capillarity can be exploited efficiently for measuring glucose concentration with high accuracy, reproducibility and excellent linearity over the range of 0 – 630 mg dL^{-1}. The MNA device was fabricated using a silicon die by standard

lithographic and etching processes to produce 100 μm long microneedles on the front side and a reservoir grooved onto the back-side. A 200 μm long internal channel connected the microneedle to the reservoir. Two different types of MNA devices were fabricated; type 1 chip had a bore diameter of 4 μm and was densely packed (1 x 10^6 needles/cm^2); whereas type 2 chip had a bore diameter of 7 μm and density of 6.25 x 10^5 needles/cm^2. These devices were used to test capillarity in three solutions i.e. deionised water, PBS and artificial ISF. It was found that fluid uptake was faster for the densely packed microneedles with smallest bore diameter; type 1 chip taking only 5 seconds to fill the reservoir in comparison to 35 seconds for the type 2 chip. These results showed that bore size and high density of microneedles can significantly influence capillary forces. In order to develop these chips as biosensors, screen printed electrodes (WE and CE's) were fabricated and modified with GOx enzyme and potassium ferricyanide ($K_3[Fe(CN_6)]$). The biosensor was inserted deep enough into the reservoir that, the working volume was reduced to just 5 μl. Chronoamperometric measurements of glucose over the range of 0 – 35 mM were measured *in vitro* using artificial ISF and PBS (control) using both type 1 and type 2 chips. Performance was evaluated at 10 s steps for different sampling times from 5 – 200 s through quantification of several analytical parameters (accuracy, linearity, reproducibility, sensitivity, and resolution). In all test conditions, both MNA devices showed good linearity over the entire concentration range, at any given sampling time and was comparable to the stand-alone sensors (controls – without microneedles). Sampling over 5 and 200 s, the current and sensitivity deceased over time; but the best performance, in terms of compromise between sensitivity, accuracy and reproducibility was obtained for a sampling time of 30 s, for which the type 1 chip recorded accuracy within 20% of actual glucose levels over 96% of measures completed. Hence, this result was in agreement with FDA standards, indicating that for glucose concentrations above 75 mg dL^{-1} (4.2 mM), 95% of measurements have to be within ± 20 % of actual glucose levels. The limit of detection (LOD) for type 1 chip was 0.3 mM in ISF. Refer to Table 1.1 for more details on the aforementioned analytical parameters for both devices.

Table 1.1 Comparison of performance between type 1 and type 2 chips against a stand-alone biosensor (control) at the optimal sampling time of 30 s, in terms of analytical parameters such as accuracy, linearity, reproducibility, sensitivity, and resolution; for glucose concentrations in the range 0–35 mM, in both ISF and PBS. Reprinted with permission[46]. Copyright © 2015 Elsevier.

	Type 1 biosensor		Type 2 biosensor		Stand-alone biosensor	
	ISF	**PBS**	**ISF**	**PBS**	**ISF**	**PBS**
Accuracy (*A*) (measures within ±20%)	96%	92%	92%	96%	96%	99%
Linearity (R^2) (0−35 mM)	0.995	0.993	0.998	0.998	0.994	0.999
Reproducibility (%CV_{av})	8.56%	6.37%	8.74%	7.06%	6.55%	7.42%
Sensitivity (*S*) (μA/mM)	0.43	0.46	0.46	0.43	0.49	0.46
Resolution (LoD) (mM)	0.3	0.2	0.9	0.5	0.6	0.51

1.2.1.2.2 Solid MNA based glucose biosensors

As discussed in previous sections, early studies into MNA based glucose monitoring in the ISF were primarily concerned with the development of microfluidic glucose sensors. These adapted technology from the MEMS industry and mostly utilised silicon as a raw material to fabricate the sensors due to their high compatibility with the manufacturing processes. However, in line with the more recent studies reporting *in situ* glucose sensors assaying whole blood, recently, several authors have successfully demonstrated solid MNA-based *in situ* glucose sensors measuring in the ISF. Moreover, simpler fabricational strategies have also been demonstrated alongside such innovations. In this section, devices that are strictly developed for the purpose of glucose monitoring have been described.

One of the first works that described a solid MNA for CGM in the ISF was reported by Moniz *et al*. in 2012[12]. Here, the MNA's were fabricated photolithographically using backside exposure of SU-8 (epoxy-based negative photoresist). The microneedles were 500–750 μm in height and had a tip diameter of 10 μm. These microneedles were coated with gold (Au) and assembled with GOx by 1-Ethyl-3-(3-dimethylaminoproprly) carbodiimide (EDC)/N-hydroxyscucciniminde (NHS) coupling, followed by the addition of a nafion membrane incorporating an electron transfer mediator; tetrathiafulvalene (TTF). *In vitro* amperometric evaluation demonstrated that these MNA devices can perform well in the clinically relevant range (2 – 20 mM) with a linear response in current, measured in the microampere domain. Using a similar approach, Hwa *et al*. developed a glucose sensor on Au electrode by assembling GOx enzyme using the activated carboxy terminus (EDC-NHS chemistry) of a self-assembled monolayer (SAM) with 3-Mercaptopropionic acid (MPA)[47]. A silver (Ag) coated microneedle was used as the RE and an Au microneedle as the CE.

This set up was arranged onto a base plate, with an integrated Bluetooth device on the top side for data transfer to a computer. *In vitro* characterisation using agarose gel prepared with different concentrations of glucose showed a linear response for glucose concentrations ranging from 50 mg dL^{-1} to 400 mg dL^{-1}. The stability of the sensor was also analysed, and it was found that 80% of the enzyme activity can be retained over 7 days. This is resultant of the enhanced stability of glucose immobilised on a SAM of MPA. However, the stability of the GOx enzyme needs to be improved further, especially to improve shelf-life, therefore the authors point towards the addition of a hydrogel layer on top of the enzyme layer or layer by layer assembly of GOx using suitable polymers.

Valdes-Ramirez *et al*. described a microneedle-based self-powered biofuel-cell (BFC) sensor for subdermal glucose monitoring[48]. On-body BFC's are attractive because they eliminate the need for external power source by harvesting biochemical energy from the wearers transdermal fluid (via the conversion of chemical to electrical energy from electrochemical reactions involving biochemical pathways) and provide power signals that are proportional to the concentration of the analyte. The microneedle-based BFC glucose sensor was realised by incorporating modified carbon pastes into the bores of a hollow MNA forming a bioanode and a cathode. Of the electrode material available, carbon pastes are attractive because they offer optimal plasticity for efficient packing into the hollow microneedles. They are widely employed in electroanalysis and these electrodes offer the advantage of low background current, low cost, easy fabrication and convenience for modification (via the inclusion of modifiers). The bioanode was developed by mixing carbon paste (graphite powder – 87%) with GOx (10%) and a mediator - tetrathiafulvalene (TTF- 3%), whereas the cathode was formed by mixing carbon paste with Pt black in a 1:1 weight ratio. These pastes were extruded into six hollow microneedles, with three acting as the bioanode and three as the cathode. For electrochemical characterisation, the circuit was completed with an Ag|AgCl reference electrode and a Pt wire counter electrode. Artificial ISF containing glucose over the concentration rage of 0 – 25 mM was used for evaluating the performance of the biosensor. Power density as a function of concentration was found to show a linear behaviour, with proportional increase in current over the entire concentration range. The power density for control solution (i.e. without glucose) was 0.4 μW cm^{-2}, which continued to increase between 3 – 5 μW cm^{-2} over the normal glucose concentration rage of 5 – 10 mM and the highest power density value recorded at 7 μW cm^{-2} for 25 mM glucose. Stability of the BFC glucose biosensor was also evaluated over a

continuous measurement period of 60 hrs with ISF containing 10 mM glucose and 20.6 mg mL^{-1} BSA. The results showed that 75% of the original power density can be retained for over 60 hrs; indicating good resistance to biofouling effects. Moreover, selectivity was further analysed in the presence of common electrochemical interferants such as ACT, AA, UA and lactic acid, under physiological conditions. The interferants were found to have no significant effect on the power density obtained for 10 mM glucose obtained by the BFC sensor. This is in fact a distinct advantage to the self-powered BFC glucose sensor when compared to common amperometric devices. The authors claim further improvements to this device, such as the integration of an energy storage device and a responsive closed-loop insulin delivery system.

More recently, Sharma *et al.* described a cost-effective fabrication strategy to produce MNA-based biosensors for CGM[49]. Here, the base MNA was developed by micromoulding using SU8 50 (negative epoxy-based photoresist). Master templates were initially developed using aluminium through electrical discharge machining (EDM) and used to create PDMS micromoulds. By a process of spinning and vacuuming, SU8 50 was cast into the mould. This was then cross-linked using UV to produce a base MNA with 64 microneedles arranged as four 4 x 4 arrays. A two-electrode configuration was then realised by selective metallisation of the arrays. To produce the WE, three of the arrays were coated with titanium (15 nm) and platinum (50 nm) by conformal sputtering. By masking these arrays, the remaining array was metallised with silver (100 nm) and treated with $FeCl_3$ to obtain the Ag|AgCl reference electrode. GOx enzyme was then electropolymerized onto the working electrodes using phenol. The microneedles were ~ 1000 μm in length and had a base diameter of ~ 600 μm. Optical coherence tomography (OCT) showed the penetration depth achieved by a similar shape MNA made out polycarbonate, with the same dimensions to be 800 μm, thus 80% of the microneedle length is anticipated to be in contact with the ISF and mass transport driven by diffusion of glucose to the MNA surface. *In vitro* studies showed that the sensor could measure glucose concentration as low as 0.5 mM, with a response time 15 ± 2 s and detect glucose over a range of 0 – 30 mM at +0.7 V against the integrated RE and CE. However, after sterilisation by gamma irradiation (of 25 kGy), the I_{max} values were found to decrease, potentially indicating a lesser enzymatic activity. *In vivo* studies were carried out for short period (i.e. 3 to 6 hrs) using the sterilised MNA devices. Here, the MNA's were applied to the forearm of healthy volunteers. It was seen that device needed an hour to reach a stable baseline and this was because of the time it takes for polyphenol

films entrapped with GOx to equilibrate with the dermal fluid. The sensor was able to match responses from finger stick measurements and was also able to match active changes induced by diet (post the consumption of a slice of cake – bolus), but with a time lag as reported previously (i.e. 0 – 45 mins)[28]. The major challenge denoted by the authors is associated with fixing the sensor in the subdermal space.

Sharma *et al.*, further published a study addressing optimisations based on *in vivo* studies in humans[50]. The device fabrication and the GOx immobilising strategy used was the same as before[49], however, SU8 50 was replaced for polycarbonate to form micromoulded MNA arrays. Four individual MNA's were fabricated, with three metallised using platinum (WE) and one with silver (CE) using the same procedure outlined above. The CGM devices were applied to the foreman of the volunteer by application of moderate thumb pressure for 1 min and secured using a tape. *In vivo* study was conducted in three phases: (1) 6 hr measurements in healthy volunteers; evaluating tolerability (2) 24 hr measurements in healthy volunteers; evaluating tolerability and skin penetration and (3) 24 hr measurements in patients with Type 1 diabetes (T1D); evaluateing performance against a standard laboratory method. Pain was scored using Visual Analogue Scale (VAS). Tolerability was measured using a 100 mm – VAS to evaluate pain from insertion and from continuous wear throughout the study and compared against the insertion of a 20-G intravenous (IV) cannula. In order to determine both the insertion depth and their placement throughout the study, OCT was utilised. In phase 1, tolerability measurements were analysed in 8 healthy volunteers. Out of the 8, 7 subjects had barely noticeable skin response following insertion and removal, whereas 1 had mild erythema. Any visible skin reaction was found to disappear within an hour of removal. Median tolerability score for the MNA was 10, which is at the low end of the scale indicating mild pain (5 – 44); whereas for the IV cannula the median score was 30. In phase 2, the median score obtained from 100 mm VAS was 10 for the MNA and 39 for the IV cannula. OCT evaluation showed no significant variation in penetration depth from the time of insertion (i.e. 0 hrs – 495 μm) up to 24 hrs, with a median penetration depth of 440 μm. On evaluating the performance *in vivo* in 10 patients with T1D, the current measured successfully tracked venous blood glucose concentrations, showing a clinically acceptable correlation. The mean absolute relative difference (MARD) was 9% when compared with venous blood glucose values and 96.6% (out of 205 data points) of the values were in the clinically relevant A + B region in Clark's Error Grid Analysis. The percentage absolute relative difference between two sensors on the same

device was only 1%. The variation on the same device is associated with masking during the process of metallisation, creating a difference in the overall electroactive surface area on the microneedles. However as mentioned in their previous study, the devices required pre-calibration for 2 hrs before insertion, chronoamperometric data indicated a lag-time of up to 15 mins and significantly, two devices were found to lack functionality completely, following sterilisation via gamma irradiation method. Overall, this research indicates good clinical acceptability for the device.

1.3 Other Analytes

Microneedle research is gaining more and more significance into the detection of molecules other than glucose. The ISF present in skin microenvironment offers a unique opportunity to measure dynamics of therapeutic drugs, biomarkers, electrolytes, pH, small molecules and neurotransmitters in a minimally invasive manner as part of routine monitoring during treatment, rapid detection and or POC diagnostics. There are reports suggesting that as many as 80 markers are present in skin microenvironment that shows a good correlation with venous blood[17]. An attractive feature of MNA based devices is that, each microneedle can be modified independently, so as to enable multi-analyte detection in real-time. The following sections gives account of studies reporting single and multi-analyte detection using MNA based electrochemical sensors.

1.3.1 Single analyte detection

Using hollow MNA made out of E-shell 200 by standard UV rapid prototyping system, Windmiller *et al*. packed modified carbon paste into individual needles to realise low potential electrochemical detection of lactate[51]. Lactate monitoring is important because, high concentrations (i.e. 1 – 2 mM at rest) in blood, can reduce pH and induce damage to the muscle tissues. The hollow microneedles used were pyramidal in shape, with a height of 1500 μm and possessed a diameter of 425 μm. Carbon pastes were modified initially with rhodium (100 mg), as it is known for its low potential detection of H_2O_2 and thereby minimises the interference from co-existing electroactive species. The modified paste was then combined with lactate oxidase (10 mg) and homogenised along with the addition of mineral oil as a binder and polyethyleneimine (PEI) as an enzyme stabiliser (providing electrostatic entrapment of lactate oxidase within the matrix). Attaching the hollow microneedle to a 3 ml syringe, the carbon paste was extruded into the microneedle; ensuring complete packing, whilst a copper wire was also being inserted alongside to form an

electrical contact. Excess paste was then removed, the external surface of the paste smoothened with a wax paper and any residues removed by ultrasonication. The performance of this biosensor was evaluated through chronoamperometric experiments at -0.15 V against Ag|AgCl RE, over a concentration range of 0 – 8 mM for lactate in 1mM increments. The calibration curve showed a high linearity over the entire concentration range (R^2 = 0.990), with low SD (σ < 10 nA) and a detection limit of 0.42 mM. The influence of electrochemical interferants such as AA, UA and ACT was found to be negligible, with a resultant SD of just 1.5%; when measuring a lactate concentration of 1 mM. Moreover, the sensor was found to have excellent stability, as repeated measurements over a period of 2 hrs with 2 mM lactate resulted in a rise in current of only 9.7%.

Utilising a similar approach, research from the same group later developed MNA based *in situ* biosensor for continuous alcohol monitoring[52] and detection of organophosphorus nerve agents[53]. In the former, hollow microneedles were fabricated using a medical grade liquid crystal polymer (LCP) by injection moulding. These microneedles possessed a height of 800 μm and a microneedle bore of 100 μm. A press-fitting process was then adopted for scalable fabrication of electrochemical transducers by inserting Pt and Ag wires of 100 μm dimeter into lumen of the microneedles to produce an integrated three-electrode system. The platinum wire was then electropolymersied with PPD film to prevent electroactive interferents. Alcohol oxidase was then immobilised on to the PPD modified Pt WE by using chitosan as a binder (for stability and biocompatibility). Finally, the biosensor was modified with a nafion layer in order to prevent leaching of biosensing elements and to exclude negatively-charged interferents. The analytical performance of the biosensor was measured over a concentration range of 0 – 80 mM of ethanol, by chronoamperometry for 35 s at an applied potential of 0.6 V (vs Ag|AgCl). The current was found to increase linearly over the entire concentration range (R^2 = 0.9886), with a sensitivity of 0.062 nA mM^{-1} and the RSD between responses from five devices was only 3.3%. A similar response was seen from the biosensor when evaluated in artificial ISF, where a linear response was seen over the entire concentration range as above (R^2 = 0.9930), with a sensitivity of 0.0452 nA mM^{-1} and an RSD of 3.56% (n = 5). Results from an interference study (using 20 mM ethanol) in the presence of 100 μM of AC, UA and L-cysteine; as well as 10 μM AA only showed a negligible deviation of 6%. As the device was intended for continuous alcohol monitoring, the response stability of the biosensor was further analysed in artificial ISF containing 20.1 mg mL^{-1} BSA. Chronoamperometric scans using 30 mM ethanol was recorded over a period

of 100 mins at regular intervals and impressively, the device showed less than 10% variation from the original response. Using an *ex vivo* skin model, the performance of the biosensor was further demonstrated (Figure 1.8, A). Here, the biosensor was allowed to penetrate mice skin sample that was placed over the artificial ISF compartment in a manner than allowed the tip to be submerged in fluid. The concentration of ethanol was then modulated, and performance evaluated as before (Figure 1.8, B). Results here were found to corroborate well with that of *in vitro* measurements. These experiments demonstrate that enzymatic layer is stable in complex biological fluids and that having the enzyme layer immobilised on to WE's that were incorporated into the microcavity adds an element of protection from the skin insertion process.

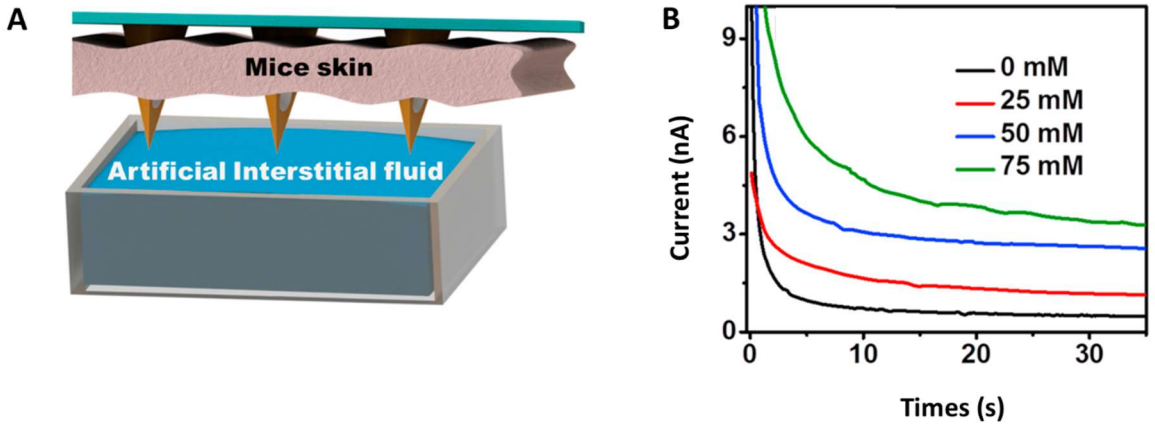

Figure 1.8. Alcohol biosensor. (A) schematic showing the detection of alcohol using a MNA device that was penetrated through mice skin and the tips submerged into artificial ISF, where the concentration of the ethanol was modulated. (B) chronoamperometric responses from the MNA towards different concentrations of ethanol in real-time. Reprinted with permission[52]. Copyright © 2017 Elsevier.

The sensor fabricated for the detection of organophosphorus chemical agents employed three hollow microneedles packed with modified carbon-pastes (similar to that developed in Windmiller *et al.*[51]). Two of the microneedles was used to construct the WE and CE and the third modified with Ag|AgCl ink to produce a reference electrode[53]. In order to produce the carbon paste, the percentage of graphite powder used was 65%, with the remaining 35% being the binder, mineral oil. The enzyme organophosphorus hydrolase (OPH) was then immobilised onto the WE using a Nafion layer, which not only helps to prevent leakage of the enzyme but also provides an anti-interferance barrier. The enzyme nafion layer was further combined with bovine serum albumin (BSA) to enhance enzymatic stability and drop casted onto the WE, which upon drying resulted in the formation of an OHP biofilm. The detection process of the biosensor relies on the anodic detection of *p*-

nitrophenol, which is product of the enzymatic reaction of the OP substrate on the OPH/nafion coating on the WE microneedle surface. Unlike the electrochemical methods used thus far, especially that of fixed potential amperometric detection, square wave voltammetry (SWV) was utilised in this study. This method is promising because it provides effective discrimination again background (charging) current alongside high speed (1-5 sec scan) and high sensitivity. *In vitro* characterisation of the biosensor showed a well-defined oxidation peak at +0.75 V in response to a methyl paraoxon (MPOx) over the range of 20 – 180 μM. The responses were linear (R^2 = 0.999) with a LOD of 4 μM. The biosensor was found to highly selective as an interference study with physiological levels of AA (250 μM) and UA (250 μM) produced no augmented response, even when an artificial ISF was used. The biosensor also displayed long-term stability when measured over 2 hrs (RSD = 3.74%). *Ex-vivo* assessments were also carried out by exposing mice skin to different concentrations of MPOx and measurements were made *in situ*. When compared to the *in vitro* measurements at 50, 100 and 150 μM, the oxidative response measured *in situ* appeared to be reduced; with 84, 93 and 85% of the signal being recovered; with regards to the respective concentrations. This points out the viscous nature of the skin microenvironment.

In the work that showcased a bi-component MNA design, for which glucose biosensing has already been described in this review (*section* 1.2.1.1); the authors had also described glutamate biosensing[11]. Glutamate is an important neurotransmitter that plays a crucial role in both normal brain functioning and pathological conditions such as epilepsy and Alzheimer's disease. Clinical monitoring of this neurotransmitter is a highly invasive procedure requiring access to cerebrospinal fluid via catheters or a microdialysis probe for further analysis. MNA based biosensors are can make this process highly accessible, as it has been found that blood glutamate levels correlate well with that of CSF levels. In different to the protocol used for glucose immobilisation, where the Ag|AgCl and the Pt electrode were electropolymerized in a single step, at +0.75 V (vs Ag|AgCl RE), in the presence of the monomer *o*-phenylenediamine, sodium sulfate and GOx enzyme; in order to prepare the glutamate biosensor, the enzyme was drop-coated on to Ag|AgCl and the Pt electrodes and sandwiched between two layers of PPD, in order to conserve the costly enzyme. Initial, *in vitro* characterisation showed that by selecting a potential of +0.40 V vs Ag|AgCl RE, the effect of interferants can be minimised. By applying this potential, chronoamperometric scans were completed over the physiological range of 0 – 140 μm, in 0.1 M PBS and undiluted human serum samples. In PBS, sampling at t = 15 s, the calibration curve showed

high linearity (R^2 = 0.995) over the entire concentration range, with high sensitivity (7.129 nA μM^{-1}), low relative SD (*RSD* = 3.51%) and a LOD of 3 μM. Likewise, characterisation in human serum samples also showed high linearity (R^2 = 0.992) on the calibration curve over the entire concentration range, high sensitivity (8.077 nA μM^{-1}), low RSD of 6.53% and a LOD of 21 μM; which albeit being higher is still below the limit of normal physiological levels. Additional studies on selectivity for 100 μM glutamate when measured in the presence of 60 μM AA, 500 μM UA, 200 μM Cys and 200 μM ACT showed negligible deviation of up to 6.37%. As for stability assessment, 8 hrs of continuous measurement of 100 μM glutamate showed a stable current response, retaining 105% of the original response. This highlights the utility of MNA's for continuous *in vivo* quantification of glutamate in a minimally invasive manner.

Miller *et al*. reported the first example of MNA based ion selective transdermal sensor for on-chip potentiometric detection of potassium ions (K^+)[54]. K^+ is one of the main electrolytes routinely assessed via blood tests. The sensor integrated hollow microneedles to a microfluidic chip, where the extracted fluid was passed downstream to a solid-state ion-selective-electrode (ISE). Two types of transducers i.e. 3D pyrolysed carbon (*PC*) and 3D porous graphene (PG) electrodes, were compared for electrochemical performance, selectivity and stability. The MNA's were made from E-shell 300, which is biocompatible via two-photon polymerisation. The microneedles had a height of 1450 μm, base diameter of 440 μm and a triangular bore of 165 μm. The microfluidic chip were made by layer by layer assembly using poly(methyl methacrylate) (PMMA) and the adhesive layers were utilised to form a fluidic channel using CO_2 laser ablation. For electrochemical sensing, a three-electrode system consisting of Pt CE and Ag|AgCl RE, in addition to the two different WE electrodes, were incorporated into the microchannel. Initially, when comparing both electrodes, the *PC* electrode showed better electrochemical performance, with a detection range from 10^{-5} to 10^{-2} M with a near Nernstian slope of 57.9 mV per decade and rapid stabilisation (~20 s). Moreover, interference study with sodium ions showed no effect on the electrochemical response. The *PC* electrode was then integrated with the microfluidic chip, and the response was measured downstream at the ISE from KCl solution with different K^+ concentrations injected in the chip after a short period (200 s), allowing for stabilisation. The measured amperometric response was linear, with an ideal Nernstian response (obtained after subtraction of ion dissociation due the Ag|AgCl wire) and sensitive to physiological K^+ levels.

More recently, Skoog *et al*. developed a titanium MNA coated with nitrogen incorporated ultrananocrystalline diamond (N-UNCD) thin films for electrochemical detection of UA and dopamine (DA) without any surface modifications[55]. The N-UNCD films are superior to silicon, SiO_x and gold, as they offer excellent response stability in harsh environments and not susceptible to degradation. Moreover, these films provide enhanced anti-fouling properties due to low adsorption of proteins and improved electrical properties due to the wide band gap and large electrochemical potential window. Hence, they are ideal candidates for extended *in vivo* applications. The titanium microneedles were fabricated using 3-axis computerised numerical control milling, with 7 microneedles in staggered orientation. These were conical in shape, with a height of 340 μm and a base diameter of 250 μm. N-UNCD films were coated on the titanium MNA by microwave plasma chemical vapour deposition. For *in* vitro characterisation linear scanning voltammetry was used to analyse UA and DA, by running scan from -0.2 to +0.8 V at 10 mV s^{-1}. Measuring response to UA concentrations from 0 – 200 μM, a distinct oxidation peak was observed at +0.48 V; for which the peak current measured was linear to the concentration range (R^2 = 0.99). Response of the un-modified electrode to DA also showed a linear response (R^2 = 0.997) when the peak potential at 0.65 V was analysed against a concentration range of 0 – 30 μM. Although the individual peaks were separated by ~ 200 mV, simultaneous detection was not possible, and overlapping signals were seen.

Kuem *et al*. developed a dual diagnostic system by attaching a MNA at the end of an endomicroscope which aided in diagnostic imaging of polyps as well as detection of nitric oxide (NO)[2]. They also used the MNA device for detecting elevated NO levels in melanoma *in vivo*. The MNA's were fabricated from polycaprolactone (PCL) by micromoulding. The PCL MNA surface was modified using polydopamine (PD) for immobilisation of PEDOT as a channel layer. The biosensor was fabricated with a three-electrode configuration; with the WE and CE made of titanium (10 nm), palladium (10 nm) and gold films (100 nm) formed on the surface by e-beam lithography, vacuum metal deposition and lift-off processes. After forming the titanium layer, PD was further deposited on the surface to form a metal diffusion barrier layer. The RE was integrated by selective deposition of silver (200 nm layer) using a shadow mask. The PCL/PD/PEDOT microneedle was then functionalised with hemin molecules; which provided a high binding constant and affinity towards the detection of NO. The microneedles were 700 μm tall.

The sensor was further integrated with a PDMS microfluidic channel (3 mm height) that was filled with PBS containing diethylamine NONOate sodium at various concentrations (1×10^{-6}, 2×10^{-6}, 4×10^{-6}, 8×10^{-6}, and 16×10^{-6} M); as a precursor to release NO. A potential of 0.1 V vs Ag|AgCl was used for amperometric detection of NO. Initial characterisation towards the detection of NO showed that, the current response from the sensor decreased in the presence of increasing concentrations of NO (0 – 16 μM) (Figure 1.9, A). The biosensor was also found to be highly selective, showing no changes in their current response when measured in Dubelcco's Modified Eagle Medium (DMEM) with 10% serum proteins and in the presence of potential interferants such as such as BSA, glucose, galactose, Fe^{3+}, H_2O_2, ovalbumin or lysozyme (Figure 1.9, B). The sensitivity of the biosensor when measured in PBS and DMEM was ~1.56 μA cm^{-2} μM^{-1} and ~1.44 μA cm^{-2} μM^{-1}, respectively. Further *in vitro* characterisation using RAW 264.7 macrophage cell line showed that the biosensor could dynamically monitor the generation as well as suppression of NO. When *in vivo* measurements were made in mouse models, those with melanoma had an average drop in sensor current 8.34 ± 0.16 μA, whereas in normal mouse skin the average current drop was only 3.26 ± 0.11 μA (Figure 1.9, C). Similarly, when the sensor was applied onto polyps (identified by the endomicroscopic imaging *in vivo*), a current drop of 4.12 ± 0.38 μA could be detected in association with the release of elevated NO levels; as opposed to a normal region in the colon, where no significant current change had been measured (Figure 1.9, D). Collectively, these results indicate that the sensor could detect NO levels in cancerous tissues with high selectivity.

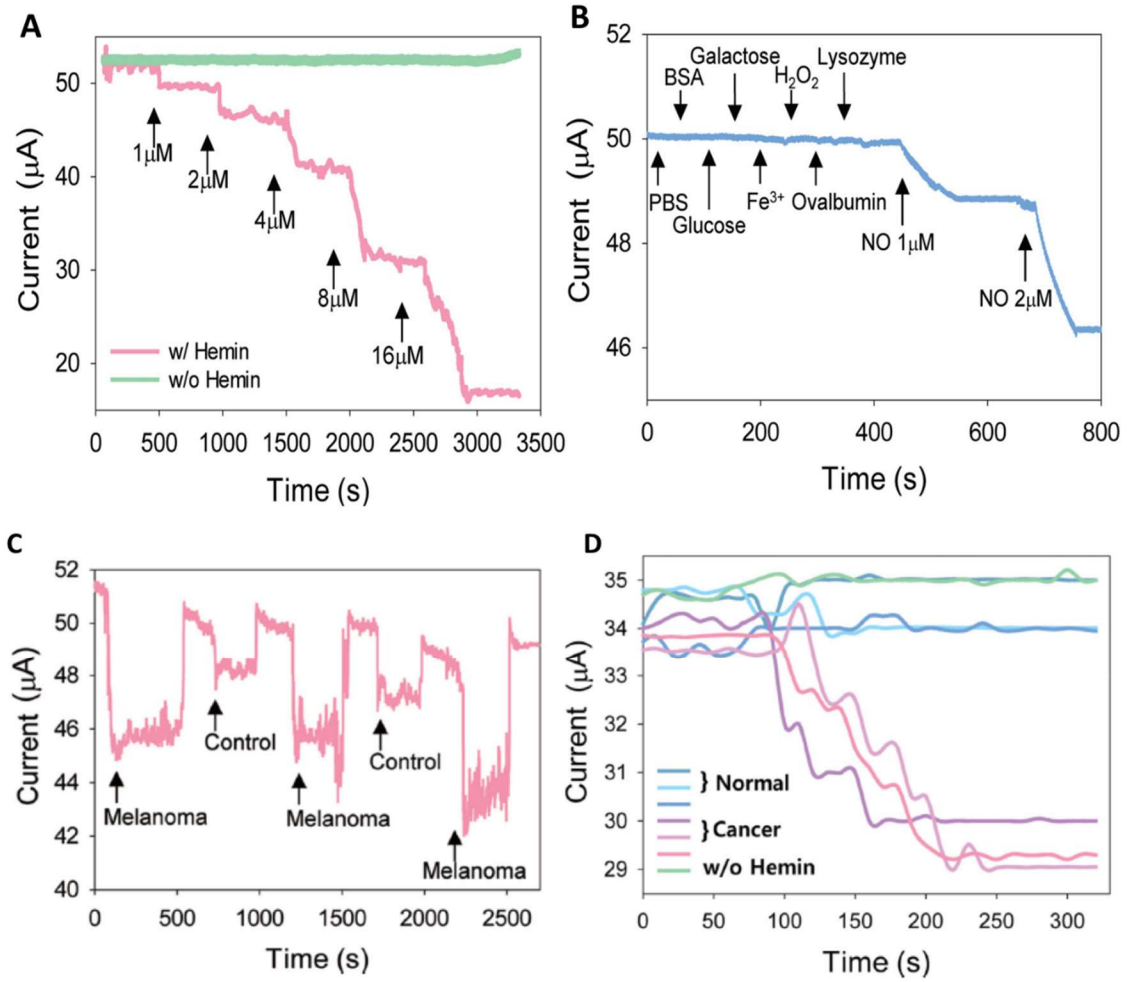

Figure 1.9. Detection of NO levels. (A) Real-time detection of various concentration of NO in DMEM, showing a decrease in current response. (B) Selectivity of the biosensor in the presence of interferants. (C) Alternating MNA biosensor response in normal and melanoma skin with reference to NO. (D) MNA biosensor response from cancerous (polyps) and normal tissue. (Green lines in A and D, indicates the importance of Hemin functionalisation. Reprinted with permission[2]. Copyright © 2015, John Wiley and Sons.

As seen from the progression of this review, the fabrication of MNA based sensors is becoming more simple, transferable, affordable and importantly offers the scalability that earlier devices failed to deliver. The advent of micromoulding technology has been a great benefactor for the development of such devices. Most recently, McConville and Davis successfully utilised micromoulding to develop MNA based electrochemical sensors from simple nanocomposite formulations developed by solution mixing[56]. Fabrication of the MNA's involved three stages. Initially, a suspension with 50 mg of palladium (Pd) nanoparticulates (<1 μm in diameter) was dispersed in dichloromethane (DCM), 50 μL and transferred to the micromould with the intention of precoating the template to necessitate a greater quantity of interfacial Pd and thus enhance the electroanalytical performance.

Secondly, the bulk of the MNA was formed by solution casting 50 mg of Pd within 50 μL of a 50% w/v solution of polystyrene (PS)/polycarbonate (PC) in DCM. Finally, 50 μL of the same composition (containing 50 mg of Pd) was further added to form the top of the baseplate backing. This was followed by centrifugation; to remove air bubbles and for efficient packing of the polymer/nanoparticle mixture within the structure of the microneedles. To solidify the MNA, DCM was then allowed to evaporate at room temperature and pressure for 4 hours; with the MNA demoulded afterwards. The MNA surface was further modified through self-assembly of L-cysteine in order to improve electron transfer kinetics. The microneedles were 350 μm in height and had tip diameter of 7.2 μm. Cyclic voltammetric (CV) characterisation of the MNA biosensor using a redox couple, potassium ferrocyanide showed that, modification with L-cysteine was pivotal in enhancing the electrode kinetics as without out it, their MNA electrode did not show the reversible redox processes that is associated with ferrocyanide. The above characterisation involved the whole of the MNA, therefore a skin mimic was prepared by entrapping the redox couple into a hydrogel formulation and then layered with Parafilm™. The MNA biosensor was then allowed to pierce through the Parafilm™ barrier layer, into the hydrogel for evaluation of the redox couple. In response, the MNA biosensor produced a lower current response as the overall electroactive surface area of the microneedle was reduced. Nevertheless, a good electrochemical response was seen towards the redox couple, but with larger peak to peak separation. Although this study showcased a versatile strategy towards the fabrication of MNA based electrochemical sensors, major challenges remain, especially to that associated with the optimisation of the filler to matrix ratio, in order to obtain good mechanical characteristics as well as to improve electrode kinetics. Only the fabrication of the WE's were demonstrated here. Moreover, there needs to be a careful evaluation of biocompatibility of the composite MNAs, especially concerning the release of Pd following *in* situ application, because the microneedle surfaces were found to be highly granular.

1.3.2 Multi-analyte detection

In 2011, Miller *et al*. reported the first study on the development of MNA based biosensors towards simultaneous detection of AA and H_2O_2 using modified carbon fibre electrodes integrated within in hollow microneedles[57]. The hollow microneedles were fabricated from E-shell 200 by digital micromirror device based stereolithographic process, which allows rapid prototyping of microneedles; over 200 devices in 3 hrs. The

microneedles were tetrahedral in shape, with a height of 1030 μm, had a triangular base with side lengths of 1120 μm and the bore measured 375 μm in diameter. The carbon fibres were modified selectively with Pd (by electrodeposition) and o-aminophenol (*in situ* diazotination and electrografting of the diazonium salt) to enable simultaneous electrochemical detection of H_2O_2 and AA, respectively. With the help of a precision alignment tool, the fibres were then inserted in the hollow aperture of the microneedles and secured with an acrylic adhesive on a PMMA substrate. Preliminary electrochemical characterisation via CV towards the detection of the redox probe ferrocyanide at 5 mM concentration showed a well-defined oxidation and reduction peak, with the average formal potential measured at 20 mV vs Ag|AgCl reference electrode. The average peak separation was 125 mV. Pd catalysed oxidation of H_2O_2 was then investigated. Measuring over the range 0 – 500 μM, the CV showed a linear increase in reductive current, exhibiting a linear range over 100 – 500 μM, with an LOD of ~15 μM. Similarly, AA was detected using linear sweep voltammetry (LSV), which consequently demonstrated selective detection of AA, at a low potential of 195 mV. A calibration for this was not provided and although the device was developed to showcase simultaneous detection, this feature was not showcased.

One year later however, utilising the same strategy as shown above, the same group proposed the use of MNA based electrochemical sensors for simulation detection of three different analytes[58]. Here, the carbon fibres were replaced with modified carbon pastes in order to detect pH, glucose and lactate. The modified carbon pastes housed within each hollow microneedle were separately connected to wires on a flexible flat cable to enable simultaneous detection of analytes. Electrochemical detection of pH was achieved by chemically depositing RR diazonium salt; whereas for selective detection of lactate and glucose, the carbon pastes were modified with rhodium incorporating the respective enzymes. Detection of pH was demonstrated through CV scans run from -0.7 V to 0.8 V at 100 mV s^{-1}, at a regular interval of 0.5 pH units, over the range of 5.0 – 8.0 pH. The response was measured by evaluating the shift on the anodic peak potential of the quinone moiety on the RR diazonium salt. The results showed a highly linear (R^2 = 0.99) negative shift in the oxidative peak potential with increasing buffer acidity over the entire pH range studied. Detection of glucose and lactate was then performed by chronoamperometric scans at a fixed potential of -0.05 V and +0.15 V, respectively; for different pH values (i.e. 5.0, 6.0, 7.0 and 7.5). The calibration curves obtained were linear for both analytes over a concentration range of 2 – 12 mM; with the current decreasing over more acidic pH. This

study also demonstrated multiplexed detection by analysing the selectivity of the sensor when using a mixed buffer solution (0.1 M PBS). For example, the response of the lactate biosensor was analysed when the sample was a mixture of glucose and lactate at a concentration of 4 mM. No response was seen from the lactate sensor when glucose was added, but addition of lactate produced a current response of 38 nA; similar to that obtained from its individual characterisation. Similarly, the glucose biosensor did not produce any response when lactate was added, but the current response increased by 10 nA, when 4 mM glucose was added to the buffer solution. Additionally, the MNA biosensor was able to confirm the pH values simultaneously. This shows that, by individually addressing each microneedle-based electrode in an array, simultaneous detection of analytes is possible.

1.4 Discussion and Future directions

Over the past two decades, research efforts have intensified into developing MNA based biosensors. Predominantly, the focus of such research is on developing CGM devices for diabetes management. This is driven by the increasing number of deaths associated with diabetes (and related complications). The World Health Organisations (WHO) recent global report on diabetes estimated that approximately 422 million adults are living with diabetes in 2014[59]. The number of deaths reported in 2012, directly from diabetes was 1.5 million; whilst an additional 2.2 million deaths were resultant of higher-than-optimal blood glucose, increasing the risk for cardiovascular and other diseases. These numbers will continue to rise due to a lack of access to core facilities for glucose analysis using venous plasma and or POC devices, particularly in the developing countries; difficulty in distinguishing between Type 1 and Type 2 diabetes and lack of patient adherence to a strict treatment regime. Research into MNA based diagnostic and CGM devices are ideally positioned to address these key issues, but several challenges needs to be overcome. These includes: (1) low cost and efficient fabrication (including efficient miniaturisation of the devices with on-chip sensor, integrated with transducers and read-out systems) to ensure that the technology is globally accessible. (2) efficient interaction with the skin in term of both skin penetration without mechanical/functional failure and efficient interlocking of the microneedle within the skin, in order to avoid displacement through patient movements; (3) reliable collection of biofluids through the microneedle for in line quantification (where microfluidic devices are employed) or efficiency in analysing the biofluid *in situ* (where solid MNA based sensors employed). In both cases, sensors should account for a high degree of accuracy, selectivity, sensitivity, LOD and reproducibility[20].

As seen from the studies concerned with glucose monitoring, tremendous progress has been made despite the relatively short period of research into MNA based devices. This has led to the several clinical studies, and even commercialisation of CGM (by Arkal Medical) based on the principles reported in the studies by Chua *et al*. and Jina *et al.;* whereby glucose diffuses passively from the ISF to a biosensor external to the chip[44,45]. This device named, *Glucopod*™, functions by employing the classical GOx chemistry, consisting of a disposable sensor, reusable transmitter and wireless smart receiver. Recent trend on CGM devices have stepped away from the hollow MNA devices and have successfully utilised solid electroactive microneedles for *in situ* biosensing. These are less complex in terms of the sensor design and integration, and more advantageous in the sense that the larger electroactive surface of the solid microneedles can help detection of biomolecules with high sensitivity[60]. In line with this progress, fabrication strategies are becoming simpler, embarking on the use of technologies associated with micromoulding. However, a major challenge is associated with micromould maintenance, which may require constant replacement in order to replicate the finite structure of the microneedles with high accuracy.

Recent works have now demonstrated extended use of MNA based sensors in detecting clinically relevant analytes and molecules, both in terms of diagnostics and continuous monitoring purposes. Some promising applications has been demonstrated such as the continuous monitoring of alcohol, detection of elevated NO levels in cancer, monitoring of pH and detection of organophosphorus chemical agents. In terms of fabrication, prominent approaches that have been employed thus far includes; a bi-component microneedle design (where solid electroactive microneedles are inserted into the aperture of a hollow microneedle), incorporation of modified carbon fibres and pastes within the hollow microneedles, and solid microneedles that are metallised to form electroactive surfaces. Although the earlier studies relied heavily on silicon as the material of choice, increasingly polymers are used to fabricate both solid and hollow microneedles. The detection is based on passive accumulation of analytes on the surface of the MNA-based electrodes once they are inserted in the skin. With MNA based sensors whether it is used for detection of glucose or other biomolecules, two key factors that are currently overlooked and needs to be addressed involves: (1) effective placement within the skin, unhindered by muscle movements especially when considering long-term on-body monitoring and (2) miniaturisation of the device[20].

Although MNA platforms developed for biosensing appears to be transferable towards the detection of several analytes *in situ*, research is still focused on fabrication. Such studies are primarily focusing on easier fabricational strategies alongside an attempt to improve analytical sensitivity towards a range of analytes. This is of course relevant, as there are a plethora of molecules and markers that requires the device to possess a high sensitivity and selectivity in order for it to be detected. This in particular includes, detection of disease specific biomarkers. There are numerous studies indicating the potential for MNA's to be used as rapid immunodiagnostics devices, by successfully utilising the principles of enzyme-linked immunosorbent assay (ELISA)[13,61–63]. Overall, the technological gap, combined with the fact that, microneedle-based sensor technology is yet to take full advantage of the skin biochemistry to address a large range of clinical applications, will undoubtedly drive the field forward.

1.5 Aims and objectives

Dermal biosensing using MNA-based electrodes have attracted significant research interests because the active components of the electrodes can be modified independently to detect in real-time, and continuously monitor, biomolecules of clinical interest from biofluids within solid tissues in a minimally invasive manner. The electrochemical detection strategies employed by these sensors are distinctly advantageous as they are generally low cost, non-complex and can be effectively utilised by a minimally trained individual at the POC[20]. Research thus far has demonstrated biosensing devices employing hollow and solid designs as well as their combinations i.e. hollow microneedle accommodating a solid microneedle /modified carbon fibre/Pt wire WE's as well as those filled with modified carbon pastes. Though the early studies were dependant on sophisticated micromachining and lithographic process using silicon as the choice of material for fabrication, progress over recent years have made polymers an ideal alternative and employing micromoulding as a facile fabrication strategy to produce MNA-based sensors[64]. Solid microneedle designs are highly compatible with such a fabrication strategy, and by utilising injection moulding or hot embossing processes, scalability for the device manufacturing can be improved drastically[65]. Conventionally, solid polymeric microneedles produced in this manner is subsequently metallised by coating with gold or platinum using e-beam lithography or by sputtering to develop electroactive surfaces. Although metallisation with gold and platinum renders excellent electroactive surfaces for biomolecular detection, it is still not as cost-effective, especially when envisaging a global accessibility. In line with progress of research

presented in this thesis, McConville and Davis, very recently published research undertaken to develop MNA-based biosensors by micromoulding using composite formulation involving PS or PC matrix and Pd microparticles[56]. Composite formulations are an attractive option because, cost-effective and versatile formulations can be produced with desirable functional and mechanical properties using a wide range of materials. However, the major challenge associated with composite formulations is to achieve the right mechanical and electrochemical characteristics by incorporating an optimal level of the conductive filler. In order to obtain a good electrochemical behaviour in a non-conjugated matrix it is often the case that a high amount of filler is to be incorporated as found by McConviller and Davis, where 50% of the sensor was made of Pd microparticles. Hence, careful considerations must be given to the choice of the active material, their functional properties (i.e. electrochemical and mechanical) and the processing conditions under which they are effectively incorporated into the non-conjugated matrix.

The principal aim for this thesis was to develop MNA biosensors using nanocomposite formulations for rapid intradermal bioanalysis. Nanocomposite formulations was chosen due to their adaptability in fabricating a biosensor with the desired functional properties. Importantly, composites maintain processability similar to their polymeric matrices, hence they favour a highly scalable fabrication method such as injection moulding, which consequently enables the fabrication of MNA based electrodes in a single step[66].

Carbon nanotubes (CNT's), characterised by their ultra-high specific surface area, and excellent mechanical, electrical and electrocatalytic properties are ideally suited as active materials within polymeric matrices to form nanocomposite MNA based electrodes[67]. Electrochemical sensing based on CNT's is an established field, as their material properties allow for rapid-electrode kinetics, reduce the overvoltage, lower the limits of detection and further impart antifouling properties towards the electrochemical processes of many analytes[68]. In relation to the fabrication of various electrochemical sensors, CNT's have been typically used as modifiers of glassy carbon electrodes (GCE's) or Au electrodes. However, they can also be fabricated as electrodes themselves; as indicted by CNT-paste electrodes[69–71]. This implies that MNA's developed from CNT based polymeric nanocomposites have the potential to replace metallic and or metallised MNA's for transdermal biosensing. While the improvement in mechanical and electrical properties upon the inclusion of the CNT's into polymeric matrices have been extensively investigated, the challenge here was to determine, whether such composites will adhere to the finite

structure of the MNA's and the feasible ratios that may define optimal electroactivity without compromising mechanical integrity.

In order to realise the fabrication of CNT-based nanocomposite MNA's towards intradermal bioanalysis, the following objectives were assessed in subsequent chapters:

1. **Investigate the suitability of epoxy to form nanocomposite MNA's.** This was divided into three stages: (a) Develop a methodology to fabricate MNA's using neat epoxy by evaluating different epoxy formulations, (b) validate a methodology for evaluating mechanical properties of the MNA's and (c) assess strategies to incorporate CNT's into epoxy and utilise or further adapt the fabrication strategy developed initially to develop nanocomposite MNA's. (Chapter 3)

2. **Investigate the suitability of Poly (lactic acid) (PLA) to form nanocomposite MNA's.** This involved: (a) fabrication of MNA's from neat PLA by micromoulding, (b) developing a methodology towards the incorporation of CNT's into PLA, (c) assessment of mechanical characteristics of the MNA's, (d) optimisation and evaluation of electrochemical performance *in vitro* and *ex vivo*. (Chapter 4)

3. **Improve the electrochemical behaviour of the nanocomposite MNA's.** Optimisations were carried out by critically evaluating the processing conditions (i.e. sonication), incorporation of surfactants and evaluating the influence of differing lengths and diameters of CNT's alongside differing functional groups. (Chapter 5)

4. **Cytotoxicity evaluation of the nanocomposite MNA's.** Toxicity assessment from indirect contact and the effect of electrochemical measurements on cells. (Chapter 6)

Chapter 2. General materials and methods

2.1 Overview

The overall aim of the research presented in this thesis was to develop solid electroactive MNA-based electrodes for rapid intradermal bioanalysis. This chapter describes the generic methods implemented during fabrication, characterisation and evaluation of developmental strategies as well as functional performance of the MNA's. Methods developed to investigate specific experimental aims are detailed in respective chapters.

2.2 Fabrication

2.2.1 Development of micromoulds

Micromoulds were developed using a Sylgard® 184 silicone elastomer kit; purchased from Dow Corning (Midland, MI, USA). A commercially available MNA i.e. Derma Stamp (amazon.co.uk, ASIN: B007ATO220I), consisting of 35 microneedles with a length of 1 mm was used as the template. In order to fabricate the negatives, the two-part silicon elastomer was mixed in a ratio of 10:1 and poured into a flat bottom container made of aluminium foil, with a dimeter of 3 – 4 cm. The MNA stamp was then immersed fully into this mixture and degassed at a low vacuum pressure of ~10 mbar for 2 – 3 hrs; ensuring complete removal of trapped air-bubbles. The container with the MNA stamp was then placed on a hot plate and the stamp was affixed upright after raising it slightly above the base of the container. In this set-up, the elastomer was cured at 90°C for 2 – 3 hours. The MNA stamp was then manually ejected, and the foil peeled off to reveal the micromould. These micromoulds were used throughout this body of work to fabricate MNA's from the various materials utilised.

2.2.2 Development of MNA's

In this body of work, development of nanocomposite MNA-based electrodes was attempted by using epoxy and PLA as the matrix component. With reference to this, MNA's were initially fabricated from the matrix material alone and mechanically characterised. This was followed by evaluations of the processing conditions under which functionalised MWCNT's can be successfully incorporated into the polymeric matrices. Finally, the utility

of such nanocomposites to be developed as electroactive MNA's with good mechanical properties was determined.

The methods used for fabrication and optimisation of nanocomposite formulations and MNA's were developed throughout the course of this thesis and are thus comprehensively detailed in the relevant chapters. Therefore, in the following sections, only a brief account of the final optimised method that was used to develop MNA's from various materials are detailed.

2.2.2.1 Poly (lactic acid) MNA fabrication

The PLA used throughout the body of work presented in this thesis was filaments commonly used for 3D printing (Makerbot, Germany). Employing a micromoulding approach, PLA based MNA's were fabricated by melting centimetre long segmented pieces of the filament at 180°C, under low vacuum (~20 mbar), inside the micromould for 4 hrs[63]. Upon cooling, solid PLA based MNA devices were manually ejected from the micromould.

2.2.2.2 Epoxy MNA fabrication

Three different epoxy formulations were evaluated towards the development nanocomposite MNA's. (1) a commonly used 2-part epoxy resin, RX771/C (Robnor Resins Ltd (Swindon, Wilshire, UK); (2) medium epoxy formulation fabricated using an electron microscopy (EM) grade Agar 100 resin (Agar Scientific, Stanstead, Essex, UK) and (3) a hard epoxy formulation fabricated using the same EM grade Agar 100 resin. Initially, the development of MNA's from the various epoxy formulations alone were investigated. The optimised method found, involved application of a low vacuum pressure of 200 mbar for 45 mins prior to thermal curing inside the micromould at respective temperatures overnight. Further details can be found in Chapter 3, s*ection 3.3.1*. Attempted fabrication methods for developing epoxy-nanocomposite MNA-based electrodes are also detailed in Chapter 3, *section 3.3.2.*

2.2.2.3 PLA/CNT nanocomposite MNA fabrication

Carboxyl functionalised MWCNT's (*f*-MWCNT) with a length and diameter of 10 – 30 μm and 20 – 30 nm respectively, was purchased from Cheap Tubes Inc. (Cambridgeport, USA) and used to fabricate PLA-based nanocomposite MNA's by employing a solution mixing approach. In chapter 4, nanocomposite MNA based electrodes were fabricated using the following method. Initially, the *f*-MWCNT's (at different loadings) were dispersed in an

organic solvent (chloroform) by bath sonication (operation at 37 kHz) for an hour. Filaments of PLA constituting the appropriate weight fractions were then added to the solvent/*f*-MWCNT mixture and allowed to dissolve completely by magnetic stirring at 45°C for 1.5 hrs. Bath sonication was then employed for another hour, so that the PLA-*f*-MWCNT mixture can be intercalated efficiently. This process was aided by maintaining the temperature on the sonic water bath at ~45°C. Once this process was completed, the whole mixture was homogenised further by stirring on a hot plate at 45°C for 48 hours. The mixture was then poured into a glass petri dish and the solvent was evaporated at room temperature (RT) for 48 hours to develop nanocomposite films. To ensure removal of solvent completely from the nanocomposite films, they were further dried in a thermal oven at 60°C overnight. Further details on the development of nanocomposite films can be found in Chapter 4, *section 4.3.1*.

The dried nanocomposite films were used to fabricate nanocomposite MNA's by micromoulding. Briefly, the optimised method found involved; sectioning the nanocomposite films in to ~1 x 1 cm pieces and filling them into the micromould at a specified weight of 0.175 grams. Electrochemical response stabilisation by using a specified weight of the nanocomposite films in order to achieve a define base-plate thickness is described in *section 4.3.4* and evaluated in *section 4.4.4*. The nanocomposite filled micromould was then heated in a thermal oven at 200°C. The resultant pliable material was then manually compressed into microcavities of the micromould to form the microneedles. Manual compression was repeated three time at 30 min intervals to ensure complete MNA formation in the micromould. An electrical contact was then made by minimally compressing a coiled wire into the backing of the base-plate surface during fabrication. This wire covered ~85% of the base-plate surface. Design and optimisation of an electrical contact is further detailed in Chapter 4, *section 4.3.4*. The micromould was then removed from the thermal oven and allowed to cool at RT for 30 mins to ensure firm connection of the electrical wire with the MNA-base plate. To seal the electric contact and to form a thick base, the micromould was filled with polycaprolactone (PCL) pellets (Polymorph®, Mindsets ltd, Essex, UK) and melted it over the base-plate at 100°C for 2 hours. After further cooling at RT, a nanocomposite MNA, complete with the electrical contact was ejected from the micromould manually. For electrochemical evaluation base-plate was concealed by allowing the microneedles to pierce through a layer of Parafilm^{TM} and sealing it around the

microneedles by application of heat at 40°C for 2 mins. Optimisations involving Parafilm™ is further detailed in Chapter 4, *sections 4.3.4* and *4.4.4*.

In chapter 5, attempts were made to improve the functional performance of the MNA's. In relation to this a successful approach found was to replace the bath-type sonicator with a probe-type sonicator (model: Q705, Fisherbrand™, Loughborough, UK). With reference to sample processing, using a probe-type sonicator caused a rapid rise in temperature with time, therefore, an acetonitrile dry ice bath was employed to keep the sample temperature low. The sonic probe was inserted half way into the container for even circulation of sonication energy at 100 % amplitude. The sonication energy was further delivered in pulses of 20 sec with a 30 sec rest period in between to prevent equipment and sample overheating. For dispersion of *f*-MWCNT, an optimised sonication time of 3 mins was used and for efficient intercalation with the polymer, an additional minute of sonication was employed after dissolution of PLA into the *f*-MWCNT dispersed. Further details relating to this method optimisation can be found in Chapter 5, *sections 5.3.1* and *5.4.1*.

In addition to the long –COOH functionalised MWCNT's used to fabricate the nanocomposite MNA's thus far, shorter versions of the nanotubes (l = 1 – 12 µm and O.D < 20 nm) with same and different functional groups (i.e. –COOH, $–N_2$, $–NH_2$), were additionally utilised to analyse the influence of MWCNT dimensions and functional groups on the performance of the nanocomposite MNA's. This required a method optimisation, whereby the concentration at which the MWCNT's were dispersed was altered from 0.5 to 0.05 wt%, whilst also adopting the improved sonication strategy. Further details to this optimisation can be found in Chapter 5, *sections 5.3.3* and *5.4.3*. As lowering the concentration maybe beneficial in improving the dispersion of all types of MWCNT's evaluated in the thesis, this final optimisation was applied to develop MNA based nanocomposite MNA's universally; regardless of the functional group or dimensions.

2.3 Characterisation and evaluation

2.3.1 Mechanical characterisation

2.3.1.1 Evaluation of axial and shear fracture strengths

At present, there exists no standardised tests and equipment to demonstrate the mechanical performance and safety profiles of MNA's[72]. However, a combination of tests, involving evaluation of axial fracture strength (AFS) and shear fracture strength (SFS) are

generally accepted to give a more complete profile of the mechanical behaviour of MNA's that can be correlated with successful insertion and removal from the skin. AFS measures the force required for a microneedle to fail under axial stresses (i.e. force applied parallel to the microneedle vertical axis)[73–75]. SFS on the other hand, measures lateral forces that a microneedle can withstand[74]. The mode of failure can be associated with bending, buckling or even fracture of the microneedles[72]. In this body of work, a texture analyser (TA) equipped with a video capture and synchronisation system (Stable Microsystems Ltd, Surrey, UK) was adopted to carry out the mechanical evaluation of all MNA's fabricated[75]. TA was used, because unlike the commonly used displacement force test stations, no further adaptations to the equipment was necessary as probes and fixtures were commercially available for effective placement and measurement from the microneedles[76]. AFS and SFS was evaluated by using the compressional mode of operation on the texture analyser. Envisioning the development of nanocomposite MNA-based electrodes, certain inhomogeneity between the microneedles were anticipated, due to improper dispersion. Therefore, the mechanical behaviour of a single microneedle was evaluated for both tests throughout the research presented in this thesis. A detailed account of the experimental parameters involved, and discussion of the methodology is given in Chapter 3, *sections 3.3.3, 3.4.3* and *3.5*.

2.3.1.2 Skin penetration studies

For skin penetration studies (and *in situ* biosensing studies detailed in Chapter 4, *section 4.3.6*), freshly excised ears were recovered from pigs that had been euthanised for unrelated studies at the Pirbright Institute (Pirbright, UK) and reused in accordance with the 3Rs (replacement, reduction and refinement) principles and ARRIVE guidelines. Full-thickness skin was removed from these freshly excised ears by blunt dissection and stored at - 80°C prior to usage. (For *in situ* biosensing studies, the porcine ears were transported on ice to the laboratory and used with 3 hours of excision).

MNA's were inserted into the skin by gradually applying a force up to 15 N using the thumb and holding it for 30 s before removal. An electronic weighing scale was used to carry out these penetration tests. Thereafter, the perforations were visualised by staining with saturated methylene blue solution, which selectively stain cells of the viable epidermis and not the stratum corneum. Assessment of penetration depth was not demonstrated at present and therefore the images obtained post-staining served as a quick qualitative test.

2.3.2 Electrochemical characterisation

During the different stages of fabrication, optimisation and evaluation, the performance of the nanocomposite MNA-based electrodes were evaluated using various electrochemical methods such as Cyclic voltammetry (CV), differential pulse voltammetry (DPV) and amperometry. In the section that follows, a brief technical background on these electrochemical methods are given. These are based mainly on popular texts by Joseph Wang, V.S. Bagotsky; and Allen J Bard, Larry R. Faulkner[77–80].

2.3.2.1 Fundamentals of electrochemistry

The field of electrochemistry is concerned with the interplay between electrical and chemical effects i.e. the measurement of electrical quantities such as current, potential, or charge and their relationship to chemical parameters[77]. Electrochemical systems study processes and factors that affect charge transfer across the interface between an electronic conductor (an electrode) and an ionic conductor (an electrolyte); referred to as the electrode-solution interface and these are heterogenous in nature due to different phases involved. The transfer of charge occurs through the movement of electrons in a solid phase and by the movements of ions in the solution phase. There are two types of electrochemical measurements, namely potentiometric and potentiostatic. Both types require at least two electrodes and an electrolyte solution, which constitute the electrochemical cell. The electrode that responds to the target analyte or where the reaction of interest is occurring is referred to as the working electrode. The second is termed as the reference electrode; which is of constant potential (i.e. independent of the solution properties, used as point of reference for potential control and measurement). An electrochemical cell can be classified as *galvanic* if electrical energy is produced through a spontaneous redox reaction, or *electrolytic* if an external potential is supplied to drive the charge transfer process.

Potentiometry is a static or passive technique (i.e. there is zero/negligible flow of current) that measures potential differences between the two electrodes in a system under equilibrium conditions; providing information about ion activity. Whereas, potentiostatic (i.e. controlled-potential) techniques; employed throughout this thesis, are based on dynamic (non-zero current) situations, in order to study the charge-transfer at the electrode-solution interface. More specifically, an electrode potential is used to drive a charge-transfer reaction and the resultant current is measured. In effect, the applied potential can force an

atomic or molecular species to gain (reduction) or lose (oxidation) electrons (collectively termed as a redox reaction), to and from the electrode. This electron-transfer causes current to flow in an external circuit. As the redox process occur at characteristic potentials for a given analyte, the potential at which the current flows can indicate the identity of the redox-active species. Potentiostatic techniques can thus be used to measure any compounds that are electroactive.

The objective of potentiostatic electroanalytic experiments is to identify a current response that is related to the concentration of the analyte being evaluated. This is achieved by monitoring the electron transfer during a redox process, which in turn follows Faraday's law; where it is stated that, the number of moles of reactant reduced or oxidised during an electrode process is directly proportional to the electrical charge that passes through the electrode. Therefore, for systems controlled by thermodynamic laws, the potential of the electrode can be used to determine the concentration of the analyte at the surface [C_O (0, t0] and C_R (0, t) according to the Nernst equation:

$$\mathrm{E} = E^{\mathrm{o}} + \frac{2.3RT}{nF} \log \frac{\mathrm{C_o}\,(0,t)}{\mathrm{C_R}\,(0,t)} \qquad \text{Equation 2.1}$$

where, E^{o} represents the standard reduction potential for the redox couple; R is the universal gas constant (8.3144 J mol^{-1} K^{-1}), T is temperature in Kelvin, n is the number of electrons transferred and F is the Faraday's constant (96,487 coulombs). Thus, the current measured as a result of the change in the oxidative state in an electrochemical reaction is called the Faraday's current and this is a direct measure of the rate of the redox reaction.

It is important to recognise that the total current measured not only accounts for faradic processes, but also includes non-faradaic processes. The latter is detailed in *section 2.3.2.2*

2.3.2.2 Electrode-solution interface

The interface acts to disrupt the electrolyte solution because the interactions between the solid and electrolyte are considerably different than those present in homogenous solutions. This difference will be exaggerated for electrodes under potentiostatic control because of the influence of the charge held at the electrodes. These factors constitute to the formation of strong interactions occurring between the ions/molecules in the solution and

the electrode surface; giving rise to a region called the electrical double layer. A brief explanation of this is given below.

The term, “electrical double layer” was first proposed by Helmholtz in 1850. This model assumed no electron transfer process to be occurring at the electrode surface and the solution to be composed entirely of electrolytes. The interaction of ions in solutions with the electrode surface was assumed to be electrostatic due to the fact that, the electrodes holds a charge density resulting from the excess or deficiency of electrons at the electrode surface. In order for the interface to remain neutral, ionic zones are formed (through redistribution of ions) with opposite charge close to the electrode surface. A positively charged electrode thus attracts a layer of negative ions from the electrolyte (and vice versa). As shown in Figure 2.1, the electrical double layer is in fact made up of several distinct parts. The innermost layer (i.e. closest to the electrode) is known as inner Helmholtz plane (IHP). This contains solvent molecules and non-fully solvated specifically absorbed ions. This plane cuts through the centre of the absorbed species. The next layer is termed, the outer Helmholtz plane (OHP) and it cuts through the centre of solvated counter-ions approaching closest to the surface. They are attracted to the surface by long range coulombic forces and they lower the electrical potential at points adjacent to the particle surface. Collectively, both these layers are called the compact layer. The Helmholtz model however does not take into account thermal agitations, which acts to loosen the compact layer. This limitation was addressed by Gouy-Chapman; adding a diffuse layer. This is a three-dimensional region of scattered ions extending from the OHP to the bulk solution and it reflects a dynamic balance between the electrostatic attraction and the tendency to diffuse away through random thermal motion. Based on these opposing forces, the concentration of ions at the diffusion layer decreases exponentially at a given distance from the electrode. Overall, the surface charge forming a layer and diffuse shield forming the other layer, is the basis of electrical double layer.

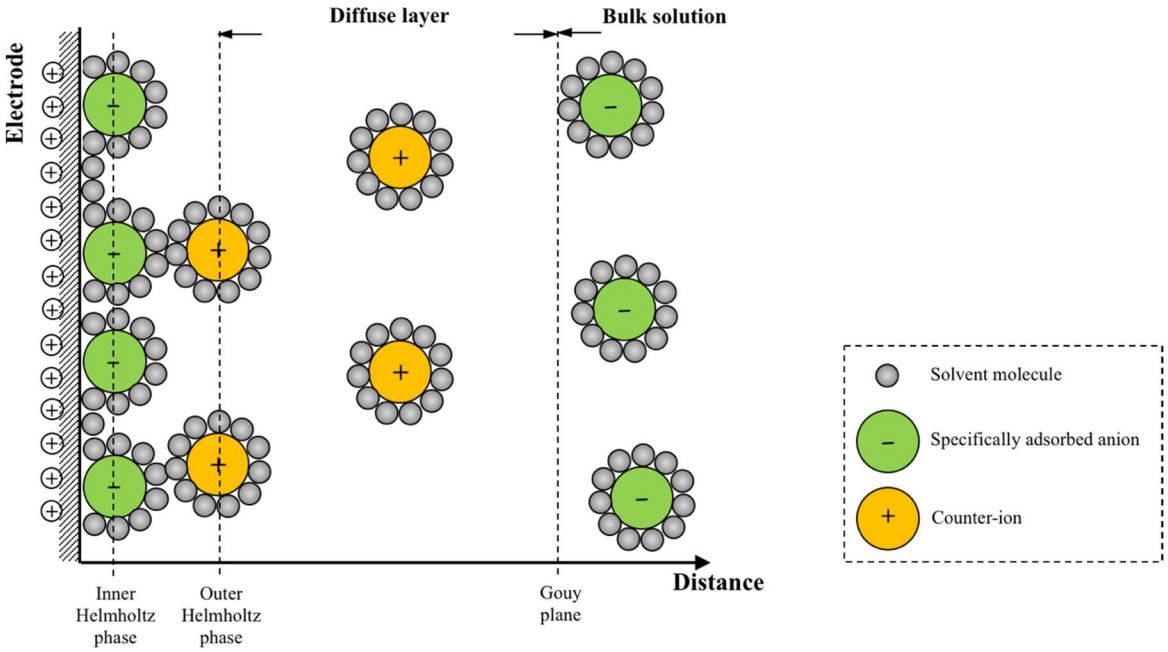

Figure 2.1 Model of electrical layer. Shows specifically absorbed anion, solvent molecules and counter-ions.

Experimentally, the electrical double layer/the electrode-solution interface has been shown to behave like a capacitor; which is defined as an electrical circuit composed of two metal sheets separated by a dielectric material (Figure 2.2). The capacitive behaviour can be explained on the basis where charge-transfer reactions ceases to occur over particular voltage ranges due to unfavourable thermodynamic or kinetic conditions. However, the electrode-solution interface can still change from adsorption or desorption, with reference to a changing potential, electrode area or solution composition. These processes are referred to as nonfaradaic processes. In this case, while a charge is not crossing the interface, it can still flow in an external circuit until the equation for capacitance (Equation 2.2) is satisfied. This flow of charge is called the charging current.

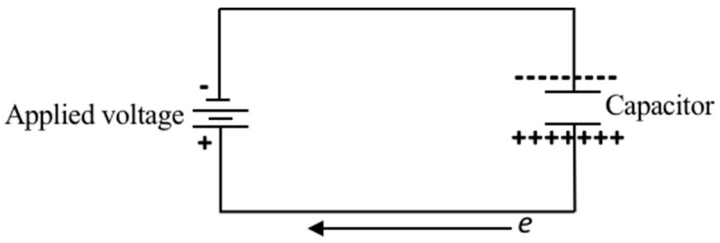

Figure 2.2 Capacitor. Charge accumulating on both plates as a result of applied voltage.

The behaviour of the capacitor is governed by the equation:

$$q = EC \qquad \text{Equation 2.2}$$

where q represents the charge stored on a capacitor, E is the potential (in volts, V) and C is the capacitance (in Farads, F). The charge is proportional to the potential difference and this can be translated to the double-layer as:

$$q = C_{dl}\, A\, (E - E_{pzc}) \qquad \text{Equation 2.3}$$

where C_{dl} is capacitance per unit area and E_{pzc} is the potential at which there is zero change (i.e. when the double layer is neutral). The double layer capacitance is measured as combination of the compact and the diffuse layer; which is typically in the range of 10 – 40 μF cm^{-2}. Overall, the double layer in responsible for the charging current and it can act to limits the detectability of potentiostatic techniques, especially when the concentrations of the electroactive species are low.

2.3.2.3 Electrode reaction

In terms of electrode kinetics, it can be postulated that when the voltage is increased, the rate of reaction and therefore the current would increase exponentially. Consequently, this implies that an unlimited quantity of current can pass through the electrode. However, this is not the case, as indicated by following expression:

$$i_c = -nF\, Ak_{red}\, [O]_o \qquad \text{Equation 2.4}$$

According to equation 2.4, for a fixed area of electrode (A), the reaction can be controlled by the rate constant (k_{red}) and the concentration of the reaction at the surface $[O]_o$. (i_c indicates current from a reduction reaction, n is the number of electrons transferred and F is the Faraday's constant). If there is large rate constant, then any reactant close to the surface of the electrode is immediately converted into products, hence the current becomes dependent on the amount of fresh reactant reaching the electrode surface from the bulk solution. This movement in and out of the electrode-solution interface is important in predicting the flow of current. The section below gives a brief description of the ways in which material can move within the solution to the interface in a process known as mass transport.

The pathway to an electrochemical reaction occurring at the electrode surface is rather complex and it occurs in a sequence of events. This is shown in Figure 2.3. The rate of reaction is dependent on the slowest steps of the process. A simple reaction only involves mass transport; for movement of electroactive species from the bulk solution the electrode surface, electron transfer at the electrode surface and transport of the product back to the bulk solution. More complex reactions however includes, additional chemical reactions preceding or following the electron transfer process and surface reactions such as adsorption, desorption or electrodeposition. Whether a reaction is controlled by mass transport or electron transfer is dependent on the analyte being evaluated and experimental aspects such as electrode material, media, the potential being applied, time scale and the mode of mass transport.

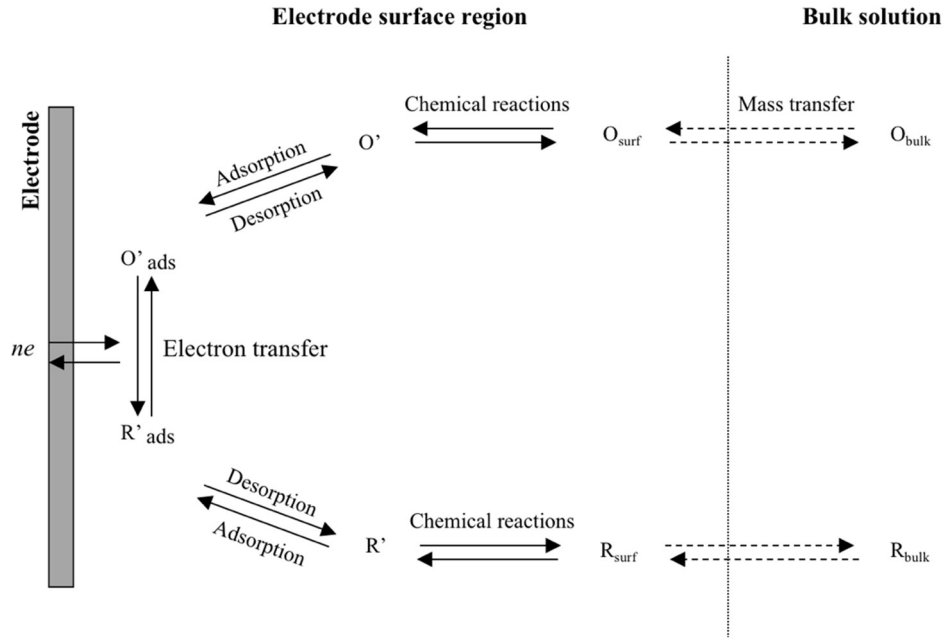

Figure 2.3 Various pathways to an electrochemical reaction.

If a reaction is solely dependent of the rate at which the target analyte reaches the surface, the current is said to be mass-transport limited. The rate of mass transport (from the bulk to the surface) is governed by flux (*J*); defined as the number of molecules penetrating a unit area of an imaginary plane, in a unit of time (units: mol cm^{-2} s^{-1}). It is described by expression:

$$J\,(x,t) == \frac{i}{zFA} \qquad \text{Equation 2.5}$$

where $J(x, t)$ refers to the flux of the species, i is current in ampere (A), z is the number of electrons involved in the reaction, F as before is the Faraday's constant and A indicates the area of the electrode in cm^2.

Mass transport occurs in three different modes: (1) diffusion, (2) convection and (3) migration. Diffusion occurs when there is concentration gradient (from regions of high to low concentrations) and it acts to minimise the concentration gradient. Convection indicates transport by gross physical movement to the electrode surface. It can occur naturally through thermal or density gradient and artificially by inducing flow by means of stirring or using a rotating disc. Finally, migration accounts for movement of particles along an electrical field. In other words, this is an electrostatic effect arising from the application of voltage to the electrodes. The interface as results becomes charged and any charged species near the interface will either be attracted or repelled by electrostatic forces. By taking these factors into account, the rate of mass transport can be re-written as follows (Nernst-Planck Equation);

$$J(x,t) = \underbrace{-D\frac{\partial C(x,t)}{\partial x}}_{\text{Diffusion}} - \underbrace{\frac{zFDC}{RT}\frac{\partial \emptyset(x,t)}{\partial x}}_{\text{Migration}} + \underbrace{C(x,t)\,V(x,t)}_{\text{Convection}} \qquad \text{Equation 2.6}$$

where D is the diffusion co-efficient ($cm^{-2}\ s^{-1}$), $\partial C(x, t)/\partial x$ is the concentration gradient (at distance x and time t), $\partial \emptyset(x, t)/\partial x$ is the potential gradient (z refers to the charge and C indicates the concentration gradient; of the electroactive species) and $V(x, t)$ indicates the hydrodynamic velocity of the solution. The flux measured is proportional to the current (i) according to the equation below:

$$i = -nFAJ \qquad \text{Equation 2.7}$$

As indicated through Equation 2.6, it is very difficult to calculate flux when all three processes are involved. Therefore, the situation is often simplified in electroanalysis by suppressing migration and convection by adding a strong background analyte, which is usually an inert salt (e.g. KCl) and thus the movement of electroactive species becomes limited by diffusion alone. As a concentration gradient is established adjacent to the surface of the electrode, resultant of the reactions occurring at the surface, a diffusional flux is set-up. This can be expressed as Fick's law, which indicates that the rate of diffusion is

proportional to the slope of the concentration gradient. Equation 2.6 can thus be simplified as following:

$$J\,(x,t) = -D\,\frac{\partial C\,(x,t)}{\partial x} \qquad \text{Equation 2.8}$$

And, the current generated from an oxidation or reduction can be expressed as function of the concentration gradient by combining equations 2.5 and 2.8 as follows:

$$i = zFAD\,\frac{\partial C\,(x,t)}{\partial x} \qquad \text{Equation 2.9}$$

2.3.2.4 Electrochemical cell set-up

In all electrochemical experiments, a three-electrode cell is commonly employed; consisting of a working electrode (WE), an auxiliary electrode (AE) - also known as the counter electrode (CE) and a reference electrode (RE). The WE is where the electrochemical reaction occurs. The most important aspect with regards to their construction is that, the material used to compose the WE should be redox inert in the potential range of interest[82]. Depending on the voltage being applied, the WE can act as either the anode or cathode. The CE is used to close the circuit in the electrochemical cell. It does not take part in an electrochemical reaction and they are made of inert materials such platinum, gold, graphite or glassy carbon. The CE will assume the role of anode or cathode, depending on the role of the WE. Current is recorded as the electron flow between the WE and CE. Therefore, the total surface area of the CE has to be greater than the WE in order to ensure that kinetics of the reaction occurring at the CE does not limit those on the WE. As previously indicated in *section 2.3.2.1*, the RE has a constant equilibrium potential and it is used as a point of reference against which the potential of other electrodes can be measured. More specifically, the potentiostat controls the potential being applied to the WE as a function of the RE potential and importantly, to determine the analyte potential, the CE and WE potentials are measured against the RE. The standard hydrogen electrode (SHE), saturated calomel electrode (SCE) and the silver/silver chloride (Ag|AgCl) electrode are commonly used RE's in aqueous media. However, the latter is more commonly employed due the simplicity in handling them and their potential is determined by the reaction:

$$AgCl_{(s)} + e^- = Ag_{(s)} + Cl^- \qquad \text{Equation 2.10}$$

2.3.2.5 Electroanalytical methods

2.3.2.5.1 Cyclic voltammetry

Cyclic voltammetry (CV) is a voltammetric technique that is most widely used to acquire qualitative information about electrochemical reactions. CV can be employed to rapidly gain information about the thermodynamics of the redox process, the kinetics of electron-transfer reactions and on coupled chemical reactions or adsorption process.

In CV experiments, the potential applied to the WE is a triangular waveform (as shown in Figure 2.4A), scanning linearly between two predetermined limits at a known scan rate[83]. It starts from E_1 and when the voltage reaches E_2 the scan in reversed and swept back to E_1. As it scans, the current response at the WE is being recorded as a function of the applied potential. This current versus potential plot is termed as a cyclic voltammogram and is shown in Figure 2.4B. During CV experiments, the solution is left unstirred/static and in this condition, the redox current is determined by factors such as the concentration of the reactant, surface area of the electrode, co-efficient of diffusion and the scan rate. The behaviour of the voltammogram shown in Figure 2.4B can be explained as follows. Since the solution is static, the electroactive species being oxidised or reduced is becoming depleted in the region closest to the electrode surface. Therefore, as the potential is swept past the redox potentials of the electroactive species in solution, the current is seen to increase and then decreases as the reactant near the surface is being used up. More specifically, this behaviour can be attributed to mass transport, which is by diffusion and it is slow; indicating that a steady state concentration is not achievable near the electrode surface. The depletion zone thus grows and the rate of mass transport decreases. As a result, the current is prevented from increasing exponentially with the applied potential. The current reaches maximum as the mass transport becomes rate determining and since, the concentration gradient is decreasing, the rate of mass transport also decreases; causing the current to decay. Relating this to the voltammogram, as the potential is swept in the cathodic direction, the current increases as the analyte is being reduced and when the scan is reversed in to anodic direction, the reduced analyte is being re-oxidised. The recorded voltammogram has certain well-defined characteristics.

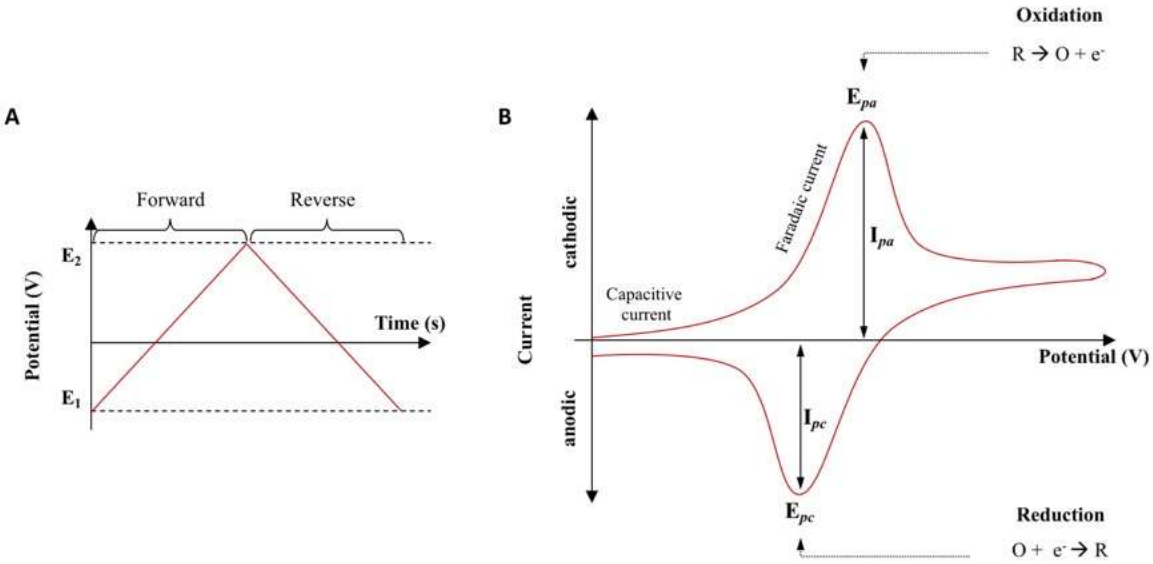

Figure 2.4 Cyclic voltammetric process. (A) Triangular waveform indicating the applied potential programme, where E_1 and E_2 indicates a potential switch and (B) typical cyclic voltammogram for a reversible redox process.

1. If the reaction is reversibly, then the separation between peak potentials (ΔE_p) would be close to 58/n mV (at 25°C).

2. The ratio of the peak currents at the anode (I_{pa}) and at the cathode (I_{pc}) is equal to one.

3. The peaks currents are proportional to the concentration and increases (because faster scan rates lead to a decrement in the size of the diffusion layer) with the square root of the scan rate as given by the Randles-Sevcik equation (Equation 2.11).

$$I_{pa} = (2.69 \times 10^5)\, n^{3/2}\, ACD^{1/2}\, V^{1/2} \qquad \text{Equation 2.11}$$

where A is the area of the electrode in cm^2, C is concentration in mol cm^{-3}, D is the diffusion coefficient in $cm^2\ s^{-1}$ and v is the scan rate in Vs^{-1} and n is the stochiometric number of electrons (for example, $n = 1$ for ferrocyanide reduction reaction as shown below):

$$Fe(CN)_6^{3-} + e^- \rightarrow Fe(CN)_6^{4-} \qquad \text{Equation 2.12}$$

4. A linear Randles-Sevcik plot (peak current vs scan rate) is indicative of reversible electron transfer process involving freely diffusing redox species. Any deviations

from the linearity indicates electron transfer occurring via surface absorbed electroactive species.

5. The formal potential of the redox process for a reversible couple is centred between E_{pa} and E_{pc}, as shown by the expression below:

$$E^o = \frac{E_{pa} + E_{pc}}{2} \qquad \text{Equation 2.13}$$

6. An irreversible electron transfer reaction shows considerably different behaviour on the recorded voltammogram i.e. individual peaks are reduced in size and widely separated; peak potential shifts with the scan rate and there will be a large separation between the peak potentials.

2.3.2.5.2 Differential pulse voltammetry

DPV is one of the most widely utilised pulse techniques[84,85]. The pulse implies a potential step and it is used to increase the ratio between faradaic and non-faradaic (or charging) currents, which consequently improves quantitation of the detection limits of an analyte up to 10^{-8} M concentrations. In DPV, the pulses of fixed amplitude (10 – 100 mv) are superimposed on a linear potential ramp and applied to the working electrode (Figure 2.5). Each potential step has a duration of about 50 ms. The current is then measured at two points i.e. the first, just before the application of the pulse (at point *a*) and the second, at the end of pulse (at point *b*, after ~40 ms). This way of sampling ensures that the charging current measured is negligible because it decays exponentially after the potential step, while the faradaic current decays more slowly. Therefore, by sampling late in the pulse life, mainly the faradaic current is measured. The difference between the first and second current measurement is determined for each pulse and plotted against the applied potential. This gives a voltammogram consisting of peak(s). The height of the peak is directly proportional to the concentration of the analyte, while peak potential can be used to identify the electroactive species. Moreover, the width of the peak indicates electron stoichiometry.

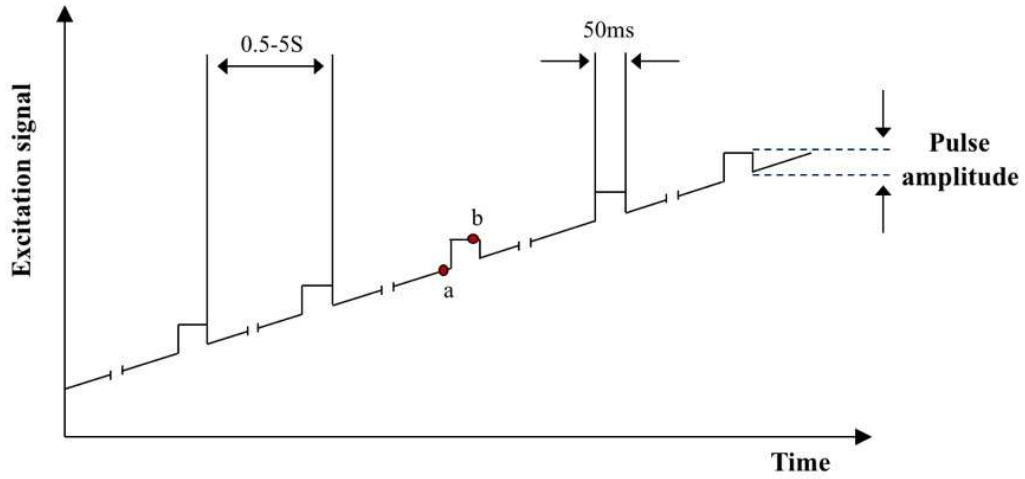

Figure 2.5 Differential pulse voltammetry. Excitation signal showing fixed amplitude pulses superimposed on a potential ramp.

2.3.2.5.3 Amperometry

In amperometry, current is measured at a fixed potential against a reference electrode[86]. The is the most common and simple electrochemical detection method. By keeping the potential fixed, the changes associated with electrical double layer charging at the electrode-solution interface causing non-faradaic currents can be avoided. Therefore, the response is a large amplitude faradic current, through heterogenous electron transfer (as indicated in Figure 2.3) from the electroactive species undergoing redox reactions. In amperometric experiments, the potential is initially fixed until a steady state current is obtained. In order to achieve this, the solution is stirred, and it thus provides greater efficiency for mass transport ensuring that the concentration gradient at the WE is constant. The analyte is then added successively, but only after a steady state is achieved before each addition. This results in an increment in the current being measured; where its magnitude is proportional to the concertation of the analyte. In turn, the concentration is proportional to the rate of redox reaction at the WE.

2.4 Cell culture techniques

Human keratinocyte cell line (HaCaT, donated by Professor Green formerly from MRC centre, at the University of Sussex) and A375 (ECACC 88113005) human malignant melanoma cells (Sigma Aldrich, Gillingham, UK) were routinely cultured for cytotoxicity assessments carried out in Chapter 6. This section details the experimental procedure for routine culture and experimental usage.

2.4.1 Thawing, culture, subculture and storage

Both cells were received cryopreserved in 95% media and 5% DMSO. For culturing, the cells were thawed rapidly in a water bath at 37°C and then transferred into T75 flasks containing 15 mL of pre-warmed, complete, Dulbecco's modified Eagle medium (DMEM, with a high glucose content of 4.5 g/L and supplemented with foetal bovine serum (FBS) at 10% and 15%, respectively for HaCaT and A375 cell culture). The flasks were then incubated under standard conditions (i.e. 37°C under 5% CO_2 - 95% air) for 24 hrs in order to allow the cells to attach. The media was then aspirated, and the attached cells were washed with PBS before replacing with fresh media. The cells were then allowed to grow (with media changes every 2 - 3 days) until they reached 75 – 80% confluency, at which point they were subcultured/passaged. This involved, detachment of the cells by incubating with 5 mL of pre-warmed trypsin-EDTA for 5 – 8 mins at 37°C; neutralisation of trypsin by adding 10 mL of complete media; gentle mixing, followed by centrifugation at 500 xg for 5 mins to form pellets; re-suspension of the pellet in 1 mL of pre-warmed complete mediate and redistribution into new sterile T75 flasks. HaCaT cells were routinely seeded in a ratio of 1:5 to 1:10; whereas for the A375 cells, the ratios were 1:3 to 1:10. Alternatively, for storage purposes, after trypsinisation and centrifugation, the cells were re-suspended in 1 mL of complete mediate containing 10% (v/v) dimethyl sulfoxide (DMSO). This suspension was transferred to cryogenic tubes, frozen at -80°C for 48h in a freezing pot and then transferred to liquid nitrogen vapour (-130°C) for long-term storage.

2.4.2 Quantification of cell number using a haemocytometer

To determine the seeding density, the re-suspended cells were diluted 1:10 in complete media. A 10 µL aliquot of this suspension was then loaded onto the chambers of a Neubauer haemocytometer. Cell counts were made manually in at least the four outer counting squares of the haemocytometer using an inverted light microscope (20x magnification). A total cell count was calculated using the following equation:

$$Total\ number\ of cells/mL = \frac{total\ cell\ count\ \times\ dilution\ factor\ \times\ (1\ \times 10^4\ cells/ml)}{number\ of\ squares} \qquad \text{Equation 2.14}$$

Once a total cell count was obtained, the volume of the cell suspension required to seed the desired number of cells per flask was calculated by dividing the required number of cells by the total number of cells/mL.

2.5 Statistical analysis

Mechanical forces were measured and recorded using Exponent Lite software (version 6.1.9.0; Stable Microsystems Ltd, Surrey, UK). Similarly, CHI760 (version 14.02; CH Instruments, Inc, Austin, TX, USA) was used to measure DPV traces, with respect to their peak potential and total peak area. GraphPad Prizm 6 (GraphPad Software, La Jolla, CA, USA) was used to analyse the data. Where appropriate, statistical differences between groups were assessed using two-sided Student's t-test, repeated measures, one- or two-way analysis of variance (ANOVA). Differences were considered statistically significant where $p < 0.05$. All data are expressed as mean ± standard deviation.

Chapter 3. Investigating the potential for developing Epoxy/Carbon Nanotube composites based MNA electrodes

3.1 Introduction

Epoxy is the most widely utilised matrix for manufacturing advanced composites for applications in aircraft/aerospace engineering, electronics, electromagnetic interference (EMI) shielding, sensors and biomedical devices[87]. Epoxy resin is a thermosetting, cross-linked, low-molecular-weight polymer that provides attractive material properties such as high specific strength, stiffness, adhesivity to a range of substrates, good thermal and chemical resistance and low shrinkage during curing[88]. For structural applications, the major drawback of epoxy is attributed to their inherent brittleness[87]. As such, over the past two decades extensive research efforts have gone into their reinforcement with the addition of CNT's and this dates back to the time when the first ever polymer nanocomposite was produced, in 1994 by Ajayan *et al.*[89]. Interestingly, the first ever CNT-based nanocomposite for electrochemical sensing was also produced using epoxy as a matrix, in 2005 by Pumera *et al*.; due to their simplicity in processing via add-mixing[90]. In this primary study, crucial comparisons were made with differing length and diameters of CNT's (i.e. length: 0.5 – 200 μm, outer diameter: 30 – 50 nm and length 0.5 – 2 μm, outer diameter: 20 – 30 nm); where they found enhanced electrochemical activity for the long-carbon nanotube composites towards ferricyanide, nicotinamide adenine dinucleotide (NADH) and hydrogen peroxide (H_2O_2). Since this initial study, there have been an increasing number of reports demonstrating excellent electrochemical behaviour of CNT-epoxy based composites. Examples include: glucose biosensors made by mixing CNT's with GOx enzyme and homogenised into epoxy resin[91]; tyrosinase enzyme incorporated CNT-epoxy biocomposite for detection of catechol[92]; highly compressed MWCNT-epoxy composites providing excellent anti-fouling properties for highly sensitive detection of serotonin[71] and hybrid composites of MWCNT-Prussian blue (PB)/epoxy, showing enhanced stability and sensitivity towards the detection of glutathione[70]. In concert with these results and the inherent advantage of using nanocomposite formulations i.e. offering a wide range of design possibilities; MNA fabrication via epoxy nanocomposite processing offers a unique opportunity to develop simple, low-cost and highly sensitive electrochemical biosensors.

However, the above studies have all incorporated a very high percentage of CNT in to their composites (>15%, w/w), which poses a significant challenge to the design of MNA's due to the increased viscosity of the composites; making dispersions harder and the resultant clustering of CNT's impacting on both the fabrication and the mechanical strength of the microneedles. Therefore, effective dispersions at lower concentrations are ideal.

In the sections below a brief introduction is given to CNT's first and foremost, with respect to their fabrication, material properties and electrochemical behaviour. Following which a detailed account is given on the processing of epoxies, methods of developing epoxy-based nanocomposites and finally, the influence of CNT's in improving mechanical and electrical properties.

3.1.1 Carbon Nanotubes

CNT's are allotropes of carbon, with a cylindrical structure composed of hexagonal graphitic sheets of sp^2 hybridised carbon-carbon chemical bonds[93]. The existence of these cylindrical graphitic structures was reported and studied from the early 1950's by several researchers, however Iijima's detailed analysis of the helical arrangement of carbon atoms on seamless co-axial cylinders published in 1991 is considered to be first discovery report[94,95]. Since then, CNT's have attracted significant research interests with potential applications as nanoelectronics and photovoltaics devices, superconductors, electrochemical capacitors, sensors, nanowires and advanced nanocomposite materials[96]. With respect to the sp^2 arrangement, each carbon atom is covalently bonded to three neighbouring carbon atoms via sp^2 orbitals. The strength on this sp^2 carbon-carbon bonds accounts for the extraordinary mechanical strength displayed by the CNT's. In addition, the fourth valence electrons remain free in each unit and they are delocalised over the entire system; thus, it accounts for the ultrahigh electronic properties displayed. Typical values reported include an ultra-high elastic module of ~1 Tpa, superior tensile strength between 11 – 63 Gpa (up to 50 times higher than steel) whilst having a density as low as 1.3 g/cm^3 ($1/6^{th}$ to that of stainless steel) and conductivities higher than copper[97–100]. In terms of dimensions, CNT's are several hundred micrometres in length, with diameters in the nanometre scale. Typical length-to-diameter ratio often exceeds 1000; thus, indicating the presence of an extremely high aspect ratio[93]. Due to their high aspect ratio, CNT's are considered nearly one-dimensional structures.

There are two main structural forms of CNT's i.e. a single-walled CNT's (SWCNT's) and multi-walled CNT's (MWCNT's). As the name suggests, SWCNT's are formed by rolling a single layer of graphite (called a graphene layer), whereas MWCNT's are made of concentric cylindrical layers (typically up to 50 layers) of graphene. Aside from the two main structural forms, there are three different chiralities for CNT's: armchair, zigzag and chiral[101,102]. This is shown in Figure 3.1[103]. These chiral types are formed based on the orientation of the tube axis (or rolling axis) relative to the hexagonal lattice structure of the graphene sheet. The chiral vector is denoted by a pair of indices, namely *n* and *m*; where m = 0 the nanotube is zigzag, n = m indicates armchair and all other configurations where n ≠ m is described as chiral. CNT's can behave as either semi-conducting or metallic depending on their chirality. The armchair type possess conductivity similar to metals (higher than copper) whereas the other two types are semi-conducting[104]. With reference to MWCNT's,

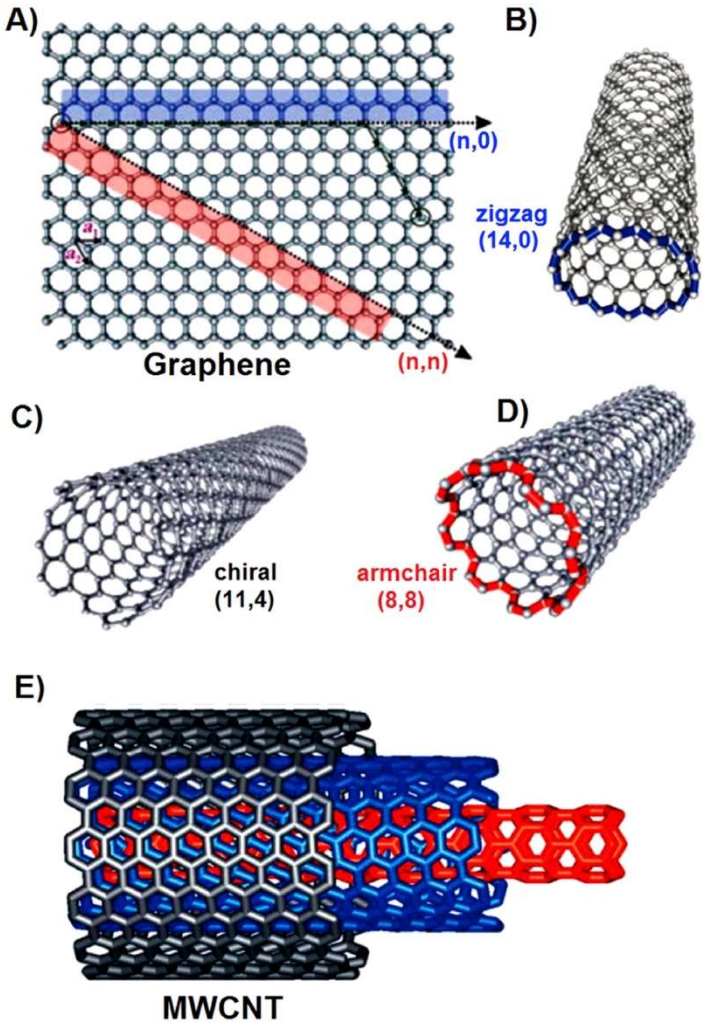

Figure 3.1 Three different structural forms of CNT's. (A) Graphene layer, showing the chiral vectors; calculated as n a_1 + m a_2. (B) zigzag (n = m), (C) chiral (n ≠ m) and (D) armchair (m = 0). (E) MWCNT's made with three layers having different chirality. Reproduced with permission[103]. Copyright 2017, Elsevier.

each graphene layer can have different chirality. Consequently, they possess a high surface area, unique physical properties, chemical stability and high electrical conductivity. For applications in nanoelectronics, SWCNT's are commonly utilised because they can offer scatter free ballistic transport[105]. MWCNT's on the other hand, have been found to be fairly diffusive or quasi-ballistic[106]. For applications as electrochemical sensors, which is the intended objective for this thesis, MWCNT's are preferred over SWCNT's. A detailed explanation for this is given in *section 3.1.1.1*.

Arc discharge, laser ablation, high pressure carbon monoxide (HIPCO) and catalytic chemical vapour deposition (CCVD) are common methods employed to synthesise CNT's[94]. Due to a high degree of control and its scalability, the latter is primarily used for CNT synthesis[14,93]. However, the growth mechanisms are ill defined for all methods of fabrication. For example, in CCVD, the control of structure, semiconducting/metallic ratio and the nature and density of the defects are poorly understood[107]. SWCNT's remain to be very expensive to produce due to the extensive post-purification methods required to obtain specific chiralities and diameters, which ultimately defines their applications[108].

CNT's usually aggregate forming bundles and ropes due to strong Van der Waals interactions between the tubes. Consequently, they are extremely difficult disperse and align in any polymeric matrices. To overcome this issue, several strategies have been developed[96]. These includes: (1) mechanical dispersion via ultrasonication, ball milling, calendaring and extrusion (melt compounding). (2) Covalent functionalisation; whereby acid treatments are used to create functional groups (commonly hydroxyl, carboxy and amino) in an attempt to improve interfacial interaction with the matrix involved. However, covalent functionalisation disrupts the translational symmetry of CNT's by changing some of the sp^2 carbon atoms into sp^3 carbon atoms; thus, negatively impacting electronic and transport properties. (3) Non-covalent functionalisation strategies have therefore been used as an effective alternative to covalent functionalisation. This involves adsorption of surfactant or biomacromolecules to CNT surfaces and they prevent agglomeration by causing electrostatic repulsion between the nanotubes. This process in turn preserves all intrinsic properties of the CNT's. However, translation of non-covalent strategies to nanocomposites are challenging because they could influence the functional properties either positively or negatively. Typically, a combinatorial approach is commonly employed to realise the full potential of CNT's in nanocomposites.

3.1.1.1 Electrochemical behaviour of CNT's

Both SWCNT and MWCNT have been successfully utilised for the synthesis of polymer nanocomposites, with enhanced mechanical and electrical properties. However, the latter is more commonly used for electroanalysis. SWCNT's are considered a large singular molecule whereas MWCNT's are referred as a mesoscale graphite system. The electrocatalytic activity of CNT is a result of edge-plane-like graphitic sites[109,110]. This occurs at the open ends and along the tube axis of MWCNT's. However, the walls of MWCNT's are similar to the basal plane of highly ordered pyrolytic graphite[109]. The edge plane displays considerably faster electrode kinetics compared to the basal plane. In relation to electrochemical behaviour, this means that an electrode composed of edge-plane-like graphitic sites will produce a reversible voltammogram, whereas a basal-plane-dominated electrode will produce an irreversible behaviour; yet again depending on the amount of edges available[111]. It has been demonstrated by Davis *et al*. that the basal planes are, in fact, electrochemically inert[112]. Therefore, the structure of MWCNT's provides a vast number of active sites that can enhance the electrocatalytic behaviour of biosensors. The electrocatalytic activity of MWCNT is further dependant on the method of CNT synthesis. It has been evidenced that CCVD-grown MWCNT's display a higher electrocatalytic activity compared to the arc-discharge process, due to the higher density of edge-plane-like sites on the open end of the CNT in the former; whereas as the latter have closed ends and resemble the basal plane of highly ordered pyrolytic graphite[113]. The aforementioned factors are critical when considering the development of an electroactive polymer nanocomposite.

3.1.2 Processing of epoxy and their composites

Epoxy resins are pre-polymers containing two or more ring-like epoxide groups of the form as shown in Figure 3.2. They are of many types and these thermosetting resins are cured using a variety of curing agents; which in turn dictates the properties of the final product[88]. Therefore, fabrication of epoxy-CNT based MNA's can be divided into three-stages: (1) developing a strategy to fabricate mechanically strong MNA's using different types of epoxy formulations (i.e. screening); (2) mechanical studies to evaluate the strength of MNA's developed using various epoxy formulations and (3) assessing processing

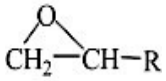

Figure 3.2. Epoxide group

conditions to incorporate CNT's into the epoxy matrix and translating the fabricational strategy used for fabricating neat epoxy MNA's to form nanocomposite MNA's.

Diglycidyl ether of bisphenol A (DGEBA) is the most widely used epoxy resin[114]. They are produced by reacting epichlorohydrin with bisphenol-A in the presence of a basic catalyst (chemical structure as shown in Figure 3.3)[88]. DGEBA is tough and have excellent adhesive properties[114]. For incorporating CNT's, viscosity of the resin is one of the most important parameters to be considered. DEGBA is viscous, with a honey-like consistency, but their viscosity can be lowered significantly upon warming. Several types of curing agents also exist for cross-linking the polymer, of which amine and anhydride curing agents are most widely employed[88,114]. As previously mentioned, brittleness is the major limitation of the epoxies, but this can be addressed to some extent by selecting appropriate curing agents. In this study, DGEBA resin with a combination of amine and anhydride curing agents were chosen to evaluate their potential to form MNA's with good mechanical properties.

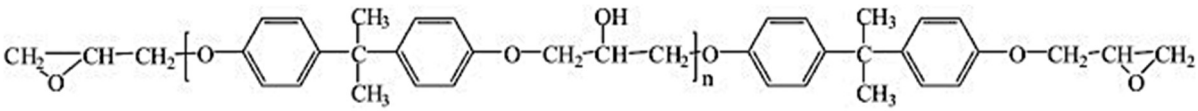

Figure 3.3. Structure of DGEBA

Several strategies are used to fabricate epoxy/CNT composites. These include solution mixing, bulk mixing/blending and *in situ* polymerisation[115]. The choice of these processes consequently affects the mechanical and electrical properties of the composites. With reference to *in situ* polymerisation, due to enhanced interaction with the polymer, the lowest electrical percolation threshold and the highest mechanical properties for the composites has been observed with this technique[115]. However, as the epoxy is a thermosetting resin, blending and solution mixing is the most popular strategy employed in the fabrication of composites. Blending is a facile approach utilising high shear forces or add-mixing to mix the individual components together. Usually this results in poor CNT dispersion efficiency and it may not be possible to incorporate high CNT loadings with this technique because of the high viscosity of the epoxy resin[87,115]. As an alternative, solution mixing is highly advantageous because it facilitates enhanced dispersion of CNT's in epoxy. The approach here is to dissolve the epoxy in a solvent and then CNT is dispersed into this mixture by magnetic stirring or sonication. This is followed by removal of the solvent by controlled evaporation and moulding of the composite material into the desired shape. It is now well

established that the addition of CNT can significantly influence the curing kinetics of the epoxy resin; of which there are two important steps: gelation and vitrification[116]. Vega *et al*., found that the time for gelation and vitrification was decreased slightly with the addition of 0.2 wt% of CNT; whilst pointing out that a higher CNT concentration would have a more significant effect on the curing kinetics[117].

The changes in mechanical and electrical properties with the addition of CNT's into epoxy matrices have been extensively documented. However, as the aim is to develop a facile strategy for fabricating MNA-based electrochemical sensors, blending and solution mixing processes were particularly attractive due their simplicity. With reference to this, a brief discussion on mechanical and electrical properties is given below.

3.1.2.1 Mechanical properties

The poor dispersibility and weak interfacial interactions of CNT's with the epoxy matrix is well known. To overcome these issues CNT's are typically modified covalently or with chemical functional groups. However, comparisons are difficult to establish between studies, due to the use of different combinations of epoxies and hardeners as well as variations in processing conditions within the solution mixing and blending processes. The use of different CNT types, geometries and functional chemistries further adds to the difficulty in drawing comparative analysis with regards to mechanical properties. Nevertheless, some of the important results are highlighted below.

With reference to pristine MWCNT's, incorporation of high amounts of MWCNT's (< 1 wt%) with manual homogenisation did not yield significantly enhanced mechanical properties[118]. At 1 wt% of CNT loading, the percentage improvement in tensile strength (TS) and Young's modulus (YM) was 20% and 100% respectively. These results hardly improved, when 4 wt% of MWCNT was incorporated into the epoxy matrix. The TS obtained was identical to 1 wt% at 20%, whereas the YM increased marginally by 15%. This is because, the homogenisation process became difficult at higher CNT loadings due to high sample viscosity and resulted in highly aggregated nanocomposites[118]. When solution mixing was employed however, the mechanical properties were seen to improve with the increment in CNT loading; producing an improved TS of 50% and YM of 100% at a CNT loading of 3 wt%[119]. When oxidised MWCNT's are used in combination with high powered ultrasonication, an even higher loading of CNT's (i.e. 8 wt%) could be incorporated in the epoxy matrix; producing a TS and YM that are ~27% and ~65% higher,

respectively, when compared to neat epoxy[120]. This increase in TS and YM are not comparatively higher to those found in the aforementioned studies, but when considering the fact that electrochemical sensors are often constructed with a high concentration of CNT; these results are encouraging. Instead of oxidised MWCNT, amino-functionalised MWCNT's are popular within epoxy composites as they can form covalent bonds with the epoxy resin. For example, at just 0.1 wt% CNT loading, the enhancement in TS was found to be 12% and YM at 56% for non-solution mixed composites[121]. Collectively, these results provide a good scope for fabricating epoxy-based nanocomposite MNA's by blending or solution mixing processes, without compromising on the need for incorporating high CNT loadings; necessary to achieve good electrochemical properties.

3.1.2.2 Electrical properties

With reference to the electronic conductivity of nanocomposites, the traditional view has been that, electrical conductivity can be increased through enhanced dispersion of the CNT's or by reducing the overall size of the aggregates[122]. The reasoning behind this, as demonstrated by Grossiord *et al.*[123] and Xu *et al.*[124]. was that, a good dispersion can increase the number of complete conductive paths in the nanocomposite. Better dispersion has been shown to reduce the probability for nanomaterials to re-aggregate into clusters, such that more of the conductive pathways are built up by binary conductive materials in the system[125]. An enhanced dispersion can also help lower the percolation threshold significantly such that, excessive amount of the nanomaterial will not be required to develop highly conductive nanocomposites[126]. As opposed to the traditional view, numerous studies have demonstrated that aggregation is actually beneficial to bring about good bulk conductivity in nanocomposites[127–131]. The major argument presented in these studies, in favour of the alternate view, is associated with the fact that, nanoparticles can become isolated with layers of the matrix surrounding it if the suspension in highly stable. This would decrease the likelihood for nanoparticulates coming into contact with one another, thus inhibiting the formation of a conductive network and therefore, the overall conductivity would decrease.

With regards to the fabrication of MNA's from epoxy/CNT-based nanocomposites, processing is the most critical step and the following factors must be accounted for as they amount to have a synergistic effect on the final functional properties of the nanocomposite device. Firstly, due to the finite structure of the microneedles, efforts must be undertaken to reduce the size of CNT aggregates, as they can act as localised stress points that would

initiate mechanical failure during the process of microneedle insertion and removal. Therefore, although a high loading of CNT can help achieve better conductivities and electrochemical properties, it may not be favourable as microneedles are required to have sufficient mechanical strength for penetrating the human skin effectively. Secondly, reducing the size of the CNT agglomerates through enhanced dispersion will have a knock-on effect on the electrical percolation threshold; helping to achieve high electrical conductivities at a low percolation threshold. This is highly beneficial, because the critical concentration of the filler required can be minimised, which in turn helps to avoid any determinantal effects resulting from the formation of large aggregates. Most importantly, an excellent interfacial interaction is required between the CNT and the epoxy matrix to allow for efficient processing; which consequently helps realise the benefits as described above.

A very broad range of percolation thresholds has been reported for CNT-epoxy composites from 0.012 wt% to over 4 wt%[122]. Špitalský *et al*. reported that a percolation threshold as low as 0.012 wt% can be achieved for solution-mixed oxidised MWCNT-epoxy composites; reaching a maximum conductivity of 10^{-2} S/m at a low CNT concentration of 1 wt%[132]. The authors suggested that, a mild oxidation treatment would reduce damage to the CNT's electronic structure and therefore provide better electrical conductivity. In an attempt to improve interfacial interaction, Liu *et al*. compared polyethylenimine-functionalised-MWCNT's (covalently or non-covalently) with pristine MWCNT-epoxy composites[133]. They found that both covalent and non-covalent functionalisation significantly reduced the conductivity of the composites, however non-covalently functionalised CNT provided conductivity that was 3-fold higher at 10^{-6} S/m. However, this was considerably worse than pristine MWCNT's, which achieved10^{-2} S/m at 1 wt% loading. In contrast, palmitic acid-modification of MWCNT's not only aided better dispersion of the nanomaterial, but also helped improve electrical conductivity depending on the ratio of CNT to palmitic acid. At the optimal ratio (1:1, CNT to palmitic acid), the percolation threshold was found to be between 0.03 to 0.06 wt% and the maximum conductivity reported was 10^{-3} S/m at a CNT concentration of 0.8 wt%[134]. Alternatively, dos Santos *et al.* showed that an initial de-bundling process with an anionic surfactant; sodium dodecyl sulphate (SDS), followed by surfactant removal and dispersion into solubilised epoxy, can help improve conductivity by 5 orders of magnitude (from 10^{-12} S/m to 10^{-7} S/m) at a low concentration of 0.5 wt%[135]. Recent studies have further reported that CNT's of high aspect ratios[136] and low-viscosity

epoxy resin[137] can help lower the percolation threshold and improve the conductivity of the composites.

A general consensus is difficult to obtain from the studies described above. Broadly, this can be attributed to the range of processing conditions employed, variation in the geometries of CNT being used and different epoxy formulations. However, in an attempt to produce high quality suspensions with individualised CNT's, the studies described above have commonly adopted a multifactorial approach. This involved, various CNT surface modification strategies to allow efficient interfacial interaction and dispersion; which is enhanced through the use of high powered sonication in solubilised epoxy.

3.2 Aims and objectives

The aim of this chapter is to fabricate MNA's from epoxy-CNT composites which can be developed into biosensors.

The objectives of this chapter are to:

1. Develop and optimise fabrication of MNA's from neat epoxy.
2. Mechanically characterise the epoxy MNA's by skin insertion tests, whilst also validating physical characterisation by using Texture analyser.
3. Investigate the potential for developing composite MNA's by blending and solution mixing processes.

3.3 Materials and methods

The porcine ear skin used in this study were obtained from animals euthanized for unrelated work and used freshly. Hairs were removed using an electric trimmer. Sylgard® 184 silicone elastomer was purchased from Dow Corning (Midland, MI, USA). Polylactic acid (PLA) filaments was from Makerbot (Germany). Standard 2-part epoxy resin (RX771/C) and its amine hardener (HY3100) was purchased from Robnor Resins Ltd (Swindon, Wilshire, UK). Electron Microscopy (EM) grade Agar 100 resin was purchased from Agar Scientific (Stanstead, Essex, UK). This is a four-part mix with the resin and two anhydride hardeners (DDSA: dodecenylsuccinic anhydride; MNA: methyl nadic anhydride) as well as an accelerator (BDMA: benzyldimethlyamine). Microneedle templates (Derma stamps) were obtained from Amazon UK (https://www.amazon.co.uk). Ethanol (AR-grade) was purchased from Sigma Aldrich (Gillingham, UK).

3.3.1 Fabrication of PLA and Epoxy MNA's

MNA's were fabricated using a micromoulding approach. Negatives of the template MNA's stamps were made using a two-part silicon elastomer kit, mixed in a 10:1 mass ratio and degassed under a vacuum pressure of ~10 mbar (Fistreem digital vacuum oven, Loughborough, UK) for 2 – 3 hours. The template MNA stamps were then set in this elastomer and heat cured at 90˚C for 2 – 3 hours to produce the micromoulds. The length of the microneedles in the template array was 1 mm. PLA MNA's were fabricated by melting fragmented filaments in the micromould at 180˚C under a vacuum pressure of ~20 mbar for ~4 hours. Upon cooling, the MNA's were manually ejected from the micromould.

To fabricate epoxy-based MNA's, different grades of the resin was used. This included a commonly used 2 part-epoxy resin, RX771/C (referred to as standard epoxy) and an EM grade Agar 100 resin, from which medium and hard epoxy formulations could be developed by varying the ratio of epoxy to hardeners. As a micromoulding approach is employed, it was hypothesised that the resin might not be able to percolate into microneedle imprints in the micromould without the application of external pressure. However, the resin manufacturers had suggested that, usage of a very low vacuum (i.e. approaching 0 mbar – absolute vacuum) whilst thermally curing the epoxy samples can exaggerate air bubbles, that are formed *in situ* duration the cure reaction. Entrapped air bubbles within the finished epoxy is detrimental to their mechanical integrity. Taking this into consideration, the varying pressure conditions were investigated in separate experiments (after mixing all the

components together), to determine the conditions under which a complete MNA can be successfully developed using all epoxy formulations. The vacuum pressure variations applied before thermal curing of all epoxies in separate experiments were: (1) 980 mbar for 10 mins (recommended by the manufactures to remove air bubbles incorporated when mixing the different constituents; and hence used as control); (2) 600 mbar for 45 mins; (3) 200 mbar for 45 mins and (4) 20 mbar (near full vacuum) for 45 mins.

Briefly, for producing the standard epoxy MNA's, the RX771/C epoxy resin and its harder was warmed to 60˚C, before mixing at a mass ratio of 10:1 (resin:hardener). The epoxy formulation was then poured into the micromoulds and cured at 80˚C overnight, after the application of vacuum pressure variations as detailed above, in separate experiments. Similarly, EM grade medium and hard epoxy formulations were prepared according to the manufacturer guidelines; poured into micromould and cured at 60˚C overnight, once again after the pressure variations had been applied in separate experiments. The MNA's formed were manually ejected from the micromoulds.

3.3.2 Fabrication of nanocomposite MNA's

Carboxylic functionalised–MWCNT's (i.e. *f*-MWCNT's, *length*: 10 – 30µm, outer diameter: 20 – 30nm) were used to develop the nanocomposite MNA's by blending and a solution mixing process. A loading of 5 wt% of CNT was investigated here. Nanocomposite MNA fabrication was initially investigated by blending the CNT's into the warmed epoxy (at 60°C, in order to lower the viscosity) by hand. This was later optimised by the addition of a sonication step using an ultrasonic bath (operation at 37 kHz) for 20 mins. The respective hardeners and accelerators were then warmed to 60°C and add-mixed to the homogenised nanocomposite suspension. In order to develop the nanocomposite MNA's, the epoxy/*f*-MWCNT suspension was poured into the micromoulds and thermally cured under the optimised conditions found for developing neat epoxy MNA's. To develop solution-mixed nanocomposites, the epoxies were initially dissolved in ethanol (30%, v/v). Appropriate amounts of *f*-MWCNT's was then added into this media, homogenised mechanically and de-bundled by bath sonication for 45 mins. According to Ventura *et al.* the solvent was then allowed to evaporate over 2 hours at 80°C[138]. Hardeners and accelerators (both warmed to 60°C) specific to each epoxy was then added and mixed thoroughly by hand. Finally, the solution-mixed nanocomposite was poured into the micromoulds and cured under the optimised conditions found for developing the neat epoxy

MNA's or after an additional step, whereby the micromould containing the nanocomposite was centrifuged at 1500 xg for 30 mins. Once cured, all epoxy samples were ejected manually.

3.3.3 Mechanical characterisation

\Two types of stresses must be overcome for successful insertion and removal of the MNA's. The first signifies the force that is required to break the microneedles axially and this must be higher than what is required for skin insertion. The second is associated with lateral forces, resulting from non-uniformity of the skin contour, inadvertent slippage during insertion and removal as well as reasonable human movements during insertion. The former is termed "axial fracture strength" (AFS) and the latter, "shear fracture strength" (SFS). A texture analyser (TA) equipped with a video capture and synchronisation system was used for all mechanical analysis (Stable Microsystems Ltd, Surrey, UK). The experimental set up is shown below (Figure 3.4). To measure AFS, a single microneedle was affixed upright on to the platform of the TA and the force was applied parallel to the microneedle vertical axis. The instrument recorded as the probe sensed a weight of 0.001 N. The probe speed was set to 0.1 mm s^{-1} and the target force was set to 5 N. To measure SFS, microneedles were aligned perpendicularly to the probe, with the probe covering approximately 50% of the microneedle length. Microneedles in adjacent rows to the one being measured were removed for probe clearance. The target force was 1.96 N.

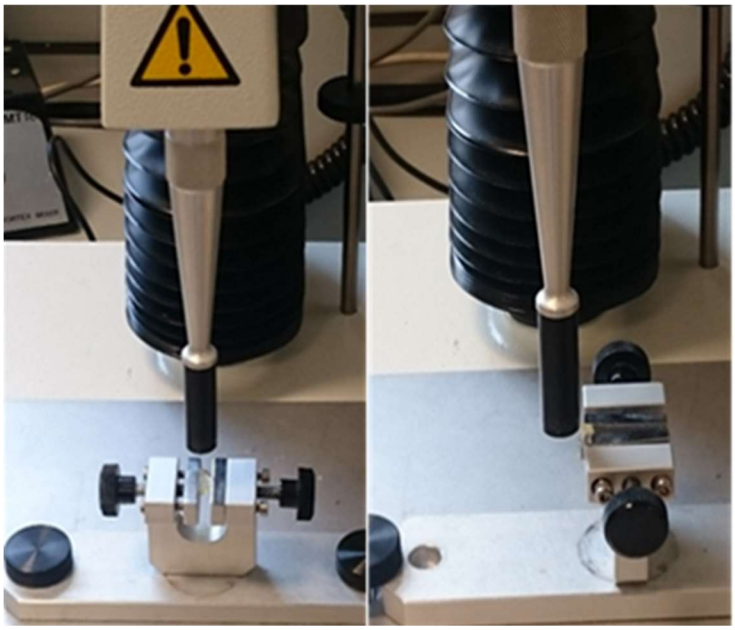

Figure 3.4. Experimental set-up for measuring AFS (left) and SFS (right). MNA was affixed using a clamp attachment, which was secured to base of the TA.

3.3.4 Skin penetration

Porcine ear skin was used for all skin penetration studies as it resembles similar morphological characteristics to human skin. Aqueous saturated methylene blue (a hydrophilic dye) was used to visualise skin perforations upon microneedle insertion. Typical skin insertion forces range from 0.1 – 0.3 N due to variations in the stratum corneum thickness[24]. MNA's can be inserted into the skin using an applicator or by applying sufficient pressure by hand. However, the latter is widely accepted to become the most common method of application. With this method, the major concern is associated with the fact that, forces applied by hand pressing would significantly vary between individuals. This can negatively impact on the mechanical strength of the MNA's. Therefore, to assess a maximum margin of safety for epoxy-based MNA's, when applied by hand, the skin penetration test was carried out on a weighing scale by gradually increasing the pressure applied up to 15 N and holding it for 30 s. The resultant skin penetrations were visualised to determine any microneedle deformity or mechanical failure.

3.3.5 Imaging

Images were taken using a digital stereo microscope equipped with a 3MP camera. (Motic®, HK).

3.3.6 Statistical analysis

Mechanical forces were measured and recorded using Exponent Lite (version 6.1.7.0, Stable Micro Systems Ltd, Surrey, UK). GraphPad Prism 7 software (GraphPad Software, Inc., CA, USA) was used for all graphing and statistical analysis. Statistical significance was demonstrated by performing one-way ANOVA with a post hoc Tukey's HSD test at a significance level of $\alpha = 0.05$. (GraphPad Software Inc., USA)

3.4 Results

3.4.1 Fabrication of Epoxy MN's

Microbubble or nanobubble formation is a continuous process that may result from the curing reaction of the epoxy. When curing under a low vacuum pressure, these microbubbles can expand and become more exaggerated. This is shown in Panel A, Figure 3.5; where all epoxy samples showed an extensive amount of air bubbles entrapped within the finished

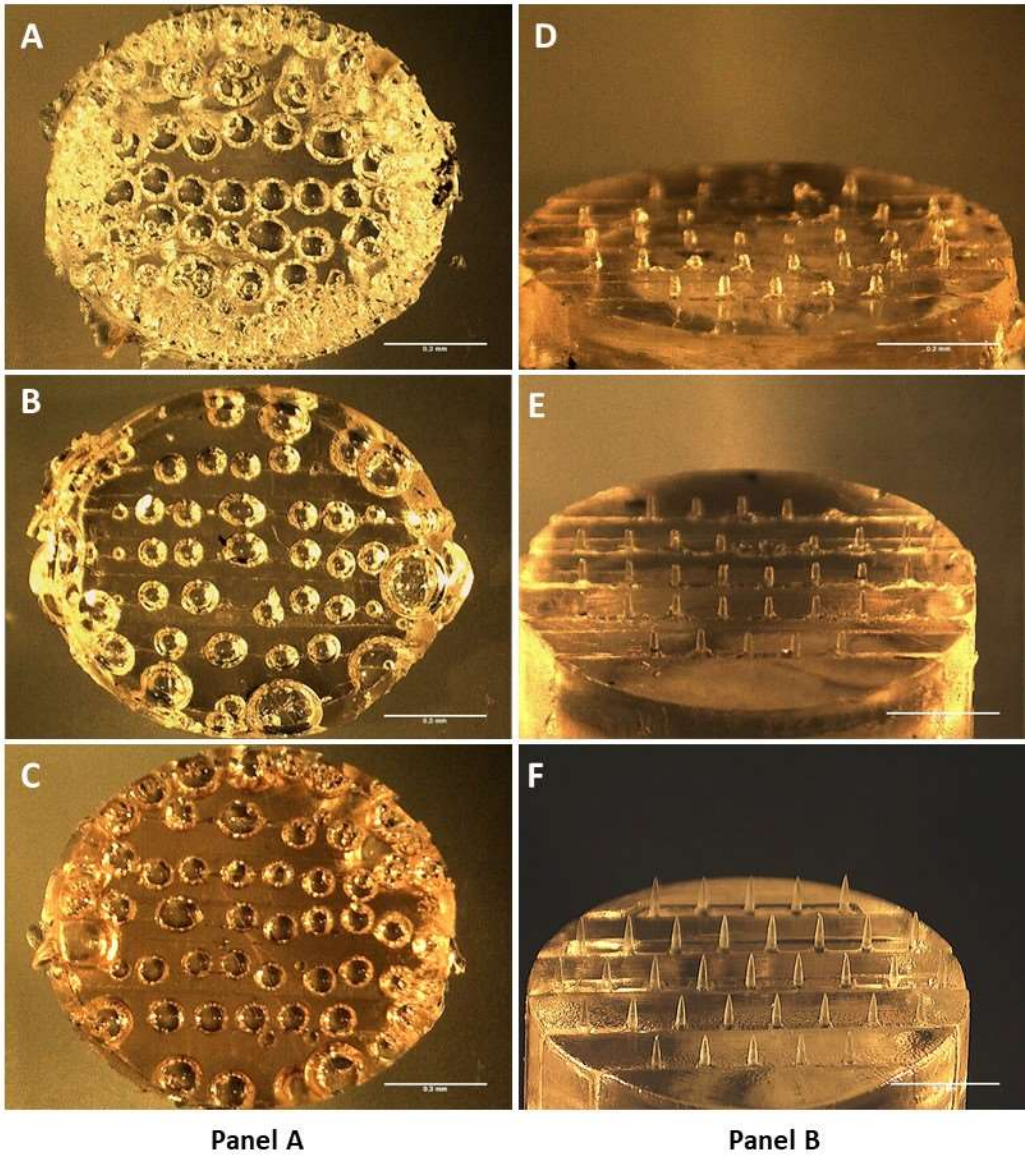

Figure 3.5. Optimisation of fabrication conditions for epoxy MNA's. Panel A shows air bubbles entrapped in cured samples when a low vacuum pressure of 20 mbar was applied prior to thermal curing overnight; (A) RX771C – standard epoxy (B) medium epoxy and (C) hard epoxy. Panel B shows optimal processing conditions by using hard epoxy as a representative example: (D) small stubs were formed under 980 mbar vacuum pressure, which elongated the pressure was reduced to 600 mbar (E) and (F) a complete MNA formed after reducing the pressure to 200 mbar. Scale bar represents 0.3 mm.

product, when a full vacuum pressure (i.e. 20 mbar) was applied for 45 mins prior to thermal curing. Hence, the optimum conditions under which epoxy-MNA's can be developed was investigated first and foremost. As per manufacturer guidelines, initially a high vacuum pressure of 980 mbar was applied for 10 mins. This was recommended as adequate to remove air bubbles incorporated during mechanical mixing. But, it was not known whether the high pressure was enough to form microneedles. In separate experiments, the vacuum pressure was then reduced to 600 mbar and 200 mbar with an application time of 45 minutes under each setting, for all epoxy samples. The results from these studies are shown using representative images of the hard epoxy samples, in Panel B, Figure 3.5. Under the manufacturer-recommended conditions, only small stubs were formed (d). On increasing the pressure to 600 mbar the stubs appeared more elongated (e), however a full MNA only formed when a low pressure of 200 mbar was applied. This was consistent across all the epoxy samples studied.

3.4.2 Skin Penetration

Skin penetrations tests were done by hand using all epoxy MNA's and the penetrations were visualised by methylene blue staining. MNA's were applied onto the skin by applying a maximum force of 15 N. Figure 3.6 shows a series of images taken before and after the skin penetration tests. In all cases, i.e. for standard, medium and hard epoxy, all of the microneedles in an array penetrated the skin, as visualised by methylene blue staining of the perforations caused by microneedle insertions (Figure 3.6 A.3, B3, and C.3). Standard epoxy MNA's rarely bent, however one of the needles appeared to have fractured near the base (Figure 3.6 A.2). Medium epoxy MNA's showed multiple needles with their tips bent following skin insertion (Figure 3.6, B.2), but none was seen to fracture. With the hard epoxy MNA's, the degree of tip bending appeared lower compared to that of medium epoxy (Figure 3.6, C.2), and again none of the microneedles was seen to fracture. Collectively, these results indicate that the hard epoxy formulation is least likely to be affected by skin insertion and removal.

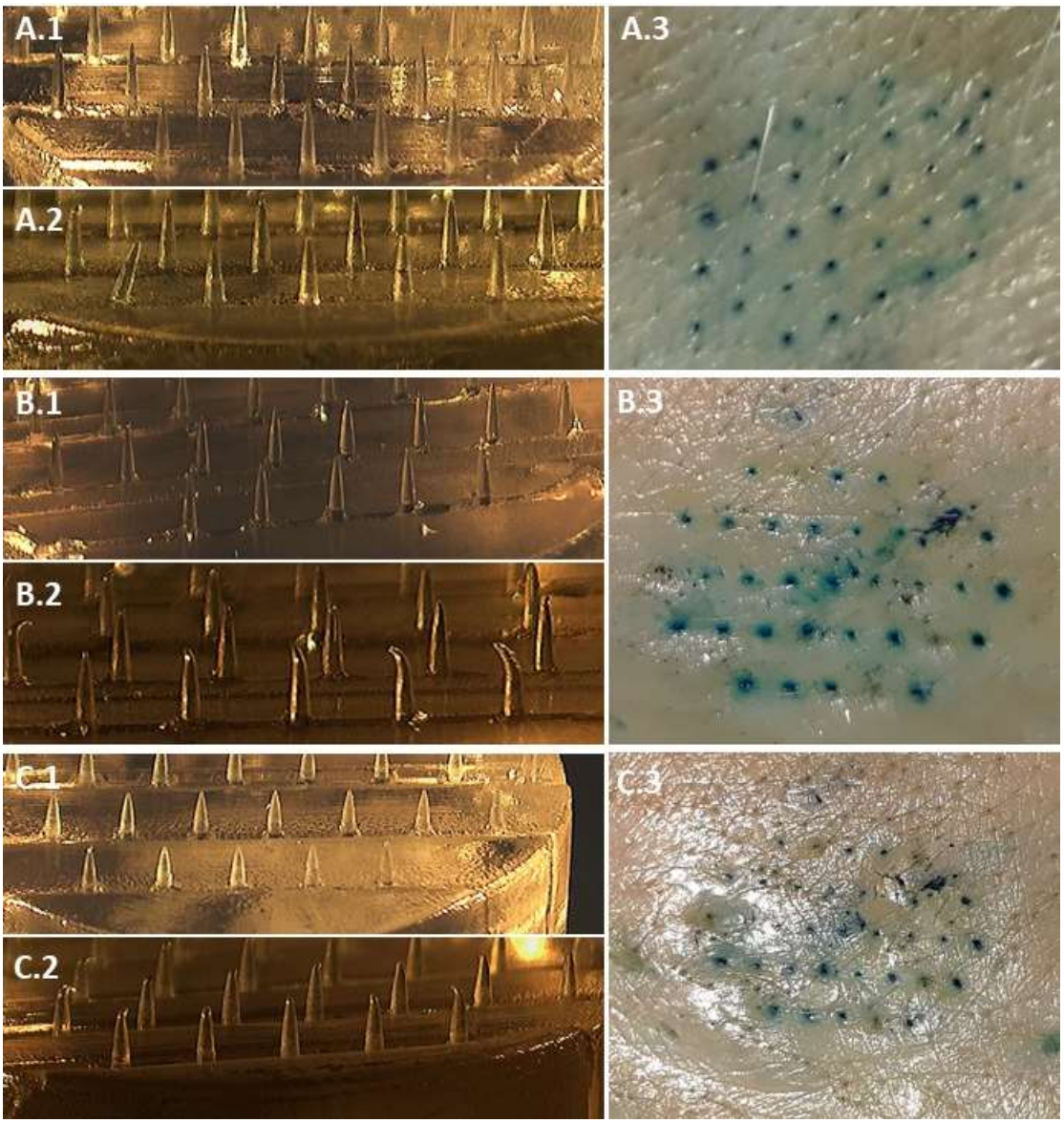

Figure 3.6. Before and after images of microneedles following skin, penetration tests done using the three grades of epoxy MNAs. Images: A1 to A3 (standard epoxy), B1 – B3 (medium epoxy) and C1-C3 (hard epoxy). A1, B1 and C1 are images of MNA's before skin penetration (visualised using methylene blue staining as A3, B3, C3) and A2, B2 and C2 are images of MNA's after skin penetration.

3.4.3 Development of a standardised protocol for evaluating mechanical properties

Envisioning the development of nanocomposite MNA's, where heterogeneity between microneedles will be evident regardless of the best efforts to produce high quality dispersions, it is important to develop a standardised protocol to quantitatively assess the mechanical strength of the microneedles. A Texture analyser (TA) was adopted for this purpose and mechanical strength was assessed in terms of AFS and SFS. MNA's fabricated from PLA

was used as control. PLA was chosen because its mechanical characteristics has been studied previously by Park *et al.* Although, it must be acknowledged that the grade of the PLA and design of MNA used by Park and colleagues were rather different to those used in this study. A typical axial load profile of PLA microneedle is shown in Figure 3.7. As illustrated in graph, at the point of impact, the sharp tip of the microneedle initially bents inward. Therefore, the surface area in contact with the rigid probe surface increases, which consequently reduces the effective stress (force per unit area) and thereby, the microneedle is able to withstand more force. Gradually, the force applied exceeded the axial strength of the microneedle, causing it to buckle. This point was taken as the AFS and for PLA, the buckling occurred at a microneedle length of around 0.2 mm. The AFS for PLA was ~1.3 N. The buckling continued until when it reached a point (at around 0.36 mm) where the surface area in contact with the probe became larger than the applied force, and the forces increased until a pre-set force of 5 N was reached.

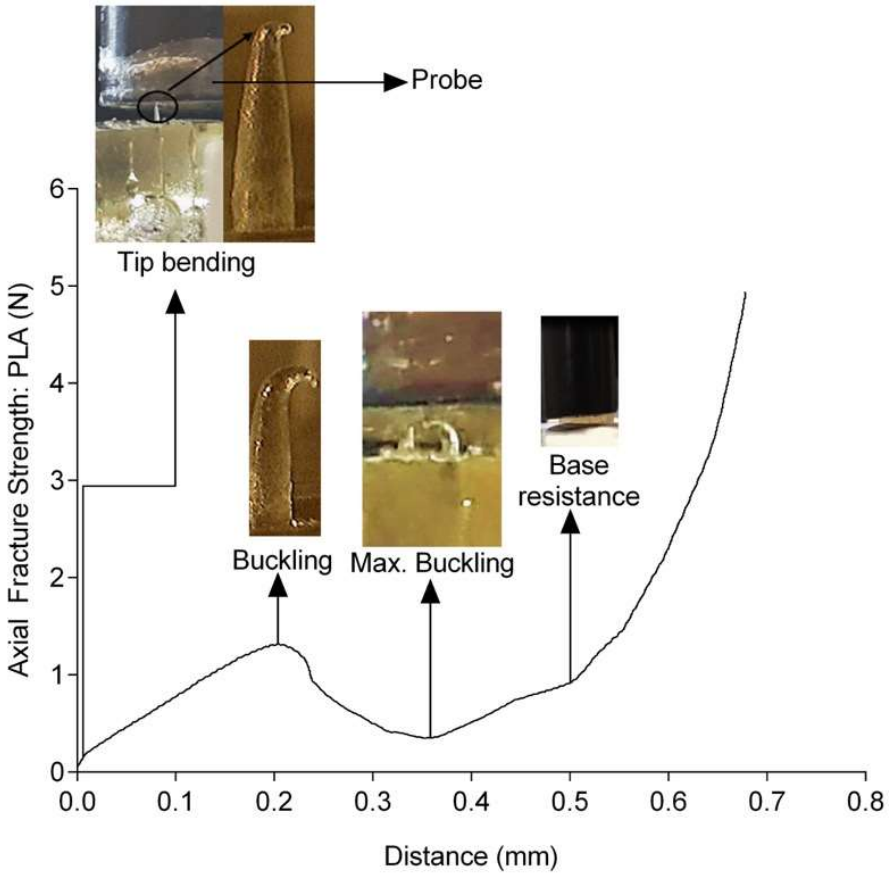

Figure 3.7. Typical axial load profile of a PLA microneedle. The graph marks events that occur during an AFS test. As the measurement was only initiated when the probe sensed a weight of 0.001 N, the distance shown the x-axis relates to the length of the microneedle at which a particular event occurred.

A typical shear strength profile for PLA is shown below (Figure 3.8). The MNA was prepared by removing neighbouring rows of microneedles as shown in the inset. Data were recorded continuously, as the probe cleared a single microneedle at a time. Therefore, each peak in the graph represents a microneedle. Here, the SFS was seen to decrease per microneedle. This is due to a 'cantilever effect'; where a larger magnitude of force is withstood when a load is applied close to the base, whereas application of force closer to the tip means less force is withstood. This effect is further emphasised using Figure 3.9 A and B, where the former shows the maximum shear force withstood by a microneedle to be ~1.2 N, when the probe was positioned close the base of the microneedle (inset, Figure 3.9 A); whereas the latter shows a four-fold reduction in shear force, at ~0.3 N, when the probe was aligned to 50% of the microneedle length (inset, Figure 3.9 B). Therefore, when measuring SFS, the force should always be applied at ~50% of the length of the microneedle. This is important because the tip concentrates most of force applied during insertion. To accurately align the probe to 50% of the length the microneedles, a metallic ink mark was made at the appropriate length using a light microscope (red ink in the inset image, Figure 3.9, B).

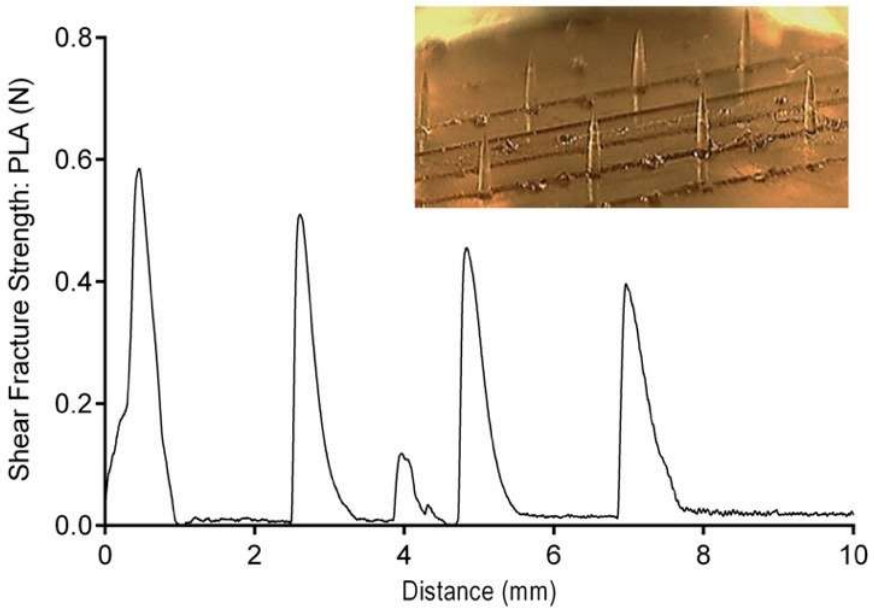

Figure 3.8. Shear strength measurement of PLA microneedles. Force declined as each microneedle was cleared by the probe. Inset shows experimental set-up where microneedles in the adjacent raw was removed to allow probe clearance.

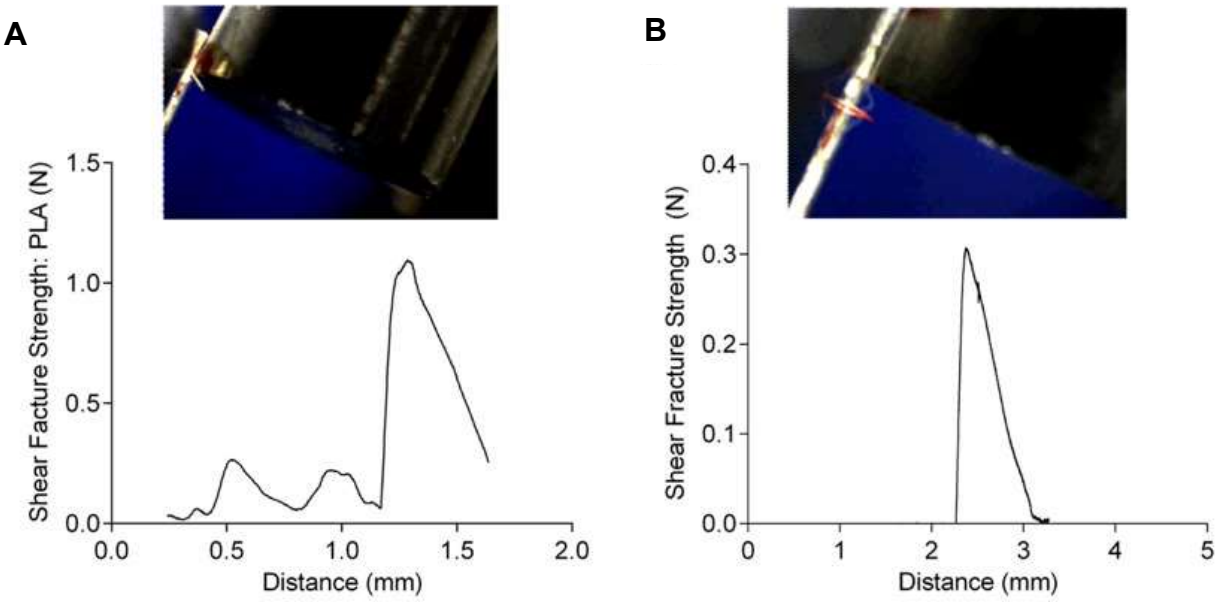

Figure 3.9. Cantilever effect. (A) probe aligned close to the base of a PLA microneedle, measuring a SFS of ~1.1 N; (B) probe aligned along to 50% of the microneedle length, measuring an SFS of 0.3N.

3.4.4 Mechanical characterisation of epoxy microneedles

The epoxy MNA's formed under the optimal conditions were subjected to mechanical testing to ultimately determine the epoxy best suited for synthesis of composite MNA's. AFS and SFS were analysed for both standard and EM grade epoxy samples. Figure 3.10 shows representative tests results using a single microneedle from all epoxy-based MNA's. On measuring the AFS, the standard and hard epoxy-based microneedles were seen to buckle once the probe had cleared a maximum microneedle length of ~0.2 mm typically; whereas the medium epoxy-based microneedle yielded typically at a shorter microneedle length of ~0.15 mm. Initially, similar to that of the PLA microneedles (Figure 3.7), the sharp tips on all of the different epoxy-based microneedles bends inwards. This occurred at low impact force, < 0.02 N and it provided an increased surface area for the applied force. Hence, the resistive force from the microneedles increased, until the point where the force applied became greater than the AFS of the microneedle; consequently, the microneedles started to buckle. With the standard epoxy, once the buckling force had been reached, the force withstood by the microneedle declined rapidly, and eventually snapped off (Figure 3.10, A). In comparison, for both medium and hard epoxy-based microneedles, the buckling stopped once the probe had cleared a microneedle length of ~0.3 mm and the resistive forces from the microneedles increased subsequently. As for PLA (*section 3.4.3*), the increment in force

resisted is resultant of the increased surface area on which the force applied is acting on (reducing effective stress).

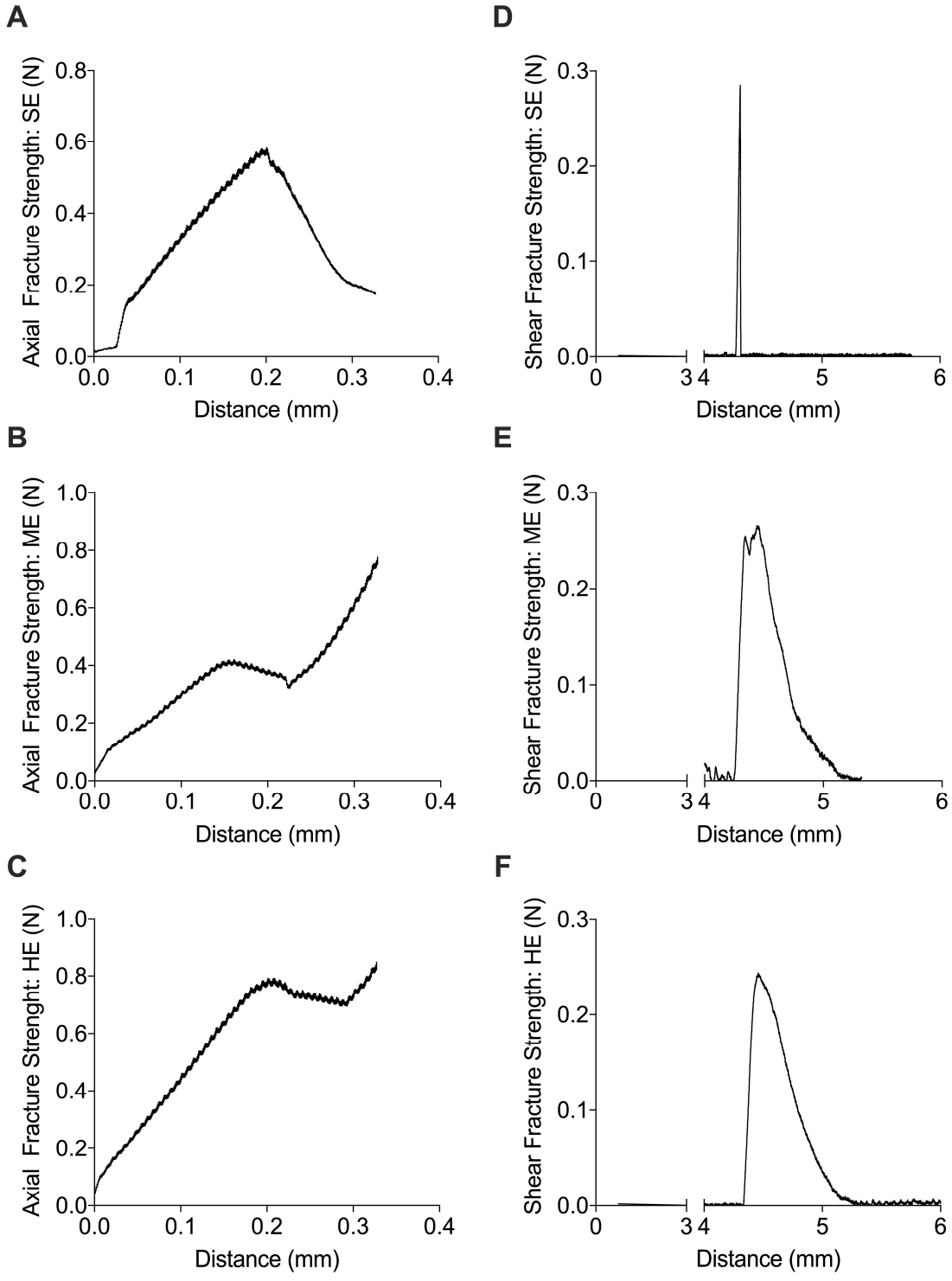

Figure 3.10. AFS (A – C) and SFS (D – F) tests for standard epoxy (SE), medium epoxy (ME) and hard epoxy (HE). The distance shown correlates to the length of the microneedle. For AFS, all of the epoxy-based microneedles were seen to buckle at a microneedle length < 0.2 N. During SFS tests, the standard epoxy-based microneedle had snapped, as indicated by the rapid drop in force at a short difference in distance of 0.007 mm.

The SFS that all epoxy samples are able to withstand were considerably lower in comparison than AFS. Notably, with the standard epoxy, the microneedle snapped on reaching a maximum force < 0.3 N (illustrated by the rapid drop in force along a short distance, Figure 3.10, D). On the other hand, medium and hard epoxy microneedles gradually bend away from the direction of the force; indicated by the slope (Figure 3.10, E and F).

Figure 3.11 shows comparison between different epoxy samples against control (PLA). Statistical analysis performed demonstrated a significantly higher AFS for PLA in comparison with standard, and hard epoxy ($p \leq 0.001$) and medium epoxy ($p \leq 0.05$). Similarly, the SFS was also significantly higher for PLA in comparison with all epoxies ($p \leq 0.001$). Comparing the AFS of different epoxies, medium epoxy microneedles were able to withstand a significantly higher force in relation to standard ($p \leq 0.001$) and hard epoxy MN ($p \leq 0.05$). Whereas for SFS, medium and hard epoxies were able to withstand significantly higher lateral forces than standard epoxy ($p \leq 0.001$ and $p \leq 0.01$, respectively).

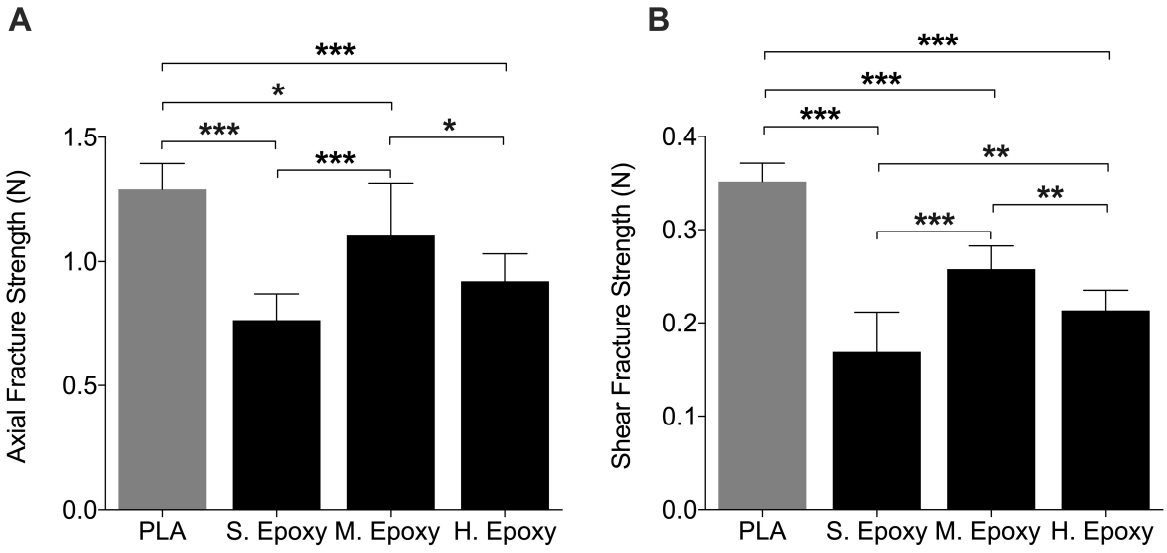

Figure 3.11. Measurement of AFS and SFS. Comparing mechanical strength of MNA's made from epoxy against PLA. Medium epoxy displayed higher AFS and SFS in comparison to standard and hard epoxy-based microneedles. PLA microneedles displayed better mechanical strength that all epoxies tests. (***$p \leq 0.001$; **$p \leq 0.01$, *$p \leq 0.05$; ns: $p \geq 0.05$ (one-way ANOVA with Tukey's test, n = 10).

3.4.5 Epoxy/MWCNT Composite MNA

Taking the above results into consideration, nanocomposite MNA synthesis was investigated using the medium EM grade epoxy. As previous studies had shown that a high

loading of CNT was needed to form good electrochemical sensors, *f*-MWCNT were used here to aid the dispersion of CNT in epoxy matrix. Initially, by adopting the strategy utilised to fabricate epoxy MNA's, 5 wt% of CNT was hand-mixed into the matrix with the aid of heat to lower the viscosity of the epoxy. The hardeners were added, mixed and poured into the micromould and cured as before. As shown in Figure 3.12, A; an array of microneedles could not be developed. Since the processing conditions were optimal for epoxy-based MNA's and some microneedles had formed, inadequate dispersion of CNT was reasoned to be the cause. Therefore, the above sample was sonicated for 20 mins before the addition of hardeners and cured accordingly. As a result, almost a complete array of microneedles subsequently formed (Figure 3.12, B). However, a large number of the microneedles seems to have formed from epoxy alone and not from the nanocomposite. This further emphasised poor dispersion and interfacial interaction between the CNT and epoxy.

In order to overcome improper dispersion of MWNCT in the epoxy matrix, solution mixing is commonly employed. Therefore, 30% ethanol v/v was added into the epoxy, followed by the addition of *f*-MWCNT and sonicated for 45 minutes at 60°C without the addition of anhydride hardeners and the accelerator. After removal of the solvent, the remaining constituents were hand mixed and allowed to cure under the optimal epoxy curing conditions. As seen in Figure 3.12, C, this improved dispersion of CNT's and evidently the microneedles formed had more CNT incorporated than those formed under the previous conditions. However, some microneedles formed had partial to no CNT content present within them. This raised the possibility that the optimal condition used so far may be insufficient. As the application of a negative pressure for longer than 45 mins can exaggerate the bubbles formed when sonicating or mechanically mixing the composite; leading to voids and cracks within the cured epoxy; a centrifugal force was applied in addition to the negative vacuum pressure in order to help pull the composite into the microneedle conduits present inside the mould. The MNA formed as result (Figure 3.12, D) showed almost a full array of nanocomposite microneedles, with only a few microneedles having noticeably little CNT incorporated. This was confirmed on closer inspection of the microneedles, as shown in Figure 3.12, G. Additionally, on manually ejecting the composite MNA from the mould, a few to almost all microneedles were observed to break off on several occasions (Figure 3.12 E and F).

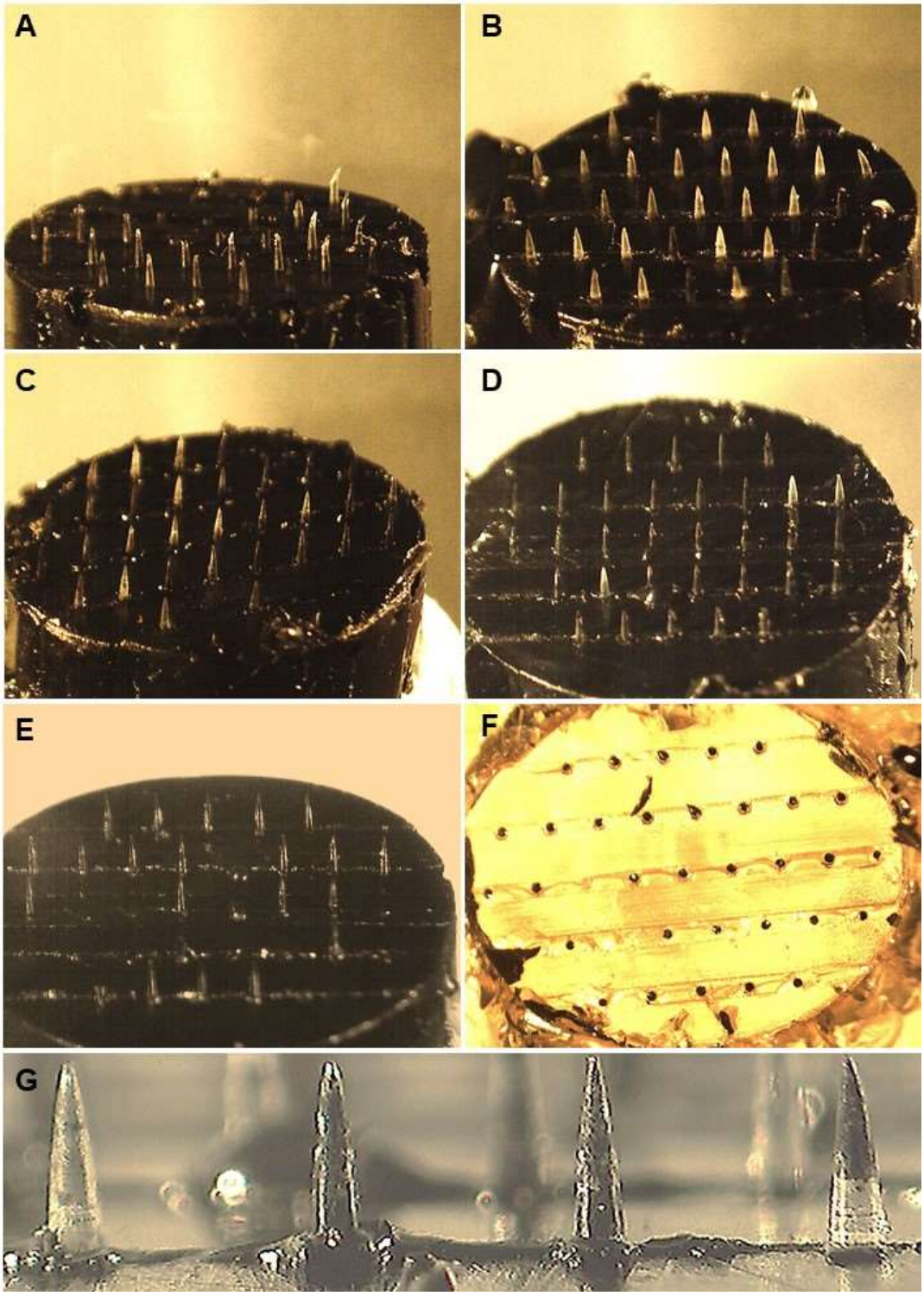

Figure 3.12. Medium Epoxy/*f*-MWCNT composite MNA's. (a) Nanocomposite MNA formed under optimised conditions; (b) nanocomposite MNA formed after sonication of epoxy/*f*-MWCNT homogenised mixture; (c) nanocomposite MNA formed after solution mixing of *f*-MWCNT by sonication (45 mins) in epoxy dissolved by ethanol; (d) nanocomposite MNA formed after solution mixing via sonication and application of centrifugal force prior to thermal curing. (e) MNA's formed via application of centrifugal force as in d; needles missing. (f) MN's broken off in the mould following centrifugal processing. (g) Variation in CNT incorporated in a MNA.

3.5 Discussion

In this chapter, the potential for developing MNA's from epoxy/CNT based nanocomposites was assessed. Initially, two different grades of epoxy systems were evaluated to determine their suitability in fabricating MNA's and the resultant mechanical characteristics. A commonly used epoxy resin was chosen as well as one of EM grade and micromoulding was employed as a facile approach towards nanocomposite MNA fabrication.

Initially, it was assessed whether MNA's could be fabricated from epoxy alone. Hypothesising that vacuum pressure is important, not only to remove air bubbles incorporated from add-mixing the epoxy formulation, but also to form the microneedles themselves; different pressure variations were investigated. It was found that whilst the application of low pressure may have removed the air bubbles incorporated when mixing the components together, microbubbles formed *in situ* during the cure reaction were exaggerated and the cured epoxy was filled with air bubbles (Figure 3.5, A – C). As the aim is to fabricate MNA's from nanocomposite formulations, it is imperative to avoid imperfections such as air bubbles because this will create voids within composites. The consequence of such is: (1) ineffective stress transfer between the epoxy matrix and CNT's; resulting in weakened mechanical properties and (2) reduced complete conductive route formation within the nanocomposite. Taking these factors into consideration, it is essential to apply a sufficient amount of pressure so that MNA's can be formed consistently, whilst also removing secondary air bubbles that were incorporated from mechanical mixing. It was found that by varying the vacuum pressure from that recommended by the manufacturers i.e. 980 mbar to 200 mbar over a period of 45 mins, prior to thermal curing, resulted in the formation of a complete MNA for all the epoxy samples. Importantly, no air bubbles were seen, thus confirming that bubble formation is inherent to the cure reaction under the application of heat. From Figure 3.5, A – C, although it may seem as if the air bubbles may have come from the cavities in the micromould, it is unlikely to be the case because the low-pressure vacuum was applied for a sufficient period of time for any trapped bubbles to escape.

Prior to the fabrication of composite MNA's, it was investigated whether the formed MNA's were capable of penetrating the skin without the addition of CNT's, which would make them significantly stronger if a good interfacial interaction between the matrix and the

filler could be achieved through efficient dispersion. Although many custom designed applicators have been created for MNA insertion with specified insertion forces and velocity[24,139]; it is envisaged that commonly MNA's would be applied by hand. Therefore, using a weighing balance, a significant amount of force (~ 15.0 N) was applied to insert the microneedles into the porcine skin. All epoxy microneedles were found to penetrate the skin efficiently. However, for standard epoxy, as seen from Figure 3.6 A2, one of the microneedles had appeared to break off the base. Out of the three standard epoxy MNA's tested, all had at least one or more microneedles breaking off during skin insertion and removal. On the other hand, the EM grade hard and medium epoxies showed some degree of bending; the latter to a greater extent. In order to help quantify the results further mechanical characterisation was carried out. Other studies investigating mechanical characteristics of MNA's have commonly used a displacement force test station, which requires further modification[74]. TA on the other hand can be fitted with different probes and fixtures, allowing highly precise measurements without modification.

TA is a highly sensitive mechanical testing equipment that can be used to measure a range of physical properties such as hardness, fracturability, adhesiveness, gel strength, extensibility etc. for a wide range of applications, using its capability to conduct compressive and tension tests. Here, the compression capability was used to determine AFS and SFS under predefined conditions. Parameters such as length, thickness, tip radius, tip angle, base diameter, density and the type of material all influence mechanical strength of microneedles. Assessment of AFS and SFS are the only tests carried out to account for these parameters. Mechanical tests on MNA has been done mainly on silicon, and but recently polymeric MNA's are being increasingly evaluated[140]. Polymeric microneedles are advantageous because they are in expensive, can be mass produced easily and has better biocompatibility that silicon and metals. Furthermore, they may offer improved resistance to shear-induced breakage due to their viscoelasticity[140]. On testing the epoxy MNA's, the standard epoxy was by far the weakest both in relation to AFS and SFS. The standard epoxy microneedles were seen to snap under both test conditions. The medium EM grade epoxy microneedles were able to withstand significantly higher AFS and SFS in comparison to standard and hard epoxy-based microneedles. This is due to the fact both standard and hard epoxy microneedles had lower viscoelastic strength than the medium epoxy. Viscoelastic properties are attractive, because it can act to cushion the impact of mechanical stress on microneedles by mechanical deformation rather than mechanical breakdown. Although

quantitative analysis identified flaws in terms of AFS and SFS that may not be attractive for skin application; all epoxy-based MN were able to penetrate porcine skin successfully. This is due to the elastic nature of the skin which absorbs some of the force being applied before being breached by the sharp tips of the microneedle. In contrast, the TA probe surface is hard, so the microneedle yields more readily upon on impact, from lower contact forces. Moreover, with an array of microneedles, the force applied will be equally distributed over a larger surface area. Additionally, multiple point of contact with the skin helps to stretch it, allowing for easier insertion in the skin.

Based on the results from skin insertion studies and mechanical characterisation, medium epoxy was chosen for composite synthesis. However, on applying the optimal conditions under which epoxy microneedles formed consistently, a full array of composite microneedles could not be developed. Hence the processing conditions were optimised in stages, first by sonication, followed by combined sonication and solution mixing, and finally by an additional centrifugation step to help pull the polymer-CNT mix into the microneedle imprints in the micromould. Overall, a better dispersion was achieved from the latter process, but the MNA's formed varied in terms of homogeneity. The strength of a composite is highly dependent on the interfacial interactions between the epoxy matrix and the CNT's, with better interactions leading to more effective stress transfer in the composite. Although sonication was used to improve results, at higher loadings of CNT, sonication may be less effective due to the higher viscosity of the mixture. Solution mixing process reduces this viscosity, however the solvent used to dissolve the epoxy may actually weaken molecular interactions of the epoxy matrix itself. As seen in this study, after optimisation with sonication, ethanol and centrifugation, multiple microneedles had broken off in the microneedle cavities inside the mould.

The matrix stiffness is also a crucial feature in forming CNT based nanocomposites. Lijie *et al.*[141]., systematically evaluated the different reinforcement role for CNT's in epoxies with differing matrix stiffness. They found that, in soft epoxy matrixes, CNT's showed a significant reinforcement because of the accelerated curing process and better interface adjoining. On the other hand, the interfacial interaction was found to be poor due to complete cross-linking between the epoxide molecules surrounding CNT's in a stiff nanocomposite. However, these results are to be seen cautiously as the CNT content was only 0.5 wt%. It is well known that the addition of CNT's up to a certain loading will increase mechanical strength of the composite and beyond which it starts decreasing. The

decrement in mechanical strength is associated with the fact that, at high loadings (> 10 wt%), some surfaces of CNT's are not completely covered by the matrix due to the large specific surface area of CNT's[142]. For this reason, the majority of studies into nanocomposite processing have used a small weight fraction of CNT's, between 0.1 – 8 wt%. Only a few studies have investigated higher CNT loadings (up to 39 wt%) and shown that they resulted in improved mechanical features, and these were achieved by shear processing[143] and melt mixing[144]. Functionalisation of CNT's can certainly improve dispersion, but to create nanocomposites with greater mechanical strengths, amine functionalisation may be a better alternative as it may form covalent bonds with the epoxy matrix as opposed to hydrogen bonds when using carboxylic functionalised MWCNT.

3.6 Conclusions

Overall, this chapter demonstrated that efficient dispersion of CNT's into epoxy is challenging, even when even when *f*-MWCNT's are used. As predicted, the inhomogeneity resultant of poor dispersion was translated into the finite structure of microneedles. A major consideration regarding the poor dispersion concerns the choice of epoxy used for synthesising nanocomposites with CNT's as a filler. Results seen here are in agreement with the notion that epoxy matrices that are less stiff may prove better for CNT incorporation. Nevertheless, this chapter showcases a cost-effective and highly scalable fabrication strategy to produce mechanically strong solid MNA's using epoxy.

3.7 Future work

Although, this chapter shows successful fabrication of MNA's from epoxies, nanocomposite MNA's could not be successfully fabricated. This is due to the poor interfacial interaction between the CNT's and the epoxy matrix, even when *f*-MWCNT's was utilised. This raises concerns regarding the suitability of epoxy as a matrix. Considering the finding that interfacial interaction may actually benefit from using a matrix that is less stiff, a "softer" blend could be prepared from the EM grade epoxy by varying the ratio of epoxy to hardeners and the accelerator and, analysed in terms of mechanical strength and nanocomposite MNA synthesis. Shear mixing maybe an alternative to sonication, as it can be used to incorporate higher loadings of CNT's; which is necessary to the function of nanocomposite MNA's as an electrochemical sensor. Critically, the PLA microneedles analysed here had better mechanical strength than all epoxies tested. Therefore, it may be a suitable alternative towards the fabrication of nanocomposite MNA's.

Chapter 4. Synthesis and characterisation of poly (lactic acid)/*f*-MWCNT composite MNA's

4.1 Introduction

Excellent interfacial interaction between the polymer and CNT is crucial to the formation of conductive MNA's with good mechanical properties. Aside from epoxy, more than 30 polymeric matrices have been investigated for mechanical re-enforcement upon the addition of CNT[67]. However, polymer–CNT composites used for electroanalysis have been primarily derived from conductive polymers (CP) and used mainly as modifiers of electrodes. CP's are attractive because they can exhibit electrical properties similar to metals and semiconductors, and can be easily synthesised as with conventional polymers[145]. Polyaniline, polypyrrole, polythiophene and their derivatives such as poly(3,4–ethylenedioxythiophene), are a group of CP compounds that has been widely investigated for electrochemical applications[146]. They are inherently conductive because of the delocalised electrons in the conjugated double bonds along their backbone which can move around the entire system as carriers of charge[147]. These conjugated systems are however unstable, because of the energy gap created in the electronic spectrum with respect to the π-bond alterations and therefore do not possess high conductivity[145,147]. Consequently, they are doped with both *p*- and *n*-type dopants, which transfer charge to the polymer chain by redox processes and induces the formation of charge carriers, which are delocalised along the polymer chain[145,147]. This facilitates metallic conductivity in the CP's. However, there are limitations. In particular to biosensing capabilities, they suffer from low sensitivity and poor selectivity[148]. CNT's are often incorporated within the CP's to improve sensitivity, selectivity, stability and reproducibility, as well as impart resistance to fouling and reduce the overpotential of oxidative chemical reactions[148]. Composites of this nature are being extensively investigated to produce ultrasensitive sensors for electrochemical detection of a range of analytes, proteins, small molecules, biomarkers and DNA[148,149]. However, CP's are difficult to process once synthesised, i.e. whereas some CP's lack sufficient mechanical strength, others are rigid, insoluble, non-biodegradable and may even be cytotoxic[145]. Mechanical properties of CP's can be improved by blending with other insulating polymers, however the insulating molecules may interfere with the conjugated system of CP's[150]. Considering these difficulties, utilising a non-conjugated or an insulating polymer maybe

be more advantageous in terms of processability and enhanced mechanical properties as required for microneedles.

CNT's can be incorporated into insulating polymeric matrices using versatile and scalable strategies to make them conductive. In general, the conductivity of the polymer depends on the concentration on filler being incorporated. High conductivities can be achieved, albeit at the expense of mechanical properties. A major challenge when producing nanocomposite MNA's is therefore to achieve high conductivity and mechanical strength at the same time. The field of study concerning insulating polymer–CNT composites for electrochemical sensing (referred to as polymer nanocomposites) is however in its infancy, as research has emphasised the fundamentals of synthesis more than their applications.

4.1.1 Polymer nanocomposites

Mechanical and electrical properties of polymer nanocomposites are dependent on a number of factors, i.e. methods of nanocomposite synthesis, functionalisation of nanotubes and different functional groups, choice of polymer, aspect ratio, dispersion and interfacial interaction[67]. A brief description of these aspects in relation to polymer nanocomposites is given below.

4.1.2 Fabrication of nanocomposites

An important consideration regarding polymer nanocomposite synthesis relates to the choice of polymer and the eventual application. Polymers with a Young's modulus greater than 3 GPa have been recommended for developing MNA's[151]. Biocompatibility is also highly desired since a dermal application is intended. Therefore, synthetic polymers such as poly(lactic acid) (PLA), polyglycolic acid (PGA), poly(lactic-co-glycolic acid) (PLGA), polycarbonate (PC), polystyrene (PS), polycaprolactone (PCL), polymethylmethacrylate (PMMA), and natural polymers such as silk, chitin and chitosan are being widely employed to make polymeric MNA's for drug delivery, biosensing and diagnostic applications[64]. Strategies commonly employed for producing these MNA's involve micromoulding, solvent/solution casting, droplet-borne air blowing (DAB) and photolithographic processes[64]. In relation to MNA biosensors, current fabrication techniques are of high cost and require multi-step processing, based on conventional micromachining technology, including photolithographic processes. Several reports have recently illustrated simpler fabrication of MNA biosensors using micromoulding[49,56]. However, multi-step processes,

higher costs of raw materials and specialised post-processing equipment negates this advantage. Therefore, incorporating conductive fillers such as MWCNT directly into polymeric matrices using a facile fabrication strategy such as solvent casting, *in situ* polymerisation and melt-mixing may be highly advantageous for scaling up the production of electrochemical MNA's. These processing techniques can however significantly influence the final properties of the polymer composites. For example, low reinforcement and poor electrical properties have been observed for melt-processed composites, while solvent casting and *in situ* polymerisation can produce high strength composites through intermolecular bond formation and provide high conductivities; more so for the latter due to better homogenisation and strong interactions between the polymer and nanotube during the growth stage rather than when mixing the components together[67,142]. However, due to the ease of processing, solvent casting is commonly adopted to produce polymer nanocomposites. Three main steps are involved in this approach: (1) CNT is dispersed into a solvent by mechanical stirring or by ultrasonication, (2) the polymer is then dissolved into this mixture at room temperature or elevated temperatures, and (3) finally the solvent is evaporated off to produce a thin composite film. The aforementioned synthetic polymers are all amenable to be utilised in this manner as they all melt at high temperatures and are dissolvable using organic solvents. Similarly, natural polymers can also be dissolved in aqueous solutions or organic solvents.

4.1.2.1 Dispersion

MWCNT's are often functionalised covalently because they have limited dispersibility in organic solvents and polymeric matrices otherwise. Although, the cost of such functionalisation is defective electronic and transport properties in CNT's; some studies have shown that carboxylated nanotubes still retain good electrochemical activity[152,153]. The solvent used in itself also affects the dispersity of CNT's. A comparative analysis of CNT dispersion in various solvents with their Hansen solubility parameter found that, the state of dispersion is related to the dispersive component rather than the total solubility parameter of the solvent[154]. Solvents with a low polar (<14 MPa) and hydrogen (<12 MPa) component produced a stable and dispersed solution. This included N, N'-dimethylformamide, chloroform and 1-methyl-2- polypropylene. Those above the corresponding polar and hydrogen component values led to precipitation of the CNT (e.g. acetone, hexane, ethanol, dichloromethane, etc.)[154]. When the nanotubes are functionalised with –COOH and –OH groups on their end caps and sidewalls; they impart high solubility

in polar solvents as well[155]. However, even with functionalisation, simple mechanical stirring is inadequate to disperse the CNT's effectively. Bath sonication is commonly employed to assist dispersion. The sonication parameters vary depending on the type of CNT, mode of CNT synthesis, aspect ratio, functionalisation and solvents[156]. By using simple bath sonication, it has been shown that high-performance nanocomposites can be developed using –COOH functionalised MWCNT incorporated into various polymers such as PLA, PS and polyurethane (PU)[157–162] (*refer to tables 4.1 and 4.2*). The functionalisation of MWCNT's further acts to improve interfacial interaction between the polymer and the nanotubes via non-covalent links.

4.1.2.2 Mechanical properties

MNA's developed from polymer nanocomposites are highly attractive because of the ease of the processing, low cost, scalable fabrication methods and the wide range of polymers available offering tuneable mechanical properties. Table 4.1 shows examples of polymeric nanocomposites developed by solution mixing and solvent casting that may be relevant to the formation of MNA's with sufficient mechanical strength. It demonstrates a large spread in the mechanical performance of the nanocomposites. It must be acknowledged that processing conditions significantly influence the mechanical properties of the nanocomposites. Since efficient dispersion is key to all performance aspects of the final composites, among the processing conditions, sonication parameters play a crucial role. However, sonication parameters largely varied between the studies, based on the type of sonicator (i.e. bath vs horn), power, time and temperature. Therefore, generalised correlations and dependencies are difficult to establish. The collection of data presented in the Table 4.1 should be sufficient however, to guide research into the development of nanocomposite MNA's.

From a close inspection of the data presented in table 4.1, the following conclusions can be made. For all solution-based nanocomposites, the addition of CNT generally improves the mechanical strength. Mechanical reinforcement occurs until a critical value is reached for the filler content. Above this value, the nanocomposites deteriorate in mechanical strength due to aggregation of the CNT and therefore may become inferior to the matrix alone. Nanocomposites developed from covalently functionalised nanotubes display enhanced mechanical properties when compared to raw nanotubes in all cases. This is resultant of better interfacial interaction with the polymeric matrix. When comparing

nanocomposites developed from raw MWCNT's with –COOH and $–NH_2$ functionalised MWCNT's, an interesting relationship was found whereby, at low loadings $–NH_2$ functionalised MWCNT's had improved tensile strength compared to –COOH functionalised MWCNT's. At higher loadings however, this relationship was reversed[163]. Two possible reasons were reported for this: (1) the long alkyl chain provides greater repulsion between the nanotubes, increasing the available surface area of $–NH_2$ functionalised MWCNT's in comparison to acid functionalised MWCNT's. Therefore, the amount of polymer available is insufficient for proper wetting of the large volume of the MWCNT surface. This leads to the formation of voids in the final composites. (2) The amine functional groups on the nanotube may interfere with the imidization process of polyamic acid to polyimide, resulting in unreacted polyamic acids that may act as stress points for mechanical failure. Although covalent functionalisation of MWCNT's helps to improve mechanical properties, nanocomposites prepared from CNT's grafted with polymeric chains display enhanced mechanical properties at lower loadings. This is because polymer grafting helps to maximise CNT dispersion; resulting in effective load transfer to the matrix. In relation to the CNT's themselves, improvements in mechanical strength can also be achieved by using longer CNT's, but only after adjusting for the time required to reach optimal dispersion. Longer CNT's require longer sonication times to be dispersed efficiently. As a final remark, comparisons between different polymers are difficult to establish because of the differences in processing conditions and in general, in line with our previous results, mechanical reinforcement is higher for a ductile matrix than for a rigid matrix.

Table 4.1 Mechanical properties of solution/solvent casted nanocomposites.

Type of CNT	CNT dimensions (diameter in nm, length in μm)	Matrix	% of CNT loading	% ↑ of tensile strength	% ↑ of Young's modulus	Reference
SWCNT	< 2nm, 0.5 – 500μm	PU	0.50	10	100	[164]
MWCNT	—		5.00	-20	200	[165]
COOH – MWCNT	10 – 20nm, 20μm		20.00	180	740	[157]
NH_2 – MWCNT	40 – 60nm, 0.5 – 40μm		4.00	270	70	[166]
OH – CNT (not specified)	10 – 20nm, 50μm		5.00	103.81	—	[167]
Alkoxysilane modified MWCNT	15 – 30nm, 50μm		0.50	60	260	[168]
MWCNT with P3HT-g-PCl compatibiliser	25 – 70nm, —	PC	0.50	47	46	[169]
SWCNT	—		2.00	53	56	[170]
MWCNT	— ,2000μm	PLA	5.00	—	150	[171]
ClO_2/OH functionalised MWCNT	20 – 40nm, 1.5μm		0.10	20	—	[158]
MWCNT& MWCNT- COOH	9 – 20nm, 5μm		2.5, 2.5	— , 28	25, 80	[159]

Table 4.2 (contd) Mechanical properties of solution/solvent casted nanocomposites.

MWCNT-COOH and PLA(530g/mol)-grafted-MWCNT	10 – 15nm, 10 – 20µm	PLA	1.00, 1.00	9, 44	4, 44	[160]
MWCNT	~30nm, 15µm and ~30nm ,50µm	PS	1.00, 1.00	25, 25	35, 42	[161]
MWCNT	20 – 60nm, ~1 – 100µm		0.1, 0.5,1.0,2.0	24.4, 17.9, 21.6, 18.8	2.47, 2.01, 2.35, 2.18	[162]
CPP-grafted MWCNT	14nm, 1.5µm		0.50	100	100	[172]
MWCNT	5 – 20nm, 1 – 10µm	PCL	10.00	170	166	[173]
MWCNT and COOH – MWCNT	—		1.2, 1.2	-3.5, 12.1	86.3, 164.3	[174]
COOH – SWCNT	5 – 10nm, 5 – 30µm	PMMA	5.00	300	—	[175]
PMMA-grafted MWCNT	16.6nm, 1.2µm		0.15	360	94	[176]
Poly (3 – hexylthiophene)-g-PMMA & PMMA-MWCNT	25- 70nm, —		0.10, 0.10	86, 0	104, 57	[169]
Unclear – CNT and PGMA (coated) – CNT	28.2nm, —		5.00, 5.00	-51, -0.4	33, 94	[177]
SWCNT	1 x10^7 nm, 2 x 10^4 µm	PDMS	1.20		300	[178]
MWCNT, COOH – MWCNT, NH_2 – MWCNT	40 – 60nm, 0.5 – 40µm	PI	6.98, 6.98, 6.98	18.62, 31.37, 7.84	39.13, 60.86, ~45.65	[179]

Table 4.3 (contd) Mechanical properties of solution/solvent casted nanocomposites.

MWCNT-COOH, NH – MWCNT	40 – 70nm, 50 – 100μm	PI	5.00, 5.00,	~54.08, ~28.57	~45.83, ~16.6	[163]
Polyetherimide-g-COOH – MWCNT	10 – 50nm, —		0.38	60	50	[180]
MWCNT-COOH	1 – 20nm, 1 – 100μm	Chitosan	0.8, 2.0	99, 99	97, 93	[181]

4.1.2.3 Electrical properties

Polymeric nanocomposites exhibit a percolating behaviour, whereby the formation of an interconnected network of nanotubes dramatically increases the conductivity of the polymer. A critical weight/volume fraction of CNT is required to reach the percolation threshold in an insulating polymer, at which point the composites turn electrically conductive. At the percolation threshold, conductivity between adjacent nanotubes maybe achieved by electron hopping, however at higher concentrations a conductive network is established throughout the composite. Over the last decade, a wide range of values for conductivity and percolation threshold have been reported in the literature. These values have been shown to be strongly dependant on the polymer type, composite processing methods, dispersion, degree of functionalisation, alignment, aspect ratio and the type of CNT. As with the mechanical properties, correlations and dependencies between the aforementioned parameters are difficult to establish. Therefore, a focused survey of the available literature on polymer nanocomposites developed by solution mixing/solvent casting is shown in the Table 4.2.

It is generally well accepted that chemical functionalisation disrupts the extended π-conjugation of CNT's and thereby reduces electrical conductivity. However, functionalisation of CNT's is often necessary to produce multifunctional composites. Some investigators have therefore studied the effect of functionalised CNT's on the electronic properties of composites. For example, Tamburri *et al.* found that functionalising SWCNT's with –COOH and –OH groups enhances the conductivity of the composites by a factor of 7.5 in comparison to untreated SWCNT's[182]. The matrix used in this study was that of a conjugated polymer. Therefore, when incorporating functionalised SWCNT's, effective bridges are formed between the conductive domains of the polymer. This is a result of better interfacial interaction with the polymer, as when measuring pure SWCNTs, no differences in conductivity were found between the treated and untreated. Kim *et al.* found similar results with nanocomposites developed from MWCNT-COOH and PCL, inferring that better dispersion within the polymer may take precedence over damages caused by chemical functionalisation of CNT's[169]. The effect of different functional groups on CNT based composites has also been studied. It has been found that NH_2 – MWCNT/PI nanocomposites provide higher conductivities than COOH – MWCNT/PI nanocomposites, especially at lower loadings of CNT's[179]. This is because NH_2 – MWCNT's were more homogenously dispersed compared to COOH – MWCNT's in PI. Furthermore, in contrast to the

aforementioned studies, it was found here that unmodified nanotubes provided better electrical conductivity in composites regardless of the poor dispersion. These differences can somewhat be attributed to the degree of functionalisation and therefore the extent of damage to the electronic structure of CNT's.

Lau *et al.* investigated whether there are differences in the intrinsic conductivity of MWCNT's after functionalisation[153]. They compared various functionalisation techniques such as acid reflux, thermal and dry UV-ozonolysis and found that, the conductivity increased by 12, 80 and 330-fold respectively. The large increase in conductivity for dry UV-ozonolysis is mainly due the fact it caused the least structural damage to CNT's. Furthermore, they were able to attribute the increasing conductivity after functionalisation to an increasing concentration of oxygenated groups; promoting electron transfer between the carbon atoms. As a final remark on the impact of various functionalisation strategies, covalent grafting of polymers to CNT's can significantly improve mechanical properties at low loadings. Yoon *et al.* investigated the influence of grafting polymers on the electrical properties of PLA/MWCNT-g-PLA nanocomposites[160]. They found that PLA-g-PLA/MWCNT nanocomposites reduced the electrical conductivity and became very resistive upon increasing the PLA chain length that was grafted onto MWCNT's.

Overall, the literature data gathered here presents a wide range of values for electrical conductivity and percolation threshold. Other than those factors mentioned above, a high aspect ratio, processing conditions, polymeric matrix and nanotube type can all influence the electrical conductivity of final composites. Nevertheless, the ease of fabrication and the excellent electrical conductivities reported for nanocomposites incorporating CNT's offer much promise in the effort to produce an electrochemical MNA from nanocomposites for biosensing applications.

Table 4.4 Electrical conductivity measures of solution/solvent casted nanocomposites

Type of CNT	CNT dimensions (diameter in nm, length in µm)	Matrix	% of CNT loading	Matrix conductivity (S/m)	Composite conductivity (S/m)	Percolation threshold (wt%)	Reference
OH – MWCNT	10 – 20nm, 50µm	PU	5.0	—	1.2×10^{-6}	< 0.5	167
MWCNT with P3HT-g-PCL as a compatibiliser	25 – 70nm, —	PC	5.0	10^{-13}	64	—	169
PPE – SWCNT	—		7.0	10^{-13}	4.81×10^{2}	0.11	183
MWCNT-COOH, PLA (530g/mol) grafted-MWCNT	10 – 15nm, 10 – 20µm	PLA	1.0, 1.0	$\sim 4.13 \times 10^{-9}$	$\sim 5.0 \times 10^{-2}$, $\sim 4.0 \times 10^{-9}$	—	160
MWCNT	— ,2000µm		3.0	—	40	—	171
MWCNT	15 – 30nm, —		3.0	4.0×10^{-14}	$\sim 1 \times 10^{-4}$	0.21 – 0.33	184
PPE - SWCNT	—	PS	7.00	10^{-14}	6.89	0.05	183
MWCNT	30nm, 50 – 55µm		5.00	—	10^{-2}	<1	185
MWCNT	—		1.00	$\sim 10^{-20}$	1.46×10^{-6}	—	186
COOH – MWCNT	>50nm, 10 – 20µm		1.50	—	10^{-5}	0.8	187
ADA dispersed SWCNT	—	PCL	3.00	$<10^{-9}$	$\sim 10^{-6}$	0.08	188

Table 4.5 (contd) Electrical conductivity measures of solution/solvent casted nanocomposites

MWCNT and COOH – MWCNT	—	PCL	2.0, 2.0	10^{-15}	10^{-4}, 1	—	174
MWCNT	—	PMMA	0.40	$<10^{-10}$	$\sim10^{3}$	0.003	189
SWCNT and $SOCl_2$ doped SWCNT	—		10.0, 13.5	—	1.7 x 10^{3}, 10^{4}	0.17	190
Unclear – CNT and PGMA-CNT	28.2nm, —		8.00, 8.00	—	~28, ~17	—	177
MWCNT dispersed in chloroform, toluene and acetone	10 – 30nm, 1 – 10μm		20.0, 20.0, 20.0	8.0 x 10^{-13}	4.0 x 10^{-3}, 4.0 x 10^{-4}, 1.0 x 10^{-4}	4, 7, 10	191
MWCNT, COOH – MWCNT, NH_2 – MWCNT	40 – 60nm, 0.5 – 40μm	PI	6.98, 6.98, 6.98	6.5 x 10^{-16}	2.4 x 10^{-3}, 3.8 x 10^{-6}, 5.8 x 10^{-5}	—	179
COOH – MWCNT, NH - MWCNT	40 – 70nm, 50 – 100μm		5.00, 5.00	6.09 x 10^{-16}	93.8, 103.2	—	163
MWCNT	60 – 100nm, 5 – 15μm	PDMS	2.5	—	0.02	1.5	192

4.1.2.4 Considerations for the choice of polymer

In relation to the fabrication of MNA based sensors, polymeric nanocomposites can be used as effectively as their matrix material alone in order to fabricate MNA's easily and on a large scale. Several candidate polymers have been used to fabricate mechanically robust MNA's for applications across the board in microneedle research. However, concerning the evolving field of MNA based transdermal sensors, solid and hollow polymeric MNA's have only been utilised as a penetrative structural support and not as active components themselves. Examples include PCL and epoxy for solid sensors[49,65], while Miller *et al*., used an acrylate based photopolymer under the trade name of E-Shell® for rapid prototyping of hollow MNA's[57,58]. Metallisation is a popular strategy used to convert the solid MNA's into biosensors, whereas hollow MNA's can be used to conceal modified carbon fibres and pastes for selective and multiplexed detection of a range of analytes. On comparison, solid MNA sensors are far more advantageous because their 3D surface provides a larger electroactive surface area for biomolecular detection[60]. Therefore, their overall current response is greater alongside an improved signal to noise ratio.

The addition of CNT's can certainly improve the mechanical and electrical properties of a wide range of polymers as shown in Tables 4.1 and 4. 2. Notably, this range also includes those polymers that have been typically used to develop MNA's. As stated previously, a number of techniques have been developed to enable rapid prototyping of polymeric MNA's, however micromoulding is commonly used due to its cost-effectiveness, excellent reproducibility of the master structures and high scalability. It is important to note that processability using this technique is highly dependent on the fact most of these polymers are either dissolvable in organic solvents and or can be melted at high temperatures[64]. The development of polymeric nanocomposite MNA's was envisioned to encompass a two-step process in a broad sense: (1) preparation of polymeric nanocomposite material/film from a homogenous suspension of CNT's embedded in a polymeric matrix and (2) fabrication of MNA's from the nanocomposites by micromoulding. A key challenge to these steps is processability and this can be made favourable by lowering the concentration of fillers (CNT) being used, which subsequently makes processing simpler by lowering viscosities for sample and melt processing. From table 4.2, it can be seen that polymeric hosts such as PU, PC, PLA, PS, PCL, PMMA and PI, all exhibit very low percolation thresholds.

Nanocomposites developed from these polymers also show the potential to achieve very high conductivities. For example, Kim *et al.* reported a maximum conductivity value of ~3000 S/m for PMMA/MWCNT composites with a CNT loading of only 0.4 wt%[189]. This is however an exception with many others reporting a relatively high CNT loading (> 5 wt%) being used to achieve high conductivities in different polymeric matrices. Concerning these host polymers, nanocomposites developed from PLA, PCL and PI in particular show significant improvements in conductivity with lower loadings of CNT (< 5 wt%).

Micromoulding is an efficient fabrication strategy to produce MNA's out of both PLA and PCL. Previous researches have shown that MNA's developed from these materials can penetrate the skin easily and without any mechanical damage[2,63]. However, in terms of mechanical properties of the polymers, PLA is stronger than PCL. In comparison to these polymers, PI is difficult to process by solvent dissolution or melting because of the presence of rigid aromatic moieties in their structure. Nanocomposites produced from this host polymer have only been processed from its precursor polyamic acid (PAA). A high temperature (250 – 300°C) is also required for the imidization process[193]. Therefore, taking these considerations into account, PLA may represent an ideal host matrix for the fabrication of nanocomposite MNA's.

PLA is a thermoplastic aliphatic polyester derived by various methods of polymerisation of naturally occurring carbohydrates[194]. This polymer has attracted a great deal of interest because of specific characteristics that are lacking in other polymers, such as renewability, biodegradability, biocompatibility, mechanical strength and importantly cost-effective processability[194]. In terms of the biomedical applications of PLA, extensive research is being carried out on drug delivery systems, tissue engineering and as biodegradable matrix for surgical implants[66,194]. In order to extend its applications, enhancement of mechanical strength is deemed necessary for PLA because of their low impact toughness. A popular approach to achieve this is by incorporation of nanofillers such as CNT's, which can impart excellent mechanical and electrical properties to the matrix. Incorporation of CNT's within PLA is readily achievable as the polymer can be melted at moderately high temperatures and is soluble in organic solvents of low boiling points. As with many of the polymers, research into PLA/CNT based composites is still in its infancy, with research focused more so on synthesis than its applications. Biosensors based on

PLA/CNT composites have only been reported as modifiers of electrodes in a few recent studies[195,196].

4.2 Aims and objectives

The aim of this chapter is to demonstrate a convenient route of fabrication for developing electrochemical MNA's from composites of PLA and carboxyl functionalised MWCNT's (*f*-MWCNT). Once developed, these MNA's will be characterised for mechanical strength and electrochemical performance.

The objectives of this chapter are to:

1. Investigate nanocomposites film synthesis with different loadings of *f*-MWCNT embedded homogenously in PLA.
2. Develop a method to fabricate nanocomposite MNA's using the nanocomposite films and assess the limit of fabrication.
3. Evaluate the mechanical strength of the nanocomposite MNA's with different loadings of *f*-MWCNT.
4. Design and optimise MNA's for assessment of electrochemical behaviour
5. *In vitro* electrochemical characterisation of nanocomposite MNA's
6. *In situ* electrochemical characterisation of nanocomposite MNA's using freshly excised porcine ear skin.

4.3 Materials and methods

4.3.1 Fabrication of PLA/f-MWCNT composites

Due to the ease of processing, solution mixing and solvent evaporation (i.e. solvent casting) was identified as an appropriate method to fabricate PLA/*f*-MWCNT composites. In this approach, CNT's are dispersed using a solvent that would dissolve the polymer of choice. However, dispersion of the CNT's is a major challenge due to strong van der Waals forces between the tubes. Therefore, a combinatorial approach utilising *f*-MWCNT's and sonication was employed here. The CNT's were dispersed in an organic solvent (chloroform) to produce nanocomposites with minimal aggregation. Based on literature describing nanocomposite manufacture, the following protocol was implemented. Briefly, *f*-MWCNT's (length: 10 – 30µm, outer diameter: 20 – 30nm) at different loadings (3 – 6%) were dispersed in 48 ml of chloroform using an ultrasonic bath operating at 37 kHz for 1 hour. PLA filaments were then dissolved into the chloroform by magnetic stirring at 45°C for 90 minutes on a hot plate. This mixture was then sonicated for another hour with the temperature controlled at ~45°C (using the thermostat of the bath sonication), for efficient intercalation of the *f*-MWCNT with PLA. Final homogenisation was completed by magnetically stirring the solution on a hot plate at 45°C for 48 hours. The mixture was then

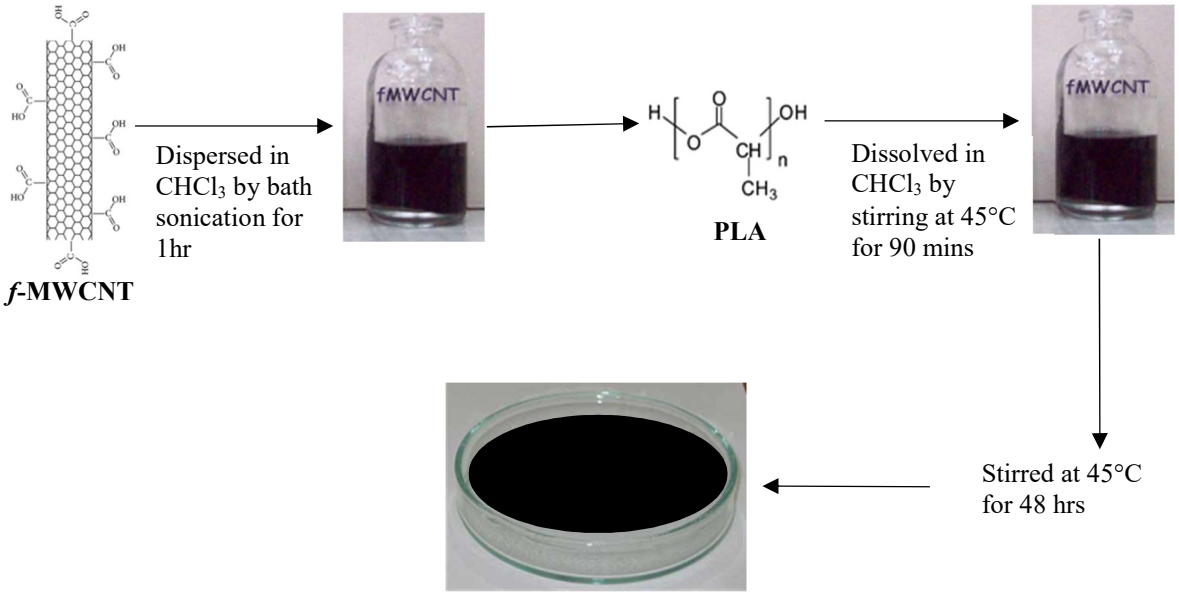

Figure 4.1. Nanocomposite film synthesis. Illustration of the stages involved are shown.

poured into a glass petri dish and the solvent was evaporated at room temperature (RT) for 48 hours. The resultant composite film was then dried further in a thermal oven at 60°C overnight to remove any residual chloroform. A schematic illustration of the process of fabrication nanocomposite films is shown in Figure 4.1 above.

4.3.2 Micromoulding

MNA's were produced by adapting a micromoulding approach developed by McAllister *et al.*[9]. Initially, a PDMS micromould (negative template) was produced from the Sylgard® 184 elastomer kit (Dow Corning, Midland, MI, USA) against a commercial template MNA (Derma Stamp, amazon.co.uk, ASIN: B007ATO20I). To fabricate the nanocomposite MNA's, the film of PLA/*f*-MWCNT was cut into small pieces (~1 x 1cm) and filled into a micromould at a specified weight of 0.175 grams (optimisation of weight described in *section 4.3.4*). The nanocomposite filled micromould was then heated in a thermal oven at 200°C for 2 hours. This caused the nanocomposite material inside the micromould to become pliable, upon which, it was manually compressed into the microcavities of the micromould to form the microneedles. Manual compression was repeated three times at 30 min intervals to ensure MNA formation in the mould. The micromould was then removed from the thermal oven and the nanocomposite material was allowed to cool at RT for 30 mins. Micromoulds were then filled with PCL pellets and melted on top of the nanocomposite material at 100°C for 2 hours to form a thick base. After further cooling at RT, the MNA's were manually ejected from the mould. PLA MNA's were made similarly, but with vacuum assisted micromoulding at 180°C for 4 hours.

4.3.3 Mechanical characterisations

A TA.TX Plus texture analyser (Stable Microsystems Ltd, Surrey, UK) was used to assess the microneedle AFS and SFS as previously described in Chapter 3 (*section* 3.3.3).

4.3.4 Electrochemical characterisation

Electrochemical measurements and data acquisition was carried out using a CHI 630B pontentiostat (CH Instruments, Austin, TX) controlled using the manufacturer's own software (version 10.18). A three-electrode system was employed consisting of an Ag|AgCl (3M KCl) reference electrode, a platinum wire auxiliary electrode and the nanocomposite

MNA's as the working electrode. The initial characterisation and optimisation of the device was carried out by analysing the cyclic voltammetric (CV) response of the nanocomposite MNA's towards 1mM potassium ferricyanide in 1M KCl, across a potential window of 0 – 1V. The electrochemical response was analysed in terms of conductance (at a scan rate of: 0.01 Vs^{-1}) and capacitance (at a scan rate of: 0.1 Vs^{-1}) of the MNA electrode.

In terms of optimisation, the initial work involved designing an electrical contact to measure the electrochemical response. Three main strategies were investigated: (1) affixing an electrical wire across the centre of the supporting base of a MNA using conductive epoxy, (2) electrical wire fixed to the side wall of the micromould before fabricating the MNA and (3) after ensuring the MNA's formed by compressing the nanocomposite material inside the mould, a coiled wire covering ~85% of the nanocomposite surface was affixed by minimal compression to the supporting base while the material was pliable. The designs are illustrated in Figure 4.2. In all cases, after a period of cooling (or curing in terms of conductive silver epoxy) to ensure a firm connection with the composite material, the electrical contact was sealed with PCL by melting it (at 100°C) over the surface, forming an insulating layer. Upon further cooling at RT, the MNA was manually ejected from the mould.

Second optimisation involved isolation of the electrochemical response generated by the MNA's to the microneedles alone. As the MNA is moulded completely from the nanocomposite material, contact of an analyte to the base will alter the electrochemical response significantly. Therefore, the microneedles of each test array were pierced through a layer of Parafilm® and sealed around the nanocomposite by application of heat at 40°C for 2 minutes. Comparisons were made between sealed and unsealed MNA. Finally, the height of the supporting base structure was optimised by using a specific weight (0.175g) of the polymer nanocomposite material to provide the lowest path of resistance. The specified weight also helped minimise conductive variation between MNA's of the same CNT loading and of different loadings studied in this work.

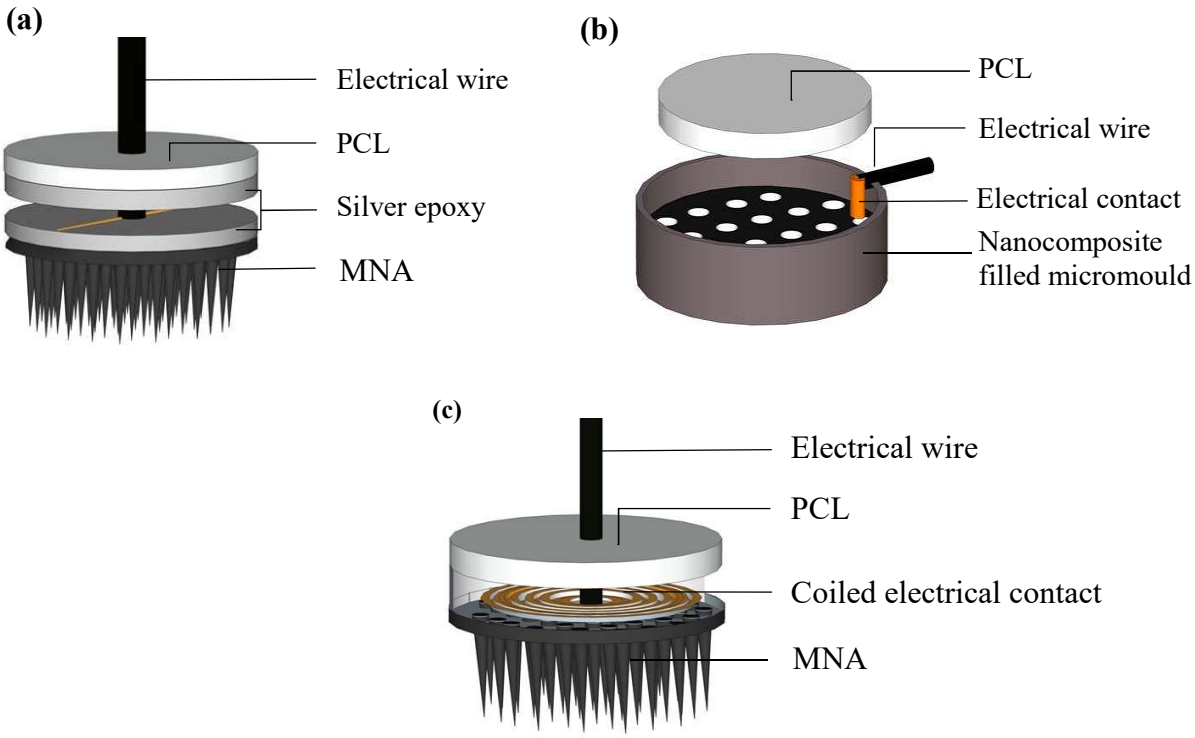

Figure 4.2. Designing an electrical contact. (a) Contact made through the middle by affixing the wire between two layers of conductive silver epoxy (b) electrical contact made by the side wall of the micromould (c) a coiled electrical contact made by compressing the coil into the nanocomposite material during MNA fabrication. All designs were implemented in a micromould. Finally, PCL pellets were melted on top to provide a seal and act as a base for easy handling.

4.3.5 Ascorbic acid

The electrochemical performance of the MNA was further evaluated using a physiologically relevant analyte i.e. ascorbic acid (AA), which is endogenously present in the skin at concentrations in the millimolar range[197]. As described previously (*section 4.3.4*), a three-electrode configuration was set up for all voltammetric measurements. Two voltammetric techniques (i.e. differential pulse voltammetry (DPV) and amperometry) were used to measure the electrochemical response of the MNA electrode towards different concentrations of AA in 0.1 M phosphate buffered saline (PBS). DPV measurements were made across a potential window of 0 – 1 V, with a scan rate of 0.008 Vs^{-1}, pulse width was 0.06 s. In order to carry out amperometric measurements a stirred solution was used and the MNA electrode was biased at 700 mV.

4.3.6 In situ electrochemical characterisation

4.3.6.1 Measuring in the skin

Full-thickness skin was removed from freshly excised porcine ears by blunt dissection (harvested from euthanised animals from unrelated studies, donated by Dr. Ryan Waters, Pirbright Institute, UK). To evaluate the performance of the MNA as a penetrable biosensor, a skin diffusion experiment was set up in a Franz diffusion cell (Figure 4.9A). Briefly, one end of the skin was pinched and clamped between the donor and receptor chambers. The clamped skin was then pierced with a hypodermic needle to equalise the pressure and allow direct fluid flow between the two chambers. Both chambers were then filled with PBS. The reference and the auxiliary electrodes were placed inside the donor chamber, while the MNA was used to penetrate the skin which in turn securely held the MNA in place for the duration of the experiment. Measurements were taken at time intervals over 160 mins across a potential window of 0 – 1 V using DPV. Control measurements were taken without the diffusion cell set-up. Ear skin samples from five animals were used to account for inter-sample variability.

4.3.6.2 Evaluation of a burn would model

Once the skin had been allowed to equilibrate for 160 mins with PBS in the diffusion cell, controlled burn wounds were induced in the skin using the flat end of a stainless-steel rod (12mm in diameter) heated to 100°C (in a thermal oven) and kept in contact with the skin for two minutes. Throughout this procedure, the skin was maintained in the Franz diffusion cell setup above. After the burn was induced, the PBS was allowed to re-diffuse in to the skin for another 160 mins. Electrochemical measurements were taken before and after the burn using DPV across a potential window of 0 – 1V.

To evaluate the diagnostic potential of the electrochemical signature of the skin, the influence of the burn was measured at specified distances from the edge of a burn site. Using the MNA's DPV responses were measured again at the site of the burn, 1 mm away and 10 mm away. As before the measurements were taken after PBS was allowed to re-diffuse into the skin. Responses were measured from five ear skin samples.

4.3.7 Imaging

Microneedle topology and dimensions were analysed using field emission gun scanning electron microscopy (FEG-SEM; Carl Zeiss SIGMA, Germany). Topological and cross-sectional imaging of the microneedle was carried out after sputter coating the samples with a 4 nm layer of gold. MNA perforations in the skin was visualised by methylene blue staining and acquired using a stereo digital microscope equipped with a 3-megapixel camera (SMZ-168, Motic, HK). Photographs of MNA's were taken using a digital camera.

4.3.8 Statistical analysis

Data were processed in Microsoft Office Excel 2016, analysed using GraphPad Prism 7 (GraphPad Software Inc., USA) and expressed as mean ± standard deviation. Graphing of electrochemical data was performed using Igor Pro, version 6.0 (WaveMetrics Inc, USA). Where appropriate, statistical differences between groups were assessed using the two-sided Student's t-test, repeated measures and one- or two-way ANOVA with Tukey's post-hoc test for pair-wise comparison. Differences were considered statistically significant where $P < 0.05$.

4.4 Results

4.4.1 Fabrication of nanocomposite films

Nanocomposite films of *f*-MWCNT/PLA were made successfully at CNT loadings greater than 3 wt%. With an hour of sonication, *f*-MWCNT were adequately dispersed into suspension without any evidence of sedimentation (as seen from the images shown in the schematic, Figure 4.1). The nanocomposite films produced were smooth and even with average thickness of ~800 μm. Different loadings were produced to determine the threshold at which MNA's form consistently. As discussed before the percentage of CNT added to the composite significantly influences the mechanical and electrical properties of the composite. Significant increases in Young's modulus and tensile strength for MWCNT/PLA composites have been reported between 0.25 – 5 wt%[171]. For carboxylic acid-functionalised MWCNT's, a CNT loading of 2.5 wt% was required to achieve optimum mechanical strength[159]. In contrast, conductivity increases with the incorporation of higher percentages of CNT. For MWCNT/PLA composites prepared via solvent casting, at least 3 wt% of CNT was required to initiate conductivity and the best conductivity has been reported at 10 wt%[171]. With higher loadings, it was anticipated that processing will become more difficult because of the higher viscosities. Therefore, the fabrication limit of the MNA was assessed with the increment in CNT loading.

4.4.2 Fabrication of nanocomposite MNA's

Preliminary work here determined the fabrication limit when employing a micromoulding approach. In order to produce nanocomposite MNA's, the micromoulds were filled completely with ~1 x 1 cm pieces of the nanocomposite films incorporating different loadings of *f*-MWCNT and heated to 200°C with the aim of melting it to form the MNA's. The following observations were made from this work: (1) Even at the lowest loading used here i.e. 3 wt%, the nanocomposite film did not melt, but rather became malleable with the application of heat. (2) Therefore, minimal to moderate manual compression was applied (with the increment in CNT loading) to the malleable nanocomposite films to determine if MNA's would form consistently and with sufficient mechanical strength, that it may be ejected from the micromould with the microneedles intact after a period of cooling. (3) Nanocomposite MNA's could be formed efficiently from 3 – 6 wt% of CNT loaded

nanocomposites films. For nanocomposite films above 6 wt% CNT loading, the nanocomposite material did not become sufficiently malleable under the application of heat and consequently manual compression was inadequate to form the MNA's. Therefore, 6 wt% was determined as the maximum loading tenable with the current fabrication method. (4) Manual compression should only be applied with a moderate amount of force and when the material is sufficiently malleable, this is important for the ease of fabrication and the reusability of PDMS micromoulds. SEM of the MNA's produced are shown below (Figure 4.3)

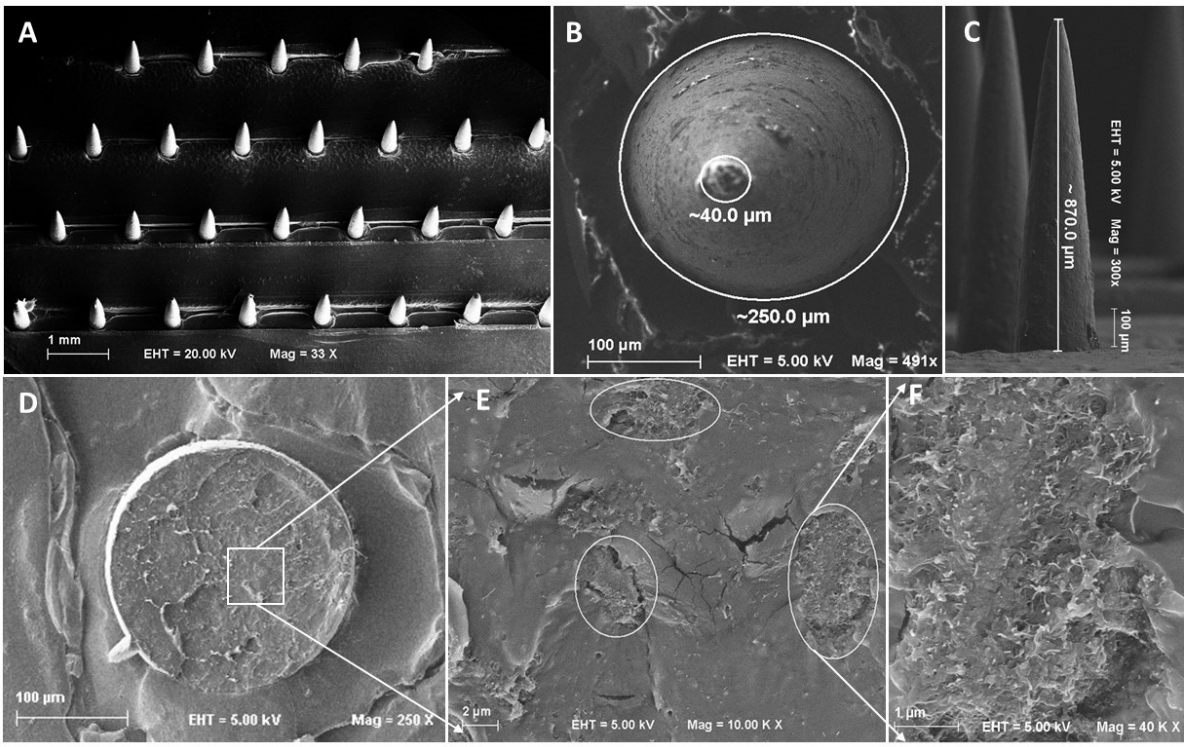

Figure 4.3. SEM images of 6% f-MWCNT/PLA composite MNA. (A – E, SEM images) – (A) conical microneedles were formed consistently by micromoulding; (B) Tip diameter = ~40.00 µm and Base diameter = ~250 µm (C) accessible microneedle height of 870.0 µm produced from a 1 mm long template (the ridges of each row masks the remaining height) (D) cross-sectional view of a physically broken microneedle (stump shown); (E) enlargement of a segment highlighting aggregates in the image. (F) Enlarged view of an aggregate.

Figure 4.3, A – C shows SEM of a composite MNA at 6% *f*-MWCNT loading. Each array consisted of 35 microneedles, arranged unequally in 5 rows with a centre-to-centre distance of 1 mm (within rows) and 1.2 mm (between rows). Each microneedle was conical with a slightly convex surface and measured approximately 870 µm in length and 250 µm in base diameter. The slightly rounded tips were approximately 40 µm in diameter (Figure 4.3, B

and C). Though MNA's were produced by manual compression using a micromoulding approach, the surface of the needles appeared to be relatively smooth (Figure 4.3, B and C). However, on inspecting the cross-section of a single microneedle (i.e. the stump of a broken microneedle), clusters of CNT were found embedded in the polymeric matrix (Figure 4.3, D, E and F). The cracks seen (Figure 4.3, E) are caused by the high intensity electron beam in the SEM, and though its appearance may seem random, their localisation might depend on the concentration of the nanotubes i.e. cracks maybe prominent on areas where the concentration of CNT is comparatively less. The formation of clusters as seen here will have significant impact on the mechanical and electrical properties of the composites.

4.4.3 Mechanical characterisation

Figure 4.4 shows evaluation of AFS and SFS of composite MNA's in comparison with MNA's developed from PLA alone. As the composite matrix is non-homogenous, variation in mechanical strength between microneedles are expected. Therefore, individual microneedles were evaluated. The general trend for AFS and SFS points towards increasing mechanical strength with the increment in CNT loading. In relation to AFS (Figure 4.4, A), composite microneedles of all CNT loadings including those of PLA were able to withstand compressive forces higher than relative skin insertion forces, which range from 0.1 – 0.3N due to variations in the stratum corneum thickness[76]. Significant improvement in AFS were found between 3 wt% vs 5 wt%, and 4 wt% vs 6 wt% ($p < 0.01$). In comparison to PLA, there was no significant improvement in AFS at any given CNT loading and at 3 wt% CNT loading, AFS was significantly lower. In relation to SFS (Figure 4.4, B), for CNT loadings up to 5 wt%, the composite microneedle yielded significantly lower SFS in comparison to PLA ($p < 0.0001$). However, at 6% CNT loading, the SFS significantly improved in comparison to PLA. Overall, these results show that MNA's with a CNT loading of 6 wt% hold the best mechanical properties.

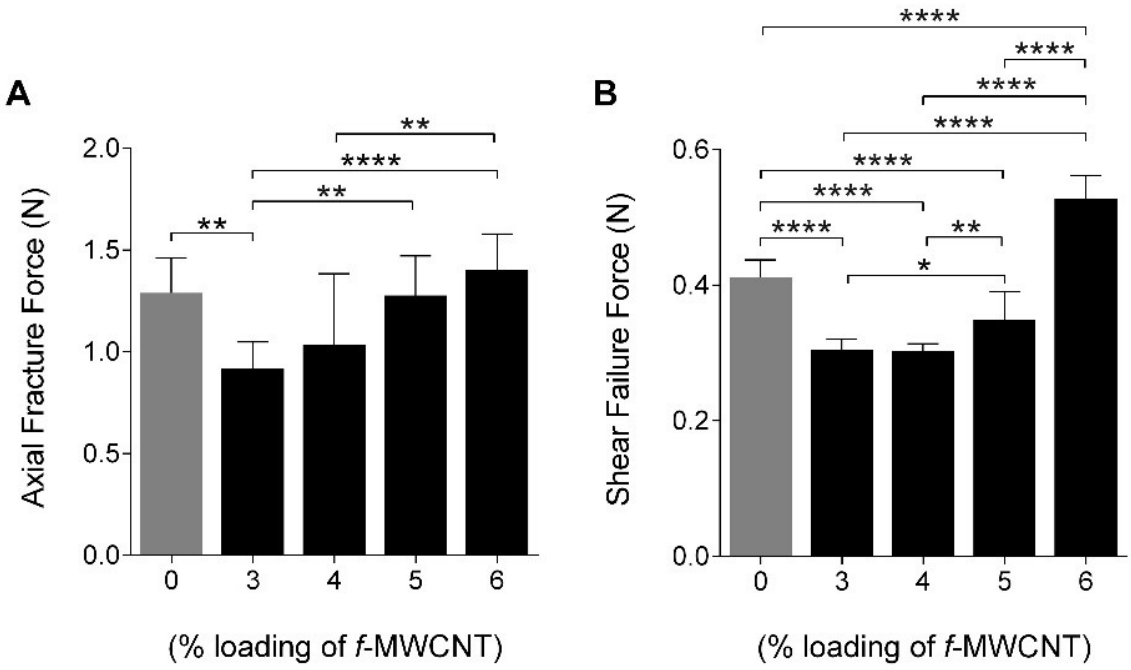

Figure 4.4. Mechanical characterisation of composite vs PLA MNA's using texture analyser. (A) AFS of nanocomposite microneedles increased with the increasing loading of *f*-MWCNT. AFS of microneedles with 4 – 6% *f*-MWCNT loading were comparable to that of neat PLA, whereas 3% was significantly weaker. (B) SFS of nanocomposite microneedles were significantly lower at 3 – 5% *f*-MWCNT loading, however at 6% *f*-MWCNT loading, the microneedles yielded a significantly higher SFS compared to that of neat PLA. (*p < 0.05, **p < 0.01, ***p < 0.001, ****p < 0.0001, one-way ANOVA with Tukey's multiple comparisons test (n = 10).

4.4.4 Electrochemical characterisation

4.4.4.1 Design and characterisation of an electrical contact

Nanocomposite MNA's fabricated with the highest percentage of CNT loading (i.e. 6 wt%) was used to optimise an electrical contact and characterise the electrochemical behaviour of the MNA's. The design concepts showing in Figure 4.2 were analysed by evaluating the MNA's response towards ferrocyanide ($Fe(CN)_6$); which in turn determined whether the nanocomposites MNA's were electroactive. From the designs evaluated here, a measurable electrochemical response was only seen with the coiled design as shown in Figure 4.5, A. Here, responses from three MNA's with 6 wt% of CNT loading are shown. A substantial increase in current in response to 1 mM $Fe(CN)_6$ in comparison to the baseline (1 M KCl) is seen for all the MNA's. In relation to the electrochemical response itself, the redox processes typically observed for $Fe(CN)_6$ was not evident. Also, large variations in

current generated between the three MNA's were apparent. Nevertheless, this result implies that the nanocomposite MNA's were electroactive. However, it does not indicate whether the microneedles alone were sufficient to produce an electrochemical response. The responses seen in Figure 4.5, A were generated from the microneedles as well as its supporting base, composed entirely of the nanocomposite material, immersed in the analyte solution.

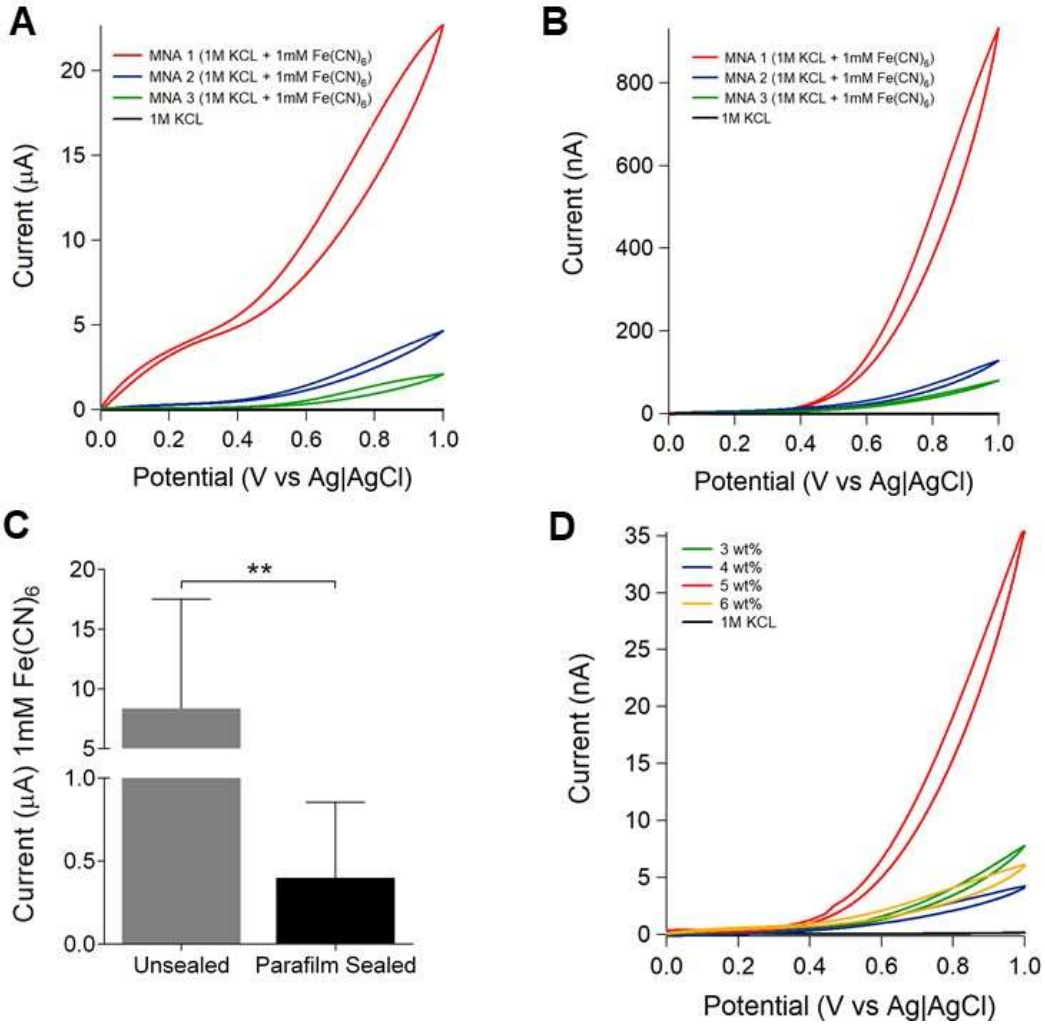

Figure 4.5. Electrochemical response of MNA's towards 1mM $Fe(CN)_6$. (a) Response from a coiled electrical contact recorded for three MNA's with 6 wt% CNT loading (b) lower response recorded after sealing the supporting base of the MNA's with Parafilm® (c) evaluating the MNA response at 1 V for unsealed and Parafilm® sealed MNA's. (d) representative CV traces showing non-linear responses from MNA's incorporating different loadings of CNT. (**p < 0.01, one-way ANOVA with Tukey's multiple comparisons test (*n = 3*).

The base of the MNA's were therefore concealed with Parafilm® as detailed in *section* 4.3.4 (see Figure 4.10, D) and the measurements were repeated. The responses generated as

a result are shown in Figure 4.5, B; comprising three different MNA's at 6 wt% CNT loading. It is readily noticeable that the current generated in response to $Fe(CN)_6$ was at least two orders of magnitude lower in comparison to unsealed MNA's. For a more accurate comparison between the unsealed and the Parafilm® sealed MNA's, the current generated at a potential of 1 V was analysed from the CV traces. This is shown in Figure 4.5, C; which indicates a significant decrease in current generated for the Parafilm® sealed MNA's ($p < 0.01$, two-sided unpaired t-test, $n = 3$). This significance is relatively low, because similar to the unsealed MNA's, there was large variations in the current generated at 1 V between the sealed MNA's. The variation was confirmed as the relative standard deviation (RSD – calculated by multiplying the standard deviation by 100 and dividing the product by the average) was found to be 109% and 114% for the unsealed and the Parafilm® sealed MNA's, respectively. This variation was problematic when comparing MNA's with different loadings of CNT as seen in Figure 4.5, D. The observed trend indicates no relationship between CNT loadings and the overall current generated i.e. a linear relationship can be anticipated between the current response and the increment in CNT loadings. Nevertheless, the results shown here are promising as it shows that, at all CNT loadings investigated in this study, the bulk nanocomposite based MNA's were electroactive.

Although an electrical contact was optimised for the MNA's assessed so far, it was noticeable that the depth at which the electrical contact was made varied significantly between MNA's. This was because the amount of nanocomposite material used to make each MNA had varied significantly. Consequently, a large variation was seen between the MNA's and different CNT loadings. Therefore, the nanocomposite MNA fabrication process was optimised by adopting to use a specified weight of the nanocomposite material in an attempt to define a constant base height thickness. In order to determine the specified weight, additional factors such as the thickness of the coiled wire and the effect of compression on the insertion depth of the coil inside the nanocomposite material was further evaluated. Consequently, it was found that a base height of approximately ~2mm was sufficient for effective placement of the electrical contact and the weight of the nanocomposite material required to achieve this height was 0.175 ± 0.001g. A digital image of the resultant MNA is shown in Figure 4.6. Minor variations in base height was still evident due to application of compressive forces, causing the nanocomposite material to creep along the sidewalls of the micromould during the process of fabrication.

Figure 4.6. Digital image of an optimised MNA fabricated using the nanocomposite material. The electrical contact was sealed with PCL.

Electrochemical measurements were repeated using the optimised MNA's (Figure 4.7). As a result, the electrochemical responses between different MNA's of the same composition (i.e. 6 wt%) showed very little variation (Figure 4.7, A). However, the redox processes associated with the $Fe(CN)_6$ was still not evident. In line with the previous results, the response to $Fe(CN)_6$ showed a significant rise in current to that of the baseline (1M KCl). As the variation had been minimised, the effect of Parafilm® seal on the current generated at a potential of 1 V was re-analysed. Figure 4.7, B shows the difference between the unsealed and the Parafilm® sealed MNA's to be highly significant ($p < 0.0001$ two-sided unpaired t-test, $n = 3$). The mean current responses for the unsealed MNA's were 32.28 ± 3.082 µA and 0.1313 ± 0.0154 µA for the Parafilm® sealed MNA's. With this optimisation, the RSD was effectively reduced to 10% and 12% for unsealed and sealed MNA's, respectively. The current generated by the Parafilm® sealed MNA's at 6 wt% is two orders of magnitude lower than the unsealed MNA's at 6 wt%. Figure 4.7, C shows representative CV traces for MNA's fabricated with a CNT loading of 3 – 6 wt%. A current response was seen at all CNT loadings, but without any redox peaks associated with them; importantly however, the trend is indicative of an increasing faradaic current being generated with the increment in CNT loadings. To draw comparison from the CV traces whilst also accommodating for variations between MNA's and batches, the current generated at 1 V was analysed for 10 MNA's from 3 different batches accommodating 3 – 6 wt% of CNT loadings (Figure 4.7, D). This reaffirmed the general trend observed from CV traces, as the increase in current measured was significantly greater when the loading of the CNT was increased. The mean responses were 1.964 ± 1.008 nA, 22.4 ± 8.616 nA, 63.49 ± 16.41 and 109.7 ± 14.71 nA for MNA's incorporating 3 – 6 wt% of CNT's, respectively.

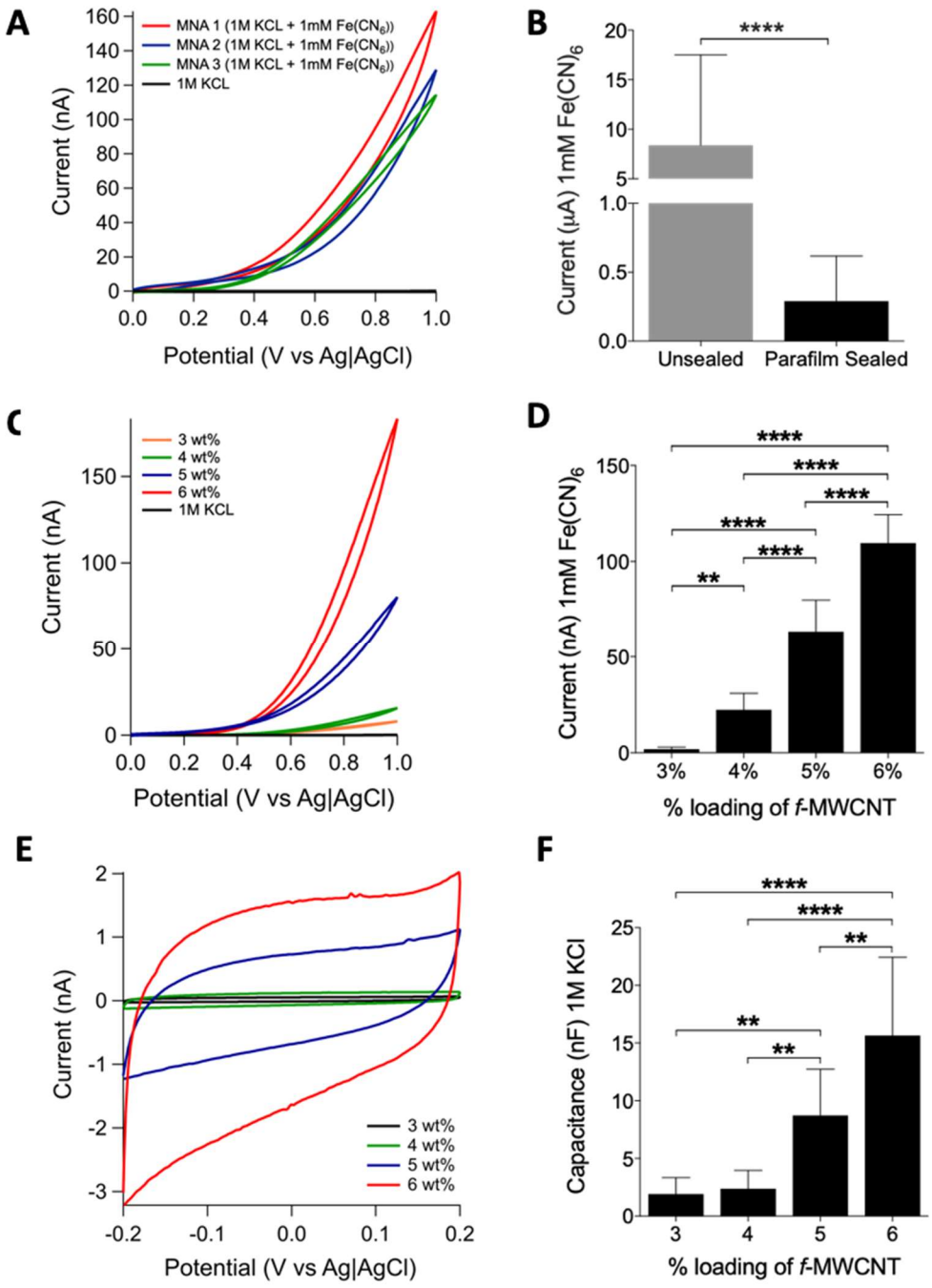

Figure 4.7. Electrochemical response of the MNA's towards 1mM $Fe(CN)_6$ after optimising the weight of the composites. (A) CV showing stable responses at 6 wt% CNT loading (*n = 3*). (B) Due to the minimised variation, the difference between unsealed and Parafilm® sealed MNA's were highly significant ($p < 0.0001$ two-sided unpaired t-test, n = 3*)*. (C) Representative CV traces showing linear increment in current responses from MNA's incorporating different loadings of CNT. (D) Evaluating the current measured from the CV traces at a potential of 1V, shows the responses to be significantly higher with increasing CNT loading. (E) Representative CV traces and (F) analysis of their capacitance with respect to MNA's incorporating different loadings of CNT. The CV traces indicates a linear trend with the best electrochemical behaviour seen at a loading of 6 wt%; as confirmed by statistical analysis of their capacitance. However, the capacitive response between MNA's incorporating 3 and 4 wt% was insignificant. (Figure D and F, (**p < 0.01, ****p < 0.0001, one-way ANOVA with Tukey's multiple comparisons test (n = 10)).

From evaluating their RSD's, (i.e. 47%, 36%, 25% and 13%, for 3 – 6 wt%, respectively) it was found that the variations were lower as the % loading of CNT increased. As such, MNA's incorporating 6 wt% of CNT produced the best results. For further characterisation, the capacitive behaviour of the MNA electrodes was evaluated using CV. Figure 4.7, E shows representative traces at a potential window of -0.2 to 0.2 V. A quasi-rectangular shape without any redox peaks is evident at all loadings; indicative of a good capacitive behaviour. The current densities scaled with the loading of CNT's, and the MNA's incorporating 5 and 6 wt% showed a higher integrated area, which points towards their superior electrochemical performance over the other loadings investigated. The capacitive current at each loading was evaluated by measuring the difference in current at 0 V over the scan rate; shown in Figure 4.7, F. With the increment in the CNT loadings, the capacitive current was seen to increase significantly, except from 3 wt% and 4 wt%. The highest capacitive current of 15.65 nF was measured at 6 wt% CNT loading. Variability among the different loadings was relatively high, though it was inversely proportional to increment in CNT loadings. At 6 wt%, the capacitive variability was found to be 23.41% (RSD). Overall, as the best electrochemical behaviour was seen at a CNT loading of 6 wt%, further analysis was based on this composition only.

4.4.5 Ascorbic acid analysis

DPV and amperometry were used for quantitative determination of AA using the MNA's incorporating a CNT loading of 6 wt%. AA is the most abundant electroactive biological compound that is known for its reductive properties and extensively investigated for their rapid determination, as they play a crucial role in various biochemical processes and industrial applications[197]. For DPV measurements, the response towards AA was determined from 200 μM to 1 mM using three devices and their representative DPV voltammograms are shown in Figure 4.8, A. This shows an asymmetric anodic peak for all concentrations analysed, at a low potential of 0.320 ± 0.02 V. Calibration data acquired by analysing the peak area for the oxidative responses at each concentration averaged from three MNA devices are shown in Figure 4.8, B. This indicates a linear relationship between the concentration of AA and the current measured (r^2 = 0.9282). The limit of detection (LOD), determined as 3 times the standard deviation at the lowest concentration over the slope of the calibration line was 164.38 μM, with a sensitivity of 1.113 nC μM^{-1}. RSD

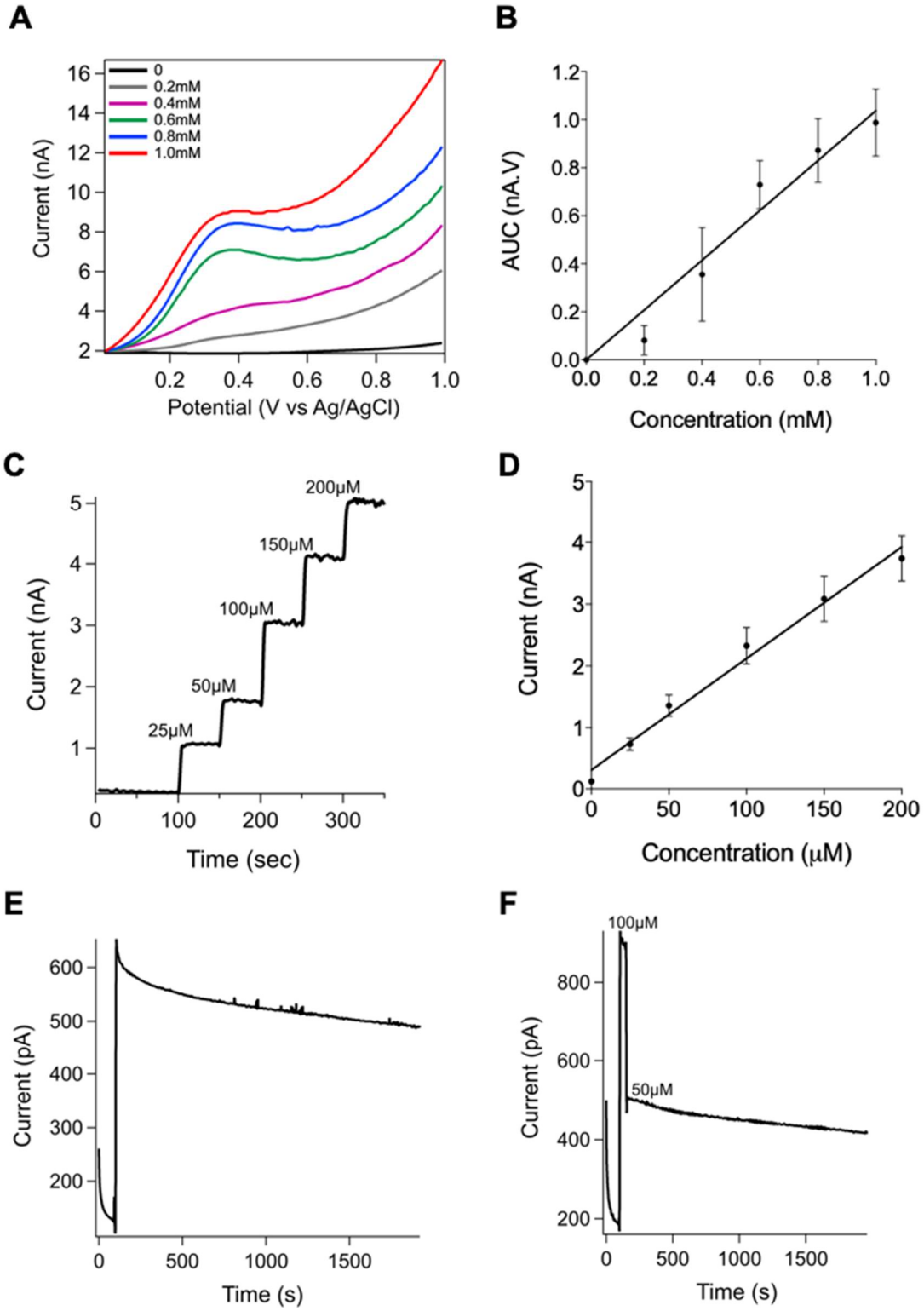

Figure 4.8. Quantitative determination of ascorbic acid. (A) Oxidative response of a single MNA towards different concentrations of AA measured by DPV (representative traces). (B) Calibration plot for the oxidative peak seen at 0.320 V based on three devices (n = 3). (C) Amperometric response of MNA's towards varying concentration of AA and (D) their respective calibration plot from three devices. (E) Response stability following an injection 100µM AA for 30 mins. (F) Response decay within 6 seconds of diluting the concentration from 100µM to 50µM.

between the three MNA's were 24%. Similarly, the amperometric response shown in Figure 4.8, C illustrates that the MNA's were able to discern varying concentrations of AA effectively. The calibration plot shown in Figure 4.8, D is again based on evaluation of the response from three devices and shows a linear response (r^2 = 0.9522). Here the detection limit was 16.79 μM, with a sensitivity of 18.04 pA μM^{-1}. The 90% response time to the stepwise change in concentration of AA was 6 s and the response was stable, showing minor decay in current, when measured over 30 minutes (Figure 4.8, E). Average RSD for the responses between three devices was 12 ± 1.5%. The MNA's were also able to detect dynamic changes in concentration, as shown by signal decay following dilution (Figure 4.8, D). The response time for this decay was equivalent to the signal response time at 6 s. These results show that the unmodified non-conjugated polymeric nanocomposite MNA's developed here are electroactive for biosensing purposes and possesses a good sensitivity over a wide detection range.

4.4.6 *In situ* analysis

4.4.6.1 Measurements in the skin

In situ biosensing capabilities of the nanocomposites MNA was demonstrated by performing electrochemical measurements in freshly excised porcine ear skin. Figure 4.9, A shows the experimental set-up implemented to allow diffusion of PBS through the skin. The skin was artificially stretched to ensure successful penetration of all microneedles, as visualised by methylene blue staining (inset, Figure 4.9, A). It was initially observed that, without diffusion a discernible electrochemical response could not be detected from DPV measurements, regardless of time. (Figure 4.9, B - black line). However, after just 5 mins of diffusion, two distinct oxidative peaks appeared, at 0.23 ± 0.02 V and 0.69 ± 0.04 V (Figure 4.9, B). The representative traces shown in Figure 4.9, B indicates a rise in oxidative response over time, but more prominently for the oxidative species at 0.69 V (by ~600 % after 160 mins of PBS diffusion). On evaluating this oxidative peak, a linear relationship is seen (Figure 4.9, C, r^2 = 0.8939) and since the magnitude of change is greater for this oxidative species, it was chosen for further analysis for the remainder of this study. On repeating the DPV measurements across skin samples from five animals, a similar trend was found and importantly, both oxidative peaks were readily identifiable; earmarking this as a signature waveform. The variability among animals were assessed by measuring the

oxidative response at 0.69 V after 160 mins of PBS diffusion. This indicated a significant variation between animals (one-way ANOVA, p = 0.001)) and the mean response was 0.687 ± 0.367 nC across all samples (Figure 4.9, D). However, the variation was only significant when comparing responses from all samples with that of skin 2, where the mean response was 1.282 ± 0.618 nC.

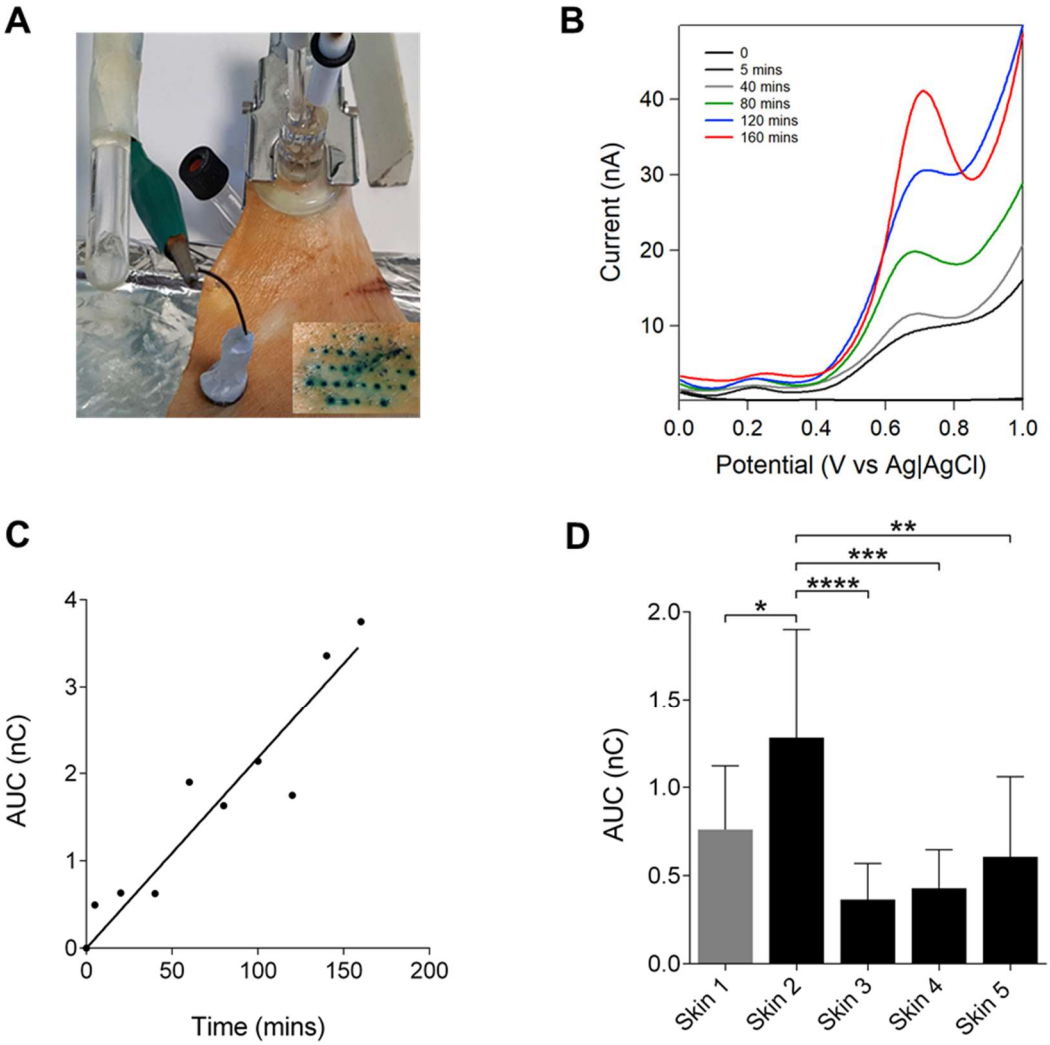

Figure 4.9. In situ bioanalysis. (A) Experimental set-up using a Franz diffusion cell for transdermal electrochemical measurements of the skin. Inset showing successful penetration of the microneedles visualised by methylene blue staining. (B) DPV traces after diffusion of PBS – two distinct oxidative peaks were seen within 5 mins of PBS diffusion, at a potential of 0.23 V and 0.69 V. (C) Linear plot of AUC against time for the biggest change seen at a potential of 0.7 V. (D) Variation of the oxidative peak at 0.7 V across five skin samples (*p < 0.05, **p < 0.01, ***p < 0.001, ****p < 0.0001, one-way ANOVA with Tukey's multiple comparisons test, n = 5 animals).

4.4.6.2 Burn wound model

The utility of the signature waveform as found here and hence the ability of our MNA's to monitor dynamic changes in the microenvironment of the skin was assessed by inducing

artificial burn wounds. Two experimental conditions were investigated: (1) before and after burn measurements on the same skin site and (2) comparing the burnt skin site to an adjacent control (non-burnt) site. As detatiled previously (*in section 4.3.6.2*), measurements after the burn were taken once the PBS was allowed to re-diffuse in to the skin. Under both conditions, attenuation of the oxidative peak at 0.69 V was clear from the representative DPV traces shown in Figure 4.10, A and B. This was found to be significant, as the oxidative response was suppressed by, 0.4137 nC on the same skin site and 0.6915 nC on burnt skin site to an adjacent control site ($p = 0.0070$ and $p = 0.0048$, respectively; two-tailed paired t-test, Figure 4.10, C). This difference is unlikely to be due to diffusive or evaporative water loss caused by the application of heat, since this was accounted for by allowing PBS to re-diffuse into the burnt site for 160 min. Neither is the difference likely to be due to the creation of microconduits in the skin by successive applications of MNAs, because in the second experimental condition only a post-burn measurement was taken. The impact of any mechanical failure can also be excluded as there was no evidence of damage to the MNA after six repetitive insertions and removals (Figure 4.10, D). Although not evaluated at present, the oxidative peak with the lower magnitude, evident at 0.23 V also seems to be supressed following the burn (Figure 4.10, A and B).

To determine whether an electrochemical waveform as found here, would hold a diagnostic value, the impact of the burn on the skin was measured at progressive distances away from the burnt skin site. The representative DPV traces shown in Figure 4.10, E indicates a trend where, as expected the oxidative response at 0.69 V was severely attenuated at the burnt skin site (red line). Interestingly, the effect of the burn was still evident at a non-burnt site that was 1 mm distant to the burn skin site (blue line). However, measurements taken at a site 10 mm distant to the burnt skin site revealed an oxidative response comparable to that of the non-burnt skin (black line). On analysis of the peak area, there was no significant difference between the burnt and 1 mm distant skin sites ($p = 0.0692$); whereas the 10 mm site produced significantly higher responses ($p < 0.05$) compared to that of the burnt skin site and the 1 mm distant site, with a mean difference of 3.245 nC and 2.746 nC, respectively (Figure 4.10, F). The mean responses at the 10 mm distant site was further ~270 % higher, because in these experiments PBS was allowed to diffuse into the skin for a longer period of time (i.e. both before and after the burn was induced). This further validates the claim for burn induced suppression of the oxidative response at 0.69 V and, further

indicates that an equilibrium had not yet been established for the oxidative responses seen. Collectively, these results show that the nanocomposite MNA's based electrodes developed here can efficiently function as a transdermal biosensor.

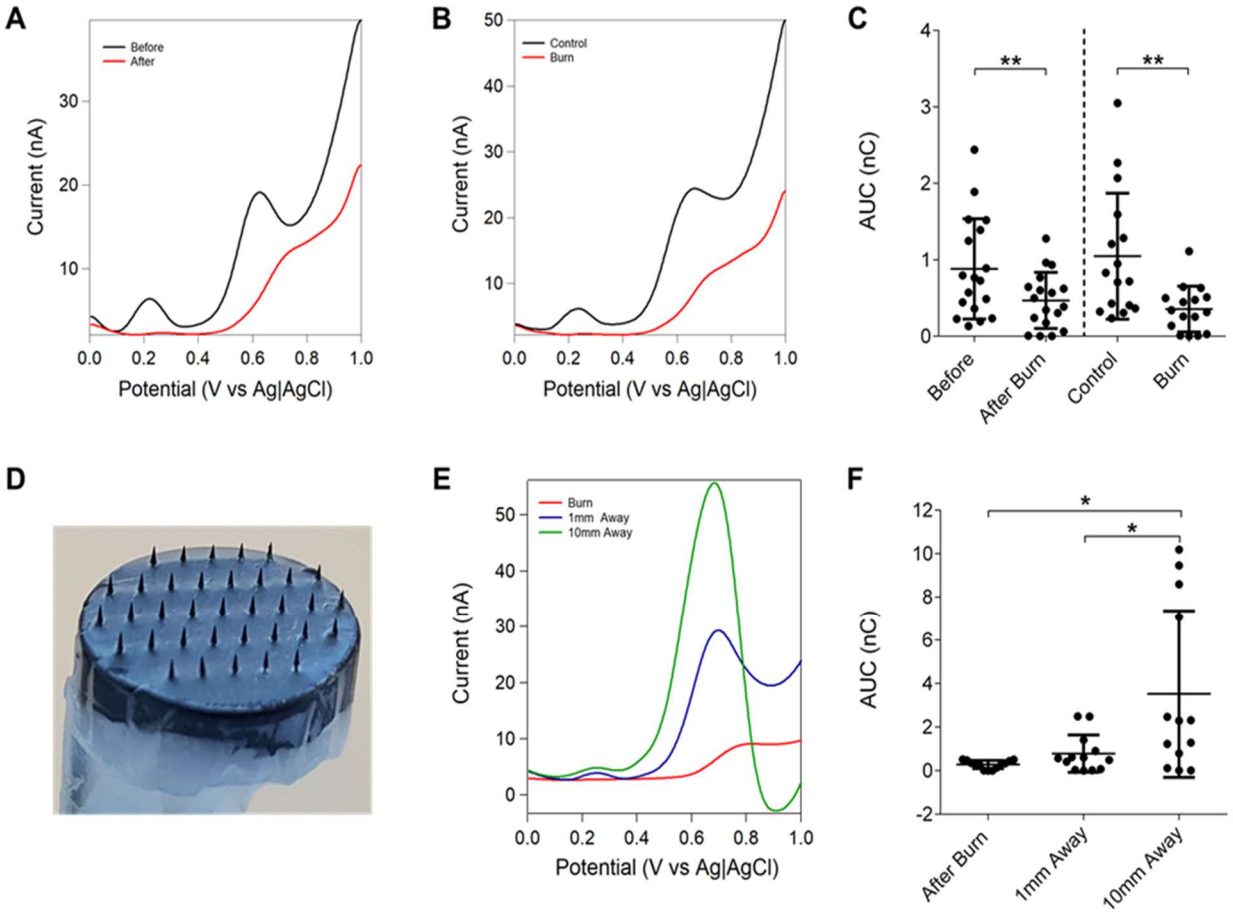

Figure 4.10. Burn wound model. (A) Typical DPV responses for before and after burn on the same skin area (B) Typical DPV response for a skin burn and an adjacent control (non-burn) skin area. Both traces show an attenuation of response for both oxidative peaks at 0.23 V and 0.69 V following the burn (red lines). (C) AUC of the oxidative peak at 0.69 V was significantly attenuated following thermal injury (**$p < 0.01$ by two -tailed paired t-test) under both conditions above. (D) Digital photograph of a MNA after 6 times of repeated insertion and removal, showing no evidence of mechanical failure. (E) Typical DPV response obtained when measuring specific distances away from the edge of the burn site (F) Differences in peak area at 0.69 V, measured at progressive distances away from the burn site. No significant difference was found between the burn site and 1 mm away, but significant differences exist between sites at 1 mm and 10 mm as well as the burn site and 10mm distant site (*$p < 0.05$, repeated measures one-way ANOVA with Tukey's HSD test). (n = 5 animals)

4.5 Discussion

By adopting a facile fabrication strategy for both composite processing (i.e. solvent casting) and MNA fabrication (micromoulding), novel electrochemical MNA based electrodes have been successfully developed from PLA/*f*-MWCNT composites. These nanocomposite MNA electrodes were directly connected to an electrochemical analyser for the first time as bulk electrodes, without any surface modifications and evaluated for their potential as a transdermal biosensor. Initially, on analysing the efficiency of the fabrication strategy by SEM, it was found that MNA's could be formed consistently with a high structural fidelity. However, on close inspection of the morphology of the nanocomposites MNA's (SEM, Figure 4.3, E-F), numerous clusters were evident. The formation of these clusters can be attributed to localised aggregation of CNT's during the solvent evaporation process[198,199]; which in turn, may also give rise to some CNT-free regions depending on the loading[199]. Such morphologies have a significant impact on the electrical and mechanical properties of the composites. In relation to solvent casting, this is due to a strong localised interaction between the CNT's and therefore the effective volume fraction of CNT is higher compared to that of a homogenous network[199]. The high CNT loading as used here typically produces a vastly agglomerated network. However, this may have a positive impact on conductivity, as contacts between CNT's can be improved once the percolation network has been formed. Additionally, the use of compressive forces to form the MNA's can also be advantageous in improving the conductivity of the MNA's; as evidence suggests that application of compressive forces can impart a certain degree of mobility to the CNT's in a composite, thereby improving conductivity by enhancing the interaction and contacts between the CNT's[199,201,202]. In contrast, it is generally accepted that agglomerates will act as stress concentrators of mechanical failure under physical stress, i.e. they prevent effective load transfer between the polymer and CNT's[203]. This may not always be the case, however, as a recent study has found that a mixture of particles of different sizes could help occupy spaces better within the polymer, resulting in a stronger network with better mechanical properties[204]. Usage of *f*-MWCNT's and compressing moulding to form the composite MNA's are two further processes that can enhance mechanical properties[201].

Analysis of the mechanical properties of the nanocomposite MNA's revealed that, at all loadings they could withstand the compressive forces (i.e. AFF) required for skin

penetration. The insertion forces required for a single microneedle is highly dependent on the interfacial area at the tip. Davis *et al*. reported that, for a single microneedle of 25μm tip diameter, the expected insertion force is 0.058N regardless of the microneedle height[73]. Our composite microneedles with a slightly larger tip diameter, at all CNT loadings withstood forces at least 15-fold higher (24-fold higher for 6% composite MNA's). However, there was no significant improvement in AFS for the nanocomposite MNA's at any given loading when compared to that of MNA's fabricated from PLA alone. It is possible that intermolecular forces were weakened when dissolving the polymer. The PLA MNA's used here for comparative purposes were developed from non-solvent casted PLA, as these have been shown to penetrate the skin effectively. In agreement with the literature, the SFS of composite microneedles were considerably lower than AFS[140]. This suggests that MNA's are more susceptible to failure from shear forces than axial forces[76]. Concerning the specific microneedle geometry, the SFS of the nanocomposite and PLA MNA's were higher by ~120% and ~70%, respectively; when compared with MNA's developed from another biodegradable polymer polyglycolic acid (PGA) with a similar height and base diameter[140]. However, only MNA's with a CNT loading of 6 wt% produced higher SFS forces with reference to PLA. This further supports the notion that dissolution of the polymer may have weakened intermolecular forces. The higher AFS and SFS for MNA's incorporating a CNT loading of 6 wt% are most probably a result of enhanced matrix stiffness and better interfacial interaction provided by the increased *f*-MWCNT loading, since the carboxyl groups can interact via hydrogen bonding with carbonyl groups in the PLA chains[205,206].

Developing an appropriate electrical contact is not only essential to maximise the electrochemical signal transduction but also to enable scalable fabrication of MNA's. Wire bonding onto support structures using conductive epoxy is a commonly employed approach for establishing an electrical contact[49]. Hence, such a strategy was investigated alongside others, as shown in Figure 4.2. It was found that an electrochemical response could only be detected by a coiled-type contact, because it maximised the surface area for capturing charge transferred from the electrocatalytic reactions. As the MNA's were entirely fabricated from the nanocomposite material, it was important to isolate the electrochemical response to the MNA's alone. This was achieved by concealing the supporting base of the MNA's by piercing the microneedles through a layer of Parafilm® and sealing it with the application of heat. Albeit being two orders of magnitude lower, due to the reduced surface area available

for electrocatalytic reactions, an electrochemical response could still be detected from the microneedles alone; indicative of the biosensing potential of the nanocomposite MNA's. In fact, an electrochemical response could be detected from microneedles alone, for all CNT loadings investigated here. However, initial characterisation showed large variations in the electrochemical response between MNA's incorporating the same and different loadings of CNT (Figure 4.5 A and D). This was attributed to a combination of factors, i.e. variation in the amount of the nanocomposite material used to fabricate the MNA's and the corresponding variation in insertion depth of the electrical contact. Therefore, as an effective optimisation step, the amount of the nanocomposite material used to make each MNA was fixed at 0.175g, which consequently achieved a base height of ~2mm, at which point the electrical contact was made. This optimisation resulted in an increase in current towards 1 mM $Fe(CN)_6$, proportional to the loading of CNT's and showed minimal variation between different MNA's. Importantly, on re-analysing the effectiveness of the Parafilm® seal, it was found that the RSD was only slightly lower for unsealed MNA's (10%) in comparison to those that were sealed (12%). This confirms that the seal was effective, however the higher RSD between MNA's could be a result of larger microtears in the Parafilm® caused by the penetration of microneedles or an uneven coverage of the seal along the length of microneedles/base of the MNA even with the application of heat. It was also found that, for some MNA's incorporating 3 wt% of CNT, a measurable electrochemical response could not be detected. This is in line with the previous literature indicating that at least 3 wt% of CNT was required to initiate conductivity in solvent casted CNT/PLA nanocomposites[171]. A major finding derived from evaluating the current response at 1V and the capacitive current between different loadings, is that the RSD between MNA's progressively decreased as the % loading of CNT increased. This can be explained on the basis that past the percolation threshold of PLA (reportedly at values > 3 wt%), there is enhanced interaction between the CNT's in the composite[171,184]. As a result, the effect of heterogeneity (causing electrochemical signal variation) maybe be overcome at a higher loading.

As the characterisation results collectively point towards the better electrochemical performance of MNA's incorporating 6 wt% of CNT's, they were used for electrochemical quantification of AA. DPV showed an asymmetric anodic peak; indicative of irreversible oxidation of AA at a low potential of ~0.320 V, with a LOD of 164.38 μM. The oxidation of AA is reversible producing dehydroascorbic acid; but, this is unstable and rapidly

undergoes a salvation reaction producing non-electroactive 2,3-diketogulonic acid[197]. Hence, the overall reaction is described as irreversible. Moreover, the final product of this reaction can readily absorb onto the electrode surface; resulting in fouling[197]. As CNT's are effective in reducing the overvoltage for electrochemical reactions, the oxidative peak observed here was at lower potential that those reported previously by researchers using unmodified platinum (Pt) and carbon paste working electrodes; (at 0.530 V and 0.470 V, respectively)[207]. Although their LOD was lower, at 87 μM for the Pt and 20 μM for CP electrodes, the LOD achieved by nanocomposite MNA's were remarkable (164.38 μM); considering that bulk composite-based electrodes in a MNA format have been connected to an electrochemical analyser for the first time. In comparison, quantification of AA by amperometry using the MNA's produced a more stable step wise increase in current based on the concentration analysed with a lower LOD at 16.79 μM. The RSD between MNA's were also lower at 12% for amperometry in comparison to 24% by DPV and importantly, comparable to the variation observed during their characterisation. Hence, it is possible to normalise the response from the MNA's. Nevertheless, these results show that the nanocomposite MNA's are fit for biosensing purposes.

Electrochemical measurements made in the skin validated our MNA's for transdermal biosensing purposes. With the diffusion of PBS, the nanocomposite MNA's were able to detect distinct oxidative species in the skin at specified potentials of ~0.23 and ~0.69 V. The voltammograms recorded over a period of time showed that the concentration of these oxidative species increases over time. This is because, the lateral diffusion of PBS into the skin helps establish a concentration gradient, that allows passive movement of intra or extracellular oxidative species, on to the electrode surface, that are then oxidised at a specified voltage. As shown in Figure 4.9, B; the rise in concentration was prominent for the oxidative species detected at a potential of 0.69 V. Analysis of this peak, revealed a linear relationship, though it can be assumed that a steady state equilibrium will be established over time. However, further recordings did not ensue at this time, as the skin was maintained to represent conditions *in vivo* for further experimentation. Importantly, this electrochemical signature comprising both oxidative species were readily identifiable across all samples measured. But there existed significant variation between the animals. The implication of such variation is that, it may be difficult to assign a threshold value that could help differentiate between normal and pathological conditions.

The established signature waveform may hold potential diagnostic value in addressing skin-related wounds and injuries. For example, early recognition of burn wounds that may not heal and scar will inform a definitive decision on surgical intervention, improving final functional and cosmetic outcome. Using the MNA developed here, it was initially assessed whether an artificial burn can induce changes to the signature waveform. This showed significant suppression of the oxidative peak at ~0.69 V that was unbiased by experimental conditions (Figure 4.10). However, tissue damage, denaturing and cross-linking of proteins are factors that might contribute to the attenuation of the response at 0.69 V. The diagnostic potential of the signature waveform was further validated, as the effect of the burn could be measured at progressive distances away from the burnt skin site. These results collectively indicate that the nanocomposite MNA's can effectively discern dynamic changes in the skin. Thus, it proves the excellent potential of these MNA's to be turned in transdermal biosensors.

4.6 Conclusions

In this chapter, the utility of nanocomposites produced from PLA/*f*-MWCNT's via simple solvent casting process to be turned into electrochemical MNA's were investigated. Micromoulding coupled with manual compression was found to be effective in forming with MNA's consistently with high structural fidelity. The fabrication steps discussed here are simple and easy to scale up, with further adaptation possible using compression moulding or hot embossing technique allowing rapid prototyping capabilities. A maximum loading of 6 wt% was found tenable with the current fabrication method. Mechanical strength and electrochemical behaviour of the MNA's were evaluated with reference to MNA's incorporating different loadings of *f*-MWCNT's and both properties were found to be optimal at the highest loading i.e. 6 wt%. Consequently, these MNA's were used for electrochemical quantification of AA by DPV and amperometry. The nanocomposite MNA's were able to distinguish varying concentration of AA using both techniques; achieving detection limits of 164.38 µM for DPV and 16.79 µM for amperometry. *In situ* measurements in the skin, followed by evaluation of a burn wound model showed that the MNA's can dynamically monitor electrochemical changes within the skin microenvironment and therefore can function effectively as a transdermal biosensor. Interestingly, an electrochemical signature comprising two distinct oxidative species were identified from freshly excised porcine ear skin. Characterisation of the oxidative species may be necessary as they may not only relate to skin pathologies (as shown with the thermal injuries) but can also provide crucial information on electrochemical interferants for biosensing applications.

4.7 Further work

The nanocomposite fabricated MNA's discussed in the work are effective at a CNT loading of 6 wt%, however further optimisation is needed to improve their electrochemical behaviour to reduce the resistive behaviour as seen with their CV; thus, improving the sensitivity of these electrodes further. This is crucial as quantitation of clinically relevant analytes and biomarkers maybe challenging due the their sub-micromolar physiological concentrations.

Chapter 5. Optimisation of MNA's electrochemical behaviour

5.1 Introduction

A major aspect of improving the functionality of the MNA's developed previously, is careful evaluation of the processing methods to improve the dispersion of the CNT's within the nanocomposites. To date, controlled dispersion of CNT's within polymeric matrices remains a challenge due to the strong van der Waals interactions associated with CNT aggregates[208]. Functionalised CNT's are proven to improve the interfacial interaction with the polymeric matrices[96], but the stability of their dispersion during processing is dependent on optimal sonication parameters. However, there exists an inverse relationship between high energy sonication and final functional properties, which is associated with structural damages to the CNT's[209]. Therefore, the use of surfactants to aid the dispersion of CNT's and further stabilise their suspension in solvents/polymeric matrices provides an attractive optimisation step towards improved nanocomposite properties. As discussed in *section* 4.1.2.2 and 4.1.2.3, the functional groups can not only influence the mechanical properties of the composites but also, they have a significant impact on electrical properties. The percentage loading of CNT and the aspect ratio of the nanotubes can also play a significant role in electrochemical properties. This chapter investigates the optimisation of electrochemical behaviour of the MNA's in relation to the factors described above; as shown in the schematic in Figure 5.1.

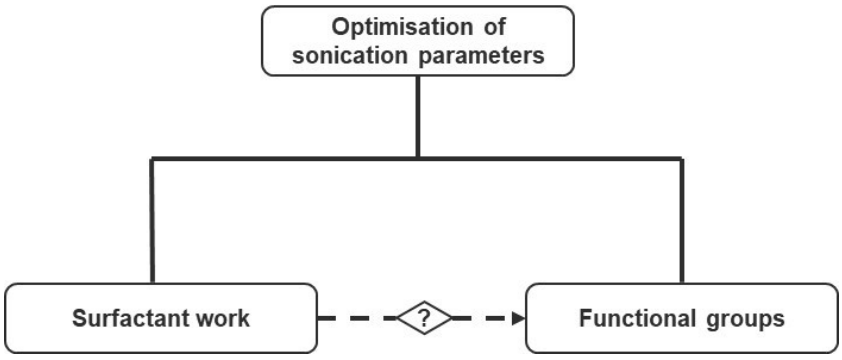

Figure 5.1. Schematic of investigation. Sonication parameters will be optimised initially. These parameters will be applied to the surfactant work and if successful, the developed method will be translated to produce nanocomposite MNA's using MWCNT's with different functional groups. Each process will be compared against the base MNA (i.e. 6 wt% bath sonicated).

A brief discussion concerning the specifics of each these aspects is given in the following subsections.

5.1.1 Optimisation of sonication parameters

Although nanocomposites are extensively researched, evaluation of their final properties have given results far off the theoretical predictions[210]. Central to this issue is effective dispersion of the CNT's in the nanocomposites. This is often achieved through high energy sonication, however a consensus on the parameters used has not been reached. This is largely due to the fact that, the sonication parameter needs to be optimised for the type and aspect ratio of the CNT, and most of the studies claiming effective dispersions are based on qualitative observation through SEM and TEM[211,212]. Composite processing requires careful monitoring of the CNT dispersion during the fabrication process and this is often met with challenges due to the limitations associated with appropriate instrumentations and the reliability of existing methods[213]. Consequently, the sonication parameters applied by the researchers have varied significantly.

Effective dispersion of CNT is dependent on the following conditions: (1) the energy supplied to impart shear stress via the medium used (i.e. solvent) must be greater than the binding energy holding the aggregates together and (2) the supplied energy must be lower than that required to break the CNT's, therefore retaining their structure[156]. Though bath sonicators can be used adequately to produce good dispersion as seen in the previous chapter, they are inefficient for industrial applications due to the long processing times and the uneven spread of ultrasonic energy throughout the sonic bath. The energy required varies, depending on the type of the nanotubes (SWCNT > MWCNT), the diameter of the nanotubes (larger diameters requiring less energy) and the functional groups present (reduces the energy required)[214]. With the aid of surfactants, the energy required can be as high as 50,400 $J.ml^{-1}$ if SWCNT's with low diameters are used, whereas for MWCNT's it can be as high as 8,228 $J.ml^{-1}$; with a sonication time of 120 mins in both cases[215,216]. Standard lab based sonicators operate at 20 – 37 kHz with a power output up to 280 W[208]. In comparison, commercial probe sonicators has a variable amplitude setting from 1 – 100% and the power adjusts between 100 – 1500 W[217]. By design, the probes are attached to a base unit which propagates energy down to a tapered tip, with a base dimeter ranging from 1.6 – 25.4 mm, depending on the volume to be processed. Consequently, the energy dissipates at high

intensity from the tip of the probe. However, the probe sonicators can generate heat rapidly, so there is a need for the sample to be kept cold. Recent research using probe type sonicators have shown that the time required for dispersion can be reduced to as little as 8 mins depending on the amplitude settings[218].

5.1.2 Surfactants

Surfactants are amphiphilic molecules (containing both polar and non-polar groups), that adsorb at the interface between bulk immiscible phases, (i.e. solution and particles in this case) to reduce the surface tension[219]. The polar head group constitutes the hydrophilic component, while the tail groups are the hydrophobic regions. They are classified as anionic, cationic or non-ionic based on the charge on their head groups. The two characteristics behind their utilisation as stabilising agents for colloidal dispersions is associated with adsorption at the interface and self-accumulation into supramolecular structures[220]. This in turn is governed by the characteristics of the particles, the surfactant molecules and the solvent[220]. For ionic surfactants, their adsorption is based on coulombic interactions between the charges on the head group and the solid surface. Non-ionic surfactants on the other hand, adsorbs via strong hydrophobic interactions between the solid surface and the hydrophobic tail. Ultimately, the non-covalent interaction with surfactants allows preservation of the dispersion state for a long period of time.

5.1.2.1 Stabilisation mechanism

In a typical process, the high local shear forces created by ultrasonication begins to the exfoliate the CNT bundles; creating gaps and spaces for the adsorption of surfactant molecules which ultimately propagates along the length of the CNT's and separates them into individual tubes in an unzipping mechanism[221]. These dispersions are stabilised by electrostatic or steric repulsion for ionic and non-ionic surfactants, respectively. The surfactants can adsorb on the surfaces of the CNT's in a number of ways, with their head down or tail down and as a monolayer or a multilayer[222]. Once the surfactant is adsorbed on to the CNT surface, they can self-organise to form micelles at concentrations above the critical micelle concentration (CMC)[220,222]. This self-organisation on the CNT surface can be in a specific format i.e. perpendicular orientation, parallel or perpendicular half cylinder orientation along the tube axis and could also be completely random[223]. Despite the intensified research in this area, a definitive mechanism of surfactant arrangement around

the nanotubes have not been identified. One of the critical factors that can influence the mechanism and therefore the dispersion of CNT's in aqueous media is the concentration of the surfactants. In general, the surfactant concentration needs to be above the CMC as well the CNT concentration[224,225]. When dispersing CNT's, the CMC is thought to be higher than in neat surfactants, because a certain amount of surfactants will ready adsorb on to nanotubes[226]. However, recent studies have suggested that, the surfactant concentration used should be just sufficient to coat the surface of the CNT's, as any excess amount can in fact decrease the dispersion of the CNT's[227,228]. This is because at high concentrations, the surfactants form micelles that grow in size, forming multilayers on the CNT surface as the concentration of the surfactant is increased for the same CNT concentration. This is resultant of the interaction between groups of the same polarity. Consequently, the part of the surfactant molecules extending into the liquid phase from the large multilayers can interact with that of the neighbouring CNT's[227]. This form of bridging causes flocculation of CNT's and it been found to occur at concentrations typically 10 times higher than the CMC[218]. Aside from surfactant concentration, the characteristic structure of each surfactant dictates the dispersion efficiency. For example, surfactants with separated aromatic ring structures as in sodium dodecylbenzenesulfonate (SDBS) increases the hydrophobicity and promotes π-π interactions with the CNT surface; resulting in stronger binding and higher dispersion efficiency. Similarly, as the alkyl chain length increases, so does their hydrophobicity and resultantly, the surfactant tendency to adsorb onto CNT surfaces[220,222]. This increases dispersion efficiency. Generally, when the aromatic ring factor and the alkyl chain length factor compete, the surfactants with the former dominates[227]. There are exceptions, however. For example, although cetylpyridinium chloride (CPyCl) has an aromatic ring, it is less efficient than SDBS because of its polar head group possessing a cationic charge[218].

Although research into surfactant aided dispersion and stabilisation is well established for water-soluble systems as above; more work is being increasingly carried out for dispersions in organic solvents, having recognised the potential for easily processed multifunctional polymeric nanocomposites. Organic solvent-based systems are different to water-based systems in the sense that, CNT's are wetted by the solvents and are less likely to self-assemble into aggregates[220,222]. However, as seen in the results from the previous chapter (*section* 4.4.2), a combined approach that had involved sonication in an organic solvent still produced an aggregated sample. The dispersion maybe improved to a certain

extent by moving from a bath type sonicator to that of a sonic probe, but it may still be inadequate. This is highlighted by the fact that in aqueous surfactant solutions, the maximum CNT loading that can be dispersed effectively is only 1.4 wt%[229] and the developed nanocomposite MNA's have a CNT loading of 6 wt%. Therefore, by implementing an approach that involves *f*-MWCNT's being dispersed in an organic solvent (chloroform) that contains a high efficiency surfactant might help disperse a higher volume fraction of CNT.

The choice of the surfactant must not only be concerned with dispersion efficiency but should also not limit the final functional properties of the nanocomposites. Most of the studies of the sort are directed towards improvement in thermo-mechanical properties of the composites[222]. With regards to the development of polymeric nanocomposites by solvent processing, typically non-ionic surfactants are used (i.e. Titron X-100, Tergitol NP-7, Polyoxyethlene lauryl, Span 85 (sorbitan trioleate) because of their excellent dispersive properties and in all cases improved mechanical properties have been reported at low CNT loadings[230–233]. Some promising results have also been reported in these studies for conductivity. However, at high concentration of the surfactant, the percolation threshold had increased, and a poor conductivity have been observed. This is resultant of the long hydrophilic tail and the bulky character of the non-ionic surfactant, that increases the distance between tubes, resulting in a lack of contact[222]. Sun *et al.*, employed a gemini surfactant, 6,6-(butane-1,4-diylbis(oxy))bis(3-nonylbenzenesulfonic acid) to disperse MWCNT's in toluene and subsequently develop nanocomposites with polystyrene (PS) matrices[224]. They showed that, with the addition of this surfactant, conductivity can be increased up to 800 times when compared to neat PS/MWCNT matrix. Conventional anionic and cationic surfactants have also been utilised to produce nanocomposites, however similar to that of the non-ionic surfactants it is not obvious whether a composite with perfectly dispersed CNT's will reduce the percolation threshold, resulting in enhanced conductivity[222,234]. As described before, the characteristics of the surfactants will play a crucial role alongside their respective concentrations. It has been postulated that a dynamic equilibrium exists between adsorbed and free surfactants in the dispersions that is sensitive to the surfactant concentration[235]. The excess surfactants are difficult to remove and once processed it severely impairs the performance of the composites/devices. Considering this issue, a key factor that can be manipulated is the Krafft temperature (T_K), the minimum temperature at which surfactant forms micelles. Using the cationic surfactant

cetyltrimethylammonium bromide (CTAB – a cationic surfactant) as an example, it has been recently shown that when processing the surfactant solution below its T_K, micelle formation can be supressed completely and only a fraction of the surfactant can remain in the solution below the CMC[228]. The excess can be precipitated out as crystalline needles by centrifugation or standing the solution at temperatures less than T_K. This critically solves the issue of finding an optimal surfactant to CNT ratio, as irrespective of the concentration of surfactant used, no additional surfactant remains in solution than what is required for dispersing and stabilising the suspension. Aside from this, the study also pointed to better exfoliation of the nanotubes below their T_K. This offers an attractive strategy for processing nanocomposites, without the negative impact of the surfactants.

5.1.2.2 Characterisation of CNT dispersion

Analysing the quality of dispersion whilst processing plays a significant role in the optimisation process. Commonly, researchers have employed a combination of methods to assess various aspects of dispersion. This involves particle or CNT cluster size analysis, Zeta potential (ζ) measurements and UV-Vis absorbance readings. Characterisation of CNT suspension by particle size analysis based on dynamic light scattering (DLS) techniques have been used extensively in the literature. However, they assume the particles as spherical in shape, and report an average value based on hydrodynamic diameter that are in the micrometre range[213]. However, without proper dispersion and stabilisation (resulting in particle sedimentation); it is difficult to estimate the particle size in a dispersion with accuracy. ζ potential is the potential difference between the mobile dispersion medium and the stationary layer of dispersion media attached to the particle[236]. Cationic surfactants will have a positive potential, whilst a negative potential can be found for anionic surfactants. In principle, a large ζ potential is an indicator of the binding strength of surfactants, and particles coated with surfactants with a magnitude of change > 30 mV reflects long-term kinetic stabilisation[218]. As ζ potential scales with the amount of surfactant adsorbed on to the dispersed particles, it is a useful way of analysing the effect of different concentrations[222]. Another measure of assessing dispersion quality is by UV-Vis-NIR spectroscopy. Unlike bundled CNT's, dispersed nanotubes are highly active in the 200 – 1200 nm wavelength region due to 1D van Hove singularities and hence UV-Vis can be applied to detect individual particles by relating the specificity of absorption at a given wavelength to that of

the concentration of the nanotubes[213]. Studies employing this approach have evaluated multiple positions on the spectra, however the absorption spectra for MWCNT with individualised CNT's exhibit a specific peak between 250 – 265 nm, which has been successfully utilised in many studies to quantitatively assess the amount of dispersed CNT's[237–239].

5.1.2.3 Electrochemical behaviour

Several authors have reported the benefits of using surfactants in electrochemical reactions. Hoyer *et al.*, reported that the addition of cationic surfactants cetyl trimethyl ammonium chloride (CTAC) and cetyl pyridinium chloride (CPyCl) into the electrolyte solution forming micellar media can significantly reduce electrode fouling during the voltammetric detection of serotonin by preventing the adsorption of its oxidation products on to the electrode surface through electrostatic repulsion[240]. This effect can indeed be translated to surfactant modified electrodes. Carmen *et al.*, showed that carbon paste electrodes (CPE's) modified by anionic surfactants at the submicellar concentrations can increase redox behaviour and the reversibility of the electrode processes towards epinephrine and norepinephrine[241]. Whereas, CTAC modified electrodes could effectively stabilise electrochemical reaction intermediates for homovanillic acid, which proved to be an excellent strategy for studying their reaction mechanisms[241]. More recent research has shown that CTAB-modified GCE's increase the rate of oxidation and reversibility of the electrochemical process for routine monitoring of a therapeutic drug, 6-Mercaptopurine for the treatment of acute lymphocytic leukaemia; whilst it also enhanced stability, sensitivity and selectivity towards the determination of a toxic drug 4-aminoantipyrine[242,243]. These results ultimately signify the utility of surfactants from an application perspective.

5.1.3 MWCNT functional and structural evaluations

The effect of different functional groups was briefly summarised before under appropriate *sections* (4.1.2.2 and 4.1.2.3). In this chapter, -COOH, -NH_2 and -N_2 functional groups on the MWCNT were compared for their mechanical properties and electrochemical behaviour. Functionalisation of MWCNT's with –N_2 induces pyridinic and pyrrolic functionalities, which increase the specific capacitance of the electrodes, while the quaternary nitrogen and pyridinic-*N*-oxide improve the electron transfer processes associated with the reversibility of redox processes at the electrode surface[244]. Hence, N_2-

functionalised MWCNT's may possess superior electrochemical properties when compared with the other surface functional groups. Alongside these investigations, the influence of varying length and diameters of MWCNT's on MNA fabrication, mechanical and electrochemical properties were further investigated.

5.2 Aims and objectives

This chapter aims to investigate multiple aspects associated with optimising the electrochemical behaviour of MNA electrodes. These include optimising the dispersion of *f*-MWCNT's by improving the sonication conditions and by the incorporating of surfactants. These optimisations were carried out using the developed composition for MNA's, i.e. 6 wt% *f*-MWCNT. Additionally, the influence of different functional groups, alongside varying dimensional parameters of MWCNT's were addressed in terms of MNA fabrication, mechanical and electrochemical properties.

The objectives of this chapter are to:

1. Quantitatively determine an optimal time of sonication for dispersing the nanotubes and investigate the improvements in mechanical and electrochemical properties.
2. Using the optimised sonication parameter, analyse the influence of two cationic surfactants: (1) CTAB and (2) CPyCl on mechanical and electrochemical properties of the MNA.
    a) Analyse CNT dispersion above and below the T_K of the surfactants.
    b) Evaluate different concentrations of the surfactants
3. In relation to differing dimensional parameters and functional groups on MWCNT:
    a. Assess the limit of fabrication using $–N_2$, $–NH_2$, –COOH functional groups with differing dimensional parameters. For ease of comparison, existing –COOH functionalised MWCNT's with a length (*l*) of 10 – 30 μm and outer diameter (O.D) of 20 – 30nm, was compared against all other functional groups with a *l* of 1 – 12 μm and O.D < 20 nm (including a shorter version of –COOH functionalised MWCNT's)
    b. Optimise the processing conditions to address the fabrication limit.
    c. Compare mechanical and electrochemical behaviour.

5.3 Materials and methods

5.3.1 Optimisation of dispersion by sonic probe

In this chapter, the bath sonicator was substituted for an advanced probe type sonicator (model: Q705, Fisherbrand™, Loughborough, UK) using a solid 12.7 mm diameter probe, operating at a power output up to 700 W and a frequency of 20 kHz. Optimisation of the sonication assisted dispersion was carried out using the previously established composition, i.e. 6 wt% *f*-MWCNT/PLA (referred to as base MNA's here in). In order to keep the sample cold whilst sonicating, an ice bath prepared from dry ice and acetonitrile was used. The sonic probe was inserted half way to ensure even circulation of the sonication energy, with its intensity set at 100% amplitude. The sonication energy was delivered in pulses of 20 sec with a 30 sec rest period in between to further prevent overheating. Different sonication times was applied ranging from 2 – 20 mins and the dispersion efficiency was monitored immediately using a UV-Vis spectrometer (Lambda 45, Perkin Elmer, UK) and laser diffraction particle size analyser (Mastersizer 3000, Malvern Instruments, Ltd, UK) equipped with a dispersion unit. For UV-Vis analysis, the original samples were diluted by a factor of 2000 in ice cold chloroform and a wavelength scan performed in triplicates between 240 – 700 nm at 240 nm/s for three independent samples. For particle size analysis, the parameters inputted into the software were: refractive index of 2.5, absorptive value was 0.99 and a density of 2.6 $g.cm^{-3}$. To carry out the measurements, a 20 µl aliquot was added to the dispersion unit, which was set at 1500 rpm, containing 50 ml of chloroform. The dispersion unit kept the sample suspended and homogenised, that is, continually circulated around the measurement zone. This gave reliable measurements of particle size, as the dispersion had not been stabilised by surfactants at this stage. The measurements were completed in triplicates using three independent samples. Nanocomposite MNA's were fabricated using the composites prepared with different sonication times (i.e. 2, 4, 8, 12, 16 and 20 mins) and evaluated for their mechanical strength (*section* 5.3.4) and electrochemical behaviour (*section* 5.3.5). Thus, correlating the characterisation results with physical data.

5.3.2 Surfactant assisted dispersion

Using the optimal sonication time (i.e. 3 mins), the dispersion efficiency of two cationic surfactants, CTAB and CPyCl; was analysed. They were chosen based on their

dispersive character and electrochemical behaviour. Initially, the effect of T_K on the dispersion of –COOH functionalised MWCNT was analysed. The T_K of both surfactants were 25°C. The aforementioned dry ice bath (*section* 5.3.1) was sufficient to keep the temperature between below 5°C. To maintain the temperature between 25 – 30°C, a standard ice bath was utilised, and the pulse period was shortened to 10 sec, with a longer rest period of 1 min. For analysis, UV-Vis was utilised as before (*section* 5.3.1), whilst particle size analysis and measurement of ζ potential were completed using dynamic light scattering (DLS, Zetasizer Nano, S90, Malvern Instruments, Ltd, UK); as the solution was now stabilised with surfactants. For particle size analysis and ζ potential measurements the inputted software parameters were the same as for the Mastersizer (*section* 5.3.1), however, the temperature was adjusted to 5°C and 25°C for measurements above and below the *T*K. A 12 mm O.D. glass cell was used for particle size analysis and for ζ potential measurements a gold-plated-electrode capillary cell (DTS1070, Malvern Instruments, Ltd, UK) was inserted into the aforementioned glass cell. Here, the samples were diluted as described previously for UV-Vis analysis (*section* 5.3.1). The concentration of both surfactants used here was 10 mM.

Following the determination of temperature effects on CNT exfoliation and stabilisation, the influence of different concentrations was analysed (i.e. 1, 5, 10 and 15mM) at the optimum temperature (0 – 5°C) to determine an optimal amount of surfactant for effective dispersion of CNT's. Analysis of dispersion efficiency for each surfactant concentration was analysed as before using UV-Vis, particle size and ζ potential measurements. Nanocomposites were then prepared using the different surfactant concentrations and assessed for their mechanical and electrochemical behaviour.

5.3.3 Evaluating length and functional groups

In addition to the long (l = 10 – 30 μm, O.D = 20 – 30 nm) –COOH functionalised MWCNT's used to fabricate the base MNA's, shorter versions of the nanotubes (l = 1 – 12 μm and O.D < 20 nm) with same and different functional groups (i.e. –COOH, $–N_2$, $–NH_2$), were used to analyse the influence of MWCNT dimensions and functional groups on the mechanical strength and electrochemical behaviour of the nanocomposite MNA's. As initial characterisation, the limit of fabrication was assessed by determining the maximum CNT loading that can be incorporated with the optimised sonication parameters to produce

nanocomposite MNA's using the shorter nanotubes with different functional groups (i.e.–N_2, –NH_2, –COOH). From this characterisation, it was obvious that –NH_2- and –N_2-functionalised MWCNT's required a larger volume of chloroform to promote their dispersion. Therefore, the effect of lowering the concentration from 0.5 wt% to 0.1 wt% and 0.05 wt% on the dispersibility of CNT's was investigated for all compositions including the long –COOH functionalised MWCNT's at equivalent loadings. The dispersion efficiency was quantified in terms of particle size analysis and UV absorbance as detailed in *section* 5.3.1. Using the optimal concentration (i.e.0.05 wt%), the fabrication limit was re-evaluated and the MNA's thus developed were assessed for their mechanical properties and electrochemical behaviour (*section* 5.3.4 and 5.3.5).

5.3.4 Mechanical characterisation

The AFS and SFS of the MNA's were evaluated for mechanical characterisation as previously described (*section* 3.3.3) using a Texture analyser (TA).

5.3.5 Electrochemical characterisation

Using the three-electrode set-up as described in *section 4.3.4*, initial characterisation was carried out by analysing the cyclic voltammetric (CV) response of the nanocomposite MNA's towards 1mM potassium ferrocyanide ($Fe(CN)_6$) in 1M potassium chloride (KCl), across a potential window of 0 – 1V. The electrochemical response was analysed in terms of conductance (at a scan rate of 0.01 vs^{-1}), unless otherwise stated. The electrochemical behaviour for all MNA devices fabricated here was evaluated by amperometry as described previously (*section* 4.3.5), using AA as a model analyte to allow effective comparisons.

5.3.6 Statistical analysis

Data were processed in Microsoft Office Excel 2016, analysed using GraphPad Prism 7 (GraphPad Software Inc., USA) and expressed as mean ± standard deviation. Graphing of electrochemical data was performed using Igor Pro, version 6.0 (WaveMetrics Inc, USA). Where appropriate, statistical differences between groups were assessed using the two-sided Student's t-test, repeated measures and one- or two-way ANOVA with Tukey's post-hoc test for pair-wise comparison. Differences were considered statistically significant where $P < 0.05$.

5.4 Results

5.4.1 Optimising the dispersion of CNT's via probe sonication

The change in particle size upon sonication, hence the de-bundling of CNT aggregates, was monitored by analysing the particle size using laser diffraction particle size analyser (Figure 5.2, A). As more sonication energy was applied to the sample with increasing sonication time, the particle size decreased sharply until 8 mins. The inset table in Figure 5.2, A shows that after 2 mins of sonication 90% of the population was 15.1 μm or smaller, which decreased to 8.3 μm by 4 mins and 4.9 μm by 8 mins. The trend was similar for 50 and 10% of the population. Collating the results from three independent dispersion, these differences were found to be statistically significant ($p < 0.0001$) as shown in Figure 5.2, B – D. This indicates an optimal sonication time between 2 – 8 mins, as further increase in sonication time did not reduce particle size further.

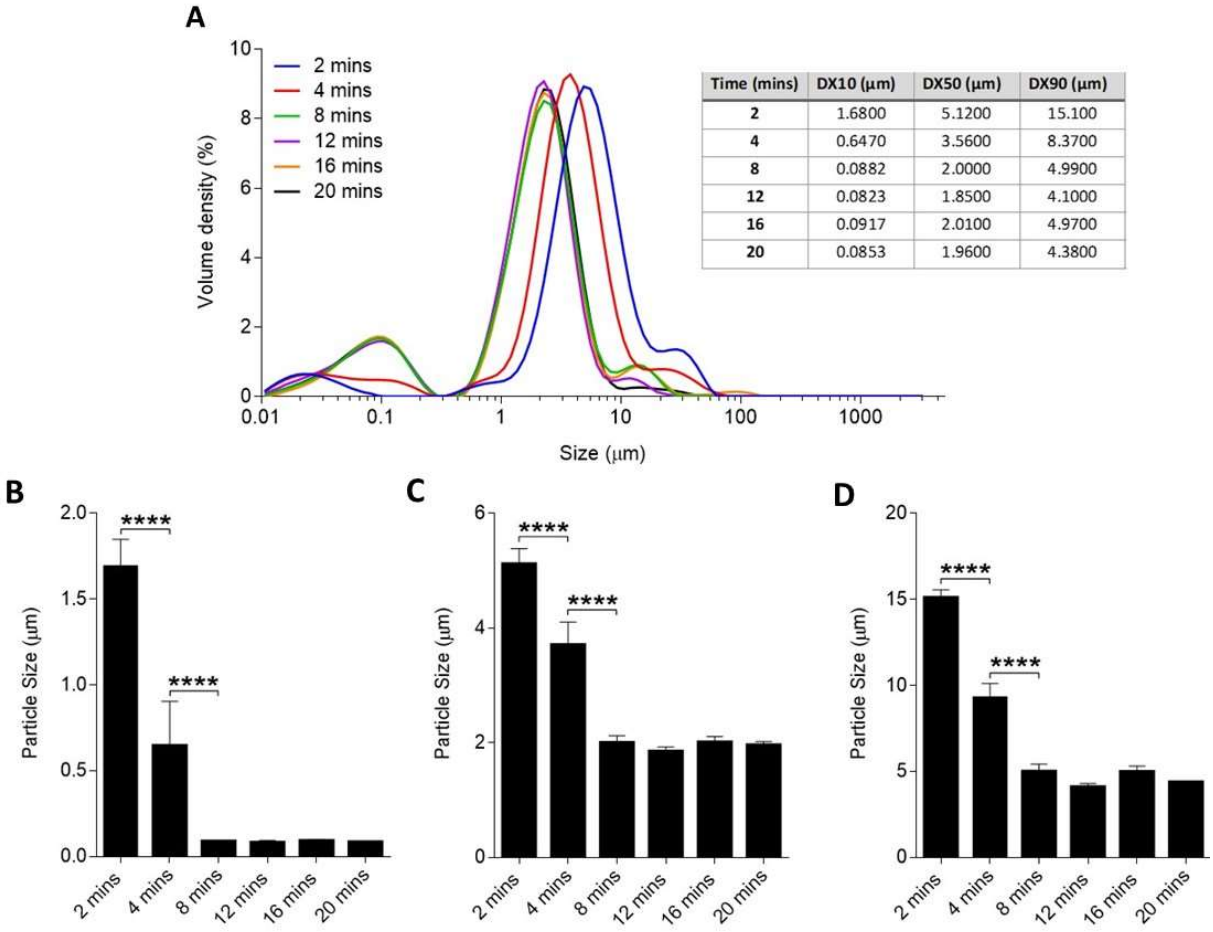

Time (mins)	DX10 (µm)	DX50 (µm)	DX90 (µm)
2	1.6800	5.1200	15.100
4	0.6470	3.5600	8.3700
8	0.0882	2.0000	4.9900
12	0.0823	1.8500	4.1000
16	0.0917	2.0100	4.9700
20	0.0853	1.9600	4.3800

Figure 5.2. Particle size vs sonication time: (A) particle size distribution by volume for CNT's with reference to increasing sonication time. Inset table: DX10 refers to 10% of the population being smaller than the reported size, similarly DX50 and DX90 refer to 50 and 90% of the population being smaller than the reported value. The general trend points towards a decreasing particle size up to 8 mins, thereafter, the change in particle sizes is seen to plateau. Further statistical analysis of the particle sizes according to their distribution is shown in B, C and D; corresponding to 10, 50 and 90% of the population respectively. Collectively, these graphs verify a significant drop in particle size between 2 – 8 mins of sonication for the different population ranges. ****$p < 0.0001$, one-way ANOVA with Tukey's multiple comparisons test. Data represent mean ± SD, $n = 3$.

To confirm the results from particle size analysis, UV-Vis technique was also used. Figure 5.3, A, illustrates the UV-Vis spectra for –COOH functionalised MWCNT dispersed in chloroform with different sonication times. The absorbance of the dispersed CNT solutions shows a maximum at ~260 nm consistent with the literature[237–239]. Evaluation of the peak maximum absorbance at different sonication times from three independent dispersion are shown in Figure 5.3, B. This is seen to increase significantly ($p < 0.0001$) with time, up to 16 mins, unlike the results from particle size analysis. No further increase in individualisation is seen past 16 mins. Additionally, a further comparison was made to bath sonicated preparation, as in previous chapter (i.e. base MNA's). The number of individualised nanotubes present in this sample is significantly lower when compared to any of the probe sonicated samples (Figure 5.3, A-B).

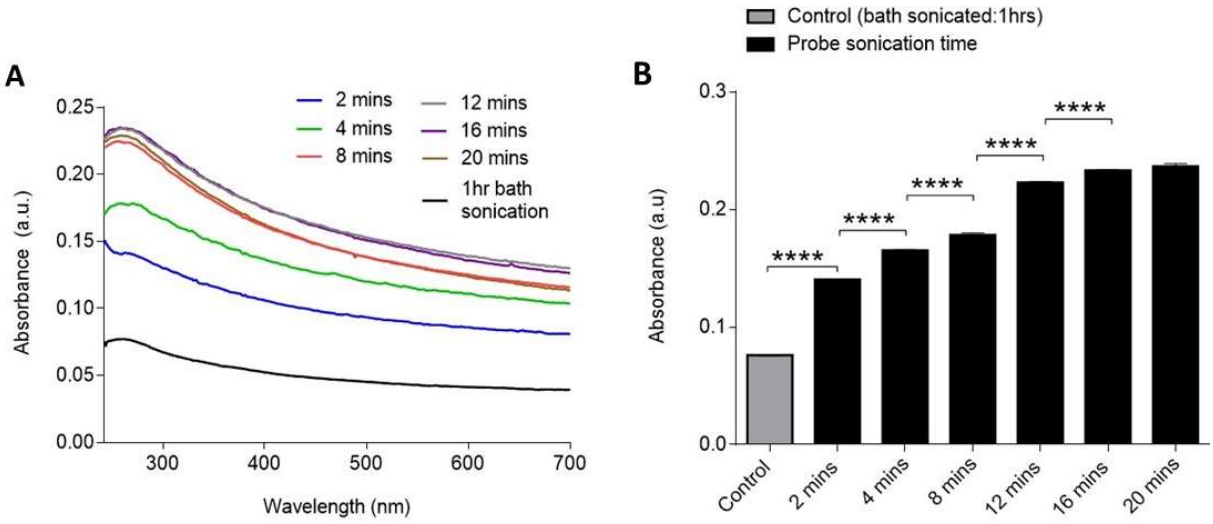

Figure 5.3. UV-Vis spectral analysis: (A) absorbance measured from 240 – 700 nm at different sonication times. The peak observed at ~260 nm corresponds to the amount of individualised CNT's and the peak absorbance is seen to increase with application of increased sonication energy corresponding to the increase in sonication time. (B) evaluation of the peak absorbance at ~260 nm showing significant increases in absorbance, and thus, individualised particles. ****$p < 0.0001$, one-way ANOVA with Tukey's multiple comparisons test. Data represent mean ± SD, *n = 3*.

To corroborate the dispersion characterisation data with physical electrochemical measurements from the MNA's, their response towards 1 mM $Fe(CN)_6$ was evaluated from the respective CV traces at a potential of 1 V (Figure 5.4). The CV traces are not shown here, because they are not different to those seen in the previous chapter (*section* 4.4.4, Figure 4.7); with no redox processes. However, compared to the base MNA, there is a significant rise in current from 3 to 12 mins. Thereafter (i.e. 16 – 20 mins), the current measured plateaued. With probe sonication, in comparison to 2 mins, there was a significant rise in current after 3 and 4 mins of sonication ($p < 0.001$, $p < 0.05$; respectively). Interestingly, there was no significant rise in current between 3 and 4 mins, and nor was there a significant difference between 4 and 8 mins, in comparison with the results seen from particle size and UV-Vis analysis. Following the sharp increase in current at 3 mins, the current gradually decreased with increasing sonication times from 12 to 20 mins ($p < 0.05$). Notably, the MNA

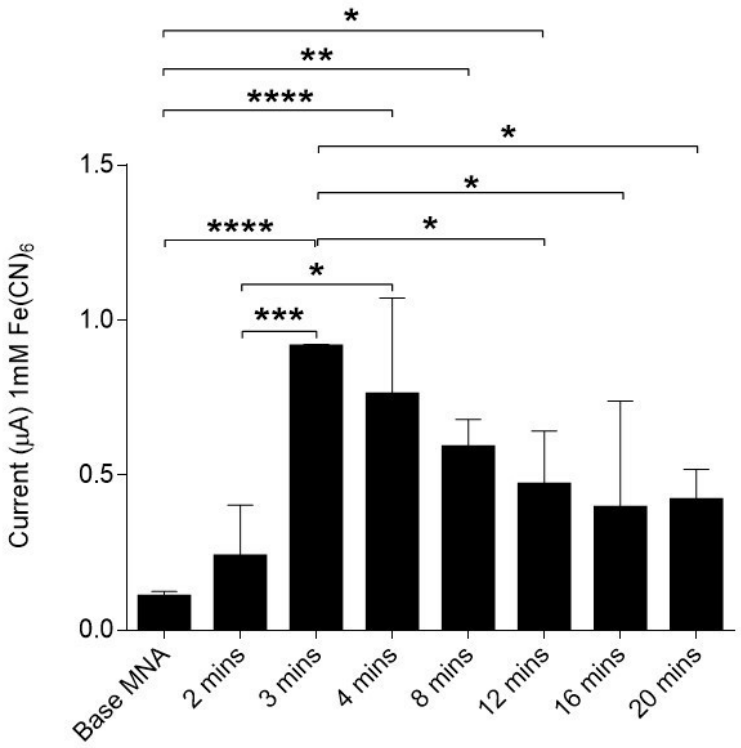

Figure 5.4. Electrochemical response of the MNA's towards 1mM $Fe(CN)_6$ after sonication optimisation: shows the current measured at a potential of 1 V from CV traces (not shown). The general trend shows a rise in current with increasing probe sonication time up to 3/4 mins and followed by gradual decline, stabilising until 20 mins. Compared to the base MNA, a significant increase in current can be seen from 3 mins to 12 mins. A significant rise in current is seen between 2 to 3 mins and 2 to 4 mins, but with no difference between 3 and 4 mins. Post 3 minutes, there is a significant drop in current from 12 to 20 mins. *$p < 0.05$, **$p < 0.01$, ***$p < 0.001$, ****$p < 0.0001$, one-way ANOVA with Tukey's multiple comparisons test. Data represent mean ± SD, $n = 3$.

devices fabricated with a sonic probe-assisted dispersion for 3 mins showed the lowest variation between MNA devices (i.e. relative standard deviation (RSD) = 0.46%). Hence, a probe sonication time of 3 mins was applied universally for the remainder of the studies. Though, it should also be noted that, when processing, the said 3 mins of sonication was applied purely for dispersion. For sufficient intercalation after polymer (i.e. PLA) dissolution into the dispersed medium, sonication was applied for another minute.

Amperometric response of the MNA devices towards varying concentrations of AA was analysed for further comparison (Figure 5.5). Evidently, the probe sonicated MNA devices showed better responses in comparison to the bath sonicated MNA's. The mean average responses obtained from these MNA's were higher by a notable 1340% in comparison to the base MNA. Average RSD for the responses between three devices was 20.14%. The LOD and sensitivity for 3-min-probe sonicated MNA's were 0.51 μM and 6.525 nA. μM^{-1}, respectively; as opposed to the bath sonicated MNA's, with a LOD of 16.79 μM and a sensitivity of 18.04 pA. μM^{-1}. Although a higher amperometric response is seen for the 2-min-probe-sonicated MNA's in comparison to the base MNA's, the difference was not statistically significant. This was due to a large variation in one of the 2-min-probe sonicated MNA devices, producing an average RSD of 38.61% between three devices. Nevertheless, as the LOD and sensitivity were much higher for the 3-min-probe sonicated nanocomposite MNA's, it further validates the reasoning for designating 3 mins as an optimal sonication time for nanocomposite processing. Past 4 mins of sonication, a reduced electrochemical response is seen for the MNA's, however a linear trend is absent; coinciding with the data for conductivity.

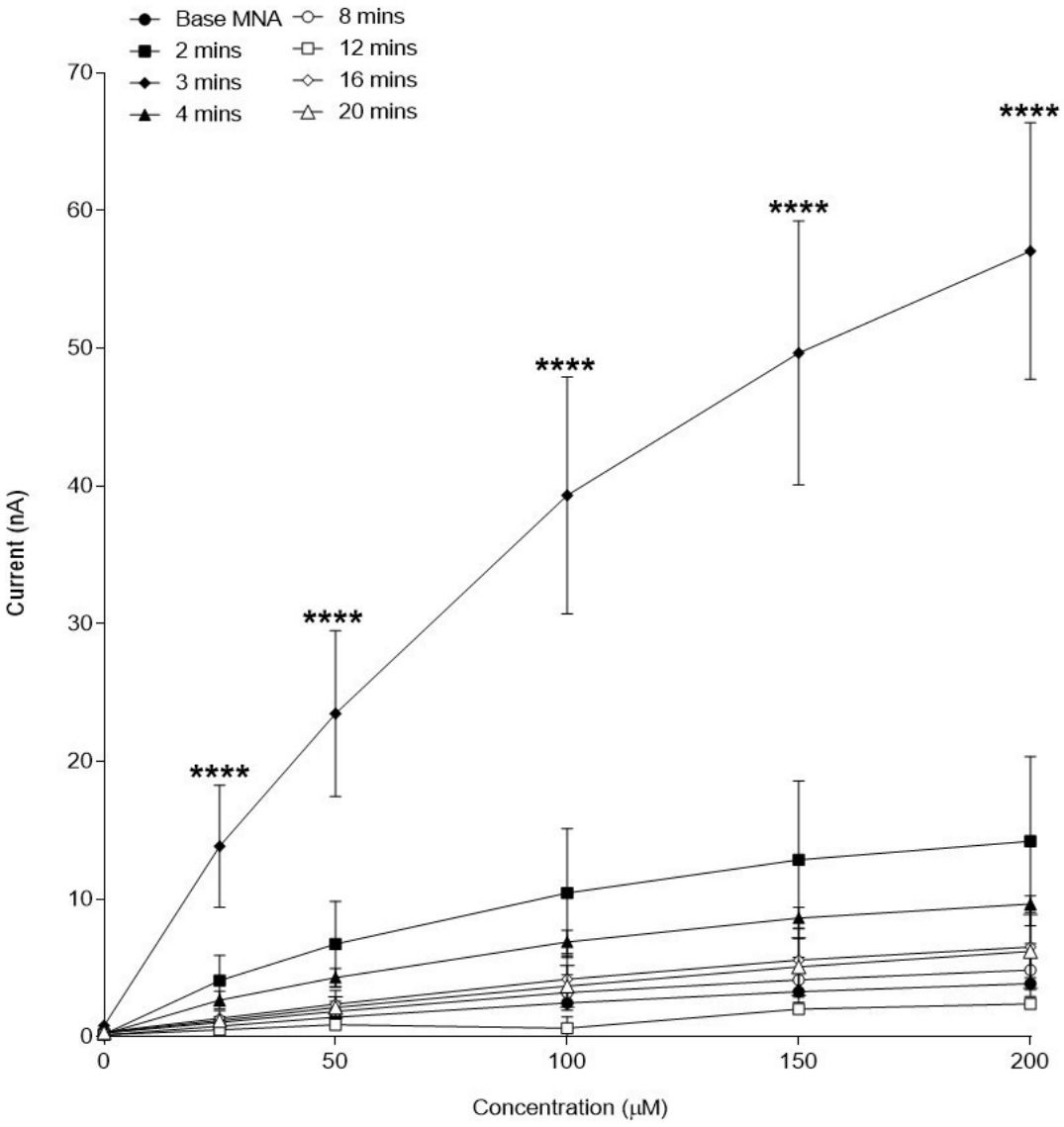

Figure 5.5. Amperometric calibration plots of AA. Electrochemical responses generated from the nanocomposite MNA's developed with different probe sonication times, compared against the base MNA. A significantly improved response can be seen from the 3 mins sonicated MNA devices in comparison to the others. ****$p < 0.0001$, one-way ANOVA with Tukeys's multiple comparisons test. Data represent mean ± SD, *n = 3*.

5.4.2 Surfactants

5.4.2.1 Dispersion efficiency via temperature

Implementing the optimised sonication time of 3 mins, the dispersion of surfactant was evaluated in terms their particle size and ζ potentials at temperatures above and below their T_K by DLS (Figure 5.6). Without the surfactants, regardless of the temperature there was no difference in particle size and ζ potential as shown by the control samples. A ζ potential of 49 ± 11.5 mV was found as average for the control samples. And, in terms of average particle size, the average diameter was 2.84 ± 0.80 µm. Regardless of the temperature, with the addition of both surfactants, the average particle size was significantly lower than control samples. However, although a rise in in ζ potential was seen with the additions of surfactants, regardless of the temperature, (with mean average for temperatures above and below T_K being 67 mV ± 15.35 and 65.4 ± 17.35 mV, respectively for CTAB and CPyCl), the

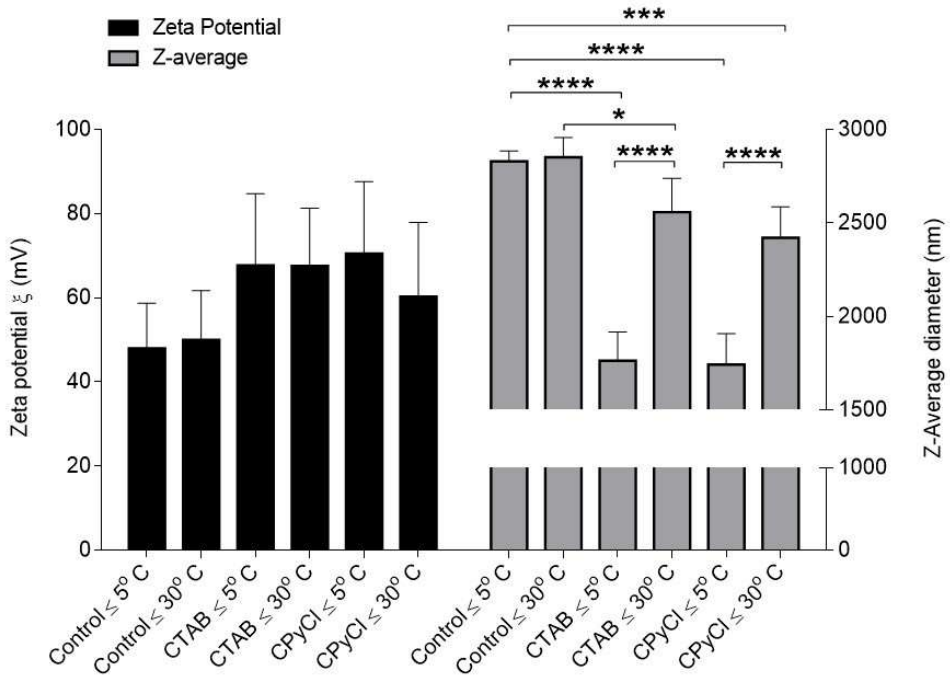

Figure 5.6. Dispersions above and below T_K: Dispersions were characterised in terms of ζ potential (left y axis) and particle size (right y axis) against the effect of temperature above and below T_K and compared to controls without any surfactants. The concentration used for both surfactants was 10 mM. For the two surfactants, a significant decrease in particle size was seen below their T_K, and the use of surfactants significantly reduced the particle size regardless of the temperature, but more significantly below the T_K of the surfactants. *p < 0.05, ***p < 0.001, ****p < 0.0001, two-way ANOVA with Tukey's multiple comparisons test. Data represent mean ± SD, *n = 3*.

difference was not statistically significant when compared to the control samples for both surfactants. With reference to the temperature, a significant decrease in particle size can be seen when sonicating below the T_K, for both surfactants. The mean difference in particle sizes were ~795 µm for CTAB and ~677 µm for CPyCl. Between the two surfactants, at a given temperature there was no significant difference in the particle size of the CNTs. These results suggest that, sonicating at a temperature below the surfactant T_K aids better exfoliation of CNT's.

Figure 5.7 reports the polydispersity index (PDI), where values ≤ 0.5 are considered mono-disperses and ≥ 0.5 are poly-dispersed samples (ISO 22412:2017). Here, the control samples at both temperatures, as well the surfactants CTAB and CPyCl at 30°C displayed a PDI of > 0.80, indicative of a wide particle size distribution. However, when the temperature was below the T_K for both surfactants, the PDI was found to be significantly lower at ~0.625 ($P < 0.0001$), suggesting that the particle size distribution is narrower. These results further evidence a strong effect of surfactant T_K on CNT exfoliation.

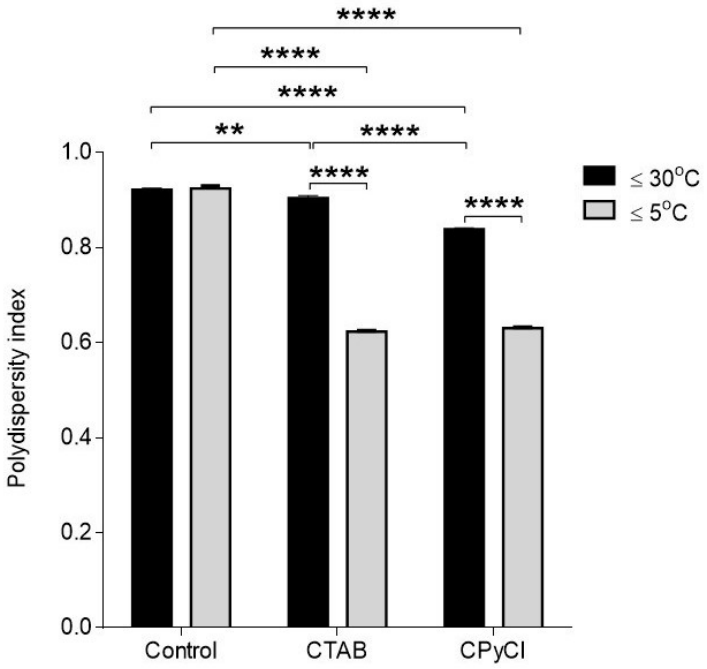

Figure 5.7. PDI of surfactants at different temperatures against control (i.e. no surfactant): An improved PDI is seen for both surfactants exfoliated below their T_K. **p < 0.01, ****p < 0.0001, two-way ANOVA with Tukey's multiple comparisons test. Data represent mean ± SD, $n = 3$.

UV-Vis absorbance for the surfactant dispersed samples and controls (i.e. without surfactants) were also measured to further validate the results above (Figure 5.8). From

evaluating the absorbance at the peak maximum ~260 nm, a similar trend was found, whereby the absorbance and therefore the amount of individualised CNT's present in the samples was higher for both surfactants at temperature below their T_K. No significant differences existed between the surfactants at any given temperature and between the control samples without any surfactants. However, a highly significant increase in absorbance was found when comparing the control samples against both surfactants at any given temperature. Hence, this further validates the results above and for further characterisation, surfactants were used below their T_K.

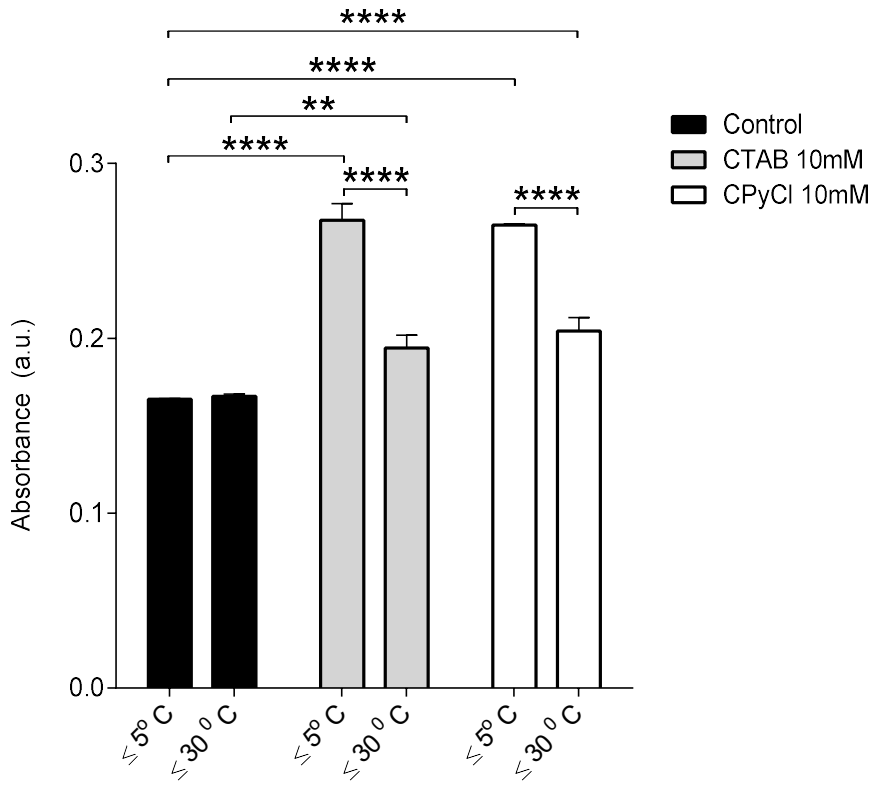

Figure 5.8 UV-Vis absorbance measured at ~260 nm for evaluating the effect of temperature. Below the T_K for both surfactants, the absorbance was significantly higher and regardless of the temperature, the exfoliation of CNT's with surfactants resulted in higher absorbance for both surfactants compared to the control. **p < 0.01, ***p < 0.001, ****p < 0.0001, two-way ANOVA with Tukey's multiple comparisons test. Data represent mean ± SD, *n = 3*.

5.4.2.2 Evaluation of different concentrations

The dispersion efficiency was also analysed by evaluating different concentrations for both surfactants (i.e. 1, 5, 10 and 15 mM) using the optimal temperature for exfoliation as shown in Figure 5.9. ζ potential is a measure of binding efficiency, therefore with increasing concentration of the surfactants, ζ potential should increase accordingly. However, this was not the case for both surfactants, as no apparent trend was evident and there is no significant difference between any of the respective concentrations (Figure 5.9, A-B). The average ζ potential for CTAB and CPyCl across all concentrations was 72.11 ± 9.69 mV and 62.45 ± 9.63 mV, respectively. On analysing the particle size for both surfactants at different concentrations, it was found that 5 mM is the critical concentration that enables maximum exfoliation of the CNT's, as the average diameter of the particle size here was 1.06 ± 0.118 μm and 1.35 ± 0.107 μm; respectively for CTAB and CPyCl. This was significantly different from all other concentrations evaluated. The general trend seen here, indicates the active role of surfactants up until 5 mM concentration, to significantly exfoliate the CNT bundles, following which, the particle size is seen to increase significantly for both surfactants at 10mM, i.e. 1.76 ± 0.155 μm and 1.74 ± 0.165 μm, respectively for CTAB and CPyCl. Further increases in surfactant concentration showed no significant increase in particle size.

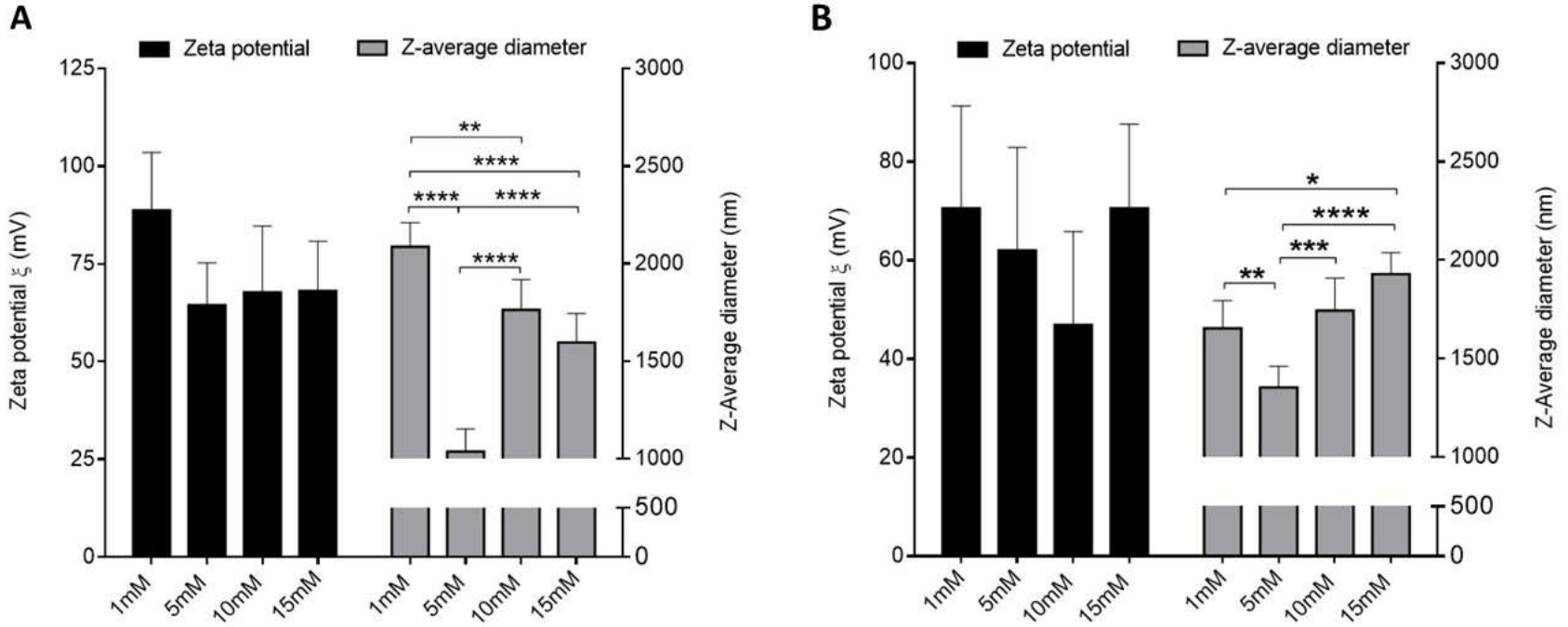

Figure 5.9. Evaluating different concentrations of surfactants: Dispersions characterised in terms of ζ potential (left y axis) and particle size (right y axis). (A) CTAB at different concentrations, no significant increase in ζ potential was found with the rise in concentration, however for particle size, there is a significant decrease in particle size at a concentration of 5 mM. (B) CPyCl shows a similar trend, with a significant decrease in particle size at 5mM. *$p < 0.05$, **$p < 0.01$, ***$p < 0.001$, ****$p < 0.0001$, two-way ANOVA with Tukey's multiple comparisons test. Data represent mean ± SD, $n = 3$.

As before, the PDI index was also taken into account, with reference to the different surfactant concentrations (Figure 5.10). The PDI at 5 mM for CTAB was 0.34 indicating a largely mono-disperse sample, whilst for CPyCl it was 0.50; indicating a higher degree of poly-dispersity. At all other concentrations, the samples were poly-disperse. Hence, these observations further indicate that 5mM was the optimal surfactant concentration.

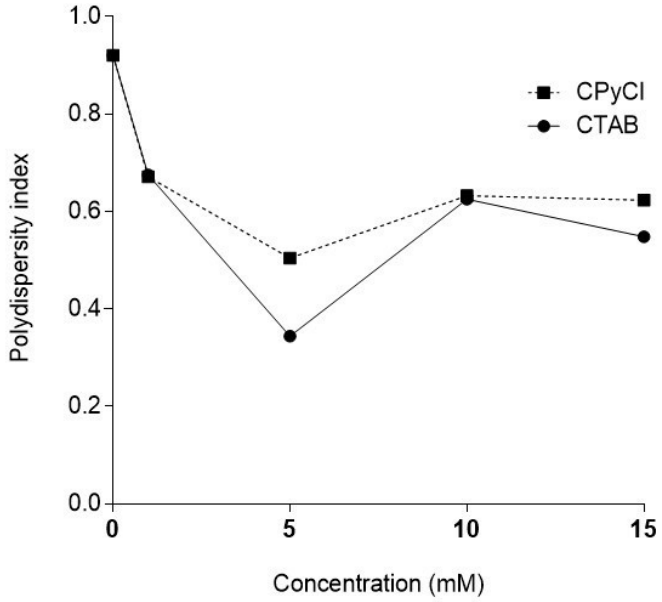

Figure 5.10. PDI of CNT's at different concentrations of surfactant. The trend indicates decreasing PDI until 5 mM, at which a significant drop in PDI is seen for both surfactants, indicating the samples were largely mono-disperse. Above this concentration, polydispersity is seen to increase and tail off.

5.4.2.3 Nanocomposite preparation

The method evaluated here concerned dispersing the surfactants below their T_K. Apart from better exfoliation of the CNT's, the other advantage this offers is the practicality to remove excess surfactants by standing at low temperatures or centrifugation. The results of these investigations are shown in the Figure 5.11. Once the CNT's were dispersed using surfactants at different concentrations, the samples were left to stand in an ice bath for 4 hours. Figure 5.11, A shows images taken afterwards. This shows CNT's being suspended with a clear top layer formed of surfactant/chloroform solution. It appeared to be the case that, the clear layer on top of suspended CNT seems to increase in volume with increasing concentrations of the surfactants. At 1 mM, such a layer was not evident. These solutions were further centrifuged to determine if the surfactants would crystallise out of the

suspension and settle to the bottom of the container. However, as shown in Figure 5.11, B, the CNT's themselves sedimented after centrifugation and this occurred regardless of whether the dispersion was carried out above or below the T_K.

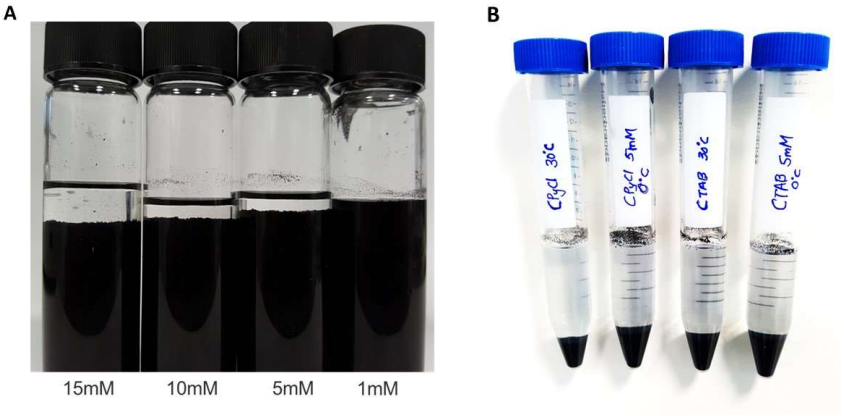

Figure 5.11. Digital photographs of nanocomposite suspensions. (A) Dispersions left to stand below the surfactant T_K for 4 hours, showing a clear layer of chloroform/surfactant solution formed on top at higher volumes for increasing surfactant concentrations. (B) When centrifuged, the CNT's were seen to pellet regardless of the temperature or the surfactant being used.

Despite these results, nanocomposites were processed at 6 wt% CNT loading at all concentrations from both surfactants. However, whilst attempting to develop MNA's by manual compression moulding, only the composites made with 1 mM concentration for both surfactants could be fabricated into MNA's. At the remaining concentrations, MNA's formed were found to be brittle; as they could not be ejected from the micromould with the microneedles intact. Therefore, the MNA's incorporating 1 mM concentration of the surfactant was used for characterisation of their mechanical and electrochemical properties.

Figure 5.12 shows evaluation of the AFS and SFS for the surfactant incorporated microneedles, compared against the sonic-probe-optimised MNA and the base MNA. The AFS and SFS measured for the probe-optimised MNA's showed no significant improvement in comparison to the base MNA (Figure 5.12, A-B). The mean axial forces were 1.40 ± 0.18 N for the base MNA and 1.30 ± 0.16 N for the probe-optimised MNA. When compared with 1 mM surfactant incorporated MNA's, there was no significant difference in AFS for CTAB with respect to the base or probe-optimised MNA; whereas for CPyCl, the corresponding AFS was significantly lower compared to the base and the probe-optimised MNA's (Figure 5.12 A). In addition, the AFS was significantly lower for CPyCl in comparison to CTAB (mean AFS were 1.31 ± 0.23 N and 1.08 ± 0.13, for CTAB and CPyCl respectively). In

relation to SFS (Figure 5.12, B), the forces withstood by the surfactant incorporated MNA's were significantly lower ($p > 0.0001$), for both surfactants, in comparison to the base and probe-optimised MNA's. The mean SFS's were 0.49 ± 0.05 N, 0.46 ± 0.03 N, 0.18 ± 0.01 N and 0.17 ± 0.01; respectively for base, probe, CTAB and CPyCl developed MNA's. There were no significant differences between the surfactants for SFS.

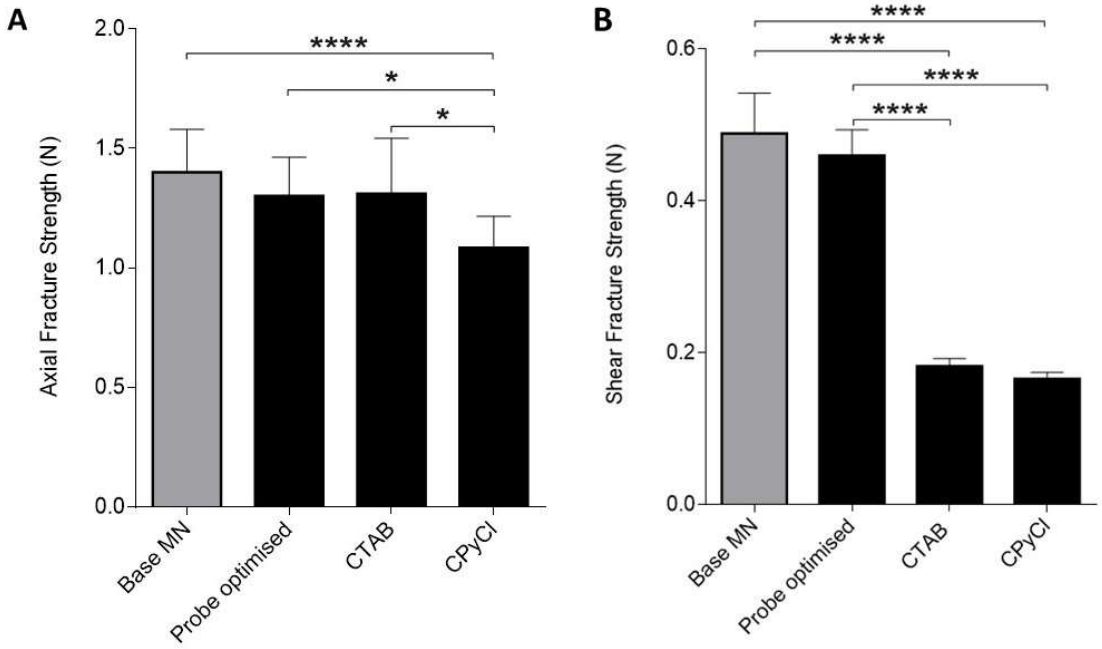

Figure 5.12. Mechanical characterisation: (A) Comparison of *AFS* between the base microneedles (i.e. bath sonicated), probe sonication optimised, and surfactant incorporated MNA's. No significant differences were found between the probe-optimised and base microneedles, whilst addition of the surfactant; CPyCl, showed significant lower *AFS* in comparison to the base and probe microneedles. CTAB incorporated MNA's were able to withstand significantly higher *AFS* in comparison to CPyCl. (B) Similar comparison was made for *SFS* and likewise no significant differences existed between the base and *probe-optimised* microneedles. However, both of the surfactants incorporated MNA's produced significantly less *SFS* in comparison to the base and probe microneedles. *p < 0.05, ****p < 0.0001, one-way ANOVA with Tukey's multiple comparisons test. Data represent mean ± SD, *n = 3*.

The electrochemical behaviour of the surfactant-incorporated MNA's was compared against the base and probe-optimised MNA's. Initially, the electrochemical response was assessed in terms of improvements in current generated at a potential of 1 V through CV recordings (Figure 5.13). (Note, the CV data is not shown, as it does not show the redox processes towards 1 mM $Fe(CN)_6$). The results indicate that, with the incorporation of surfactants, there is significant reduction in current compared to the probe-optimised MNA's ($p > 0.0001$); also, there was no significant improvement in comparison to the base MNA's.

Comparisons between the surfactants showed that, the current generated by CPyCl was significantly lower than CTAB. The mean currents measured were 0.22 ± 0.08 μA and 0.07 ± 0.01 μA for CTAB and CPyCl, respectively.

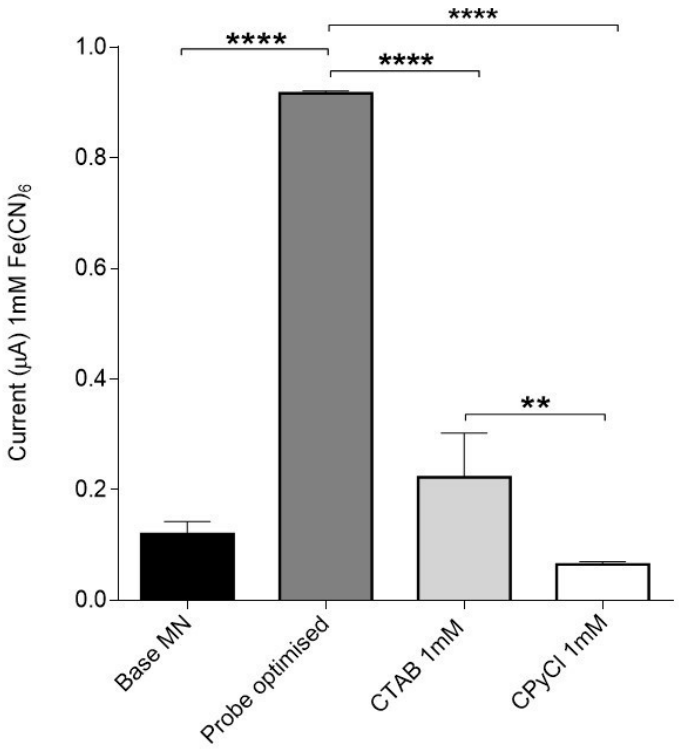

Figure 5.13. Electrochemical response of the MNA's towards 1mM $Fe(CN)_6$ after surfactant incorporation. Current measured at a potential of 1V from CV is compared for the different MNA's developed. Compared to the probe sonicated MNA's a significant reduction in current is seen for MNA incorporating both surfactants (CTAB, CPyCl). Between the surfactants, the CPyCl produced a significantly lower current response when compared to CTAB. (**p < 0.01, ****p < 0.0001, one-way ANOVA with Tukey's multiple comparisons test. Data represent mean ± SD, *n = 3.*

Amperometric response towards varying concentrations of AA was also analysed for the surfactant-incorporated MNA's and compared against the base and probe-optimised MNA's (Figure 5.14). As seen with the responses from current measurements at 1 V, the amperometric response towards AA was significantly higher for CTAB in comparison to CPyCl. LOD was found to be ~2 μM for CTAB and ~36 μM for CPyCl, with a sensitivity of 1.468 $pA.\mu M^{-1}$ and 0.334 $pA.\mu M^{-1}$, respectively. The response from MNA's incorporating CTAB was significantly higher than the base MNA's. The lowest response was found for CPyCl and at probe-optimised MNA's produced significantly higher responses than the all others as previously seen (Figure 5.5). Since incorporating the surfactants impaired electrochemical mechanical properties, surfactants were not further utilised in this study.

A

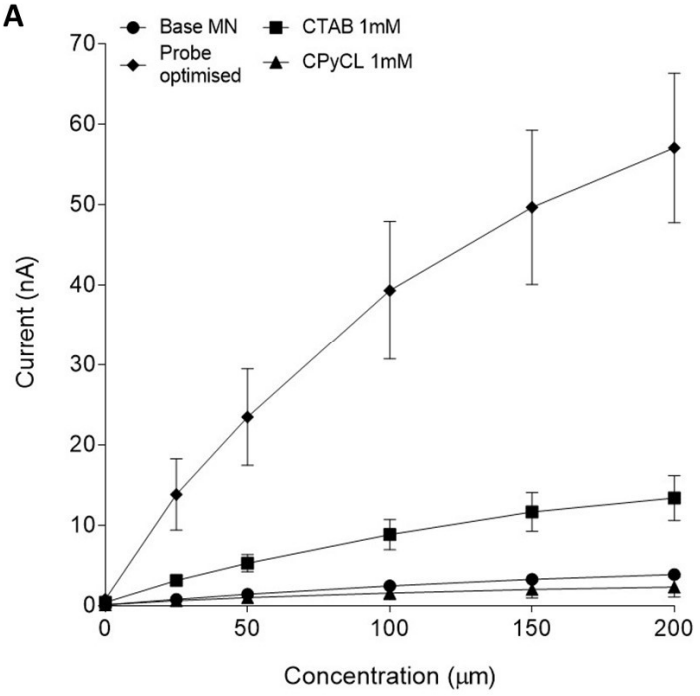

B

		Probe	CTAB	CPyCl
0 mM	Base	****	**	ns
	Probe	--	***	****
	CTAB	--	--	**
25 mM	Base	***	ns	ns
	Probe	--	**	***
	CTAB	--	--	ns
50 mM	Base	***	ns	ns
	Probe	--	***	***
	CTAB	--	--	ns
100 mM	Base	****	ns	ns
	Probe	--	***	****
	CTAB	--	--	ns
150 mM	Base	****	ns	ns
	Probe	--	****	****
	CTAB	--	--	ns
200 mM	Base	****	ns	ns
	Probe	--	****	****
	CTAB	--	--	ns

Figure 5.14. Comparison of amperometric responses from surfactant incorporated MNA devices, against the base and the probe optimised MNA's. (A) amperometric calibration plot. (B) comparative statistical analysis. **p < 0.01, ***p < 0.001, ****p < 0.0001, One-way ANOVA with Tukey's multiple comparisons test. Data represent mean ± SD, *n = 3.*

5.4.3 Evaluation of different functional groups

Different functional groups on CNT's have been reported to significantly influence the conductivity and electrochemical behaviour of nanocomposites[163,179]. Therefore, the effect of $–N_2$, $–NH_2$ and –COOH MWCNT functionalisation on the mechanical and electrochemical properties of nanocomposite MNA's were investigated in this study. The functionalised MWCNT's were of different lengths as detailed in *section* 5.3.3. Broadly, these can be characterised into long and short, referring to those with a length of 10 – 30 µm and 1 -12 µm, respectively. Thus far, the analysis has been carried out with the long i.e. 10 – 30 µm –COOH functionalised MWCNT's. Therefore, for effective comparisons a shorter version of –COOH functionalised MWCNT's was also employed, and they possessed similar dimensions to that of the other functional groups. Initial evaluations of MNA fabrication using the differing functional groups with shorter lengths were carried out using the optimal sonication protocol without any surfactants. By investigating various loadings, the fabrication limit was identified to be 3 wt% (data not shown) as they possessed sufficient mechanical strength, in order for the MNA's to be ejected effectively from the micromould

always. Therefore, the MNA's developed at this loading was compared against the probe-optimised long-COOH-functionalised MWCNT's (i.e. control) in terms of electrochemical properties.

Figure 5.15 shows the currents measured at a potential of 1 V from the respective CV traces (no redox peaks was evident from the CV traces, therefore data not shown). With reference to the different functional groups, the currents measured from the MNA's were significantly lower than that of the control ($p > 0.0001$). However, when comparing the different functional groups, a particular trend can be seen whereby the current generated is significantly higher in the order of $–N_2 > –NH_2 > –$COOH (short). Though the current response towards $Fe(CN)_6$ was significantly lower than the probe sonicated MNA's, there is a potential for this to be increased significantly as the dispersions were found to be highly viscous, particularly for the $–N_2$ and $–NH_2$ functionalised MWCNT samples. This indicated, that the concentration at which these CNT's were dispersed (i.e. 0.5 wt%), needed to be

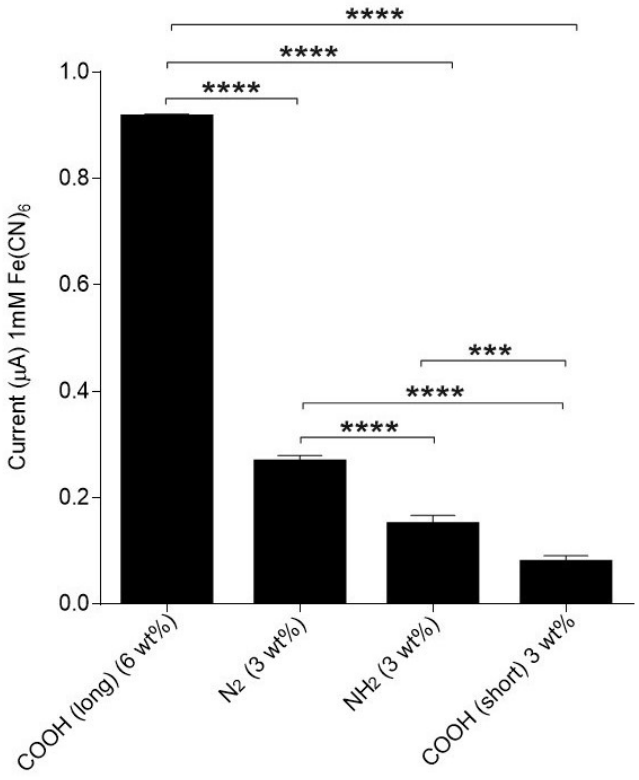

Figure 5.15. Electrochemical response from varyingly functionalised MNA's towards 1mM $Fe(CN)_6$. Probe optimised MWCNT's were the control incorporating 6 wt% –COOH functionalised long MWCNT's; compared against shorter MWCNT's with different functional groups at their fabrication limit (i.e. 3 wt%). ***p < 0.001, ****p < 0.0001, one-way ANOVA with Tukey's multiple comparisons test. Data represent mean ± SD, *n = 3*.

lowered significantly. Since lowering the concentration maybe beneficial to for all types of CNT's evaluated here, using the optimised sonication parameters, the dispersions were re-analysed, and a new fabrication limit was determined.

The light scattering particle size analysis for the dispersion of CNT's at various concentrations is shown below (Figure 5.16). From the average size volume distributions for functional groups with the shorter length (i.e. $–NH_2$ (Figure 5.16, A), $–N_2$ (Figure 5.16, B) and –COOH (short – Figure 5.16, C) and the longer length –COOH functionalised MWCNT's (Figure 5.16, D), it is evident that at a concentration of 0.5 wt% was inadequate for efficient dispersion, as the particle size here was much larger in comparison to that at 0.1 wt%. Going further down the concentration i.e. 0.05 wt%, a change was not apparent, although the trend suggests a further reduction in particle size. Therefore, these differences were evaluated statistically as shown in Figure 5.16, E -G. The data is grouped to represent different populations i.e. DX10 (Figure 5.16, E), DX50 (Figure 5.16, F) and DX90 (Figure 5.16, G). Collectively, these data confirm that at the highest concentration i.e. 0.5 wt%, particle sizes are significantly larger. Using $–NH_2$ and $–N_2$ as example, the average size for 50% percent of the population at a concentration of 0.5 wt% was above 24.6 µm and 36.3 µm respectively, as compared to 0.1 wt% where the particle sizes were 10.7 µm and 9.14 µm respectively. At the lowest concentration i.e. 0.05 wt%, for both sizes and different functional groups assessed, there is a strong indication that particle sizes are lower, but only significantly lower for the $–NH_2$ and –COOH (short) samples.

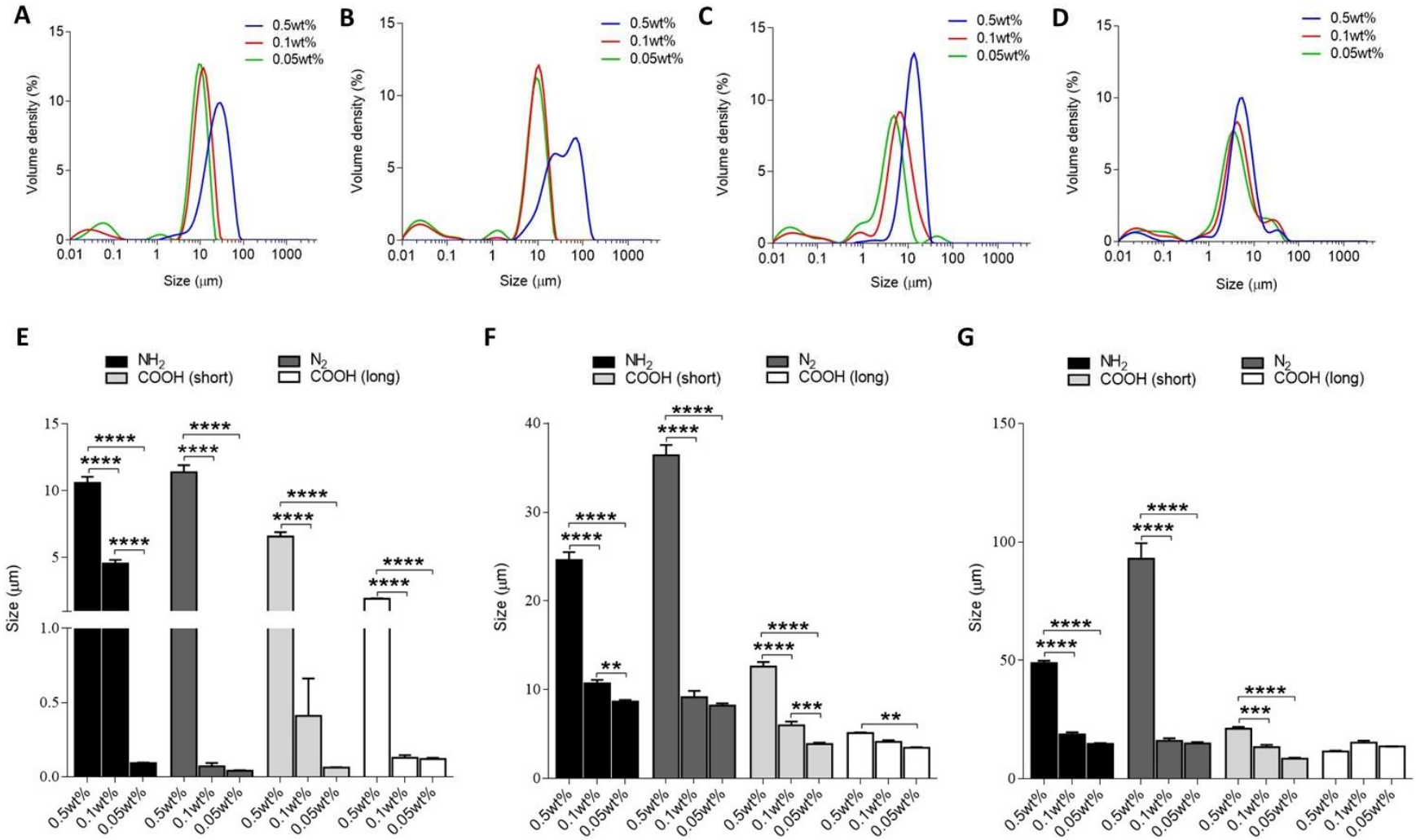

Figure 5.16. Dispersion analysis on varying CNT concentrations: A -D particle size distribution by volume for CNT's with reference to decreasing concentrations (i.e. 0.5 wt%, 0.1 wt%, 0.05 wt%) respectively for $–NH_2$, $–N_2$, –COOH (short) and –COOH (long). E – G, statistical analysis of the particle sizes according to their distribution i.e. DX10 (E), DX50 (F). DX90 (G). **p < 0.01, ***p < 0.001, ****p < 0.0001, two-way ANOVA with Tukey's multiple comparisons test. Data represent mean ± SD, *n = 3*.

For further validation, UV-Vis measurements were also taken for these samples to analyse the degree of dispersion (Figure 5.17). For $–NH_2$, $–N_2$ samples and –COOH (long) functionalised MWCNT's the absorbance readings indicate that, the samples are more significantly de-bundled at the lowest concentration (Figure 5.17, A-B and D). However, for the short -COOH functionalised MWCNT's a significant increase in absorbance was not found from 0.1 – 0.05 wt%. Nevertheless, based on the combined analysis of UV-Vis and light scattering results, it is reasonable to process the nanocomposites at the lowest concentration. However, using the new strategy, the fabrication limit needs to be further characterised.

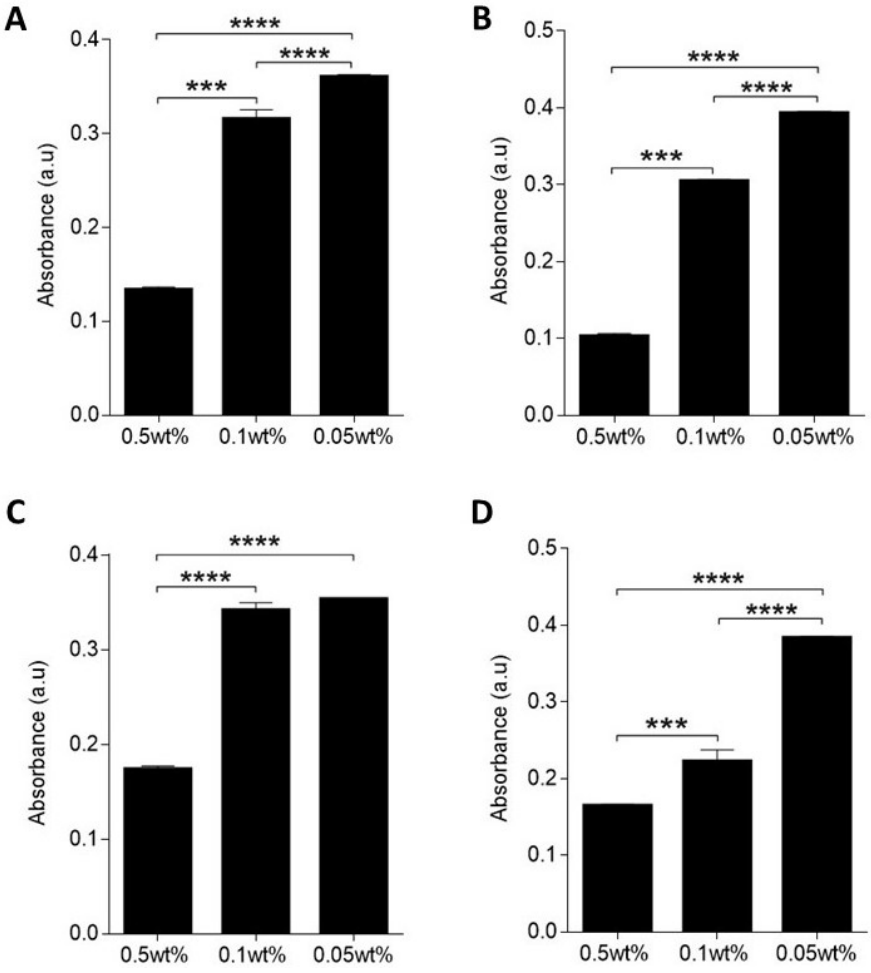

Figure 5.17. UV-vis absorbance measured at ~260nm. (A) $–NH_2$ functionalised MWCNT's, (B) $–N_2$ functionalised MWCNT's, (C) –COOH functionalised MWCNT's (short) and (D) –COOH functionalised MWCNT's (long). ***p < 0.001, ****p < 0.0001, one-way ANOVA Tukey's multiple comparisons test. Data represent mean ± SD, *n = 3*.

At a concentration of 0.05 wt%, the maximum loading of CNT at which MNA's formed consistently was determined for the different dimensionalities and the functional groups of/on MWCNT's. It was found that a complete MNA's could only be developed at 1 wt% of CNT loading for the MWCNT's with shorter dimensions, whereas for long –COOH functionalised MWCNT's, MNA's could still be fabricated with a maximum loading of 6 wt%. Figure 5.18, A shows digital images of MNA's fabricated with 6 wt% MWCNT loading (i.e. –COOH(long)), whereas Figure 5.18, B–D show weak MNA's formed at 2 wt% MWCNT loading using the shorter nanotubes. The composite film shown in Figure 5.18, F, shows large aggregates present when fabricating with composites with a high loading of 6 wt% (– COOH long).

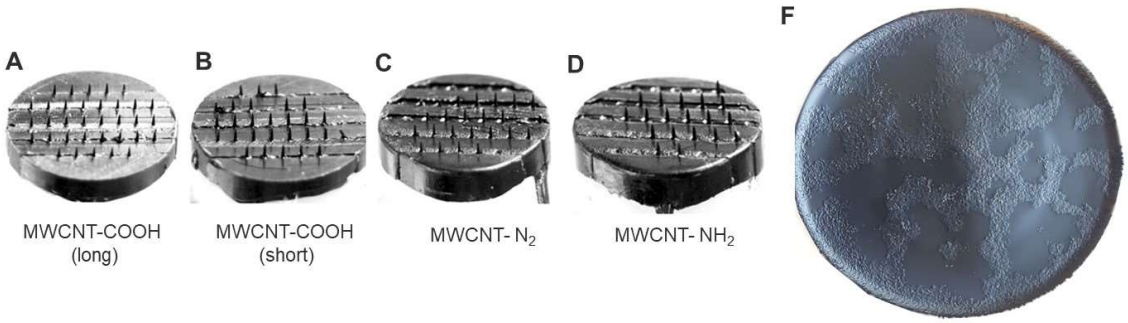

Figure 5.18. Characterising fabricational limits: Digital images shown for complete MNA's at 6 wt% CNT loading for the long –COOH MWCNT's (A) and their composite film with large aggregates (F). Fabricational limit at 2 wt% for shorter nanotubes with different functionalities.

Using the nanocomposite MNA's developed at 1 wt% CNT loading, their AFS and SFS was compared against the probe-sonicated MNA's fabricated with 6 wt%− COOH functionalised MWCNT's (i.e. control, Figure 5.19). The AFS (Figure 5.19, A) showed that, MNA's fabricated at a concentration of 0.05 wt% with a maximum CNT loading of 1 wt% could withstand axial forces as high as the probe-optimised MNA's fabricated at a concentration of 0.5 wt%, with a maximum CNT loading of 6 wt%, without any significant differences. On comparing the different functional groups, the AFS was significantly higher for the MNA's fabricated with $–NH_2$ functionalised MWCNT's as opposed to the MNA's fabricated with $–N_2$ functionalised MWCNT's ($P < 0.05$). Their mean AFS was, 1.46 ± 0.20 N and 1.15 ± 0.19 N, respectively. In terms of SFS, the MNA's fabricated from $–N_2$ and –COOH (short) functionalised MWCNT's showed comparable mechanical strength to the 6 wt% probe-sonicated MNA's, whereas the long –COOH and $–NH_2$ functional groups had significantly lower SFS in comparison. Between the MNA's developed from the newly

optimised dispersion state, the short –COOH functionalised MWCNT's produced significantly higher SFS in comparison to the longer -COOH functionalised MWCNT's. In contrast to AFS, the SFS was significantly higher for $–N_2$ functionalised MWCNT's. Regardless, the SFS and AFS measured here are adequate to penetrate the skin without any mechanical damage to the MNA's.

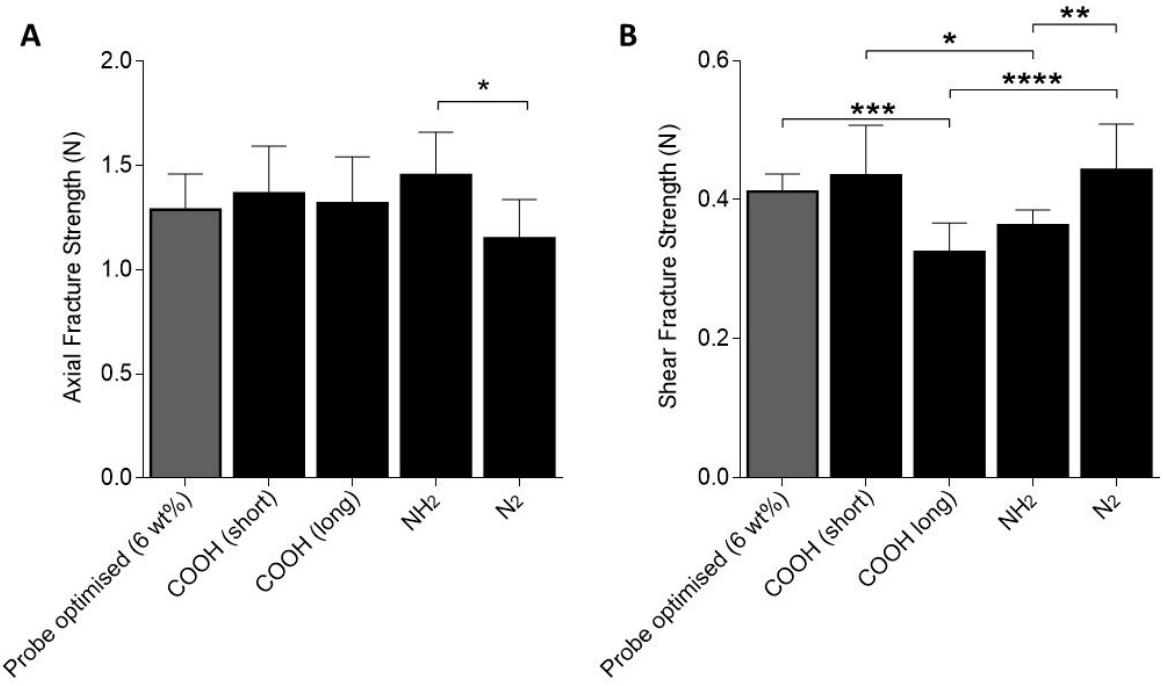

Figure 5.19. Mechanical characterisation of different functional groups and dimensional parameters. AFS and SFS were measured for MNA's fabricated at a concentration of 0.05 wt% with a loading of 1 wt% and compared against the probe-optimised MNA's fabricated at a concentration of 0.5 wt%, with a total CNT loading of 6 wt%. *p < 0.05, **p < 0.01, ***p < 0.001, ****p < 0.0001, one way-ANOVA with Tukey's multiple comparisons test. Data represent mean ± SD, *n = 3*.

The electrochemical response of the MNA's with different functional groups towards $Fe(CN)_6$ is shown in Figure 5.20. The long –COOH at 1 wt% loading was omitted from this analysis, because an electrochemical response could not be detected from it. However, surprisingly, MNA made with the shorter –COOH acid functionalised MWCNT's produced an electrochemical response. MNA's fabricated with the $–N_2$ functional group produced a

significantly higher response than both $–NH_2$ and –COOH functionalised MWCNT's. The magnitude of the response, in declining order, was $–N_2$ > $–NH_2$ > –COOH (short).

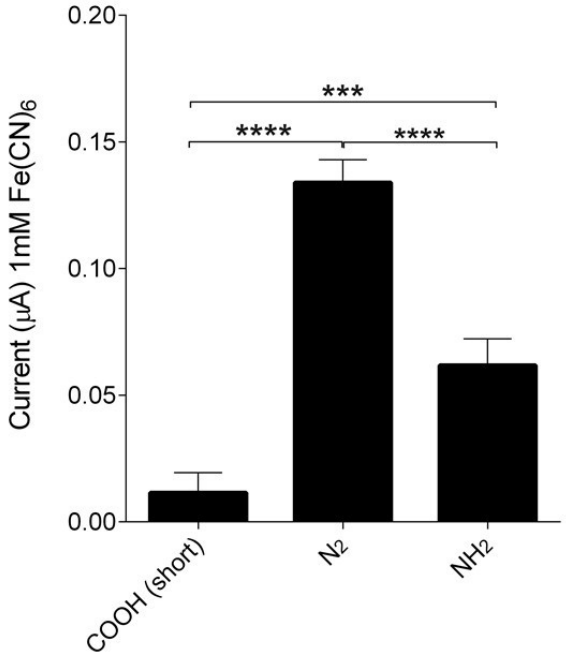

Figure 5.20. Electrochemical response of the MNA's towards 1mM $Fe(CN)_6$ with different functional groups. Current generated was significantly higher in the order of $–N_2$ > $–NH_2$ > –COOH (short). The CNT loading compared here was 1 wt%. ***p < 0.001, ****p < 0.0001, one way-ANOVA with Tukey's multiple comparisons test. Data represent mean ± SD, *n = 3*.

To further characterise the response from these MNA's, comparisons were made against the amperometric detection of AA as shown in Figure 5.21. The various functional groups $–N_2$, $–NH_2$, –COOH (short) were compared against the probe-optimised MNA's. Noticeably, at the optimal concentration, the $–N_2$ functionalised MWCNT's at 1 wt% loading produced comparable responses to that of the probe-optimised 6 wt% –COOH functionalised MWCNT's, with no significant differences between them. Clearly, the responses from the $–NH_2$ and –COOH (short) functionalized MWCNT's were significantly lower than $–N_2$ and probe-optimised MNA's. And, there was no significant difference between the responses from $–NH_2$ and –COOH functionalised composite MNA's.

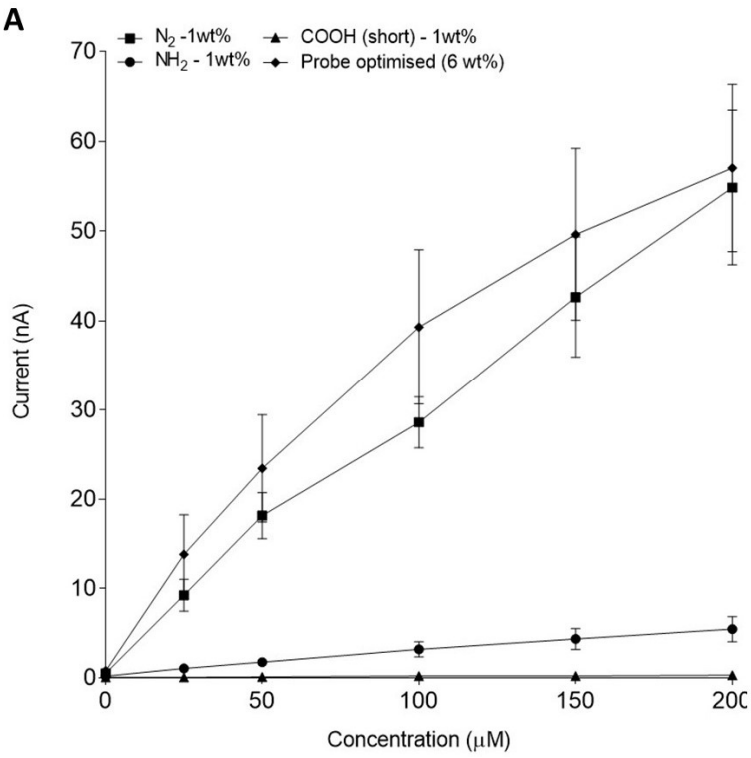

B

		N_2	NH_2	COOH(s)
0 mM	Probe	*	***	****
	N_2	--	*	**
	NH_2	--	--	ns
25 mM	Probe	ns	**	**
	N_2	--	*	*
	NH_2	--	--	ns
50 mM	Probe	ns	***	***
	N_2	--	**	**
	NH_2	--	--	ns
100 mM	Probe	ns	****	****
	N_2	--	**	***
	NH_2	--	--	ns
150 mM	Probe	ns	***	***
	N_2	--	**	***
	NH_2	--	--	ns
200 mM	Probe	ns	****	****
	N_2	--	****	****
	NH_2	--	--	ns

Figure 5.21. Amperometric responses towards varying concentration of AA from MNA devices fabrication with MWCNT's of different functionalities and dimensions. (A) amperometric calibration plots, showing comparable responses between the devices fabricated with 1 wt% –N_2 functionalised and 6 wt% –COOH functionalised MWCNT's. (B) comparative statistical analysis. **p < 0.01, ***p < 0.001, ****p < 0.0001, One-way ANOVA with Tukey's multiple comparisons test. Data represent mean ± SD, *n = 3*.

5.5 Discussion

In this chapter, various strategies were attempted to optimise the electrochemical behaviour of the existing MNA's and assess their LOD and sensitivity towards AA. CNT dispersion is the major hurdle in composite manufacturing, in order to achieve optimal mechanical and electrical properties. One of the most efficient ways to achieve this is by evaluating the sonication parameters involved. The sonication energy supplied must overcome the Van der Waals cohesive binding energy by which the CNT's are held together and at the same time should not exceed the scission pressure[156]. These two parameters are theoretically estimated to be around 0.1 MPa and 0.5 MPa for MWCNT, respectively[218]. The sonication energy supplied induces shear forces from cavitation, resulting in a sequence of events i.e. bubble formation, growth and collapse. The efficiency of cavitation is, however, dependent on solvent parameters (viscosity, vapour pressure and surface tension) as well the sonication parameter i.e. frequency, time and intensity[156]. In this chapter, the dispersion was evaluated as a function of sonication time using both laser diffraction particle size and UV-Vis spectral analysis; and corroborated with the resultant mechanical and electrochemical properties. Using the former, the particle size was found to decrease significantly up until 8 mins of sonication. The –COOH functionalised MWCNT's used here are of 20 – 30 nm in diameter and a length of 10 – 30 μm. When cross-referencing this to the obtained particle size data, it is difficult to establish whether the sizes correspond to the length or the diameter of the nanotubes; therefore, it is not possible to interpret the sizes in terms of damages to CNT's with the extent of sonication. This is in agreement with the literature[213]. Therefore, the sizes measured are interpreted as that related to the size of the irregular aggregate. The different classes of sizes observed correspond to the de-bundling process, where progressive de-bundling starts from the outermost layer[208]. The probe sonicator used here outputs an energy of ~12,300 and ~24,800 J of energy after a sonication time of 2 mins and 4 mins, respectively. During sonication, the level of energy density supplied is equivalent to the shear stress achieved[156]. Therefore, this equates to ~2.58 x 10^2 and 5.16 x 10^2 MPA (i.e. the total energy density/J.mL^{-1}), respectively; which is significantly higher than what is need for de-bundling. This is comparable to that used by Fernandez *et al.*, however they applied a sonication time of 8.5 mins at 30% amplitude (equating to 5.3 x 10^2 MPA)[218]. It is possible that the high intensity sonication (at 100% amplitude) used here might inflict structural damages to the CNT's; especially when the sonication time was increased. UV-Vis analysis

was further carried to corroborate all data from particle size analysis in this chapter. Commonly, the absorbance measured at a specific wavelength is related to the degree to which CNT's are dispersed. Here, a peak maximum was identified at ~260nm and consequently evaluated. This is consistent with the literature, indicating that well-dispersed MCNT's have an absorbance maximum between 200 – 300 nm[213]. Also, consistent with the literature is the trend observed from UV-vis, where after a critical amount of sonication (i.e. 16 mins) the absorbance profile showed very little change[229].

Because an ideal sonication time is more likely to be between 2 and 4 mins of sonication; an additional nanocomposite was processed at 3 mins. This was important, as sonication was not only applied for CNT dispersion, but also for efficient intercalation with the polymer after its dissolution in the CNT dispersed solvent. The composite MNA's produced using the different sonication times were evaluated by CV using $Fe(CN)_6$ and amperometric detection of AA. On evaluating the current measured by the MNA's, the observed trend, whereby the current is seen to increasing initially and then decrease with prolonged sonication time confirms that the electronic properties of the MWCNT's are impaired from extended periods of sonication, causing structural defects by breaking the CNT's into smaller lengths. At 3 mins however, the dispersion is optimal without breakage of the nanotubes. Thus, the current response from MNA's prepared at the optimal sonication time was significantly higher by 735.53% when compared to the base MNA's. In agreement with these results, amperometric evaluation using AA also demonstrated an improved LOD and sensitivity for the sonication optimised MNA's, at 0.51 μM and 6.525 $nA.\mu M^{-1}$, respectively, as opposed to the based MNA's with a LOD of 16 μM and sensitivity of 18.04 $pA.\mu M^{-1}$.

Using the optimised sonication conditions, the effect of the surfactants, CTAB and CPyCl, on the dispersion and hence the electro-mechanical properties of the MNA's was investigated. These surfactants were chosen based on their dispersive character, a high CMC (i.e. ~1mM), high T_K (> 25°C), compatibility with solvents and electrochemical behaviour. When manufacturing a nanocomposite, it is widely accepted that excess surfactants that remain can severely weaken the mechanical properties and reduce the conductivity of the composites as the surfactants at high concentrations will reduce contact between the CNT's[218,227,228]. Therefore, in this chapter, the utility of dispersing above and below the surfactants' T_K was investigated. This was based on a recent report illustrating that, below

the T_K, any free surfactants not adsorbed on the surfaces of CNT's will crystallise out of the suspension and sediment to the bottom of the container[228]. To establish a baseline, the MWCNT's were dispersed with probe sonication in chloroform without the addition of surfactants for 3 mins at temperatures ≤ 5°C and ≤ 25°C. This showed no differences in particle size, with an average diameter of 2.85 ± 0.105 μm. However, this contradicts a recent report that temperature significantly influenced the aggregative behaviour of CNT in solvents. That report found that sonication of CNT's in propan-2-ol at –17° C helped improve dispersibility and stability of the suspension when compared to higher temperatures as evaluated by particle size and UV-Vis analysis[245]. These improvements were reasoned to be the effect of several factors, including a reduced Van der Waals energy between CNT's at lower temperatures, reduced Brownian motion in solution so that collision between neighbouring particles are limited, increased viscosity and removal of air bubbles incorporated into the suspension by sonication. With reference to these factors, as the prepared dry-ice bath could cool the sample down to approximately –40°C, the benefits of lowering the temperature as above, could have been assimilated in this study. However, the sharp rise in temperature from utilising a probe-type sonicator could mean that sample temperature could not have been sufficiently low throughout the sonication procedure.

By dispersing the CNT's at temperatures lower than the surfactant T_K, a better exfoliation of the aggregates, alongside better stabilisation was found. In agreement with the literature, the surfactants showed no significant differences between their dispersive power[218]. CPyCl has an aromatic pyridinium ring in its structure, which would usually be expected to increase the hydrophobicity and promotes π – π interactions with the CNT surface. However, in this case, the aromatic ring is part of the polar head group with the cationic charge. This negates the positive effect of the aromatic ring[218]. Therefore, the dispersive power for CPyCl is similar to CTAB as both possess the same alkyl chain length (C17).

Typically, the concentration of surfactants, or the optimal CNT: surfactant ratio, defined by many researchers have exceeded the CNT concentration in suspension by several hundred folds. Different concentrations were analysed here as the CNT loading is high (at 6 wt%) and therefore having an optimal amount of surfactant would mean that the excess to be removed will be minimal and if the surfactant is not crystallising out of the suspension, the negative impact of excess surfactants can be minimised. Here, 5 mM was identified as

the optimal concentration, at which maximum dispersibility and stability was found for both surfactants; which again showed no significant differences between them. At higher concentrations, the particle sizes were found to be significantly larger and was more polydisperse. This could be the result of multiple layers of surfactants attaching to the CNT surface, which could even cause flocculation of the CNT's[227]. When using organic solvents, the orientation of the surfactant are different i.e. the hydrophilic groups form the core, while the hydrophobic chains form the outer layer in a configuration known as the reverse micelle[246–248]. However, very recent studies have argued that such micelles form due to the presence of a small number of polar molecules (i.e. water)[249]. The implication here is that, the extent to which the polar molecular are present alone can in fact give rise to large polydispersity; as there exists a linear relationship between the size of the polar core and size of the micelles. However, since micelle formation is suppressed by sonicating below the surfactant T_K, the particle size measurements here were unlikely to be influenced by water-surfactant reverse micelle formation.

Unlike the water-based dispersion of CNT below the surfactants T_K, excess surfactants did not crystallise out of the suspension in solvent based dispersions. In fact, the excess surfactants formed a separated layer that grew in volume proportionally to the concentration of the surfactants. Attempts to remove non-adsorbed surfactants by centrifugation had also failed. Hence, the dispersions, as prepared, were made into nanocomposites and their mechanical characteristics were first investigated. Only the nanocomposites prepared with 1 mM surfactant concentration could be fabricated into MNA's. Mechanically, the only significant difference between the surfactant-incorporated MNA's was in AFS, with CTAB withstanding more compressive force than CPyCl. Comparison of AFS between the optimised probe sonicated MNA's and the preceding base MNA's showed CPyCl incorporated MNA's to be significantly weaker. However, on evaluating the SFS, both surfactant-incorporated MNA's were found to be significantly weaker in comparison to the base and the probe-optimised MNA's. Although the dispersive power for both surfactants are quite similar, the results evaluated thus far evidences slightly better performance for CTAB. This could be associated with the fact the bulky polar head group on CPyCl, though ineffective for dispersion, may still create higher intra- and inter-layer gap between MWCNT's, hence weakening the interfacial interaction. This was in fact more apparent from the measurement of current response to $Fe(CN)_6$, where the CPyCl-

incorporated MNA's showed a significant reduction in comparison to CTAB. For both surfactants, the current generated was significantly lower than probe-optimised MNA's. This is because of the surfactant molecules interfering with the conductive pathways, resulting in lack of contact between the nanotubes[222,234]. Therefore, the benefits observed from better exfoliation of the nanotubes did not translate into better electrical properties. Comparably, the amperometric response towards AA for the surfactant-incorporated MNA's showed significantly higher responses for CTAB than for CPyCl. Amperometric responses from CPyCl was comparable to that of the base MNA's. At present, these results collectively show that, incorporation of the two cationic surfactants have detrimental effects on the functional properties of MNA's, more so on the mechanical properties than their electrochemical properties. Hence, they were not adopted for the remainder of this work.

The intrinsic properties of the CNT's (i.e. optimal dimensions and functionalities) were also evaluated in order to develop a highly sensitive nanocomposite MNA. Dispersing with the optimised sonication strategy, it was initially observed that, for the $–N_2$ and $–NH_2$ functionalised MWCNT's samples, the concentration at which the CNT's were dispersed (i.e. ~ 0.5 wt%) was too high, resulting in a highly viscous sample, with a significant amount of sedimentation immediately after sonication. This is because the long alkyl chain provides greater repulsion between the nanotubes, increasing the available surface area of $–NH_2$/$–N_2$ functionalised MWCNT's in comparison to acid functionalised MWCNT's. Therefore, the volume of chloroform available becomes insufficient for proper wetting of the large volume of the MWCNT surface. Nevertheless, MNA's could be developed from their composites, but at a low CNT loading of 3 wt%, these showed no significant improvement in comparison to the probe-optimised MNA's in terms of their electrochemical response.

The degree of dispersion can be controlled initially by varying the sonication times. However, the quality of this dispersion will deteriorate over time because of re-agglomeration and sedimentation of MWCNT's, which will consequently impinge on the final properties of the polymer composites. Addition of surfactants can certainly aid the dispersion and stability of the composites, but as seen this chapter, they impair the performance of the composites. Hence, recent studies have critically assessed the effect of CNT concentration on the time stability and hence the agglomeration rate of MWCNT's dispersed in chloroform[250,251]. These studies collectively reported that MWCNT dispersions in chloroform are stable for up to 20 days at 0.005 wt%. This points towards the utilisation

of a large volume of solvent, which consequently limits scalability. However, in this instance, the MWCNT's utilised were all functionalised and PLA was dissolved immediately after sonication into CNT dispersed solution. This gave two inherent advantages over the use of a large solvent volume. CNT functionalisation reduced the energy to form MWCNT/solvent interfaces, while PLA incorporation increases the viscosity of the dispersed system, thereby reducing the mobility of the CNT's, thus increasing stability by increasing the time for re-agglomeration. In this work, the following CNT concentrations were investigated i.e. 0.5 wt%, 0.1 wt%, 0.05 wt%. Taken together, the data from particle size and UV-Vis analysis conclusively demonstrated that, at 0.05 wt%, more of the agglomerates were de-bundled, compared to the higher CNT concentrations; regardless of the size of the nanotubes.

Using the optimal CNT concentrations, the effect of different CNT functionalities and dimensions on MNA manufacturability and performance was investigated. The fabrication limit was identified to be 1 wt% for all short MWCNT's with different functionalities (i.e. –NH_2, –N_2, –COOH), whilst MNA's could be fabricated at a maximum loading of 6 wt% for the long –COOH functionalised MWCNT's. Two likely scenarios in combination may account for these results:

a. Based on the fact that the longer –COOH functionalised MWCNT's could be developed into MNA's at a higher loading in comparison to shorter versions with the same functionality, longer MWCNT's may provide enhanced mechanical strength as a result of fewer junctions in the nanocomposite.

b. In relation to –NH_2, –N_2 functionalised MWCNT's, as discussed before the long alkyl chains of the amino group provides greater repulsion between nanotubes, therefore not only there is requirement for larger volumes for sufficient dispersion, but also a sufficient amount of polymer is required to form the nanocomposites without any voids and clusters of CNT's[163]. Hence, at high loadings, nanocomposites MNA's could not be fabricated with the –NH_2 or –N_2 functionalised MWCNT's.

In general, the MNA's developed at the optimised concentration (at 1 wt% CNT loading) showed comparable mechanical performance to the probe-optimised MNA's (utilising the long –COOH functionalised MWCNT's) at 6 wt% CNT loading, regardless of

the functionalities and dimensional differences, in terms of both AFS and SFS. However, there were some exceptions. Contrary to expectation, the – NH_2 or the – N_2 functionalised MWCNT's showed no significant improvement in mechanical properties of the MNA's in comparison to –COOH functionalised MWCNT's despite the fact the former could potentially form covalent bonds with polymer in comparison to the latter which would form hydrogen bonds. However, for a more effective comparison, the effect of loading should also be taken in to account i.e. compare against 1 wt% probe-optimised MNA's. This is relevant because it has been evidenced in the literature that at low loadings (> 2 wt%), the amine functionality improves mechanical properties of the composites significantly in comparison to the carboxyl functionality[163].

An important finding when measuring the current generated from CV for 1mM $Fe(CN)_6$ was that, the long – COOH functionalised MWCNT's at 1 wt% CNT loading did not produce an electrochemical response, whereas the shorter versions of MWCNT's with the same functionality and CNT loading produced a measurable response. The differences between the nanotubes are in their dimensions with the shorter version having lower average diameter and length. However, the shorter MWCNT's used in this study had a higher aspect ratio i.e. ~1700 as compared to ~1000 for the longer version. Hence, this could increase conductivity. Additionally, as the electrochemical behaviour is a result of the edge-plane-like graphitic sites that occur at the open ends and along the tube axis of MWCNT's, the shorter nanotubes present more electroactive sites per unit mass than the longer MWCNT's[109,110]. In combination, these factors contribute to a better electrochemical response. As expected, the $–NH_2$ functionalised MWCNT's showed a greater electrochemical response than the MNA's incorporating –COOH functional groups, due to better interfacial interaction with the polymer, while the MNA's incorporating $–N_2$ functional groups showed significantly higher responses than the former due to formation of specific groups on the MWCNT's[179,244]. Importantly, on measuring the amperometric response towards AA, the $–N_2$ functionalised MWCNT's produced comparable response to the probe-optimised MNA's. Moreover, the fact this has been achieved at a low CNT loading highly favours a facile and a more economical fabrication strategy. Hence, these results points towards the superior properties of the $–N_2$ functionalised MWCNT's for electrochemical sensing.

5.6 Conclusions

In this chapter, various strategies towards the optimisation of the electrochemical response of the MNA's were investigated. Initially, the sonication parameters were optimised and a sonication time of 3 mins was found to be optimal, under which the nanocomposites MNA's produced an enhanced current response for $Fe(CN)_6$ and significantly higher amperometric response towards different concentrations of AA as compared to the base MNA. The effect of two cationic surfactants, i.e. CTAB and CPyCl were investigated for their dispersive power. Both surfactants were found be highly effective in dispersing the CNT's below their T_K and at a specific concentration of 5 mM. Although excessive surfactants could be removed in aqueous solutions by dispersing under the T_K, in organic solvents this was not found to be the case. As a result, the MNA's could not be fabricated successfully by incorporating the optimal surfactant concentration. It was found that MNA's could only be developed at 1 mM surfactant concentration, which did not improve the final functional properties of the MNA's. Finally, the effect of having different functional groups and dimensional parameters were investigated on MNA fabrication. It was found that, in order to process MNA's with high CNT loadings, length was an important parameter; as the longer MWCNT's with –COOH functional groups could be incorporated at 6 wt% loading as compared to their shorter versions. In contrast, it was also found that the shorter MWCNT's, regardless of their functionalities (i.e. $–NH_2$, $–N_2$, –COOH), showed enhanced electrochemical behaviour at lower loadings. This can be attributed to their higher aspect ratio and or the presence of more electroactive sites per unit mass. The MNA's incorporating $–N_2$ functionalised MWCNT's showed an enhanced electrochemical response at 1 wt% loading, comparable to that of –COOH functionalised MWCNT's at a higher loading of 6 wt%.

Chapter 6. Toxicity evaluations of MNA's

6.1 Introduction

MNA's pierce the stratum corneum barrier of the skin, leaving the microneedle tips directly in contact with the viable tissue. Therefore, biocompatible materials are mandatory for fabricating these devices. PLA, utilised successfully as the matrix component for incorporating CNT as nanofillers is considered biocompatible, as they are derived from renewable sources (such as corn and sugar); and its degradation products (i.e. lactic and glycolic acid) are non-toxic[66,193]. As such, PLA has been validated for several bio-applications including surgical implants, tissue engineering, dental materials and importantly as drug delivery systems[66,193,252]. Most nanomaterials, when used in its isolated form above a certain concentration threshold, can lead to toxicity in comparison to those that are embedded in a polymeric matrix[193,253]. Regardless, when used as biomaterials for fabricating *in situ* medical devices (as in this case), biocompatibility of the devices should be addressed in terms of both intrinsic and extrinsic factors. Intrinsic factors include size, shape, roughness, design, composition, surface chemistry, porosity, sterility, duration of contact and degradation products, whereas extrinsic factors are concerned with the host, site of implantation and the microenvironment[254,255]. Evaluation of these factors involve a complex body of work, that incorporates both *in vivo* and *in vitro* assessments directed towards cytotoxicity, inflammation, allergic and irritant responses and both acute and chronic toxicity. The International Organization of Standardization (ISO) has defined a set of standards (10993) for evaluating the biocompatibility of medical devices.

Due to the brittleness, slow crystallisation rate and low thermal resistance of PLA, incorporation of carbon-based nanomaterials is an innovative approach utilised by many researchers to improve their applicability, in particular for hard and soft tissue engineering applications[252]. Hence, numerous studies have evaluated the biocompatibility of CNT-based nanocomposites and have presented some promising results. Results from these studies suggest: (1) as various fabrication processes have been adopted to develop PLA based nanocomposites (i.e. solvent casting, spin coating, melt blending, electrospinning or doctor blading), a general consensus is that, the mode of fabrication does not affect cell metabolic activity and (2) the nanocomposites (films or nanofibers) do not decrease the metabolic

activity of numerous cell types *in vitro* and, as found on many instances, they may actually increase the metabolic activity[193]. A summary of important studies concerning these statements are given below.

Electrospun scaffolds developed with MWCNT for bone tissue engineering showed that cells can remain viable in a 3D matrix for up to 14 days, and in comparison to unfilled PLA, the CNT-filled nanocomposites showed increased cell density/metabolic activity and even alignment along the longitudinal axis after 7 days[256]. Application of direct current (d.c.) electrical stimulation to randomly orientated PLA/MWCNT nanocomposite scaffolds at 100 μA showed enhanced proliferation, adhesion and elongation of cells over 7 days. However, application of a higher magnitude of current i.e. 200 μA, was proven to be detrimental to cell survival[257]. To note, the current was applied for 4 hrs on each day. Better hemocompatibility, less clotting and resistance to platelet adhesion was found for PLA/MWCNT nanocomposites at 5 wt% when compared to the neat PLA and orientation of the nanocomposites was found to further enhance the aforementioned properties[258]. A recent study evaluating biocompatibility, both *in vitro* and *in vivo* (implanted subcutaneously for 2 weeks in C57B1/6 mice) for PLA/GNP (*graphene nanoplatelets*, at 2 wt%) and PLA/CNT-COOH (0.3 and 0.7 wt%) found no adverse effects. However, longer assays are needed to study the effect of material degradation and nanofiller release in time-dependant toxicity evaluations[259]. This is important when developing CNT nanocomposite-based MNA's, as any mechanical failure during insertion and removal can leave debris in the dermal tissue which will be degraded over time[260]. Although the results described above are promising, generalisability is poor due to the diversity in raw materials, their fabrication, surface chemistry and differing amounts of nanofiller incorporated.

The influence of electrical stimulation and or electrochemical processes directly on cells and or their microenvironment is an important area of research concerning metallic implants, potential therapeutics for various forms of cancer and even as novel therapy for human immunodeficiency virus [261–265]. These studies fall under a generalised category referred to as electrical stimulation of cells and has been studied since the 1970's[261,266]. Electrical stimulation induced effects based on the application of MNA-based electrochemical sensors can be classified into electrolytic, dielectric and cell/electrode interactive effects[267]. Electrolytic effects can be defined as those brought about by the redox reactions of electroactive components at the electrode surface in solution phase or the

constituents of the cells themselves. For example, an irreversible redox process involving physiological components of the cell membrane or the formation of reactive oxygen species from electrochemical processes may lead to cell death[261]. Dielectric effects refer to electroporation and electrofusion of cells, where application of high voltage pulses may breakdown the cell membrane, in addition to the formation of pores or fusion of the cell membranes[268,269]. Finally, cell/electrode interactive effects have been shown to modulate cell viability, proliferation, gene expression, protein synthesis, morphological and cytoskeletal organisation; at a low potential loading[267,270–272]. In relation to cytotoxic effects, several authors have employed a three-electrode system connected to a potentiostat (as used for electrochemical measurements), to apply a d.c. potential to the working electrode and monitor the effect of electrochemical stimulation on cells. For example, a potential of 1.0 V applied for 3 mins resulted in inhibition of HIV infection by 90%[264]; studies investigating corrosion assisted electrochemical voltage shifts in metallic implants have shown that application of voltage outside a viability range of 500 mV of anodic current can lead to cell death via necrosis[263]. Hence, these results illustrate the utility of studying voltage induced toxicity upon the application of MNA-based electrochemical sensors.

Mechanical safety of the devices is determined by evaluating the AFS and SFS of the MNA's; which for the nanocomposite MNA's developed here, have been proven to be significantly higher than skin insertion forces. A long-term study evaluating, inflammation and nanocomposite degradation associated toxicity *in vivo* is important, but is beyond the scope of this chapter and comes secondary to primary cytotoxicity evaluations. As our MNA-based electrochemical sensor is currently aimed at rapid diagnosis and monitoring purposes, the time required for these devices to be in contact with the viable tissue is rather limited. Therefore, two important aspects were investigated; the toxicity associated with (1) short term exposure to MNA's, and (2) time-dependant exposure to voltage during electrochemical measurements.

6.2 Aims and objectives

An extensive evaluation based on all three types of cytotoxicity tests described in part 5 of the ISO-10993 (which includes, evaluation by extracts, direct contact and indirect contact of medical devices) is beyond the scope of this chapter. Therefore, here the investigations were limited to evaluating the effects of MNA-based device extracts, using both the $–N_2$ and –COOH functionalised MWCNT/PLA nanocomposite MNA's. Moreover, their effects were evaluated using two cell lines: (1) human keratinocytes (HaCaT) and (2) human malignant melanoma cell line, A375. In addition to the standardised cytotoxicity evaluations, this chapter further examined the immediate effects of application of voltage to cells when performing electrochemical measurements. Overall, these investigations will help to further characterise the devices in terms of their biocompatibility and applicability towards the development of an electrochemical biosensor.

The objectives of this chapter are to:

1. Investigate both short and long-term toxicity to cells using extracts from the two devices
2. Investigate immediate toxicity associated with electrochemical measurements via DPV and amperometry

6.3 Materials and Methods

6.3.1 Cell lines and culture conditions

The human keratinocyte cell line (HaCaT) was kindly donated by Professor Green formerly from MRC centre, at the University of Sussex. This is a spontaneously transformed human epithelial cell line from adult skin. The A375 (ECACC 88113005) human malignant melanoma cells, which had been isolated from a 54-year-old female with malignant melanoma, was purchased from Sigma Aldrich, Gillingham, UK. These cell lines were used between passages 12 and 21. Both cell lines were cultured in Dulbecco's modified Eagle medium, with high glucose (DMEM, glucose 4.5 g/L) and supplemented with 10% and 15% foetal bovine serum (FBS) for HaCaT and A375, respectively. These medium compositions are hereafter referred to as the 'complete media' for each cell line, respectively. The cell culture media (Gibco) and plastics, including tissue culture flasks and multi-well plates were purchased from Fisher Scientific, Loughborough, UK. Typical cell culture conditions (referred to as standard conditions) were applied, i.e. 37°C under 5% CO_2 (95% air), with the media being replaced every 2 days and passaged upon reaching 75 – 80% confluency.

6.3.2 Toxicity evaluation using MNA extracts

6.3.2.1 Preparation of extracts

MNA devices fabricated from nanocomposite material alone (i.e. CNT-PLA without the PCL base and the electrical wire, which will not encounter viable tissue in the intended use case) were used to prepare device extracts. For effective sterilisation of the devices, the MNA's were left in the mould and sterilised by dry heat, under vacuum, at 160°C for 2 hours using the thermal oven that was initially used to prepare the MNA's. Once the dry-heat sterilisation process was complete, the MNA's were ejected from the mould in the laminar flow cabinet and washed x3 with PBS. The devices were then dried inside the laminar flow cabinet, for 1 hour with the UV irradiation. Following which each microneedle was weighed whilst maintaining sterile conditions. The extracts were prepared at a concentration of 0.2 $g.ml^{-1}$ using complete media as the extraction vehicle, accounting for both cell lines. The different extract times and exposure times utilised are summarised below in Table 1. Briefly, two main extractions were made by incubating the device in the media for 4 hrs and 24 hrs. These 100% extracts were then diluted into 6.25%, 12.5%, 25% and 50% using the

respective complete media for each cell line and exposed to the particular cell lines for 4 hrs and 24 hrs.

Table 6.1: Extract and exposure conditions for both cell lines

Extracts	Treatments (exposure time)	
4hrs +/- 0.5hrs at 37˚C	4hrs +/- 0.5hrs at 37˚C	24hrs +/- 2hrs at 37˚C
24hrs +/- 2hrs at 37˚C	4hrs +/- 0.5hrs at 37˚C	24hrs +/- 2hrs at 37˚C

6.3.2.2 Seeding density and cell viability assessment via MTT assay

The seeding density was determined for each cell line prior to extract exposure using standard MTT (3-[4, 5-dimethylthiazol-2-yl]-2, 5-diphenyltetrazolium bromide) assay. This assay is based on mitochondrial activity, represented by the conversion of yellow tetrazolium MTT into intracellular purple formazan crystals by metabolically active cells. Briefly, after passaging the cells, a total cell count was made using a haemocytometer (*section 2.4.*2) and dilutions were made with complete media to prepare suspensions with different cell numbers. A 100 µL suspension containing cell numbers ranging from 1000 – 40,000 was then added to wells in a 96-well plate in triplicates and cultured overnight under standard conditions. The culture media was then aspirated and washed once with PBS. 100 µL of MTT, prepared at 0.5 $mg.ml^{-1}$ using media without FBS was then added to each well and incubated in the dark under standard conditions for 2 hours. The MTT was then aspirated and the wells were washed again with PBS, before adding 100 µL of dimethylsulfoxide (DMSO) to each well to dissolve the formazan crystals at RT with gentle agitation for an hour. Absorbance was measured at 540 nm, with a reference measurement at 670 nm, using an EZ Read 2000 microplate reader (Biochrom Ltd, Cambridge, UK). Once the appropriate seeding density for each cell line had been determined, the protocol for the MTT assay was further utilised to determine cell viability following exposure to the different extracts. Percentage viability was calculated using equation 6.1.

$$\%\ \text{viability} = \frac{\text{absorbance of treated cells}}{\text{absorbance of untreated cells}} \times 100 \qquad \text{Equation 6.1}$$

6.3.3 Cytotoxicity evaluation by LDH assay

The activity of lactate dehydrogenase (LDH), an indicator of cytoplasmic membrane damage, was measured in both cell lines using the Pierce™ LDH cytotoxicity assay kit (Thermo Scientific, UK). After exposure of cells to the different concentrations of the extracts, 50 µL of supernatant were transferred to a fresh 96-well plate. These extracts were mixed with the 'reaction mixture' prepared from the assay kit (50 µL/well) and incubated at RT for 30 mins, protected from light. The reaction was then terminated by adding a further 50 µL of the 'stop' solution to each well. Absorbance was measured at 490 nm with a reference measurement at 680 nm, using the same microplate reader. Maximum LDH release was determined by total lysis of untreated cells with 1% Triton™ X-100 (Sigma Aldrich, UK). Percentage cytotoxicity was calculated using equation 6.2.

$$\%\ \text{cytotoxicity} = \frac{\text{LDH activity in treated cells} - \text{Spontaneous LDH activity}}{\text{Maximum LDH activity} - \text{Spontaneous LDH activity}} \times 100$$

Equation 6.2

6.3.4 Electrochemical measurement-induced toxicity evaluation

The toxicity to cells associated with electrochemical measurements involving DPV and amperometry were measured by trypan blue exclusion (live/dead cell count). The experimental set-up utilised for these studies is illustrated in Figure 6.1. A three-electrode set up was used as described previously for evaluating ascorbic acid (*section 4.3.4 and 4.3.5*) and the electrochemical measurements were run for 2 mins using both techniques. The MNA's were prepared as previously described in Chapter 4; however certain design modifications were made for practical handling purposes. Here, once the electrical contact was made, PLA was used as the base sealing polymer instead of PCL. This is because PCL did not have an appropriate amount of rigidity to hold a metallic stem (i.e. a copper nail) in

place. The copper nail was placed head on because of its weight, in order to ensure a firm contact with the cell monolayer in the experimental set-up shown in Figure 6.1

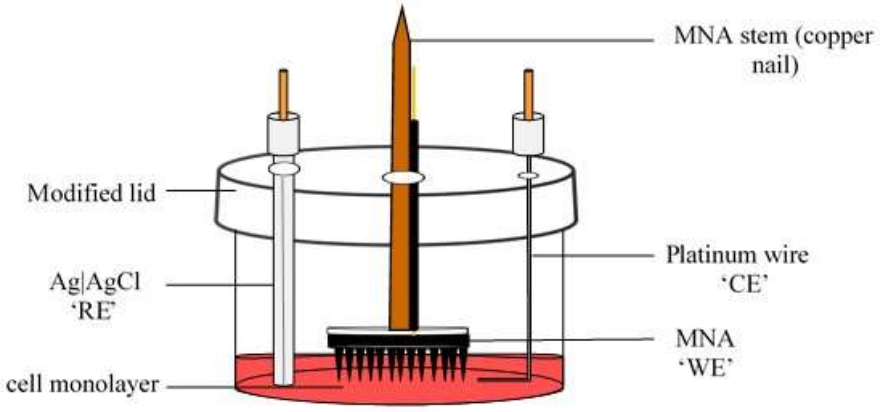

Figure 6.1. Experimental set-up for evaluation of electrochemical measurement induced toxicity. Modified lid to allow insertion of the electrodes. The MNA's were modified with a weighted stem to allow even contact with the cell monolayer. The set-up was connected to a potentiostat that was controlled by the manufacturer own software.

A standard 24-well tissue culture plate was modified for these studies by drilling three appropriately sized holes into the lids, for effective placement of the electrodes. HaCaT cells were seeded at 100,000 cells/well, whereas A375 cells were seeded at 80,000 cells/well. The MTT assays were performed once a fully confluent monolayer had been formed. To ensure sterility, the copper nail and the lid of the tissue culture plate were sterilised with 2 x washes in 70% ethanol and 3 x washes in PBS, followed by air drying under UV-light for 1 hour.

For trypan blue exclusion, the cells were detached by trypsinization and re-suspended in 1 ml complete media. An aliquot of 50 µL of the suspended cells were then mixed with an equal volume of 0.4% (w/v) trypan blue solution (Thermo Scientific, UK). 10 µL of this suspension was then loaded onto haemocytometer for cell counting. Total numbers were recorded in terms of live (clear cytoplasm) and dead (blue cytoplasm) cells. Percentage viability was determined using equation 6.3.

$$\% \text{ viability} = \frac{\text{number of viable cell count}}{\text{total cell count}} \times 100 \qquad \text{Equation 6.3}$$

6.3.5 Microscopic imaging of the cell monolayer

Visualisations of the cell monolayer was obtained using a digital stereo microscope equipped with a 3MP camera (Motic®, HK), using a 10x objective. Representative images are shown after scanning three samples and three different areas per sample.

6.3.6 Statistical analysis

Data were processed in Microsoft Office Excel 2016, analysed using GraphPad Prism 7 (GraphPad Software Inc., USA) and all data are expressed as mean ± standard deviation (SD). Where appropriate, statistical difference between groups was assessed using one- or two-way analysis of variance (ANOVA) with Sidak's multiple comparison test. Differences were considered statistically significant where $P < 0.05$.

6.4 Results

6.4.1 Seeding density

MTT was used to determine the seeding density for both cell lines as shown in Figure 6.2. The optimal seeding density was identified by a linear relationship between optical density (OD) and cell number, and at which the cells were 80% confluent. Hence, for A375 cell line 8,000 cells/well was selected whilst for HaCaT the optimum was 10,000 cells/well. The lower seeding density for the A375 cell line also caters for its high proliferating characteristic with a reported doubling time of 16 hrs[273], whilst for HaCaT, the doubling time is thought to be 24 h[274].

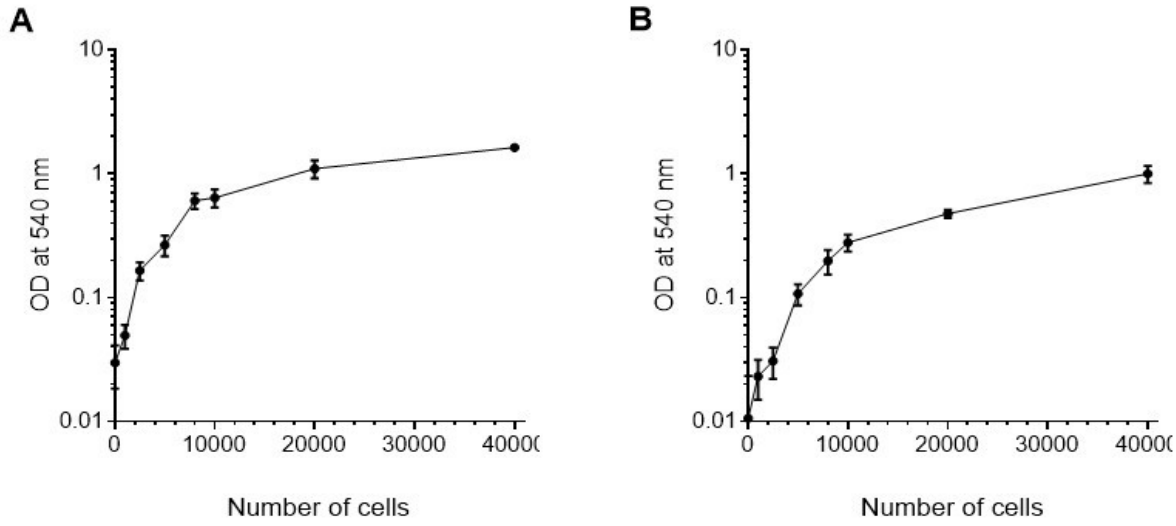

Figure 6.2 Seeding density determined by MTT assay: (A) A375, melanoma cell line and (B) HaCaT, human keratinocyte cell line.

6.4.2 Exposure to device extracts

Cell viability was determined in terms of maximum MTT metabolised by untreated cells in comparison to those exposed to different concentrations of the extracts prepared from MNA devices fabricated using both $–N_2$ and –COOH functionalised MWCNT's at 1 wt% and 6 wt% CNT loadings, respectively. Moreover, the viability assessments were carried out on HaCaT and A375 cell lines to evaluate any cell-specific variances.

6.4.2.1 –N_2 functionalised MWCNT/PLA MNA's

The effect of extracts derived from MNA's fabricated from 1 wt% –N_2 functionalised MWCNT's on A375 and HaCaT cell viability is shown in Figure 6.3. For the short exposure times, i.e. 4 hrs, both extracts (4-hr and 24-hr extract) did not influence cell viability in either cell line. In contrast, over longer exposure times, i.e. 24 hrs, both extracts showed a significant decrease in cell viability for both cell lines. The ISO standards specifies that a decrease in cell viability by 30% is toxic and hence not biocompatible. For the A375 cells (Figure 6.3, A), long-term exposure to the 4-hr extract was found to lower cell viability significantly at extract concentrations between 25 – 100%. At the lower concentrations of the extract (i.e. 25 and 50%) cell viability was reduced by 30%, though with a high SD at 20% ($P < 0.01$). However, on exposure to 100% concentrated extract, cell viability was reduced by 47 ± 13% ($P < 0.0001$), indicating that the extract can significantly affect cell viability. The 24-hr extract was also found to affect cell viability, but only at 100% concentration of the extract, where the viability was reduced by 28 ± 6% ($P < 0.001$). Similarly, for the HaCaT cells (Figure 6.3, B), at 100% concentration of the extract, cell viability was reduced almost equivalently by 27 ± 7% for both extracts, following long-term exposure to the cells. Regardless of the cell lines, for long-term exposure with either extract, a dose-dependent reduction in viability was not found.

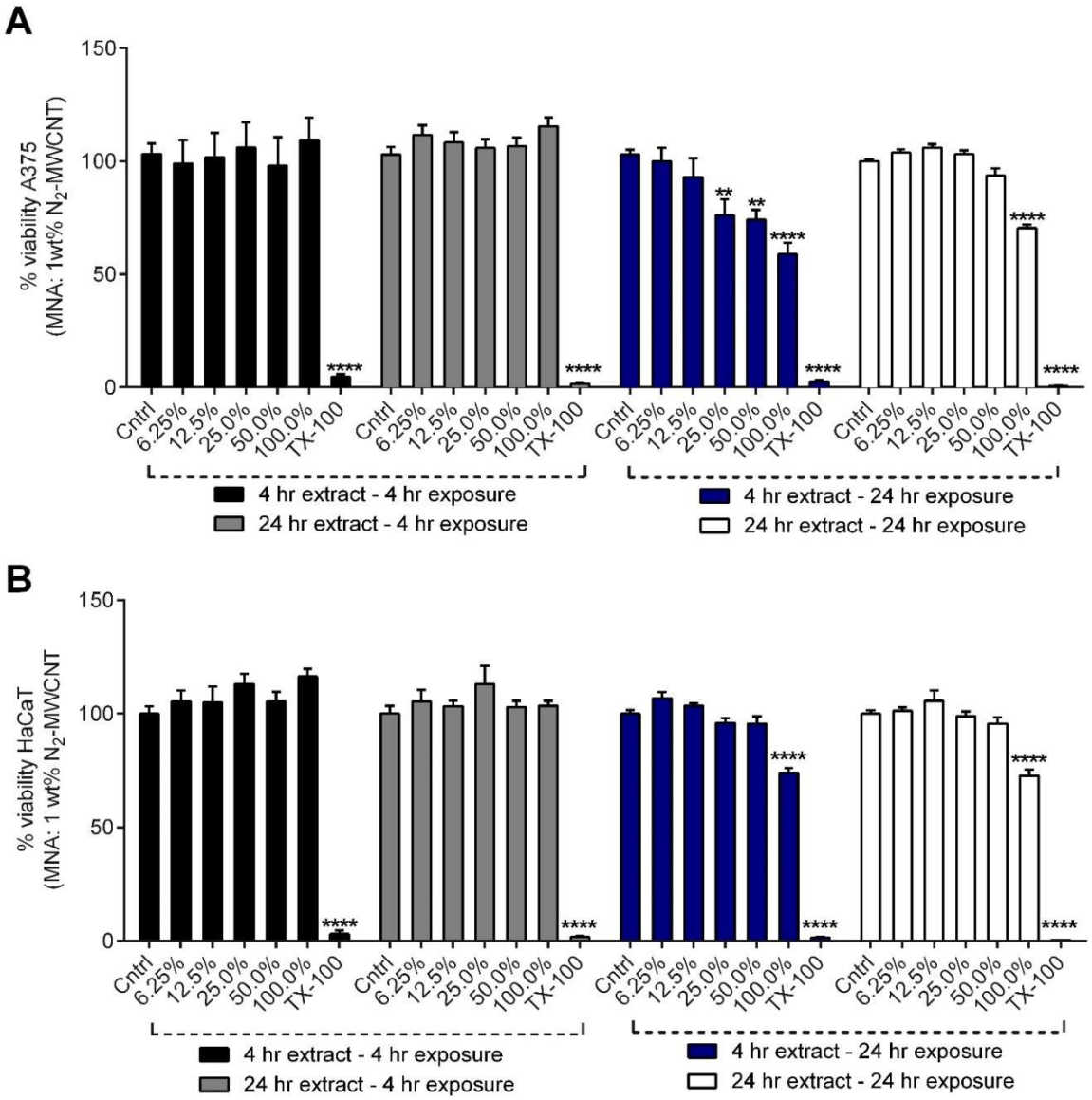

Figure 6.3. Viability of A375 (A) and HaCaT (B) cells post exposure to different concentrations of extracts prepared from 1 wt% -N_2 functionalised MWCNT/PLA based MNA devices. A375 and HaCaT cell response to varying extract and exposure conditions; showed a similar effect, with significant decline in cell viability following prolonged exposure (24 hrs) to extracts prepared from short and long-term incubation of the devices in cell culture media. (**p < 0.01, ****p < 0.0001, one-way ANOVA with Tukey's multiple comparison's test. Data represent mean ± SD, *n = 3.*

6.4.2.2 –COOH functionalised MWCNT/PLA MNA's

On evaluating cell viability upon exposure to extracts derived from 6 wt% –COOH functionalised MWCNT's (Figure 6.4), comparable results were found as previously described. Regardless of the extract, short-term exposure showed no adverse effects on cell viability for both cell lines. From long-term exposure to the 4-hr extract, the A375 cells showed significant reduction in cell viability from 12.5 – 100% (Figure 6.4, A). However, a 30% reduction in cell viability was only found at the highest concentration i.e. 100% where cell viability was found to be 62 ± 7%. Long-term exposure with the 24-hr extract also decreased cell viability by 30 ± 9 %, but only at 100% extract concentration. With respect to the HaCaT cells (Figure 6.4, B), long-term exposure to the 4-hr extract did not influence the viability of the cells. However, on exposure to the 24-hr extract, HaCaT cell viability was found significantly reduced by 16 ± 9 % ($P < 0.0001$); a reduction in cell viability less than 30%. Collectively, the results indicate that 24-hr extracts on long-term exposure have had a higher impact on A375 cell viability in comparison to the HaCaT cells.

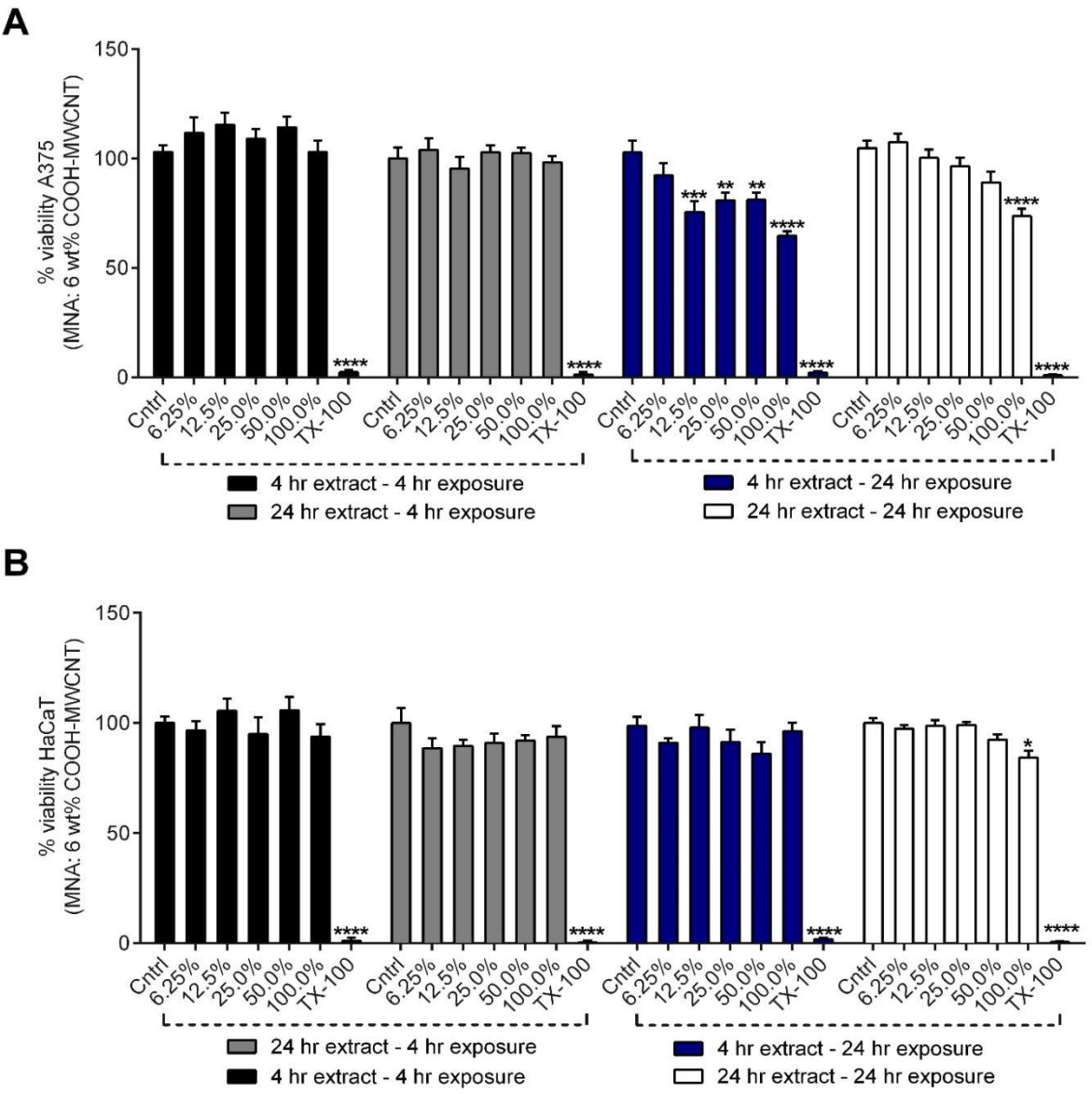

Figure 6.4. Viability of A375 (A) and HaCaT (B) cells post exposure to different concentrations of extracts prepared from 6 wt% -COOH functionalised MWCNT/PLA based MNA devices. A375 and HaCaT cell responses to varying extract and exposure conditions showed a similar effect, with significant decline in cell viability following prolonged exposure (24 hrs) to extracts prepared from short and long-term incubation of the devices in cell culture media. As an exception, the HaCaT cells showed no reduction in cell viability following long-term exposure to the 4-hr extract. (**p < 0.01, ****p < 0.0001, one-way ANOVA with Tukey's multiple comparison's test. Data represent mean ± SD, $n = 3$.

6.4.3 Cytotoxicity assessment via LDH release

6.4.3.1 –N2 functionalised MWCNT/PLA MNA's

The cell viability assay was further corroborated with cytotoxicity assessment by evaluating percentage LDH released from untreated cells (spontaneous release) and treated cells alongside a positive lysis control (maximum LDH available for release) by treating with TX-100^{TM}. LDH release upon treatment with MNA device extracts, based on $–N_2$ functionalised MWCNT/PLA nanocomposite MNA's, for A375 and HaCaT cells are shown in Figure 6.5, A-B). In contrast to the MTT, the LDH release from A375 in response to the extract treatment was comparable to that of the untreated cells; showing no evidence of toxicity regardless of exposure or the extract conditions. For the HaCaT cells, there was a significantly higher release of LDH on long-term exposure to both extracts at its highest concentration (i.e. 100%). Though the percentage increase in LDH release was less than 20% (i.e. 15% for the 4-hr extract and 6% for the 24-hr extract).

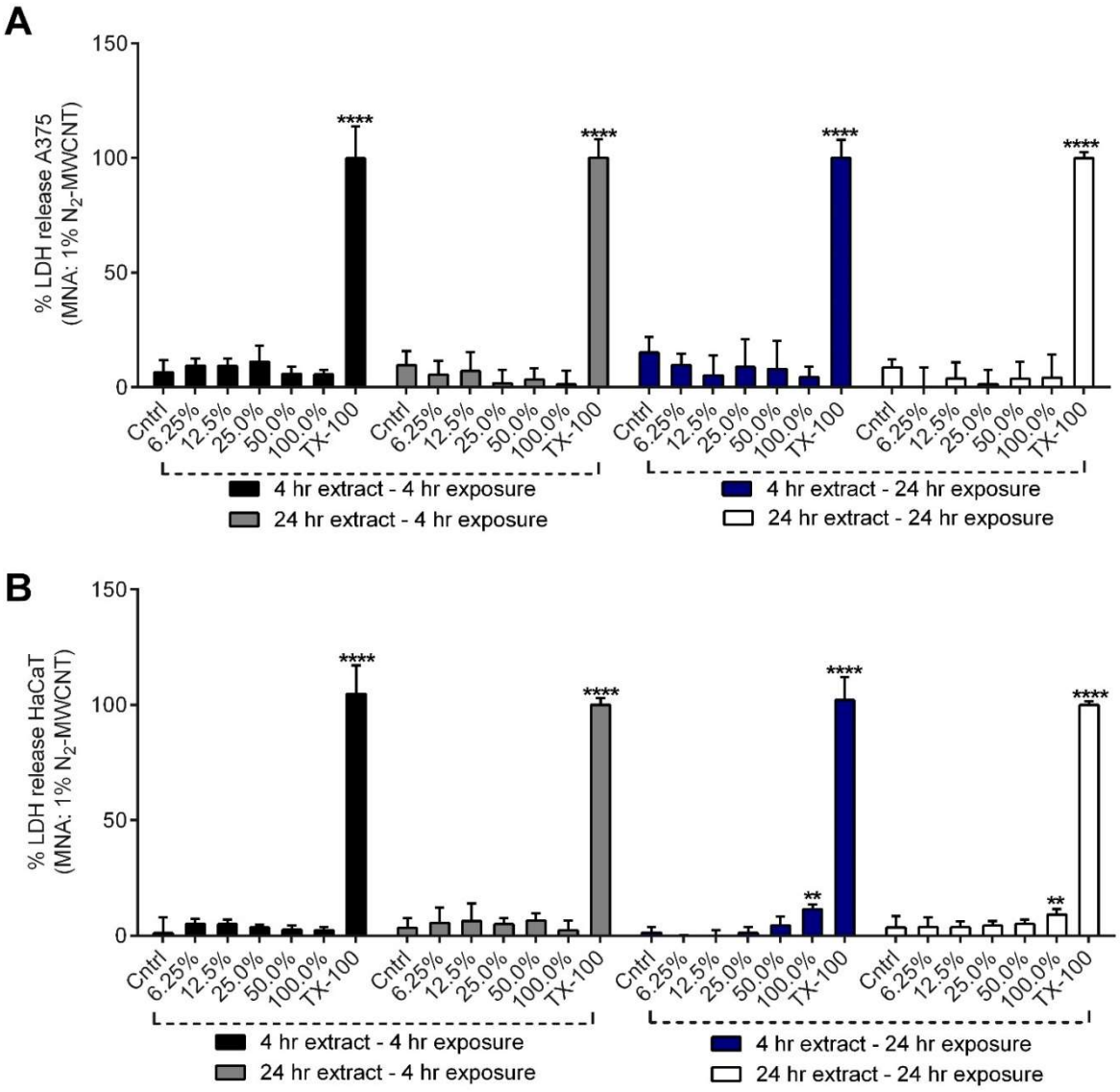

Figure 6.5 Cytotoxic effects on A375 (A) and HaCaT (B) cells post exposure to different concentrations of extracts prepared from 1 wt% –N_2 functionalised MWCNT/PLA based MNA devices. No cytotoxic effects were found post exposure for A375 cells, however for the HaCaT, long-term incubation with both extracts showed a significant increase in LDH release to the control. (**p < 0.01, ****p < 0.0001, one-way ANOVA with Tukey's multiple comparison's test (n = 3)).

6.4.3.2 –COOH functionalised MWCNT/PLA MNA's

In agreement with the results described previously, both long-term and shot-term exposure of A375 cells to extracts derived from –COOH functionalised MWCNT/PLA based nanocomposite MNA's also did not result in a significant increase in LDH activity relative to the controls (Figure 6.6, A). However, for the HaCaT's, long-term exposure with the 4-hr extracted showed significantly higher LDH release at 50% concentration of the extract ($P < 0.1$, percentage increase by 7%); whilst exposure to 24-hr extract produced significantly higher LDH release at 100% concentration ($P < 0.1$, percentage increase by 6%). Regardless, in these LDH assays, the total LDH released is less than < 15%, therefore indicating that the extracts are non-toxic to both cell types.

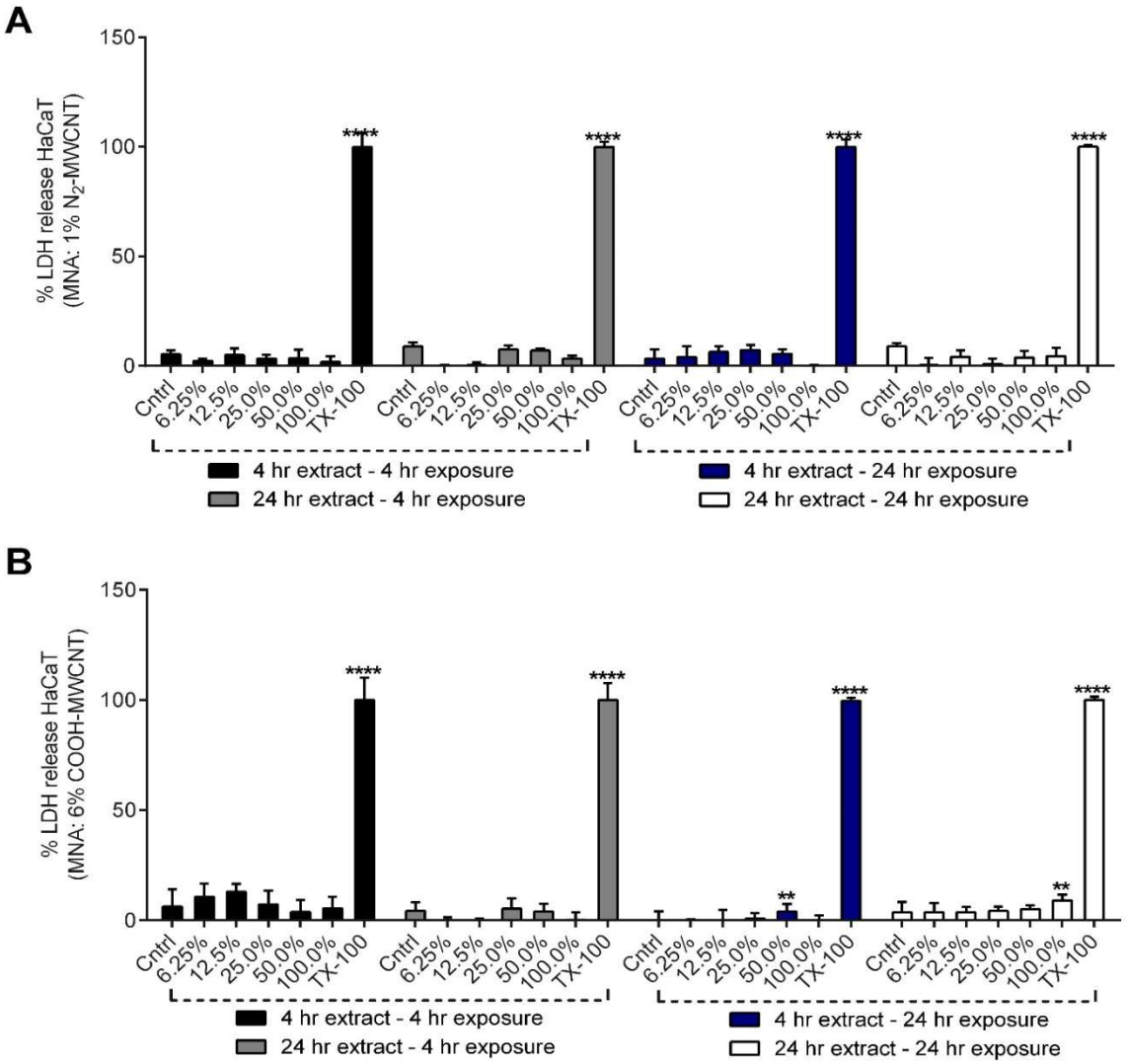

Figure 6.6. Cytotoxic effects on A375 (A) and HaCaT (B) cells post exposure to different concentrations of extracts prepared from 6 wt% -COOH functionalised MWCNT/PLA based MNA devices. No cytotoxic effects were found post exposure to extracts as the percentage LDH release was similar to untreated cells in A375 and HaCaT cells. Long-term exposure with the 24-hr extract showed a significant increase in toxicity in comparison to the control for the HaCaT cells. (*p < 0.1, ****p < 0.0001, one-way ANOVA with Tukey's multiple comparison's test. Data represent mean ± SD, *n = 3*.

6.4.4 Electrochemical measurement-induced toxicity

Toxicity associated with electrochemical measurements involving DPV and amperometry was assessed using both types of MNA's, and against both cell types (i.e. A375 and HaCaT's). The experimental setup was the same for both techniques, as shown in Figure 6.7. Control measurements were taken with the microneedles in place (i.e. on the cell monolayer), but without the application of voltage.

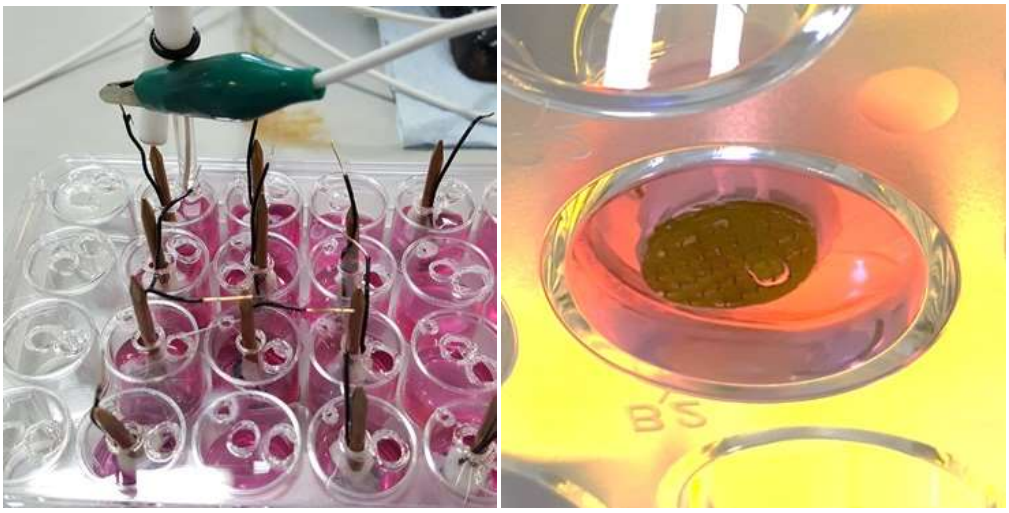

Figure 6.7. Images of the experimental set-up: (a) Three-electrode setup with the reference, working and counter electrode accurately placed in a single well in 24-well plate and (b) the MNA resting on top of the cell monolayer.

6.4.5 Cell viability evaluation on DPV recordings

The immediate effect of DPV based electrochemical recordings on the viability of A375 and HaCaT cells were evaluated (Figure 6.8). The results here indicate no adverse effect on cell viability from implementing the DPV recording on the cell monolayer. However, it must be noted that some of the cells on the adhered monolayer that came into contact with the sharp projections of the MNA's had detached and subsequently washed away during a typical experimental procedure. This was un-avoidable to an extent because of the physical manipulation involved during the placement of the MNA's and the experimental set-up. The influence of applied voltage on the detachment is unclear because the control measurements also showed detachment of the adherent cells. Figure 6.9 shows representative micrographs of HaCaT cells; indicative of the reasoning above.

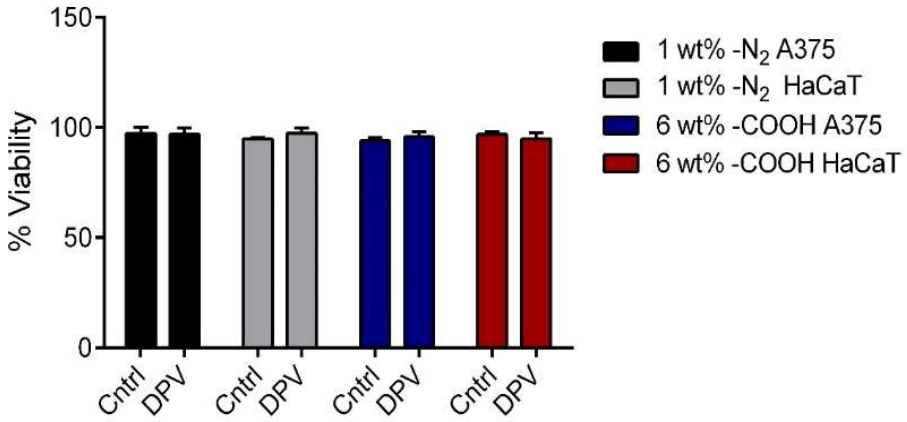

Figure 6.8. Assessment of viability via trypan blue exclusion following DPV stimulation. DPV stimulations were run from 0 – 1V, using both the -N_2 functionalised MWCNT and -COOH functionalised MWCNT/PLA nanocomposite MNA's on each cell line. Control measurements were taken without the application of voltage. Data shows no impact on cell viability after DPV stimulation. Two-way ANOVA; data represent mean ± SD, n = 3.

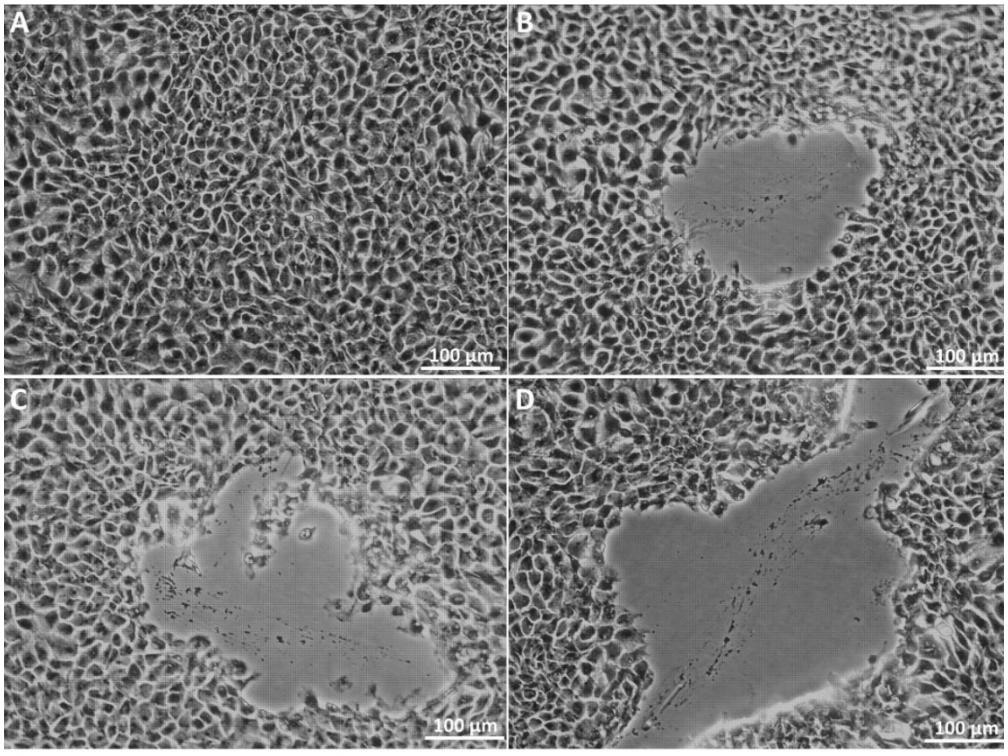

Figure 6.9 Micrographs of HaCaT cells before and after electrical stimulation. (a) Confluent monolayer of HaCaT cells; (b) control without electrical stimulation showing detachment of cells post impact from a single microneedle; (c) detachment of cells from the impact of a single microneedle following electrical stimulation and (d) experimental manipulation causing displacement of microneedles; causing more of the cells to detach.

6.4.6 Cell viability evaluation on amperometric measurements

After biasing the MNA's to a particular voltage, cell viability was assessed based on both MNA's and cell types by implementing amperometric measurements. As seen in Figure 6.10, this again showed no significant effect on cell viability even when the voltage applied was as high as 1.2 V. No difference was found in relation to the different cell types that were evaluated here. A persistent issue that remained concerned the detachment of cells upon the impact with the MNA's, which were subsequently washed away alongside the media during routine experimental procedure.

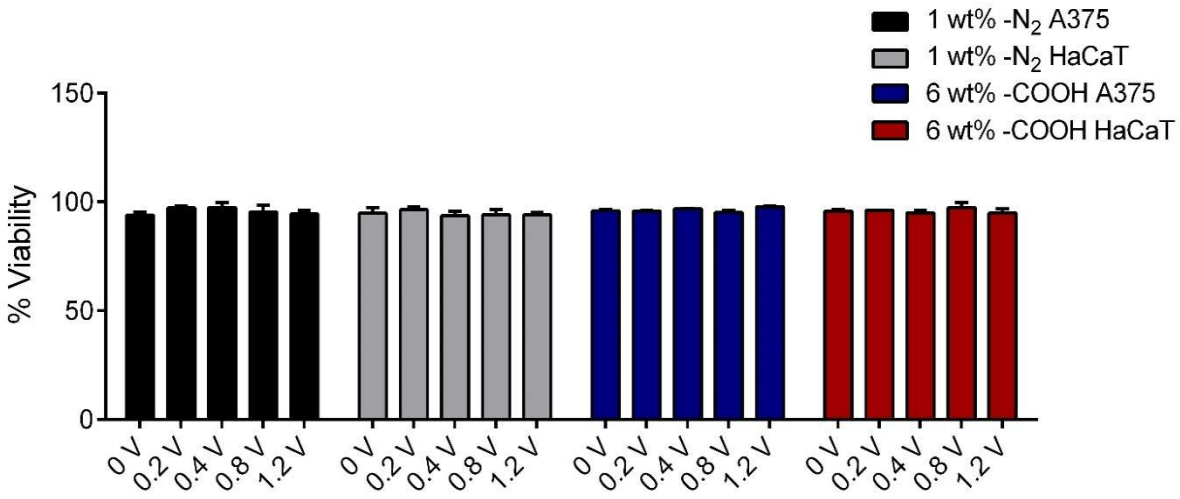

Figure 6.10. Assessment of viability via trypan blue exclusion following amperometric stimulation: The applied potential to the MNA's and hence the cells ranged from 0 – 1.2 V, with 0 V indicating a control without the application of a specific voltage. One-way ANOVA with Tukey's multiple comparison's test. Data represent mean ± SD, *n = 3*

6.5 Discussion

The ISO has specified cytotoxicity evaluation as one of the key biological evaluation and screening tests that can provide simple, fast and highly sensitive information by using tissue cells *in vitro* to monitor cell growth, reproduction and morphological effects on exposure to medical devices. The ISO describes three types of cytotoxicity tests for biological evaluation of medical devices, however the experiments here, were limited to exposure of cells to MNA device-based extracts, using the 6 wt% –COOH and 1 wt% $–N_2$ functionalised MWNCT/PLA nanocomposite MNA's. As the ISO guidelines do not account for the diversity of medical devices and especially the nature and complexity of the interaction at specific sites on the human body; primary investigation was also carried out to assess the immediate effect of electrochemical measurements on cell viability using the nanocomposite MNA's. There are numerous applications for MNA based sensors, i.e. from subcutaneous monitoring of clinically relevant analytes to detection of specific markers in cancerous tissues[2,49,52,57]; hence cytotoxicity should be addressed in both normal and pathological cell types. This is important, because cellular responses to toxic agents/treatments may vary significantly between different cell types[275]. Thus, toxicity was evaluated using normal cells e.g. kertainocytes and diseases cells e.g. melanocytes in this chapter.

Initially, when monitoring the effect on cells exposed to different concentration of the extracts derived from the two nanocomposite MNA devices, the MTT assay showed a general trend whereby cell viability was significantly reduced following long-term (i.e. 24-hr) exposure to the cells for both extract conditions (i.e. 4-hr and 24-hr). When comparing the cell viability for both cell lines on long-term exposure to the 4-hr extracts prepared from both devices, it is conclusive that the extracts had greater effect on the viability of A375 cells in comparison to the HaCaT cells (Figure 6.3 and 6.4). In fact, long-term exposure to the 4-hr extract derived from 6 wt% –COOH functionalised MWCNT/PLA did not actually influence the viability of HaCaT cells. However, it was notable that, cell viability was significantly reduced at low concentrations (i.e. 12.5%) for the 4-hr extract regardless of the MNA device on exposure to the A375 cell lines, in comparison to the HaCaT cells. In HaCaT cells, cell viability was significantly compromised only at the highest concentration of the extract (i.e. at 100%). However, the percentage reduction in cell viability was not

proportional to the concentration of the extract for the A375 cells. This non-proportionality is reported as a challenge associated with the MTT assay itself and have been reported by several authors in unrelated studies; as reviewed in Li *et al.*[276]. Most probable experimental causes involve variances in cell density and most importantly time. It has been suggested that, a dose-related toxicity can be obtained from an MTT assay, but only after significant optimisation concerning the influence of time when testing medical devices[276]. In relation to the A375 cells, the most notable difference between the 4-hr and 24-hr extract on long-term exposure was that, the 24-hr extract only reduced viability at its maximum concentration. This is contrary to expectations, as the extract prepared over 24 hrs should contain more of the leached components that is responsible for reducing cell viability as opposed to the 4-hr extract. As the components leaching into the media during incubation of the MNA device has not yet been identified, it is difficult to ascertain a possible cause. The reduction in cell viability is unlikely due to the release of nanoparticles from the nanocomposite MNA's themselves as the MWCNT's are embedded in the PLA matrix. However, in a scenario where nanoparticles are indeed released into the media, over longer incubation times, as in the case for the 24-hr extract, components of the media (i.e. mainly proteins) can adsorb on to the surface of nanoparticles forming a protein corona[277]. The nanoparticles may relate to the MWCNT's themselves, catalyst contaminants incorporated during CNT fabrication and other components from the uncharacterised PLA. Nevertheless, since the interaction between nanoparticles and the cells is mediated by the outermost layer of the nanoparticles, protein corona formation may lower the effect of nanoparticles on cell viability[278]. Such a phenomenon can therefore explain why reduction in cell viability was only associated with the maximum extract concentration for the 24-hr extract, where there may be some uncoated nanoparticles present.

In terms of differences between the MNA devices, the A375 cells shows no conceivable difference in cell viability from long-term exposure to the device extracts. However, the viability of HaCaT cells on exposure to the extracts derived from $–N_2$ functionalised MWCNT/PLA nanocomposites showed a greater reduction in comparison to the –COOH functionalised MWCNT/PLA devices (Figure 6.3 and 6.4). Between the two devices, the MWCNT's used were different not only in terms of the functional groups present, but also their structural characteristics. The $–N_2$ functionalised MWCNT's used were shorter in length, smaller in diameter and had a higher surface area in comparison to

the –COOH functionalised MWCNT's. These factors have all been shown to influence toxicity when CNT's are in their isolated form. The extent to which each factor is influential in determining cytotoxicity is yet to be established. However, a recent study has indicated that the diameter is inversely proportional to cell viability (toxic below 40 nm in diameter), while functionalisation with –COOH groups was shown to mitigate the effect on cell viability as compared to pristine MWCNT's[254]. This mitigating effect was reasoned to be effect of sedimentation in cell culture media, which in turn is influenced by the adsorption of the proteins from the cell culture media. The aforementioned study also reported that –COOH functionalised MWCNT's can attract distinct types of proteins to different extents. Therefore, the type and amount of proteins adsorbed onto the $–N_2$ functionalised MWCNT's may differ to some extent, depending on the type of interactions formed[254]. Hence, if indeed MWCNT-based nanoparticles have leached out of the nanocomposite MNA's, it is important to determine the toxicity associated with the type of nanotubes to fully comprehend the results from cytotoxicity evaluations. Overall, the MTT results indicate no cytotoxicity over short-term exposure (i.e. 4 hrs) from either device regardless of the extraction conditions. In contrast, long-term exposure showed a significant reduction in cell viability, more so for the A375 cells and for the extract prepared over 4 hrs. In terms of application, the nanocomposite MNA-based electrochemical sensors have only been evaluated for one-off measurements thus far and they were carried out in real-time. Hence the MNA's, only remain in contact with the viable tissue for a short-period of time (i.e. a few minutes), which consequently limits the possibility for constituents to leach out of the MNA's. However, in the case that constituents of the MNA's have been leached and they remain within the tissue, it may affect the viability of the cells.

Cytotoxicity was further evaluated using LDH assay, a marker of cytoplasmic damage. However, the results obtained in this study contradicted that of the MTT assay; as regardless of the extract or exposure conditions, the level of LDH activity measured indicated no cytotoxicity. Assuming that, the toxicity is caused by leached nanoparticulates from the nanocomposite MNA's; this result indicates the possibility of interference from the nanoparticles to the LDH assay. In fact, it has been recently reported in the literature that nanoparticles in general can interfere with both MTT and LDH assays[279]. For MTT, (1) the absorbance from the particles can add to the MTT absorbance, (2) particles can adsorb the formazan compound thus reducing the absorbance from the MTT assay and (3) the formazan

compound can be produced by the particles themselves hence adding to the assay absorbance. In terms of the LDH assay, (1) the particles can adsorb the LDH, thereby preventing the LDH from being measured or (2) the particles can inactivate the LDH enzyme non-specifically by generating free radicals on the surface preventing LDH from being measured. If the interference from the nanoparticles is to be factored in, an alternative explanation can be given to the MTT results as well. With reference to CNT's, Wörle-knirsch *et al.* reported that SWCNT exposure can give false-positive MTT results, as they interact with the MTT-formazan crystals formed after the reduction of MTT; resulting in stabilisation of their chemical structure[280]. As a result, the MTT-formazan crystals cannot be solubilised. Other factors involve the adsorption of proteins from the media causing in-direct toxicity[281]. However, since this only occurs at high concentrations of CNT (0.4 – 0.8 mg/ml), an amount unlikely to be released from the nanocomposite MNA's, the influence of indirect toxicity can be ruled out. In comparison to the MTT, fewer studies have reported interference to LDH assay with reference to CNT's. Importantly, the results obtained are also conflicting. In terms of SWCNT, Wörle-knirsch *et al.* initially reported that LDH activity is not influenced by SWCNT[280], however, Wang *et al.* showed that both oxidised and pristine SWCNT's can reduce the absorbance of formazan[282]. Moreover, since CNT's may not be the only type of nanoparticle present in the extract, others may adsorb/inactive LDH to different extents, depending on their type and characteristics[279]. When considering these arguments, although there were differences between the MTT and LDH assay, the toxicity was only observed at low levels and only on prolonged exposure. Thus, it gives more confidence to the use of nanocomposite MNA's for rapid bioanalysis. Further analysis is however imperative, especially in identifying the leached components present in the extract.

Other than the cytotoxicity induced by contact or leached components from the nanocomposites materials, electrochemical measurements also play a crucial role in mediating cytotoxicity. In this study, the immediate effect of electrochemical measurements on cells were investigated. It was found that regardless of the MNA device or the cell line, DPV or amperometric measurements on cell monolayers did not lead to cytotoxicity. However, the results shown here may not be representative due to an experimental limitation, that resulted in cells close to the vicinity of the MNA's to be detached from the impact of the microneedles and subsequently washed away during routine experimental procedure. As the duration of the experiment was limited to 2 mins for both electrochemical measurements,

any detrimental effects to cells is likely to have occurred for those around the vicinity of individual microneedles. Gabi *et al.* showed that at current densities higher than 0.5 A m^{-2}, myoblasts cultured directly on top of a microelectrode can undergo cell death, within 2 mins of exposure[283]. It may also be case that, the duration until which the test measurements were run was insufficient to induce any cytotoxicity. Tominaga *et al.* showed that a noticeable difference in cellular morphology could only be identified when a potential of 1 V was applied for over 10 mins[284]. In contrast, Kumagai *et al.* showed that the same potential applied for a shorter period (i.e. 5 mins) decreased the proliferation rate of cells when cultured over 3 days by ~75%[266]. Overall, further optimisation to the experimental set-up is required to accurately assess the impact of electrochemical measurements on cells and thereby assess cytotoxicity.

6.6 Conclusions

In this chapter, cytotoxicity evaluations were carried using Kertainocyte and Melanoma cell lines to assess the biocompatibility of nanocomposite MNA's fabricated by incorporating MWCNT's with differing functional groups (i.e. $–N_2$ and –COOH) into PLA matrices. Results indicate that, although the nanomaterials are embedded within a polymeric matrix, they could still release nanoparticles which can cause cytotoxicity. MTT assays confirm this, as the cell viability was reduced significantly. However, it is not currently known whether the reduction in cell viability was associated with mitochondrial damage or interference to the assay under the assumption that nanoparticles interacting with the MTT-formazan crystals can prevent its solubilisation; thereby reducing the absorbance. This is further validated by the fact that LDH assay showed no evidence of cytotoxicity and as with this assay, there are limited reports suggesting interference from nanoparticles. Preliminary investigations were also carried out to evaluate the cytotoxicity associated with electrochemical measurements i.e. DPV and amperometry. Although, the results presented here showed no evidence of toxicity, further optimisation to the experimental set-up is required to address the cytotoxicity to cells near the vicinity of the MNA electrodes. Furthermore, long-term investigations are needed to address the effect on cells post exposure to electrochemical measurements.

6.7 Further work

With respect to the cytotoxicity evaluations carried out in this chapter, future directions to the research have already been discussed. However, there are several other factors that need to be addressed further in order to obtain a comprehensive understanding of the cytotoxicity associated with MNA's fabricated from MWCNT/PLA nanocomposites. In terms of the nanocomposites, cytotoxicity associated with direct contact to the nanocomposite MNA should be evaluated to account for both short-term and long-term exposure. Within that, a crucial factor to be accounted for is the influence of surface chemistry, as MNA's have been fabricated with MWCNT's containing two different functional groups. A major concern regarding the application MNA's is mechanical safety. Even with the existing evidence that the nanocomposite MNA's produced here can withstand forces significantly higher than that required skin insertion and removal, unwanted movements and or accidental slippage during insertion/removal can decrease the margin of safety. Therefore, it is important to study the toxicity associated with the degradation products of PLA/MWCNT nanocomposites. MNA based electrochemical sensors can be used for various applications as shown by several researchers. Therefore, microenvironmental changes associated with the electrochemical measurements are an important factor to consider, particularly when used in acidic microenvironments such as that of melanoma.

Chapter 7. General discussion and future work

7.1 General discussion

The generation of minimally invasive, reliable and low-cost *in vivo* biosensors that enable, real-time detection and monitoring of clinically relevant molecules can significantly improve patient health care. As such, they are of great interest to the biomedical community. MNA based electrochemical sensors are highly opportunistic in this respect, as they sample from the intradermal layers of the skin. The electrochemical detection strategies employed by these sensors are distinctly advantageous because they combine fabricational simplicity (in terms of a low-cost and non-complex sensor design) with ease of usage; by a minimally trained individual at the point-of-care[20]. However, clinical acceptability of MNA-based electrochemical sensors is dependent on fabricating highly selective and sensitive electrodes through a scalable strategy.

Several approaches have been demonstrated towards the fabrication of MNA based electrochemical sensors. These can be categorised in to *ex situ* and *in situ* biosensors. As evident from the literature review (Chapter 1), a majority of the research concerning MNA-based electrochemical sensors is centred on transdermal glucose monitoring, and primarily, the research has focused on developing microfluidic devices to extract and analyse biofluids (i.e. *ex situ* sensors). However, challenges associated with fabrication, collection of biofluid, maintenance of flow rate, miniaturisation and systems integration have shifted the focus towards the development of *in situ* electrochemical sensors. Various formats of these devices now exist, employing both hollow and solid microneedle architectures; and have successfully demonstrated continuous glucose monitoring (CGM) as well as detection of other clinically relevant analytes. Concealing modified carbon fibres and pastes within hollow polymeric MNA's is the most prominent approach employed[51–53,57,58,285], however solid MNA-based electrodes are far more advantageous as it provides a larger electroactive surface area for biomolecular detection. Thus, yielding a greater current response and an improved signal-to-noise ratio[60]. Solid-MNA based sensors are typically fabricated from micromachined or lithographically processed silicon or metallic MNA's, that are then metallised and coated with various functional materials to produce the electroactive surfaces[2,12,42,55]. Although recent works have simplified this approach by replacing the

silicon/metallic MNA's with polymeric counterparts and by employing micromoulding as a facile fabrication strategy; the latter processes have remained[49,65]. Developing electroactive surfaces by metallising the microneedles with gold (Au) or platinum (Pt) is expensive and limits scalability. Therefore, an attractive alternative is to develop MNA-based electrodes from nanocomposites; where cost-effective and versatile formulations can be produced with desirable functional and mechanical properties using a wide range of materials. This opportunity remains largely unexplored, with only a single report published along the time-line of the research presented in this thesis[56].

Envisioning the development of nanocomposite MNA's, CNT's were chosen as the ideal candidate because their material properties allow for enhanced mechanical strength and electrochemical properties. In relation to the fabrication of various electrochemical sensors, CNT's have been used, mainly as modifiers of GCE's or Au electrodes. CNT-paste electrodes remain the only example where bulk nanocomposites are employed for electrochemical sensing[90,286,287]. Typically, these electrodes incorporate a high loading of CNT (i.e. > 15% w/w), in order to achieve good electrochemical properties. Incorporating high loadings of CNT is not problematic when considering a simple planar structure that is commonly used for electrochemical sensing. However, with reference to the finite structure of microneedles, clusters of CNT's formed at high loadings can negatively impact the mechanical strength or even the formation of MNA's. Improvements in mechanical and electrical properties upon the inclusion of CNT's into polymeric matrices have been extensively investigated; however, they have not been correlated to electrochemical properties. Choosing the right polymeric matrix is also a key challenge, as it must cater for ease of processability with nanofiller incorporation and should possess sufficient mechanical strength for skin penetration. Considering the factors described above, this thesis evaluated whether solid MNA's can be developed from nanocomposites by incorporating CNT's at an optimal loading ratio to confer appropriate mechanical and electrochemical characteristics towards their function as an *in situ* biosensor.

Primary investigations in this thesis were concerned with the selection of an appropriate matrix. Epoxy resin was initially chosen, because they offer the simplest route towards nanocomposite MNA fabrication via thermal cross-linking to achieve the desired physical form. They have also been studied extensively for manufacturing advanced nanocomposites for a range of applications including that of biosensing. As there are

numerous types of epoxies and a selection of curing agents; which ultimately govern their material properties, three different epoxy formulations were evaluated for their potential to form MNA's via micromoulding with good mechanical properties[88]. Application of low pressure was considered the most critical parameter in forming MNA's successfully. This was based on two reasons: (1) air bubbles incorporated when add-mixing the curing agents can form voids/air pockets within the finished product and they can act as the source of mechanical failure. (2) Microneedles are unlikely to form by thermal curing of the epoxy alone, as there is no pressure difference for the epoxy sample to be drawn into the microneedle cavities inside the micromould.

The challenge in developing epoxy MNA's concerned the fact that, micro or nano-bubbles can from *in situ* during the cure reaction. Therefore, if a reduced pressure is applied throughout the cure reaction, bubbles formed can expand, creating large voids in the finished product. This phenomenon was indeed confirmed by experimentation (Figure 3.4) and it was found to occur in all epoxy samples evaluated. Therefore, different pressure variations were investigated prior to thermal curing, and it was found that the pressure had to be reduced to 200 mbar for 45 mins prior to thermal curing in order to form a complete MNA. Importantly, at this reduced pressure setting MNA's could be developed from all epoxy samples. Quantitative evaluation of the microneedle strength in terms of axial fracture strength (AFS) and shear fracture strength (SFS) showed that the RX771C – standard epoxy was the weakest, with needles breaking off almost instantaneously (Figure 3.9, D); whereas the electron microscopy (EM) grade epoxy formulations displayed a more elastic fracture behaviour, with sufficient axial and shear forces for skin insertion (Figure 3.10). The EM grade medium epoxy formulation was found to produce the best results on mechanical tests and therefore was used to prepare nanocomposites.

The key characteristic to be achieved when developing polymeric nanocomposites is excellent interfacial interaction between the host polymer and the CNT's. For this reason, MWCNT's chemically functionalised with carboxyl groups (i.e. *f*-MWCNT) were used. Employing the optimised method for fabricating neat epoxy MNA's, it was found that both blending and solution mixing methods, even with sonication was inadequate to form MNA's with homogenously dispersed CNT's and indicated poor interfacial interaction with the polymer. As a final attempt, the MNA fabrication method was optimised further by adding a centrifugation step, to determine if a tight packing could be achieved. The results here were

not promising, with several microneedles formed without any CNT's present in them. Moreover, the nanocomposite microneedles that had formed appeared to be very brittle, breaking off inside the micromould during manual ejection. The key message from this chapter was that excellent interfacial interaction is critical to form nanocomposite MNA's. The most important consideration when considering epoxy as a matrix, is associated with its matrix stiffness. It has been found that soft epoxy matrixes are better suited for preparing CNT-based nanocomposites because CNT's can accelerate the curing process, resulting in better interfacial interactions between the host polymer and CNT's[141]. In stiff epoxy matrixes, homopolymerisation can occur between epoxide molecules, resulting in a poor interfacial interaction[141]. Although, there is scope for evaluating a softer blend of the EM grade epoxy, the mechanical characteristics may not be adequate for skin penetration; as on occasions almost an entire array was found to break off inside the mould when the medium epoxy formulation was used to prepare the nanocomposites.

Poly (lactic acid) (PLA) was seen as a viable alternative to epoxy for several reasons. Foremost, they possessed better mechanical strength in terms of AFS and SFS when compared to epoxy-based microneedles. PLA can form hydrogen bonds with *f*-MWCNT's, therefore a good interfacial interaction was anticipated[204,205]. Finally, they are easily processed by solution mixing using organic solvents of low boiling points[66]. In terms of electrochemical sensing, PLA/CNT nanocomposites have only ever been used as modifiers of electrodes as shown in two recent studies[194,195]. Notably, in these studies excellent electrochemical activity had been achieved at low CNT loadings (i.e. 1 wt%). However, it must be acknowledged that, these nanocomposites were prepared by *in situ* polymerisation and solution-blow spinning; processes known to produce higher performance nanocomposites when compared to solution mixing. As nanocomposite MNA fabrication is a novel approach, the potential for a solution mixing process to produce nanocomposite MNA's with good functional properties was pursued throughout this thesis. Importantly, the solution mixing process offers a convenient route to fabricate nanocomposite MNA's without compromising mechanical and electrical properties, as opposed to a simpler process such as melt-mixing[67,142].

As shown in Chapter 4, solid MNA-based sensors were fabricated successfully by micromoulding using nanocomposite films prepared by solution mixing *f*-MWCNT's with PLA. The fabrication steps discussed are simple and easy to scale up, with further adaptation

possible using compression moulding or hot embossing techniques, thus allowing rapid prototyping capabilities. The nanocomposite MNA's had excellent mechanical properties for skin penetration and they were able to function well as an electrochemical biosensor at a *f*-MWCNT loading of 6 wt%. Initial characterisation was done by measuring the responses to varying concentrations of ascorbic acid (AA) using differential pulse voltammetry (DPV) and amperometry. With reference to DPV, a linear oxidative response was seen at a low potential of 320 mV. As CNT's are effective in reducing the overvoltage for electrochemical reactions, the oxidative peak observed here was at a lower potential than those reported for unmodified platinum (Pt) and carbon paste working electrodes for AA; (at 0.530 V and 0.470 V, respectively)[113].[206] Although their limit of detection (LOD) was lower, at 87 µM for the Pt and 20 µM for CP electrodes, the LOD achieved by nanocomposite MNA's were remarkable (164.38 µM); considering that bulk nanocomposite-based electrodes in a MNA format was directly connected to an electrochemical analyser for the first time and used for bioanalysis. Amperometric analysis in comparison showed a more stable response, with a lower LOD at 16.79 µM and also showed lower relative standard deviation (RSD) between devices i.e. 12% as opposed to 24% from DPV measurements.

A crucial point in this research was the discovery that the nanocomposite MNA's can function well as an *in situ* biosensor. This was demonstrated by measuring electroactive changes in porcine ear skin by DPV (at a potential window of 0 – 1 V). It was found that the nanocomposite MNA's could successfully measure diffusion of PBS through the skin; characterised by the evolution of two oxidative peaks with time at 0.23 and 0.69 V. This electrochemical signature was universal to all skin samples analysed, however large variations were evident. Nevertheless, the diagnostic potential of this signature waveform was analysed through an artificial burn wound model. This showed an attenuated oxidative response at 0.69 V at the site of the thermal injury and importantly, the impact of the burn could be measured at progressive distances from the burnt skin site. Collectively, the above results validated that the nanocomposite MNA's are electroactive and can monitor dynamic changes the skin.

Although, a good electrochemical performance was seen for the nanocomposite MNA device fabricated with a CNT loading of 6 wt%, optimisation of this base device was necessary in order to reduce their resistive behaviour as seen from their cyclic voltammetric characterisation (CV- Figure 4.7, A), which showed no response to a ferricyanide redox

couple. With the current level of sensitivity (1.113 nC mM^{-1} and 18.04 pA μM^{-1}, respectively for DPV and amperometry), quantitation of clinically relevant analytes and biomarkers may also be challenging due their sub-micromolar physiological concentrations.

Chapter 5 details work carried out to optimise the nanocomposite MNA's. Firstly, the sonic bath used for dispersing the CNT's was replaced with a probe-type sonicator and an optimal sonication time was determined by carefully monitoring particle size via a laser diffraction particle size analyser and quality of the dispersion by UV-Vis spectral analysis. This endeavour was found to be worthwhile as the electrochemical performance from the nanocomposite MNA's could be improved drastically by sonicating the sample for 3 mins at 100% amplitude. Amperometric analysis of MNA response towards varying concentrations of AA showed that the average response from three devices was 1,340% higher in comparison to the previous version (bath sonicated nanocomposite MNA) (Figure 5.5). The improved LOD and sensitivity for the 3-min-probe sonicated MNA's was 0.51 µM and 6.525 nA μM^{-1}, respectively.

As improving the dispersion of CNT's had such a profound effect on nanocomposite electrochemical properties, it was investigated whether incorporation of surfactants would further enhance the effect. Aside from the benefits of improved dispersion, surfactants themselves can play an active role in improving the electrochemical behaviour of the electrodes. This includes, increasing the rate of oxidation and reversibility of electrode processes towards many analytes as well as reducing electrode fouling by preventing the adsorption of oxidative products by electrostatic repulsion[240–243]. Therefore, the effect of two cationic surfactants (i.e. cetyltrimethylammonium bromide – CTAB and cetyl pyridinium chloride – CPyCl) was investigated. One of the major concerns associated with the incorporation of the surfactants is the problem of excess, which can severely impair the functional performance of the nanocomposites. Therefore, choosing the accurate concentration of surfactant to be incorporated into the nanocomposite formulation is critical. Literature does exist, where researchers have identified this critical concentration, however these works were carried out in water-based systems[218,227]. Hence, they may not be directly transferable to solvent-based systems. One of the ways to get around this problem is to disperse the CNT with surfactant below their Krafft point (T_K). The literature detailing such an approach had shown that, in water-based systems, excess surfactants that remain after the exfoliation process will crystallise out of the suspension and can be easily removed

regardless of the concentration being used[228]. Taking these results cautiously, the effect of surfactant T_K on dispersibility of CNT's was initially investigated. Results were in agreement with the literature, as it was found that CNT's were exfoliated better at temperatures below the surfactant T_K for both surfactants. As a next step, the effect of different concentrations for both surfactants were also analysed (1 – 15 mM) as it was not known what an excess amount would be. Dispersing below the surfactant T_K, an appropriate concentration for both surfactant was found to be 5 mM, above which the particle sizes were seen to increase, possibly due to multiple layers of surfactant wrapping around the nanotubes. Unlike the results obtained in water-based systems, the excess surfactant at any given concentration did not crystallise out of suspension in these experiments. Rather, a clear layer of CNT free region formed on top of the suspension and it appeared to be increasing in volume with increasing surfactant concentration (Figure 5.11, A). In an attempt to remove all of the excess surfactants, the suspension was centrifuged. However, this resulted in complete sedimentation of the CNT's from suspension (Figure 5.11, B). Nevertheless, nanocomposites MNA's were fabricated with the excess surfactant at all concentrations to determine if any improvements had been made with the incorporation of surfactants. From a fabricational point of view, the nanocomposites were mechanically weak as MNA's could only be developed from those incorporating a concentration of 1 mM, for both surfactants. As expected, CV and amperometric characterisation showed poor electrochemical response from the MNA's. Further optimisation work with surfactants was not pursued in this thesis.

The final optimisation step addressed the influence of different dimensionalities and functional groups on MWCNT's, on the electrochemical behaviour of the nanocomposite MNA's. The *f*-MWCNT's used up until this point were 20 – 30 nm in outer diameter and 10 – 30 µm in length. For assessing the effect of dimensionalities MWCNT's with the same functional group (i.e. –COOH) was purchased with a smaller length (i.e. 1 – 12 µm) and outer diameter (i.e. < 20 nm). With reference to the different length parameters, the former was referred to as 'long' and the latter as 'short' MWCNT's. In addition, short MWCNT's functionalised with $–N_2$ and $–NH_2$ groups were also used to assess the influence of different functional groups. First and foremost, the research reported here determined the limit of fabrication when employing the shorter nanotubes with different functional groups. Two key observations were made: Firstly, for the shorter nanotubes, regardless of the functional groups present the maximum loading at which nanocomposite MNA's could be fabricated

with the sonication-optimised method was 3 wt%. Secondly, the concentration at which the CNT's were dispersed (0.5 wt%) was inadequate for effective dispersion of the $–N_2$ and $–NH_2$ functionalised MWCNT's in particular. This is because the longer alkyl chain provides greater repulsion between the nanotubes, which consequently yields an increased surface area that is being inadequately wetted by the available volume of the solvent[163]. The difference in maximum loading meant that an effective comparison in terms of electrochemical behaviour could not be obtained between the long and short MWCNT's with same and different functional groups. However, at 3 wt% CNT loading an interesting pattern was observed whereby the current generated was significantly higher in the order of $–N_2$ > $–NH_2$ > –COOH functionalised MWCNT's (short).

It was hypothesised that reducing the concentration at which the MWCNT's are being dispersed (i.e. 0.5 wt%) would enhance the electrochemical behaviour and mechanical strength of the MNA's. Therefore, different concentrations were evaluated, and the data obtained from particle size and dispersion analysis helped identify that 0.05 wt% is the ideal concentration at which CNT's are maximally dispersed at their lowest particle size. Using this concentration, the fabrication limit was re-assessed. Interestingly, it was found that, whilst MNA's could be fabricated from long carboxyl functionalised MWCNT/PLA nanocomposites at a CNT loading of 6 wt%, regardless of the functional groups present, MNA's could only be fabricated at a maximum CNT loading of 1 wt% from nanocomposites developed with the shorter version of MWCNT's. This result highlighted length as an import factor with reference to long and short carboxyl functionalised MWCNT's and as for the $–N_2$ and $–NH_2$ functionalised MWCNT's, insufficient amount of polymer to properly wet the increased surface area obtained from greater repulsion between the nanotubes could be an additional factor[163]. However, in order to determine the resultant effect from using MWCNT's with varying functional groups and dimensionalities, the mechanical and electrochemical properties of the nanocomposite MNA's were characterised.

With reference to the mechanical properties, it was seen that the MNA's developed at the optimised concentration with 1 wt% CNT loading produced comparable mechanical performance to that of the probe optimised MNA's composed of the long –COOH functionalised MWCNT's at 6 wt% CNT loading. However, there were no notable differences when comparing the different functionalities or dimensions. In terms of the current generated, at 1 wt% CNT loading, microneedles incorporating the long –COOH

functionalised MWCNT's did not generate a response. Interestingly, at the same loading, the shorter carboxyl functionalised MWCNT's was able to generate a response. A plausible explanation maybe be attributed to the higher aspect ratio for the shorter carboxyl functionalised MWCNT's and more importantly, as the electrochemical activity is dependent on edge-plane-like graphitic sites that occur at the open ends and along the tube axis of MWCNT's, the shorter nanotubes may present more electroactive sites per unit mass when compared to the longer MWCNT's[109,110]. Comparison between the different functional groups with the same dimensions yielded the same pattern as before, with the current generated being significantly higher in the order of $–N_2$ > $–NH_2$ > –COOH functionalised MWCNT's. In contrast, the amperometric measurements of AA showed that MNA's incorporating just 1 wt% of $–N_2$ functionalised MWCNT's can produce comparable responses to that of 6 wt% probe-optimised MNA's. This is resultant of the enhanced electron transfer process, aided by the formation of quaternary nitrogen and pyridinic-*N*-oxide groups on $–N_2$ functionalised MWCNT's. In addition, this result also points towards the efficiency of the current fabrication method, resulting in enhanced dispersions. As such, a good electrochemical response was achieved from solution mixed nanocomposites at such a low CNT loading; which is otherwise only seen when nanocomposites are developed by *in situ* polymerisation. Consequently, the lower loadings also make the fabrication more economical.

In terms of performance, as two comparable nanocomposite MNA-based devices have now been fabricated, it was essential to start assessing their biocompatibility. This was pursued in Chapter 6, where cytotoxicity evaluations were carried out using human keratinocyte cell line (HaCaT) and A375 human malignant melanoma cells (A375) in order to evaluate device and cell specific toxicity based on exposure to both MNA device extracts and uniquely, electrochemical measurements (i.e. DPV and amperometry). With regards to MNA device-based extracts, an interesting finding was that, MTT and LDH assays produced different results. With MTT, regardless of the extract prepared (i.e. 4 hrs or 24 hrs) or the device, long-term (i.e. 24 hrs) exposure was seen to reduce the viability of the cells; more so for the A375 cells in comparison to the HaCaT cells for extract concentration as low as 12.5 %. In contrast, the LDH activity measured did not actually indicate any cytotoxicity. A possible explanation for this disparity was given assuming a scenario that nanoparticles are released from the MNA based devices. Indeed, the constituent that is released from the

nanocomposite MNA's have not yet been identified. However, if nanoparticles are released, the literature details that both MTT and LDH assays can yield false-positive results[279]. However, this problem has been more commonly reported with the MTT assay. Here, nanoparticles can interact with the MTT-formazan crystals and prevent its solubilisation; resulting in reduced absorbance[280]. Electrochemical measurement induced cytotoxicity was further assessed. DPV and amperometric stimulations showed no evidence of voltage mediated cell toxicity. However, optimisations are necessary in order to address the methodological limitation whereby cells near the vicinity of the microneedles were seen to wash off due to abrasions caused by the sharp projections and from experimental manipulations.

Overall, this body of work shows that solid MNA-based electrochemical sensors can be fabricated successfully from nanocomposites of PLA and CNT, with sufficient mechanical strength for skin penetration and good electrochemical properties for rapid intradermal bioanalysis. An optimal strategy for developing nanocomposite MNA's have been demonstrated through optimisation of the processing conditions. Alongside this, specific details on how CNT characteristics (i.e. dimensions and functional groups) can influence the processing conditions and the resultant functional properties have also been demonstrated. Fabrication of only the working electrode is demonstrated here at present, but it is envisaged that reference and counter electrodes can be fabricated using a similar approach. MNA sensors produced from CNT based composites could serve as a template for a range of sensors, due to the variety of modification strategies employable.

7.2 Future directions

A number of research avenues can be explored to further optimise the nanocomposites MNA's developed in this body of work, with the aim of directing them towards practical applications.

- In terms of the design, bringing the electrical contact closer to the base or even the microneedle surface can drastically improve the electrochemical behaviour of the microneedles. This is based on the fact electrochemical reaction occur along the surface of the nanocomposite microneedles. Therefore, by placing an electrical contact close to the surface, a path of least resistance is facilitated. In polymeric

nanocomposites, the longer the conductive path the higher the resistance. This is because, the resistivity of the polymer is several orders higher than that of CNT's.

- Partially removing the layer of the polymer that forms the smooth surface of the nanocomposite MNA's by plasma etching could make the MNA's more electroactive. Electrochemical behaviour improves because the number of sites available for electrocatalysis increases. Moreover, this could be an efficient method to attach biomolecules directly to the active components (i.e. CNT's). Consequently, the MNA-based electrodes can be made highly selective with improved sensitivity.

- In this body of work, the MWCNT's used were all functionalised with different chemical groups. This was to overcome the poor dispersibility of pristine MWCNT's and to improve interfacial interaction with the polymer. Recent research has highlighted that by using probe sonication, pristine MWCNT's can be dispersed effectively in specific organic solvents including chloroform, without the addition of surfactants. Hence, this opens up another avenue to explore the impact of CNT characteristics on the functional performance of the nanocomposite MNA's. Alternatively, if it is not possible to achieve a good dispersion of pristine MWCNT's, exploring the use of PEDOT: PSS as conductive surfactants maybe a worthwhile endeavour.

- Alternative approaches to nanocomposite fabrication can be explored, especially that of *in situ* polymerisation because it is known to produce nanocomposites with a lower percolation threshold.

- As detailed in Chapter 6, future studies are required to identify the constituents that are released from the nanocomposite MNA's and correlate them to toxicity or false-positive results from the cytotoxicity assays. Moreover, the existing methodology should be adapted in order to address toxicity to cells near the vicinity of the microneedle-based electrodes induced by electrochemical measurements.

REFERENCES

1. Kim, Y. C., Edelhauser, H. F. & Prausnitz, M. R. Targeted delivery of antiglaucoma drugs to the supraciliary space using microneedles. *Investig. Opthalmology Vis. Sci.* **55,** 7387 (2014).
2. Keum, D. H., Jung, H. S., Wang, T., Shin, M. H., Kim, Y.-E., Kim, K. H., Ahn, G.-O. & Hahn, S. K. Microneedle biosensor for real-time electrical detection of nitric oxide for *in situ* cancer diagnosis during endomicroscopy. *Adv. Healthc. Mater.* **4,** 1153–1158 (2015).
3. Roy, R. S. Vaccination appliance. (1952).
4. Roy, R. S. Injection device. (1965).
5. Gerstel, M. S. & Place, V. A. Drug delivery device. (1976).
6. Kim, Y. C., Park, J. H. & Prausnitz, M. R. Microneedles for drug and vaccine delivery. *Adv. Drug Deliv. Rev.* **64,** 1547–1568 (2012).
7. Henry, S., McAllister, D. V., Allen, M. G. & Prausnitz, M. R. Microfabricated microneedles: a novel approach to transdermal drug delivery. *J. Pharm. Sci.* **87,** 922–925 (1998).
8. Mikszta, J. A., Alarcon, J. B., Brittingham, J. M., Sutter, D. E., Pettis, R. J. & Harvey, N. G. Improved genetic immunization via micromechanical disruption of skin-barrier function and targeted epidermal delivery. *Nat. Med.* **8,** 415–419 (2002).
9. McAllister, D. V., Wang, P. M., Davis, S. P., Park, J.-H., Canatella, P. J., Allen, M. G. & Prausnitz, M. R. Microfabricated needles for transdermal delivery of macromolecules and nanoparticles: fabrication methods and transport studies. *Proc. Natl. Acad. Sci. U. S. A.* **100,** 13755–13760 (2003).
10. Wang, P. M., Cornwell, M. & Prausnitz, M. R. Minimally invasive extraction of dermal interstitial fluid for glucose monitoring using microneedles. *Diabetes Technol. Ther.* **7,** 131–141 (2005).
11. Windmiller, J. R., Valdés-Ramírez, G., Zhou, N., Zhou, M., Miller, P. R., Jin, C., Brozik, S. M., Polsky, R., Katz, E., Narayan, R. & Wang, J. Bicomponent microneedle array biosensor for minimally-invasive glutamate monitoring. *Electroanalysis* **23,** 2302–2309 (2011).
12. Moniz, A. R. B., Michelakis, K., Trzebinski, J., Sharma, S., Johnston, D. G., Oliver, N. & Cass, A. Minimally invasive enzyme microprobes: an alternative approach for continuous glucose monitoring. *J. Diabetes Sci. Technol.* **6,** 479–480 (2012).
13. Corrie, S. R., Fernando, G. J. P., Crichton, M. L., Brunck, M. E. G., Anderson, C. D. & Kendall, M. A. F. Surface-modified microprojection arrays for intradermal biomarker capture, with low non-specific protein binding. *Lab. Chip* **10,** 2655 (2010).
14. Indermun, S., Luttge, R., Choonara, Y. E., Kumar, P., du Toit, L. C., Modi, G. & Pillay, V. Current advances in the fabrication of microneedles for transdermal delivery. *J. Controlled Release* **185,** 130–138 (2014).
15. Tuan-Mahmood, T. M., McCrudden, M. T. C., Torrisi, B. M., McAlister, E., Garland, M. J., Singh, T. R. R. & Donnelly, R. F. Microneedles for intradermal and transdermal drug delivery. *Eur. J. Pharm. Sci. Off. J. Eur. Fed. Pharm. Sci.* **50,** 623–637 (2013).
16. Akhtar, N. Microneedles: an innovative approach to transdermal delivery- A review. *Int. J. Pharm. Pharm. Sci.***6***,* 18-25 (2014).
17. Paliwal, S., Hwang, B. H., Tsai, K. Y. & Mitragotri, S. Diagnostic opportunities based on skin biomarkers. *Eur. J. Pharm. Sci.* **50,** 546–556 (2013).

18. Shoo, B. A., Sagebiel, R. W. & Kashani-Sabet, M. Discordance in the histopathologic diagnosis of melanoma at a melanoma referral center. *J. Am. Acad. Dermatol.* **62,** 751–756 (2010).
19. Inamadar, A. & Palit, A. Immunohistochemistry: relevance in dermatology. *Indian J. Dermatol.* **56,** 629 (2011).
20. Ventrelli, L., Marsilio Strambini, L. & Barillaro, G. Microneedles for transdermal biosensing: current picture and future direction. *Adv. Healthc. Mater.* **4,** 2606–2640 (2015).
21. Davidson, M. B. Starting insulin therapy in type 2 diabetic patients: does it really matter how? *Diabetes Care* **28,** 494–495 (2005).
22. Blonde, L. Easing the transition to insulin therapy in people with type 2 diabetes. *Diabetes Educ.* **33,** 232S-240S (2007).
23. Khanna, P., Strom, J. A., Malone, J. I. & Bhansali, S. Microneedle-based automated therapy for diabetes mellitus. *J. Diabetes Sci. Technol. Online* **2,** 1122–1129 (2008).
24. El-Laboudi, A., Oliver, N. S., Cass, A. & Johnston, D. Use of microneedle array devices for continuous glucose monitoring: a review. *Diabetes Technol. Ther.* **15,** 101–115 (2013).
25. Zimmermann, S., Fienbork, D., Stoeber, B., Flounders, A. W. & Liepmann, D. A microneedle-based glucose monitor: fabricated on a wafer-level using in-device enzyme immobilization. *IEEE* **1,** 99–102 (2003).
26. Mastrototaro, J. The minimed continuous glucose monitoring system (CGMS). *J. Pediatr. Endocrinol. Metab. JPEM* **12,** 751–758 (1999).
27. Cass, A. E. G. & Sharma, S. in *Methods Enzymol.* (eds. Thompson, R. B. & Fierke, C. A.) **589,** 413–427 (Academic Press, 2017).
28. Stout, P. J., Peled, N., Erickson, B. J., Hilgers, M. E., Racchini, J. R. & Hoegh, T. B. Comparison of glucose levels in dermal interstitial fluid and finger capillary blood. *Diabetes Technol. Ther.* **3,** 81–90 (2001).
29. Boyne, M. S., Silver, D. M., Kaplan, J. & Saudek, C. D. Timing of changes in interstitial and venous blood glucose measured with a continuous subcutaneous glucose sensor. *Diabetes* **52,** 2790–2794 (2003).
30. Battelino, T., Phillip, M., Bratina, N., Nimri, R., Oskarsson, P. & Bolinder, J. Effect of continuous glucose monitoring on hypoglycemia in type 1 diabetes. *Diabetes Care* **34,** 795–800 (2011).
31. Hermanides, J., Phillip, M. & DeVries, J. H. Current application of continuous glucose monitoring in the treatment of diabetes: Pros and cons. *Diabetes Care* **34,** S197–S201 (2011).
32. Voskerician, G. & Anderson, J. M. in *Wiley Encycl. Biomed. Eng.* (ed. Akay, M.) (John Wiley & Sons, Inc., 2006).
33. Ferri, S., Kojima, K. & Sode, K. Review of glucose oxidases and glucose dehydrogenases: a bird's eye view of glucose sensing enzymes. *J. Diabetes Sci. Technol.* **5,** 1068–1076 (2011).
34. Smart, W. H. & Subramanian, K. The use of silicon microfabrication technology in painless blood glucose monitoring. *Diabetes Technol. Ther.* **2,** 549–559 (2000).
35. Kobayashi, K. & Suzuki, H. A sampling mechanism employing the phase transition of a gel and its application to a micro analysis system imitating a mosquito. *Sens. Actuators B Chem.* **80,** 1–8 (2001).

36. Suzuki, H., Tokuda, T. & Kobayashi, K. A disposable “intelligent mosquito” with a reversible sampling mechanism using the volume-phase transition of a gel. *Sens. Actuators B Chem.* **83,** 53–59 (2002).
37. Suzuki, H., Tokuda, T., Miyagishi, T., Yoshida, H. & Honda, N. A disposable on-line microsystem for continuous sampling and monitoring of glucose. *Sens. Actuators B Chem.* **97,** 90–97 (2004).
38. Tsuchiya, K., Nakanishi, N., Uetsuji, Y. & Nakamachi, E. Development of blood extraction system for health monitoring system. *Biomed. Microdevices* **7,** 347–353 (2005).
39. Li, C. G., Lee, K., Lee, C. Y., Dangol, M. & Jung, H. A minimally invasive blood-extraction system: elastic self-recovery actuator integrated with an ultrahigh- aspect-ratio microneedle. *Adv. Mater. Deerfield Beach Fla* **24,** 4583–4586 (2012).
40. Li, C. G., Lee, C. Y., Lee, K. & Jung, H. An optimized hollow microneedle for minimally invasive blood extraction. *Biomed. Microdevices* **15,** 17–25 (2013).
41. Invernale, M. A., Tang, B. C., York, R. L., Le, L., Hou, D. Y. & Anderson, D. G. Microneedle electrodes toward an amperometric glucose-sensing smart patch. *Adv. Healthc. Mater.* **3,** 338–342 (2014).
42. Yoon, Y., Lee, G., Yoo, K. & Lee, J. B. Fabrication of a microneedle/CNT hierarchical micro/nano surface electrochemical sensor and its *in-vitro* glucose sensing characterization. *Sensors* **13,** 16672–16681 (2013).
43. Mukerjee, E. V., Issseroff, R. R., Collins, S. D. & Smith, R. L. Microneedle array with integrated microchannels for transdermal sample extraction and *in situ* analysis. *IEEE* **2,** 1439–1441 (2003).
44. Chua, B., Desai, S. P., Tierney, M. J., Tamada, J. A. & Jina, A. N. Effect of microneedles shape on skin penetration and minimally invasive continuous glucose monitoring in vivo. *Sens. Actuators Phys.* **203,** 373–381 (2013).
45. Jina, A., Tierney, M. J., Tamada, J. A., McGill, S., Desai, S., Chua, B., Chang, A. & Christiansen, M. Design, development, and evaluation of a novel microneedle array-based continuous glucose monitor. *J. Diabetes Sci. Technol.* **8,** 483–487 (2014).
46. Strambini, L. M., Longo, A., Scarano, S., Prescimone, T., Palchetti, I., Minunni, M., Giannessi, D. & Barillaro, G. Self-powered microneedle-based biosensors for pain-free high-accuracy measurement of glycaemia in interstitial fluid. *Biosens. Bioelectron.* **66,** 162–168 (2015).
47. Hwa, K. Y., Subramani, B., Chang, P. W., Chien, M. & Huang, J. T. Transdermal microneedle array-based sensor for real time continuous glucose monitoring. *Int J Electrochem Sci* **10,** 2455–2466 (2015).
48. Valdés-Ramírez, G., Li, Y. C., Kim, J., Jia, W., Bandodkar, A. J., Nuñez-Flores, R., Miller, P. R., Wu, S. Y., Narayan, R., Windmiller, J. R., Polsky, R. & Wang, J. Microneedle-based self-powered glucose sensor. *Electrochem. Commun.* **47,** 58–62 (2014).
49. Sharma, S., Huang, Z., Rogers, M., Boutelle, M. & Cass, A. E. G. Evaluation of a minimally invasive glucose biosensor for continuous tissue monitoring. *Anal. Bioanal. Chem.* **408,** 8427–8435 (2016).
50. Sharma, S., El-Laboudi, A., Reddy, M., Jugnee, N., Sivasubramaniyam, S., Sharkawy, M. E., Georgiou, P., Johnston, D., Oliver, N. & G. Cass, A. E. A pilot study in humans of microneedle sensor arrays for continuous glucose monitoring. *Anal. Methods* **10,** 2088–2095 (2018).

51. Windmiller, J. R., Zhou, N., Chuang, M.-C., Valdés-Ramírez, G., Santhosh, P., Miller, P. R., Narayan, R. & Wang, J. Microneedle array-based carbon paste amperometric sensors and biosensors. *The Analyst* **136,** 1846–1851 (2011).
52. Mohan, A. M. V., Windmiller, J. R., Mishra, R. K. & Wang, J. Continuous minimally-invasive alcohol monitoring using microneedle sensor arrays. *Biosens. Bioelectron.* **91,** 574–579 (2017).
53. Mishra, R. K., Vinu Mohan, A. M., Soto, F., Chrostowski, R. & Wang, J. A microneedle biosensor for minimally-invasive transdermal detection of nerve agents. *The Analyst* **142,** 918–924 (2017).
54. Miller, P. R., Xiao, X., Brener, I., Burckel, D. B., Narayan, R. & Polsky, R. Microneedle-based transdermal sensor for on-chip potentiometric determination of K^+. *Adv. Healthc. Mater.* **3,** 876–881 (2014).
55. Skoog, S. A., Miller, P. R., Boehm, R. D., Sumant, A. V., Polsky, R. & Narayan, R. J. Nitrogen-incorporated ultrananocrystalline diamond microneedle arrays for electrochemical biosensing. *Diam. Relat. Mater.* **54,** 39–46 (2015).
56. McConville, A. & Davis, J. Transdermal microneedle sensor arrays based on palladium: Polymer composites. *Electrochem. Commun.* **72,** 162–165 (2016).
57. Miller, P. R., Gittard, S. D., Edwards, T. L., Lopez, D. M., Xiao, X., Wheeler, D. R., Monteiro-Riviere, N. A., Brozik, S. M., Polsky, R. & Narayan, R. J. Integrated carbon fiber electrodes within hollow polymer microneedles for transdermal electrochemical sensing. *Biomicrofluidics* **5,** 013415 (2011).
58. Miller, P. R., Skoog, S. A., Edwards, T. L., Lopez, D. M., Wheeler, D. R., Arango, D. C., Xiao, X., Brozik, S. M., Wang, J., Polsky, R. & Narayan, R. J. Multiplexed microneedle-based biosensor array for characterization of metabolic acidosis. *Talanta* **88,** 739–742 (2012).
59. *Global report on diabetes*. (World Health Organization, 2016).
60. Trzebinski, J., Sharma, S., Radomska-Botelho Moniz, A., Michelakis, K., Zhang, Y. & Cass, A. E. G. Microfluidic device to investigate factors affecting performance in biosensors designed for transdermal applications. *Lab Chip* **12,** 348–352 (2012).
61. Muller, D. A., Corrie, S. R., Coffey, J., Young, P. R. & Kendall, M. A. Surface modified microprojection arrays for the selective extraction of the dengue virus ns1 protein as a marker for disease. *Anal. Chem.* **84,** 3262–3268 (2012).
62. Bhargav, A., Muller, D. A., Kendall, M. A. F. & Corrie, S. R. Surface modifications of microprojection arrays for improved biomarker capture in the skin of live mice. *ACS Appl. Mater. Interfaces* **4,** 2483–2489 (2012).
63. Ng, K. W., Lau, W. M. & Williams, A. C. Towards pain-free diagnosis of skin diseases through multiplexed microneedles: biomarker extraction and detection using a highly sensitive blotting method. *Drug Deliv. Transl. Res.* **5,** 387–396 (2015).
64. Wang, M., Hu, L. & Xu, C. Recent advances in the design of polymeric microneedles for transdermal drug delivery and biosensing. *Lab Chip* **17,** 1373–1387 (2017).
65. Sharma, S., Saeed, A., Johnson, C., Gadegaard, N. & Cass, A. E. Rapid, low cost prototyping of transdermal devices for personal healthcare monitoring. *Sens. Bio-Sens. Res.* **13,** 104–108 (2017).
66. Kaseem, M., Hamad, K., Deri, F. & Ko, Y. G. A review on recent researches on polylactic acid/carbon nanotube composites. *Polym. Bull.* **74,** 2921–2937 (2017).
67. Spitalsky, Z., Tasis, D., Papagelis, K. & Galiotis, C. Carbon nanotube–polymer composites: Chemistry, processing, mechanical and electrical properties. *Prog. Polym. Sci.* **35,** 357–401 (2010).

68. Yáñez-Sedeño, P., Pingarrón, J. M., Riu, J. & Rius, F. X. Electrochemical sensing based on carbon nanotubes. *TrAC Trends Anal. Chem.* **29,** 939–953 (2010).
69. Ahammad, A. J. S., Lee, J. J. & Rahman, M. A. Electrochemical Sensors Based on Carbon Nanotubes. *Sensors* **9,** 2289–2319 (2009).
70. Fagan-Murphy, A., Allen, M. C. & Patel, B. A. Chemically modified multiwall carbon nanotube composite electrodes: An assessment of fabrication strategies. *Electrochimica Acta* **152,** 249–254 (2015).
71. Fagan-Murphy, A. & Patel, B. A. Compressed multiwall carbon nanotube composite electrodes provide enhanced electroanalytical performance for determination of serotonin. *Electrochimica Acta* **138,** 392–399 (2014).
72. Lutton, R. E. M., Moore, J., Larrañeta, E., Ligett, S., Woolfson, A. D. & Donnelly, R. F. Microneedle characterisation: the need for universal acceptance criteria and GMP specifications when moving towards commercialisation. *Drug Deliv. Transl. Res.* **5,** 313–331 (2015).
73. Davis, S. P., Landis, B. J., Adams, Z. H., Allen, M. G. & Prausnitz, M. R. Insertion of microneedles into skin: measurement and prediction of insertion force and needle fracture force. *J. Biomech.* **37,** 1155–1163 (2004).
74. Khanna, P., Luongo, K., Strom, J. A. & Bhansali, S. Axial and shear fracture strength evaluation of silicon microneedles. *Microsyst. Technol.* **16,** 973–978 (2010).
75. Donnelly, R. F., Majithiya, R., Singh, T. R. R., Morrow, D. I. J., Garland, M. J., Demir, Y. K., Migalska, K., Ryan, E., Gillen, D., Scott, C. J. & Woolfson, A. D. Design, optimization and characterisation of polymeric microneedle arrays prepared by a novel laser-based micromoulding technique. *Pharm. Res.* **28,** 41–57 (2011).
76. Khann, P., Silv, H. & Bhansali, S. Variation in microneedle geometry to increase shear strength. *Procedia Eng.* **5,** 977–980 (2010).
77. Wang, J. *Analytical electrochemistry*. (Wiley-VCH, 2000).
78. Wang, J. *Analytical Electrochemistry: Wang/Analytical Electrochemistry, Third Edition*. (John Wiley & Sons, Inc., 2006).
79. Bagotskiĭ, V. S. *Fundamentals of electrochemistry*. (Wiley-Interscience, 2006).
80. Bard, A. J. & Faulkner, L. R. *Electrochemical methods: fundamentals and applications*. (Wiley, 2001).
81. Leite, F. L., Bueno, C. C., Da Róz, A. L., Ziemath, E. C. & Oliveira, O. N. Theoretical models for surface forces and adhesion and their measurement using atomic force microscopy. *Int. J. Mol. Sci.* **13,** 12773–12856 (2012).
82. Elgrishi, N., Rountree, K. J., McCarthy, B. D., Rountree, E. S., Eisenhart, T. T. & Dempsey, J. L. A practical beginner's guide to cyclic voltammetry. *J. Chem. Educ.* **95,** 197–206 (2018).
83. Mabbott, G. A. An introduction to cyclic voltammetry. *J. Chem. Educ.* **60,** 697 (1983).
84. Stojek, Z. in *Electroanal. Methods* (eds. Scholz, F., Bond, A. M., Compton, R. G., Fiedler, D. A., Inzelt, G., Kahlert, H., Komorsky-Lovrić, š., Lohse, H., Lovrić, M., Marken, F., Neudeck, A., Retter, U., Scholz, F. & Stojek, Z.) 107–119 (Springer Berlin Heidelberg, 2010).
85. Scholz, F. Voltammetric techniques of analysis: the essentials. *ChemTexts* **1,** (2015).
86. Haddad, P. & Jackson, P. In *J. Chromatogr. Libr.* **46,** 291–321 (Elsevier, 1990).
87. Kausar, A., Rafique, I. & Muhammad, B. Review of applications of polymer/carbon nanotubes and epoxy/CNT composites. *Polym.-Plast. Technol. Eng.* **55,** 1167–1191 (2016).

88. Jin, F.-L., Li, X. & Park, S. J. Synthesis and application of epoxy resins: A review. *J. Ind. Eng. Chem.* **29,** 1–11 (2015).
89. Ajayan, P. M., Stephan, O., Colliex, C. & Trauth, D. Aligned carbon nanotube arrays formed by cutting a polymer resin--nanotube composite. *Science* **265,** 1212–1214 (1994).
90. Pumera, M., Merkoçi, A. & Alegret, S. Carbon nanotube-epoxy composites for electrochemical sensing. *Sens. Actuators B Chem.* **113,** 617–622 (2006).
91. Pérez, B., Pumera, M., del Valle, M., Merkoçi, A. & Alegret, S. Glucose biosensor based on carbon nanotube epoxy composites. *J. Nanosci. Nanotechnol.* **5,** 1694–1698 (2005).
92. López, B. P. & Merkoçi, A. Improvement of the electrochemical detection of catechol by the use of a carbon nanotube based biosensor. *Analyst* **134,** 60–64 (2008).
93. Aqel, A., El-Nour, K. M. M. A., Ammar, R. A. A. & Al-Warthan, A. Carbon nanotubes, science and technology part (I) structure, synthesis and characterisation. *Arab. J. Chem.* **5,** 1–23 (2012).
94. Kumar, M. & Ando, Y. Chemical vapor deposition of carbon nanotubes: a review on growth mechanism and mass production. *J. Nanosci. Nanotechnol.* **10,** 3739–3758 (2010).
95. Iijima, S. Helical microtubules of graphitic carbon. *Nature* **354,** 56–58 (1991).
96. Sahoo, N. G., Rana, S., Cho, J. W., Li, L. & Chan, S. H. Polymer nanocomposites based on functionalized carbon nanotubes. *Prog. Polym. Sci.* **35,** 837–867 (2010).
97. Yu, M. F., Files, B. S., Arepalli, S. & Ruoff, R. S. Tensile Loading of Ropes of Single Wall Carbon Nanotubes and their Mechanical Properties. *Phys. Rev. Lett.* **84,** 5552–5555 (2000).
98. Xie, S., Li, W., Pan, Z., Chang, B. & Sun, L. Mechanical and physical properties on carbon nanotube. *J. Phys. Chem. Solids* **61,** 1153–1158 (2000).
99. Ibrahim, K. S. Carbon nanotubes-properties and applications: a review. *Carbon Lett.* **14,** 131–144 (2013).
100. Eatemadi, A., Daraee, H., Karimkhanloo, H., Kouhi, M., Zarghami, N., Akbarzadeh, A., Abasi, M., Hanifehpour, Y. & Joo, S. Carbon nanotubes: properties, synthesis, purification, and medical applications. *Nanoscale Res. Lett.* **9,** 393 (2014).
101. Dresselhaus, M. S., Dresselhaus, G. & Jorio, A. Unusual properties and structure of carbon nanotubes. *Annu. Rev. Mater. Res.* **34,** 247–278 (2004).
102. Zhang, M. & Li, J. Carbon nanotube in different shapes. *Mater. Today* **12,** 12–18 (2009).
103. Ansari, S. Combination of molecularly imprinted polymers and carbon nanomaterials as a versatile biosensing tool in sample analysis: Recent applications and challenges. *TrAC Trends Anal. Chem.* **93,** 134–151 (2017).
104. He, H., Pham-Huy, L. A., Dramou, P., Xiao, D., Zuo, P. & Pham-Huy, C. Carbon nanotubes: applications in pharmacy and medicine. *BioMed Res. Int.* **2013,** 1–12 (2013).
105. Tans, S. J., Devoret, M. H., Dai, H., Thess, A., Smalley, R. E., Geerligs, L. J. & Dekker, C. Individual single-wall carbon nanotubes as quantum wires. *Nature* **386,** 474–477 (1997).
106. Delaney, P., Di Ventra, M. & Pantelides, S. T. Quantized conductance of multiwalled carbon nanotubes. *Appl. Phys. Lett.* **75,** 3787–3789 (1999).
107. Jourdain, V. & Bichara, C. Current understanding of the growth of carbon nanotubes in catalytic chemical vapour deposition. *Carbon* **58,** 2–39 (2013).
108. Hedman, D., Reza Barzegar, H., Rosén, A., Wågberg, T. & Andreas Larsson, J. On the stability and abundance of single walled carbon nanotubes. *Sci. Rep.* **5,** (2015).

109. Agüí, L., Yáñez-Sedeño, P. & Pingarrón, J. M. Role of carbon nanotubes in electroanalytical chemistry. *Anal. Chim. Acta* **622,** 11–47 (2008).
110. Liu, G., Riechers, S. L., Mellen, M. C. & Lin, Y. Sensitive electrochemical detection of enzymatically generated thiocholine at carbon nanotube modified glassy carbon electrode. *Electrochem. Commun.* **7,** 1163–1169 (2005).
111. Banks, C. E. & Compton, R. G. New electrodes for old: from carbon nanotubes to edge plane pyrolytic graphite. *The Analyst* **131,** 15–21 (2006).
112. Davies, T. J., Hyde, M. E. & Compton, R. G. Nanotrench arrays reveal insight into graphite electrochemistry. *Angew. Chem. Int. Ed.* **44,** 5121–5126 (2005).
113. Musameh, M., Lawrence, N. S. & Wang, J. Electrochemical activation of carbon nanotubes. *Electrochem. Commun.* **7,** 14–18 (2005).
114. Gibson, G. in *Brydsons Plast. Mater.* 773–797 (Elsevier, 2017).
115. Gantayat, S., Rout, D. & Swain, S. K. Carbon nanomaterial–reinforced epoxy composites: a review. *Polym. Plast. Technol. Eng.* **57,** 1–16 (2018).
116. Rahaman, A. & Mohanty, A. Effect of carbon nanotubes on the curing and thermomechanical behavior of epoxy/carbon nanotubes composites. *Polym. Compos.* **35,** 441–449 (2014).
117. de la Vega, A., Kovacs, J. Z., Bauhofer, W. & Schulte, K. Combined Raman and dielectric spectroscopy on the curing behaviour and stress build up of carbon nanotube–epoxy composites. *Compos. Sci. Technol.* **69,** 1540–1546 (2009).
118. Bai, J. B. & Allaoui, A. Effect of the length and the aggregate size of MWNTs on the improvement efficiency of the mechanical and electrical properties of nanocomposites-experimental investigation. *Compos. Part Appl. Sci. Manuf.* **34,** 689–694 (2003).
119. Park, J. M., Kim, D. S., Lee, J. R. & Kim, T. W. Nondestructive damage sensitivity and reinforcing effect of carbon nanotube/epoxy composites using electro-micromechanical technique. *Mater. Sci. Eng. C* **23,** 971–975 (2003).
120. Guo, P., Chen, X., Gao, X., Song, H. & Shen, H. Fabrication and mechanical properties of well-dispersed multiwalled carbon nanotubes/epoxy composites. *Compos. Sci. Technol.* **67,** 3331–3337 (2007).
121. Valentini, L., Puglia, D., Carniato, F., Boccaleri, E., Marchese, L. & Kenny, J. M. Use of plasma fluorinated single-walled carbon nanotubes for the preparation of nanocomposites with epoxy matrix. *Compos. Sci. Technol.* **68,** 1008–1014 (2008).
122. Min, C., Shen, X., Shi, Z., Chen, L. & Xu, Z. The electrical properties and conducting mechanisms of carbon nanotube/polymer nanocomposites: a review. *Polym.-Plast. Technol. Eng.* **49,** 1172–1181 (2010).
123. Grossiord, N., Loos, J., Regev, O. & Koning, C. E. Toolbox for dispersing carbon nanotubes into polymers to get conductive nanocomposites. *Chem. Mater.* **18,** 1089–1099 (2006).
124. Xu, Y., Higgins, B. & Brittain, W. J. Bottom-up synthesis of PS–CNF nanocomposites. *Polymer* **46,** 799–810 (2005).
125. Mazinani, S., Ajji, A. & Dubois, C. Morphology, structure and properties of conductive PS/CNT nanocomposite electrospun mat. *Polymer* **50,** 3329–3342 (2009).
126. Li, J., Ma, P. C., Chow, W. S., To, C. K., Tang, B. Z. & Kim, J.-K. Correlations between percolation threshold, dispersion state, and aspect ratio of carbon nanotubes. *Adv. Funct. Mater.* **17,** 3207–3215 (2007).
127. Bryning, M. B., Islam, M. F., Kikkawa, J. M. & Yodh, A. G. Very low conductivity threshold in bulk isotropic single-walled carbon nanotube-epoxy composites. *Adv. Mater.* **17,** 1186–1191 (2005).

128. Martin, C. A., Sandler, J. K. W., Shaffer, M. S. P., Schwarz, M.-K., Bauhofer, W., Schulte, K. & Windle, A. H. Formation of percolating networks in multi-wall carbon-nanotube–epoxy composites. *Compos. Sci. Technol.* **64,** 2309–2316 (2004).
129. Hu, G., Zhao, C., Zhang, S., Yang, M. & Wang, Z. Low percolation thresholds of electrical conductivity and rheology in poly(ethylene terephthalate) through the networks of multi-walled carbon nanotubes. *Polymer* **47,** 480–488 (2006).
130. Gojny, F. H., Wichmann, M. H. G., Fiedler, B., Kinloch, I. A., Bauhofer, W., Windle, A. H. & Schulte, K. Evaluation and identification of electrical and thermal conduction mechanisms in carbon nanotube/epoxy composites. *Polymer* **47,** 2036–2045 (2006).
131. Delozier, D. M., Watson, K. A., Smith, J. G., Clancy, T. C. & Connell, J. W. Investigation of aromatic/aliphatic polyimides as dispersants for single wall carbon nanotubes. *Macromolecules* **39,** 1731–1739 (2006).
132. Špitalský, Z., Krontiras, C. A., Georga, S. N. & Galiotis, C. Effect of oxidation treatment of multiwalled carbon nanotubes on the mechanical and electrical properties of their epoxy composites. *Compos. Part Appl. Sci. Manuf.* **40,** 778–783 (2009).
133. Liu, L., Etika, K. C., Liao, K.-S., Hess, L. A., Bergbreiter, D. E. & Grunlan, J. C. Comparison of covalently and noncovalently functionalized carbon nanotubes in epoxy. *Macromol. Rapid Commun.* **30,** 627–632 (2009).
134. Barrau, S., Demont, P., Perez, E., Peigney, A., Laurent, C. & Lacabanne, C. Effect of Palmitic Acid on the Electrical Conductivity of Carbon Nanotubes−Epoxy Resin Composites. *Macromolecules* **36,** 9678–9680 (2003).
135. dos Santos, A. S., Leite, T. de O. N., Furtado, C. A., Welter, C., Pardini, L. C. & Silva, G. G. Morphology, thermal expansion, and electrical conductivity of multiwalled carbon nanotube/epoxy composites. *J. Appl. Polym. Sci.* **108,** 979–986 (2008).
136. Inam, F., Reece, M. J. & Peijs, T. Shortened carbon nanotubes and their influence on the electrical properties of polymer nanocomposites. *J. Compos. Mater.* **46,** 1313–1322 (2012).
137. Pereira, C. M. C., Nóvoa, P., Martins, M., Forero, S., Hepp, F. & Pambaguian, L. Characterization of carbon nanotube 3D-structures infused with low viscosity epoxy resin system. *Compos. Struct.* **92,** 2252–2257 (2010).
138. Ventura, I. A., Rahaman, A. & Lubineau, G. The thermal properties of a carbon nanotube-enriched epoxy: Thermal conductivity, curing, and degradation kinetics. *J. Appl. Polym. Sci.* **130,** 2722–2733 (2013).
139. van der Maaden, K., Jiskoot, W. & Bouwstra, J. Microneedle technologies for (trans)dermal drug and vaccine delivery. *J. Controlled Release* **161,** 645–655 (2012).
140. Park, J.-H., Allen, M. G. & Prausnitz, M. R. Biodegradable polymer microneedles: Fabrication, mechanics and transdermal drug delivery. *J. Controlled Release* **104,** 51–66 (2005).
141. Ci, L. & Bai, J. The reinforcement role of carbon nanotubes in epoxy composites with different matrix stiffness. *Compos. Sci. Technol.* **66,** 599–603 (2006).
142. Choudhary, V., Singh, B. P. & Mathur, R. B. in *Synth. Appl. Carbon Nanotub. Their Compos.* (ed. Suzuki, S.) (InTech, 2013).
143. Bradford, P. D., Wang, X., Zhao, H., Maria, J. P., Jia, Q. & Zhu, Y. T. A novel approach to fabricate high volume fraction nanocomposites with long aligned carbon nanotubes. *Compos. Sci. Technol.* **70,** 1980–1985 (2010).
144. Ogasawara, T., Moon, S.-Y., Inoue, Y. & Shimamura, Y. Mechanical properties of aligned multi-walled carbon nanotube/epoxy composites processed using a hot-melt prepreg method. *Compos. Sci. Technol.* **71,** 1826–1833 (2011).

145. Kaur, G., Adhikari, R., Cass, P., Bown, M. & Gunatillake, P. Electrically conductive polymers and composites for biomedical applications. *RSC Adv.* **5,** 37553–37567 (2015).
146. Kumar, R. *Conducting Polymers: Synthesis, Properties and Applications*. **2,** (2015).
147. Le, T. H., Kim, Y. & Yoon, H. Electrical and electrochemical properties of conducting polymers. *Polymers* **9,** 150 (2017).
148. Shrivastava, S., Jadon, N. & Jain, R. Next-generation polymer nanocomposite-based electrochemical sensors and biosensors: A review. *TrAC Trends Anal. Chem.* **82,** 55–67 (2016).
149. Karabiberoglu, S. U., Koçak, Ç. C. & Dursun, Z. in *Carbon Nanotub. - Curr. Prog. Their Polym. Compos.* (eds. Berber, M. R. & Hafez, I. H.) (InTech, 2016).
150. Guimard, N. K., Gomez, N. & Schmidt, C. E. Conducting polymers in biomedical engineering. *Prog. Polym. Sci.* **32,** 876–921 (2007).
151. Park, J. H. & Prausnitz, M. R. Analysis of mechanical failure of polymer microneedles by axial force. *J. Korean Phys. Soc.* **56,** 1223–1227 (2010).
152. Choudhary, V., Singh, B. P. & Mathur, R. B. Carbon nanotubes and their composites. in *Syntheses and applications of carbon nanotubes and their composites* (ed Suzuki, S.; InTech, 2013).
153. Lau, C. H., Cervini, R., Clarke, S. R., Markovic, M. G., Matisons, J. G., Hawkins, S. C., Huynh, C. P. & Simon, G. P. The effect of functionalization on structure and electrical conductivity of multi-walled carbon nanotubes. *J. Nanoparticle Res.* **10,** 77–88 (2008).
154. Ham, H. T., Choi, Y. S. & Chung, I. J. An explanation of dispersion states of single-walled carbon nanotubes in solvents and aqueous surfactant solutions using solubility parameters. *J. Colloid Interface Sci.* **286,** 216–223 (2005).
155. Lee, J., Kim, M., Hong, C. K. & Shim, S. E. Measurement of the dispersion stability of pristine and surface-modified multiwalled carbon nanotubes in various nonpolar and polar solvents. *Meas. Sci. Technol.* **18,** 3707–3712 (2007).
156. Huang, Y. Y. & Terentjev, E. M. Dispersion of carbon nanotubes: mixing, sonication, stabilization, and composite properties. *Polymers* **4,** 275–295 (2012).
157. Sahoo, N. G., Jung, Y. C., Yoo, H. J. & Cho, J. W. Effect of functionalized carbon nanotubes on molecular interaction and properties of polyurethane composites. *Macromol. Chem. Phys.* **207,** 1773–1780 (2006).
158. Seligra, P. G., Lamanna, M. & Famá, L. Promising PLA-functionalized MWCNT composites to use in nanotechnology. *Polym. Compos.* **37,** 3066–3072 (2016).
159. Chrissafis, K., Paraskevopoulos, K. M., Jannakoudakis, A., Beslikas, T. & Bikiaris, D. Oxidized multiwalled carbon nanotubes as effective reinforcement and thermal stability agents of poly(lactic acid) ligaments. *J. Appl. Polym. Sci.* **118,** 2712–2721 (2010).
160. Yoon, J. T., Lee, S. C. & Jeong, Y. G. Effects of grafted chain length on mechanical and electrical properties of nanocomposites containing polylactide-grafted carbon nanotubes. *Compos. Sci. Technol.* **70,** 776–782 (2010).
161. Qian, D., Dickey, E. C., Andrews, R. & Rantell, T. Load transfer and deformation mechanisms in carbon nanotube-polystyrene composites. *Appl. Phys. Lett.* **76,** 2868–2870 (2000).
162. Wong, M., Paramsothy, M., Xu, X. J., Ren, Y., Li, S. & Liao, K. Physical interactions at carbon nanotube-polymer interface. *Polymer* **44,** 7757–7764 (2003).

163. Singh, B. P., Singh, D., Mathur, R. B. & Dhami, T. L. Influence of surface modified mwcnts on the mechanical, electrical and thermal properties of polyimide nanocomposites. *Nanoscale Res. Lett.* **3,** 444 (2008).
164. Chen, W. & Tao, X. Self-organizing alignment of carbon nanotubes in thermoplastic polyurethane. *Macromol. Rapid Commun.* **26,** 1763–1767 (2005).
165. Koerner, H., Liu, W., Alexander, M., Mirau, P., Dowty, H. & Vaia, R. A. Deformation–morphology correlations in electrically conductive carbon nanotube—thermoplastic polyurethane nanocomposites. *Polymer* **46,** 4405–4420 (2005).
166. Kuan, H. C., Ma, C. C. M., Chang, W. P., Yuen, S. M., Wu, H. H. & Lee, T. M. Synthesis, thermal, mechanical and rheological properties of multiwall carbon nanotube/waterborne polyurethane nanocomposite. *Compos. Sci. Technol.* **65,** 1703–1710 (2005).
167. Wang, J., Xu, H., Yang, D. & Wu, Y. Preparation and properties of alkaline functionalized carbon nanotubes reinforced polyurethane composites. *Fibers Polym.* **14,** 571–577 (2013).
168. Xu, M., Zhang, T., Gu, B., Wu, J. & Chen, Q. Synthesis and properties of novel polyurethane−urea/multiwalled carbon nanotube composites. *Macromolecules* **39,** 3540–3545 (2006).
169. Kim, K. H. & Jo, W. H. A strategy for enhancement of mechanical and electrical properties of polycarbonate/multi-walled carbon nanotube composites. *Carbon* **47,** 1126–1134 (2009).
170. Khan, F., Rafi Ahmad, S. & A. Syed, A. Nanotube Composites Produced from Single-Walled Carbon Nanotubes and Polycarbonate. *JOAM* **1,** 344-347 (2007).
171. Moon, S. I., Jin, F., Lee, C., Tsutsumi, S. & Hyon, S. H. Novel carbon nanotube/poly(L-lactic acid) nanocomposites; their modulus, thermal stability, and electrical conductivity. *Macromol. Symp.* **224,** 287–296 (2005).
172. Blake, R., Coleman, J. N., Byrne, M. T., McCarthy, J. E., Perova, T. S., Blau, W. J., Fonseca, A., Nagy, J. B. & Gun'ko, Y. K. Reinforcement of poly(vinyl chloride) and polystyrene using chlorinated polypropylene grafted carbon nanotubes. *J. Mater. Chem.* **16,** 4206–4213 (2006).
173. Sanchez-Garcia, M. D., Lagaron, J. M. & Hoa, S. V. Effect of addition of carbon nanofibers and carbon nanotubes on properties of thermoplastic biopolymers. *Compos. Sci. Technol.* **70,** 1095–1105 (2010).
174. Kim, H. S., Chae, Y. S., Choi, J. H., Yoon, J. S. & Jin, H. J. Thermal Properties of Poly(ε-Caprolactone)/Multiwalled Carbon Nanotubes Composites. *Adv. Compos. Mater.* **17,** 157–166 (2008).
175. Kalakonda, P. & Banne, S. Thermomechanical properties of PMMA and modified SWCNT composites. *Nanotechnol. Sci. Appl.* **10,** 45–52 (2017).
176. Blond, D., Barron, V., Ruether, M., Ryan, K. P., Nicolosi, V., Blau, W. J. & Coleman, J. N. Enhancement of modulus, strength, and toughness in poly(methyl methacrylate)-based composites by the incorporation of poly(methyl methacrylate)-functionalized nanotubes. *Adv. Funct. Mater.* **16,** 1608–1614 (2006).
177. Koysuren, O., Karaman, M. & Ozyurt, D. Effect of noncovalent chemical modification on the electrical conductivity and tensile properties of poly(methyl methacrylate)/carbon nanotube composites. *J. Appl. Polym. Sci.* **127,** 4557–4563 (2013).

178. Worsley, M. A., Kucheyev, S. O., Kuntz, J. D., Hamza, A. V., Joe H. Satcher, J. & Baumann, T. F. Stiff and electrically conductive composites of carbon nanotube aerogels and polymers. *J. Mater. Chem.* **19,** 3370–3372 (2009).
179. Yuen, S. M., Ma, C. C. M., Lin, Y. Y. & Kuan, H. C. Preparation, morphology and properties of acid and amine modified multiwalled carbon nanotube/polyimide composite. *Compos. Sci. Technol.* **67,** 2564–2573 (2007).
180. Ge, J. J., Zhang, D., Li, Q., Hou, H., Graham, M. J., Dai, L., Harris, F. W. & Cheng, S. Z. D. Multiwalled carbon nanotubes with chemically grafted polyetherimides. *J. Am. Chem. Soc.* **127,** 9984–9985 (2005).
181. Wang, S. F., Shen, L., Zhang, W. D. & Tong Y. J. Preparation and mechanical properties of chitosan/carbon nanotubes composites. *Biomacromolecules* **6**, 3067-3072 (2005).
182. Tamburri, E., Orlanducci, S., Terranova, M. L., Valentini, F., Palleschi, G., Curulli, A., Brunetti, F., Passeri, D., Alippi, A. & Rossi, M. Modulation of electrical properties in single-walled carbon nanotube/conducting polymer composites. *Carbon* **43,** 1213–1221 (2005).
183. Ramasubramaniam, R., Chen, J. & Liu, H. Homogeneous carbon nanotube/polymer composites for electrical applications. *Appl. Phys. Lett.* **83,** 2928 (2003).
184. Lizundia, E., Sarasua, J. R., D'Angelo, F., Orlacchio, A., Martino, S., Kenny, J. M. & Armentano, I. Biocompatible poly(L-lactide)/MWCNT nanocomposites: morphological characterization, electrical properties, and stem cell interaction. *Macromol. Biosci.* **12,** 870–881 (2012).
185. Safadi, B., Andrews, R. & Grulke, E. A. Multiwalled carbon nanotube polymer composites: Synthesis and characterization of thin films. *J. Appl. Polym. Sci.* **84,** 2660–2669 (2002).
186. Velasco-Santos, C., Martínez-Hernández, A. L., Fisher, F. T., Ruoff, R. & Castaño, V. M. Improvement of Thermal and Mechanical Properties of Carbon Nanotube Composites through Chemical Functionalization. *Chem. Mater.* **15,** 4470–4475 (2003).
187. Ayman S Ayesh, Sobhy S Ibrahim & Abdullah A Aljaafari. Electrical, optical, and rheological properties of ozone-treated multiwalled carbon nanotubes–polystyrene nanocomposites. *J. Reinf. Plast. Compos.* **32,** 359–370 (2013).
188. Mitchell, C. A. & Krishnamoorti, R. Dispersion of single-walled carbon nanotubes in Poly(ε-caprolactone). *Macromolecules* **40,** 1538–1545 (2007).
189. Kim, H. M., Kim, K., Lee, C. Y., Joo, J., Cho, S. J., Yoon, H. S., Pejaković, D. A., Yoo, J. W. & Epstein, A. J. Electrical conductivity and electromagnetic interference shielding of multiwalled carbon nanotube composites containing Fe catalyst. *Appl. Phys. Lett.* **84,** 589–591 (2004).
190. Skákalová, V., Dettlaff-Weglikowska, U. & Roth, S. Electrical and mechanical properties of nanocomposites of single wall carbon nanotubes with PMMA. *Synth. Met.* **152,** 349–352 (2005).
191. Slobodian, P., Lengálová, A., Sáha, P. & Šlouf, M. Poly(methyl methacrylate)/Multi-wall carbon nanotubes composites prepared by solvent cast technique: Composites electrical percolation threshold. *J. Reinf. Plast. Compos.* **26,** 1705–1712 (2007).
192. Khosla, A. & Gray, B. L. Preparation, characterization and micromolding of multi-walled carbon nanotube polydimethylsiloxane conducting nanocomposite polymer. *Mater. Lett.* **63,** 1203–1206 (2009).

193. Tang, Q. Y., Chen, J., Chan, Y. C. & Chung, C. Y. Effect of carbon nanotubes and their dispersion on thermal curing of polyimide precursors. *Polym. Degrad. Stab.* **95,** 1672–1678 (2010).
194. Gonçalves, C., Gonçalves, I. C., Magalhães, F. D. & Pinto, A. M. Poly(lactic acid) composites containing carbon-based nanomaterials: a review. *Polymers* **9,** 269 (2017).
195. Oliveira, J. E., Mattoso, L. H. C., Medeiros, E. S. & Zucolotto, V. Poly(lactic acid)/carbon nanotube fibers as novel platforms for glucose biosensors. *Biosensors* **2,** 70–82 (2012).
196. Han, H. S., You, J. M., Jeong, H. & Jeon, S. Electrochemical sensing of H2O2 by the modified electrode with pd nanoparticles on multi-walled carbon nanotubes-g-Poly(Lactic Acid). *J. Nanosci. Nanotechnol.* **14,** 4050–4057 (2014).
197. Pisoschi, A. M., Pop, A., Serban, A. I. & Fafaneata, C. Electrochemical methods for ascorbic acid determination. *Electrochimica Acta* **121,** 443–460 (2014).
198. Liu, C. X. & Choi, J. W. Improved dispersion of carbon nanotubes in polymers at high concentrations. *Nanomaterials* **2,** 329–347 (2012).
199. Gnanasekaran, K., de With, G. & Friedrich, H. Quantitative analysis of connectivity and conductivity in mesoscale multiwalled carbon nanotube networks in polymer composites. *J. Phys. Chem. C* **120,** 27618–27627 (2016).
200. Aguilar, J. O., Bautista-Quijano, J. R. & Aviles, F. Influence of carbon nanotube clustering on the electrical conductivity of polymer composite films. *Express Polym. Lett.* **4,** 292–299 (2010).
201. Mathur, R. B., Pande, S., Singh, B. P. & Dhami, T. L. Electrical and mechanical properties of multi-walled carbon nanotubes reinforced PMMA and PS composites. *Polym. Compos.* **29,** 717–727 (2008).
202. Ghislandi, M., Tkalya, E., Schillinger, S., Koning, C. E & de With, G. High performance graphene- and MWCNTs-based PS/PPO composites obtained via organic solvent dispersion. *Compos. Sci. Technol.* **80,** 16-22 (2013).
203. Atif, R. & Inam, F. Reasons and remedies for the agglomeration of multilayered graphene and carbon nanotubes in polymers. *Beilstein J. Nanotechnol.* **7,** 1174–1196 (2016).
204. Atif, R., Wei, J., Shyha, I. & Inam, F. Use of morphological features of carbonaceous materials for improved mechanical properties of epoxy nanocomposites. *RSC Adv* **6,** 1351–1359 (2016).
205. Wu, D., Wu, L., Zhang, M. & Zhao, Y. Viscoelasticity and thermal stability of polylactide composites with various functionalized carbon nanotubes. *Polym. Degrad. Stab.* **93,** 1577–1584 (2008).
206. Sobkowicz, M. J., Sosa, R. & Dorgan, J. R. Supramolecular bionanocomposites, part 2: Effects of carbon nanoparticle surface functionality on polylactide crystallization. *J. Appl. Polym. Sci.* **121,** 2029–2038 (2011).
207. Pisoschi, A. M., Pop, A., Negulescu, G. P. & Pisoschi, A. Determination of ascorbic acid content of some fruit juices and wine by voltammetry performed at pt and carbon paste electrodes. *Molecules* **16,** 1349–1365 (2011).
208. Ma, P. C., Siddiqui, N. A., Marom, G. & Kim, J. K. Dispersion and functionalization of carbon nanotubes for polymer-based nanocomposites: a review. *Compos. Part Appl. Sci. Manuf.* **41,** 1345–1367 (2010).
209. Lu, K. L. Mechanical damage of carbon nanotubes by ultrasound. *Carbon* **34,** 814–816 (1996).

210. Thostenson, E. T., Ren, Z. & Chou, T. W. Advances in the science and technology of carbon nanotubes and their composites: a review. *Compos. Sci. Technol.* **61,** 1899–1912 (2001).
211. Hilding, J., Grulke, E. A., Zhang, Z. G. & Lockwood, F. dispersion of carbon nanotubes in liquids. *J. Dispers. Sci. Technol.* **24,** 1–41 (2003).
212. Cheng, Q., Debnath, S., Gregan, E. & Byrne, H. J. Ultrasound-assisted SWNTs dispersion: effects of sonication parameters and solvent properties. *J. Phys. Chem. C* **114,** 8821–8827 (2010).
213. Njuguna, J., Vanli, O. A. & Liang, R. A review of spectral methods for dispersion characterization of carbon nanotubes in aqueous suspensions. *J. Spectrosc.* **2015,** 1–11 (2015).
214. Yang, K., Yi, Z., Jing, Q., Yue, R., Jiang, W. & Lin, D. Sonication-assisted dispersion of carbon nanotubes in aqueous solutions of the anionic surfactant SDBS: the role of sonication energy. *Chin. Sci. Bull.* **58,** 2082–2090 (2013).
215. Tan, Y. & Resasco, D. E. Dispersion of single-walled carbon nanotubes of narrow diameter distribution. *J. Phys. Chem. B* **109,** 14454–14460 (2005).
216. Correlation of carbon nanotube dispersability in aqueous surfactant solutions and polymers. *Carbon* **47,** 602–612 (2009).
217. Qsonica (2009), Sonicators: *'Ultrasonic Processing Equipment'* [online] Available at www.sonicator.com/20-sonicators [Accessed on 11 March 2018].
218. Fernandes, R. M. F., Abreu, B., Claro, B., Buzaglo, M., Regev, O., Furó, I. & Marques, E. F. Dispersing carbon nanotubes with ionic surfactants under controlled conditions: comparisons and insight. *Langmuir* **31,** 10955–10965 (2015).
219. Pletnev, M. Y. Chemistry of surfactants in *Stud. Interface Sci.* **13,** 1–97 (Elsevier, 2001).
220. Vaisman, L., Wagner, H. D. & Marom, G. The role of surfactants in dispersion of carbon nanotubes. *Adv. Colloid Interface Sci.* **128–130,** 37–46 (2006).
221. Strano, M. S., Moore, V. C., Miller, M. K., Allen, M. J., Haroz, E. H., Kittrell, C., Hauge, R. H. & Smalley, R. E. The role of surfactant adsorption during ultrasonication in the dispersion of single-walled carbon nanotubes. *J. Nanosci. Nanotechnol.* **3,** 81–86 (2003).
222. Tkalya, E. E., Ghislandi, M., de With, G. & Koning, C. E. The use of surfactants for dispersing carbon nanotubes and graphene to make conductive nanocomposites. *Curr. Opin. Colloid Interface Sci.* **17,** 225–232 (2012).
223. Richard, C. Supramolecular self-assembly of lipid derivatives on carbon nanotubes. *Science* **300,** 775–778 (2003).
224. Sun, Z., Nicolosi, V., Rickard, D., Bergin, S. D., Aherne, D. & Coleman, J. N. Quantitative evaluation of surfactant-stabilized single-walled carbon nanotubes: dispersion quality and its correlation with zeta potential. *J. Phys. Chem. C* **112,** 10692–10699 (2008).
225. Grossiord, N., Kivit, P. J. J., Loos, J., Meuldijk, J., Kyrylyuk, A. V., van der Schoot, P. & Koning, C. E. On the influence of the processing conditions on the performance of electrically conductive carbon nanotube/polymer nanocomposites. *Polymer* **49,** 2866–2872 (2008).
226. Sa, V. & Kornev, K. G. Analysis of stability of nanotube dispersions using surface tension isotherms. *Langmuir* **27,** 13451–13460 (2011).
227. Rastogi, R., Kaushal, R., Tripathi, S. K., Sharma, A. L., Kaur, I. & Bharadwaj, L. M. Comparative study of carbon nanotube dispersion using surfactants. *J. Colloid Interface Sci.* **328,** 421–428 (2008).

228. Dölle, S., Lechner, B. D., Park, J. H., Schymura, S., Lagerwall, J. P. F. & Scalia, G. Utilizing the krafft phenomenon to generate ideal micelle-free surfactant-stabilized nanoparticle suspensions. *Angew. Chem. Int. Ed.* **51,** 3254–3257 (2012).
229. Yu, J., Grossiord, N., Koning, C. E. & Loos, J. Controlling the dispersion of multi-wall carbon nanotubes in aqueous surfactant solution. *Carbon* **45,** 618–623 (2007).
230. Gong, X., Liu, J., Baskaran, S., Voise, R. D. & Young, J. S. Surfactant-assisted processing of carbon nanotube/polymer composites. *Chem. Mater.* **12,** 1049–1052 (2000).
231. Cai, N., Gong, Y., Chian, K. S., Chan, V. & Liao, K. Adhesion dynamics of porcine esophageal fibroblasts on extracellular matrix protein-functionalized poly(lactic acid). *Biomed. Mater.* **3,** 015014 (2008).
232. Velasco-Santos, C., Mart nez-Hern ndez, A. L., Fisher, F., Ruoff, R. & Casta o, V. M. Dynamical–mechanical and thermal analysis of carbon nanotube–methyl-ethyl methacrylate nanocomposites. *J. Phys. Appl. Phys.* **36,** 1423–1428 (2003).
233. Vaisman, L., Marom, G. & Wagner, H. D. Dispersions of surface-modified carbon nanotubes in water-soluble and water-insoluble polymers. *Adv. Funct. Mater.* **16,** 357–363 (2006).
234. Vilčáková, J., Moučka, R., Svoboda, P., Ilčíková, M., Kazantseva, N., Hřibová, M., Mičušík, M. & Omastová, M. Effect of surfactants and manufacturing methods on the electrical and thermal conductivity of carbon nanotube/silicone composites. *Molecules* **17,** 13157–13174 (2012).
235. Zhong, W. & Claverie, J. P. Probing the carbon nanotube-surfactant interaction for the preparation of composites. *Carbon* **51,** 72–84 (2013).
236. Lu, G. W. & Gao, P. in *Handb. Non-Invasive Drug Deliv. Syst.* 59–94 (Elsevier, 2010).
237. Jiang, L., Gao, L. & Sun, J. Production of aqueous colloidal dispersions of carbon nanotubes. *J. Colloid Interface Sci.* **260,** 89–94 (2003).
238. Pircheraghi, G., Foudazi, R. & Manas-Zloczower, I. Characterization of carbon nanotube dispersion and filler network formation in melted polyol for nanocomposite materials. *Powder Technol.* **276,** 222–231 (2015).
239. Kim, S., Lee, Y. I., Kim, D. H., Lee, K. J., Kim, B. S., Hussain, M. & Choa, Y. H. Estimation of dispersion stability of UV/ozone treated multi-walled carbon nanotubes and their electrical properties. *Carbon* **51,** 346–354 (2013).
240. Hoyer, B. & Jensen, N. Stabilization of the voltammetric serotonin signal by surfactants. *Electrochem. Commun.* **8,** 323–328 (2006).
241. Blanco-López, M. C., Lobo-Castañón, M. J., Ordieres, A. J. M. & Tuñón-Blanco, P. Electrochemical behavior of catecholamines and related compounds at *in situ* surfactant modified carbon paste electrodes. *Electroanalysis* **19,** 207–213 (2007).
242. Gowda, J. I., Buddanavar, A. T. & Nandibewoor, S. T. Fabrication of multiwalled carbon nanotube-surfactant modified sensor for the direct determination of toxic drug 4-aminoantipyrine. *J. Pharm. Anal.* **5,** 231–238 (2015).
243. Gowda, J. I., M., M. & Nandibewoor, S. T. CTAB functionalized multiwalled carbon nanotube composite modified electrode for the determination of 6-mercaptopurine. *Sens. Bio-Sens. Res.* **12,** 1–7 (2017).
244. Hussain, S., Amade, R., Jover, E. & Bertran, E. Nitrogen plasma functionalization of carbon nanotubes for supercapacitor applications. *J. Mater. Sci.* **48,** 7620–7628 (2013).
245. Dumée, L., Sears, K., Schütz, J., Finn, N., Duke, M. & Gray, S. Influence of the sonication temperature on the debundling kinetics of carbon nanotubes in propan-2-ol. *Nanomaterials* **3,** 70–85 (2013).

246. Dhar, S., Rana, D. K., Sarkar, A., Mandal, T. K., Ghosh, S. & Bhattacharya, S. C. Physicochemical characterization of reverse micelles of Triton X using 1-anthracene sulphonate as fluorescent probe: A spectroscopic study. *Colloids Surf. Physicochem. Eng. Asp.* **349,** 117–124 (2009).
247. Desando, M. A., Lahajnar, G. & Sepe, A. Proton magnetic relaxation and the aggregation of n-octylammonium n-octadecanoate surfactant in deuterochloroform solution. *J. Colloid Interface Sci.* **345,** 338–345 (2010).
248. Anand, U., Jash, C. & Mukherjee, S. Spectroscopic determination of Critical Micelle Concentration in aqueous and non-aqueous media using a non-invasive method. *J. Colloid Interface Sci.* **364,** 400–406 (2011).
249. Klíčová, L., Šebej, P., Štacko, P., Filippov, S. K., Bogomolova, A., Padilla, M. & Klán, P. CTAB/water/chloroform reverse micelles: a closed or open association model? *Langmuir* **28,** 15185–15192 (2012).
250. Kolesnikova, A. A., Eremin, Y. S. & Grekhov, A. M. Time-stability dispersion of carbon nanotubes in chloroform. *Phys. Procedia* **72,** 51–55 (2015).
251. Eremin, Y. S., Kolesnikova, A. A. & Grekhov, A. M. Agglomeration and sedimentation of MWCNTS in chloroform. *Phys. Procedia* **72,** 56–61 (2015).
252. Pinto, V., Costa-Almeida, R., Rodrigues, I., Guardão, L., Soares, R. & Guedes, R. Biocompatibility study of PLA/GNP and PLA/CNT-COOH biodegradable nanocomposites. *Conference paper in MRS* (2015).
253. Magrez, A., Kasas, S., Salicio, V., Pasquier, N., Seo, J. W., Celio, M., Catsicas, S., Schwaller, B. & Forró, L. Cellular toxicity of carbon-based nanomaterials. *Nano Lett.* **6,** 1121–1125 (2006).
254. Allegri, M., Perivoliotis, D. K., Bianchi, M. G., Chiu, M., Pagliaro, A., Koklioti, M. A., Trompeta, A.-F. A., Bergamaschi, E., Bussolati, O. & Charitidis, C. A. Toxicity determinants of multi-walled carbon nanotubes: The relationship between functionalization and agglomeration. *Toxicol. Rep.* **3,** 230–243 (2016).
255. Liu, Y., Zhao, Y., Sun, B. & Chen, C. Understanding the toxicity of carbon nanotubes. *Acc. Chem. Res.* **46,** 702–713 (2013).
256. McCullen, S. D., Stevens, D. R., Roberts, W. A., Clarke, L. I., Bernacki, S. H., Gorga, R. E. & Loboa, E. G. Characterization of electrospun nanocomposite scaffolds and biocompatibility with adipose-derived human mesenchymal stem cells. *Int. J. Nanomedicine* **2,** 253–263 (2007).
257. Shao, S., Zhou, S., Li, L., Li, J., Luo, C., Wang, J., Li, X. & Weng, J. Osteoblast function on electrically conductive electrospun PLA/MWCNTs nanofibers. *Biomaterials* **32,** 2821–2833 (2011).
258. Li, Z., Zhao, X., Ye, L., Coates, P., Caton-Rose, F. & Martyn, M. Structure and blood compatibility of highly oriented PLA/MWNTs composites produced by solid hot drawing. *J. Biomater. Appl.* **28,** 978–989 (2014).
259. Correia Pinto, V., Costa-Almeida, R., Rodrigues, I., Guardão, L., Soares, R. & Miranda Guedes, R. Exploring the *in vitro* and *in vivo* compatibility of PLA, PLA/GNP and PLA/CNT-COOH biodegradable nanocomposites: Prospects for tendon and ligament applications. *J. Biomed. Mater. Res. A* **105,** 2182–2190 (2017).
260. Jeong, H. R., Lee, H. S., Choi, I. J. & Park, J. H. Considerations in the use of microneedles: pain, convenience, anxiety and safety. *J. Drug Target.* **25,** 29–40 (2017).
261. Haeri, M., Goldberg, S. & Gilbert, J. L. The voltage-dependent electrochemical impedance spectroscopy of CoCrMo medical alloy using time-domain techniques:

Generalized Cauchy–Lorentz, and KWW–Randles functions describing non-ideal interfacial behaviour. *Corros. Sci.* **53,** 582–588 (2011).
262. Haeri, M. & Gilbert, J. L. Study of cellular dynamics on polarized CoCrMo alloy using time-lapse live-cell imaging. *Acta Biomater.* **9,** 9220–9228 (2013).
263. Haeri M., Wollert, T., Langford, G. M. & Gilbert, J. L. Electrochemical control of cell death by reduction-induced intrinsic apoptosis and oxidation-induced necrosis on CoCrMo alloy *in vitro*. *Biomaterials* **33,** 6295–6304 (2012).
264. Tominaga M., Kumagai, E. & Harada, S. Effect of electrical stimulation on HIV-1-infected HeLa cells cultured on an electrode surface. *App. Microbiol. Biotechnol.* **61,** 447-450 (2003).
265. Veiga, V. F., Nimrichter, L., Teixeira, C. A., Morales, M. M., Alviano, C. S., Rodrigues, M. L. & Holandino, C. Exposure of human leukemic cells to direct electric current. *Cell Biochem. Biophys.* **42,** 61–74 (2005).
266. Kumagai, E., Tominaga, M. & Harada, S. Sensitivity to electrical stimulation of human immunodeficiency virus type 1 and MAGIC-5 cells. *AMB Express* **1,** 23 (2011).
267. Aizawa, M., Koyama, S., Kimura, K., Haruyama, T., Yanagida, Y. & Kobatake, E. Electrically stimulated modulation of cellular function in proliferation, differentiation, and gene expression. *Electrochemistry* **67,** 118–125 (1999).
268. Kinosita Jr, K. & Tsong, T. Y. Formation and resealing of pores of controlled sizes in human erythrocyte membrane. *Nature* **268,** 438–441 (1977).
269. Tsong, T. Y. Electroporation of cell membranes. *Biophys. J.* **60,** 297–306 (1991).
270. Tandon, N., Marsano, A., Maidhof, R., Numata, K., Montouri-Sorrentino, C., Cannizzaro, C., Voldman, J. & Vunjak-Novakovic, G. Surface-patterned electrode bioreactor for electrical stimulation. *Lab. Chip* **10,** 692–700 (2010).
271. Koyama, S., Haruyama, T., Kobatake, E. & Aizawa, M. Electrically induced NGF production by astroglial cells. *Nat. Biotechnol.* **15,** 164–166 (1997).
272. Yaoita, M., Shinohara, H., Aizawa, M., Hayakawa, Y., Yamashita, T. & Ikariyama, Y. Potential-controlled morphological change and lysis of HeLa cells cultured on an electrode surface. *J. Electroanal. Chem. Interfacial Electrochem.* **254,** 169–177 (1988).
273. Ragone, C., Minopoli, M., Ingangi, V., Botti, G., Fratangelo, F., Pessi, A., Stoppelli, M. P., Ascierto, P. A., Ciliberto, G., Motti, M. L. & Carriero, M. V. Targeting the cross-talk between Urokinase receptor and Formyl peptide receptor type 1 to prevent invasion and trans-endothelial migration of melanoma cells. *J. Exp. Clin. Cancer Res.* **36,** (2017).
274. Scheitza, S., Bonifas, J. & Blömeke, B. Variable NAT1 Enzyme Activity in Long-Term Cultured Human HaCaT Keratinocytes. *J. Toxicol. Environ. Health A* **75,** 471–477 (2012).
275. Kumar, V., Sharma, N. & Maitra, S. S. *In vitro* and *in vivo* toxicity assessment of nanoparticles. *Int. Nano Lett.* **7,** 243–256 (2017).
276. Li, W., Zhou, J. & Xu, Y. Study of the *in vitro* cytotoxicity testing of medical devices. *Biomed. Rep.* **3,** 617–620 (2015).
277. Strojan, K., Leonardi, A., Bregar, V. B., Križaj, I., Svete, J. & Pavlin, M. Dispersion of nanoparticles in different media importantly determines the composition of their protein corona. *PLOS ONE* **12,** e0169552 (2017).
278. Zanganeh, S., Spitler, R., Erfanzadeh, M., Alkilany, A. M. & Mahmoudi, M. Protein corona: opportunities and challenges. *Int. J. Biochem. Cell Biol.* **75,** 143–147 (2016).
279. Holder, A. L., Goth-Goldstein, R., Lucas, D. & Koshland, C. P. Particle-Induced Artifacts in the MTT and LDH Viability Assays. *Chem. Res. Toxicol.* **25,** 1885–1892 (2012).

280. Wörle-Knirsch, J. M., Pulskamp, K. & Krug, H. F. Oops they did it again! Carbon nanotubes hoax scientists in viability assays. *Nano Lett.* **6,** 1261–1268 (2006).
281. Casey, A., Herzog, E., Lyng, F. M., Byrne, H. J., Chambers, G. & Davoren, M. Single walled carbon nanotubes induce indirect cytotoxicity by medium depletion in A549 lung cells. *Toxicol. Lett.* **179,** 78–84 (2008).
282. Wang, G., Zhang, J., Dewilde, A. H., Pal, A. K., Bello, D., Therrien, J. M., Braunhut, S. J. & Marx, K. A. Understanding and correcting for carbon nanotube interferences with a commercial LDH cytotoxicity assay. *Toxicology* **299,** 99–111 (2012).
283. Gabi, M., Sannomiya, T., Larmagnac, A., Puttaswamy, M. & Vörös, J. Influence of applied currents on the viability of cells close to microelectrodes. *Integr Biol* **1,** 108–115 (2009).
284. Tominaga, M., Kumagai, E. & Harada, S. Effect of electrical stimulation on HIV-1-infected HeLa cells cultured on an electrode surface. *Appl. Microbiol. Biotechnol.* **61,** 447–450 (2003).
285. Miller, P. R., Skoog, S. A., Edwards, T. L., Wheeler, D. R., Xiao, X., Brozik, S. M., Polsky, R. & Narayan, R. J. Hollow microneedle-based sensor for multiplexed transdermal electrochemical sensing. *J. Vis. Exp.* (2012). doi:10.3791/4067
286. Fagan-Murphy, A. & Patel, B. A. Compressed multiwall carbon nanotube composite electrodes provide enhanced electroanalytical performance for determination of serotonin. *Electrochimica Acta* **138,** 392–399 (2014).
287. Fagan-Murphy, A., Kataria, S. & Patel, B. A. Electrochemical performance of multi-walled carbon nanotube composite electrodes is enhanced with larger diameters and reduced specific surface area. *J. Solid State Electrochem.* **20,** 785–792 (2016).